U.PORTO
FACULDADE DE CIÊNCIAS
UNIVERSIDADE DO PORTO

1D and 2D nanomaterials as building blocks for 3D composites: surfactant-mediated assembly, characterization and electrocatalytic studies

Bárbara Catarina Abreu Teixeira de Brito e Faro

Tese de Doutoramento apresentada à
Faculdade de Ciências da Universidade do Porto,
Química

2021

PhD

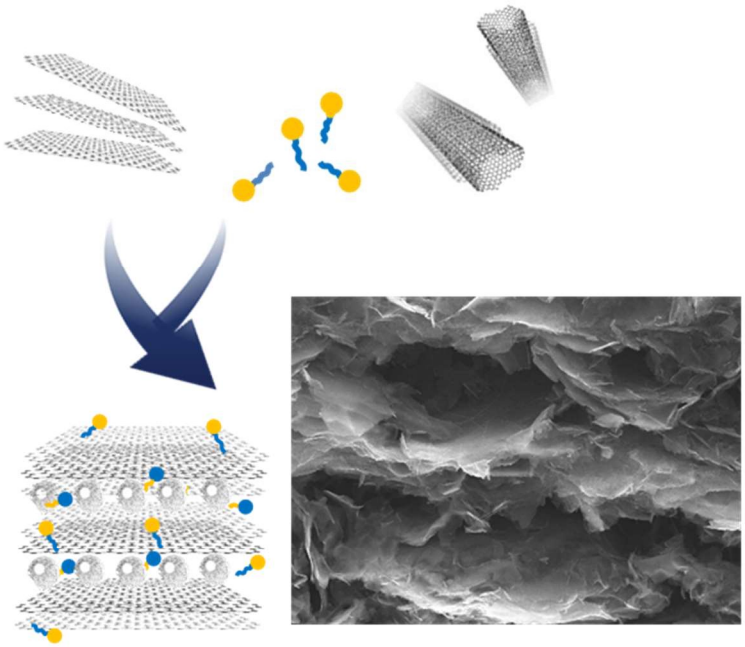

1D and 2D nanomaterials as building blocks for 3D composites: surfactant-mediated assembly, characterization and electrocatalytic studies

Bárbara Catarina Abreu Teixeira de Brito e Faro

Doutoramento em Química Sustentável
Departamento de Química e Bioquímica
2021

Orientador
Eduardo Jorge Figueira Marques
Professor Associado com Agregação
Faculdade de Ciências da Universidade do Porto

Coorientador
Ana Cristina Moreira Freire
Professora Catedrática
Faculdade de Ciências da Universidade do Porto

À minha mãe

Ao Lourenço

Acknowledgments

I would like to express my deepest gratitude to all the people and institutions that made this journey possible and fruitful.

To my supervisor, Professor Eduardo Marques, for the guidance, dedication, critical suggestions, precious discussions, and for all the knowledge shared.

To my co-supervisor, Professor Cristina Freire, for the opportunity to develop this project and inspire me to learn electrochemistry. A special thanks to Marta Nunes, for introducing me to this world, for the discussions and attention, and to Diana Fernandes, for all the valuable input.

To Professor Oren Regev for the productive discussions and sharing of knowledge.

To Professor Manuel Azenha, Vanessa Ferreira and Soraia Sá for the assistance with Raman and BET analysis, and to Rui Rocha, for the precious advice in SEM and AFM preparations.

To Ricardo Fernandes, for all the discussions and fruitful brainstorming.

To my colleagues in RG3, especially Bárbara, Isabel, Raquel and Inês – thank you for all the support, motivation, and good moments in the laboratory or around a cup of coffee.

To the younger members that worked in our group, Pedro Ferreira, Andreia Guimarães, Ana Sofia Pires, Marcos Rocha, Rui Machado, Dmitriy Moreira, Dinis Silva and Ana Sofia Silva.

To the staff, colleagues, and Professors of the Physical-Chemistry group for the support.

To CIQ-UP, REQUIMTE-LAQV, and Department of Chemistry and Biochemistry of the Faculty of Sciences, University of Porto, for providing me the conditions to develop this project.

To ChemMat Doctoral Programme and Fundação para a Ciência e Tecnologia (FCT) for the PhD grant PD/BD/128129/2016.

To my friends, for all the good moments that made these years even better.

To my family, specially to my grandmother, my sister, Bi, and my family-in-law, for the love and support, and to my mother, my eternal inspiration.

To Lourenço, for the love, endless patience, and motivation. And of course, to our little one.

Abstract

The building of self-assembled hybrid structures by the combination of carbon nanotubes (CNTs) and 2D layered nanomaterials (e.g. graphene, and inorganic graphene analogues) is an emerging area in material science and nanotechnology, posing considerable fundamental and technical challenges. In parallel, the use of both hard and soft interfaces for the fabrication of this type of nanocomposites—by the functionalization of the hard surfaces through the adsorption of surfactants (or other amphiphilic dispersants)—provides further versatility and tunability in interactions, hierarchical organization and resulting chemical, electrical, thermal, optical and mechanical properties. Consequently, innumerous possibilities for applications may appear, such as in electronics, energy, sensing and catalysis. Considering all the challenges and possibilities, the scope of this project focused on three main goals: (i) preparation and non-covalent functionalization of the 1D and 2D nanomaterials; (ii) design and implementation of the surfactant-mediated assembly of the 3D nanocomposites, and (iii) proof-of-concept studies regarding the application of the obtained structures as electrocatalysts for the oxygen reactions (relevant e.g. to fuel cells), namely the oxygen reduction reaction (ORR) and the oxygen evolution reaction (OER).

In the first part of this project, the dispersibility of multiwalled carbon nanotubes (MWNTs) using gemini surfactants with *n*-*s*-*n* structure (with *n* being the number of carbon atoms in the alkyl chain and *s* the number of carbon atoms in the spacer) was systematically investigated, varying spacer and tail length of the gemini and comparing their overall performance with that of single-tailed homologue surfactants. Using a strictly controlled experimental procedure, dispersibility curves (plots of dispersed MWNT concentration vs surfactant concentration) were obtained, allowing to determine quantitative metrics and gain molecular insight on the surfactant features that influence MWNT dispersibility.

In another work, the dispersibility of 1D CNTs and 2D graphene nanoplatelets (GnPs) was compared using two different surfactants – sodium cholate and TritonX-100. Two approaches were considered regarding the 2D nanomaterial dispersions: exfoliation of GnPs from 3D graphite and exfoliation of commercially available GnPs. One of the most significant aspects of this study was the obtention of a dispersibility master curve, implying that the dispersal process is ruled by common features, independently of the nanomaterial used (1D or 2D). SEM and AFM imaging confirmed that the applied methodology allowed to obtain well-dispersed MWNTs and few-layer GnPs. Further, this

study allowed to rationalize the dispersibility of the different carbon nanomaterials in aqueous surfactant solutions in terms of energy delivered to the system in the exfoliation process.

With a set of results in the dispersion and functionalization of 1D carbon nanotubes and 2D graphene nanoplatelets and aiming at the application of these materials as building blocks for composites, we took a step forward to study the effect of polymer/surfactant mixtures in CNT dispersibility. Four combinations of non-ionic + ionic dispersant were selected taking into account the polymer and surfactant charge: PVP+SDBS, PVP+CTAB, TX-100+PDDA and TX-100+PAS. Interesting features emerged from the application of these polymer/surfactant mixtures as dispersants for CNTs, with some systems showing strong synergism in the concentration of nanotubes dispersed. The separation of the MWNTs from the initial bundles was evaluated by SEM, and non-covalent functionalization was confirmed by zeta potential, allowing to select the most appropriate systems for further application in the building of the composites.

2D nanomaterials of the transition metal dichalcogenide (TMD) family, analogues to graphene, have been gaining interest in last years, replacing graphene in some applications. However, systematic studies regarding the preparation of these materials are still scarce. Therefore, we selected three TMDs, MoS_2, WS_2 and $MoSe_2$, to disperse with two surfactants, cationic CTAB and anionic SC, that proved to be effective in the previous studies. The results showed common features with the surfactant-assisted dispersibility of carbon nanomaterials. Further, both metal and chalcogen of the TMDs were found to play an important role in dispersibility, depending on the surfactant concentration. Due to charge effects, the surfactant used influences dramatically the profile of the dispersibility curves. The dispersed nanosheets were characterized by Raman spectroscopy and SEM, demonstrating that highly exfoliated and surfactant-coated particles can be obtained using the developed sonication/centrifugation methodology.

The work described above allowed to properly select the building blocks to build the proposed 1D/2D nanocomposites. In a first approach, we combined CNTs with graphene nanoplatelets, using oppositely charged dispersants to functionalize each surface. For this, three systems were selected to build two 1D/2D combinations: MWNTs/TTAB, MWNTs/(PVP+CTAB) and GnPs/SC. Electrostatic attraction was the driving force for composite assembly. Two building methodologies were studied: (i) a “bulk” method, where the building blocks were combined by simply mixing the individual dispersions together, followed by sonication; and (ii) an adapted layer-by-layer method, where the building blocks were added sequentially in alternate layers. The structural organization of the obtained materials was evaluated by SEM, Raman and BET analysis,

and studies of the effect of the building methodology and dispersant composition on their electrocatalytic performance regarding ORR were then thoroughly performed. Although the materials showed a modest electrocatalytic performance, the comparative study opens the path for further optimization of the composites as catalysts for the ORR.

The bulk methodology, despite yielding relatively non-organized composites, revealed to be a cost-effective, simple, and fast procedure to build composite structures using mild conditions. Therefore, we applied this methodology and substituted graphene for the TMDs WS_2 and MoS_2, comparing the effect of the metal in the electrocatalytic performance of the composites. The MoS_2/MWNT composite showed reasonable activity as a catalyst for OER, contrasting with the WS_2/MWNT composite, and thus unveiling a strong role played by the dichalcogenide metal.

Overall, this thesis comprises rigorous and systematic studies on the dispersibility and non-covalently functionalization of MWNTs, GnPs and TMDs, allowing to make molecular considerations on the features of the dispersants and the nanomaterials that influence the ability of the material to be well-exfoliated and well-dispersed. The obtained dispersions were morphologically characterized by various techniques in terms of the individualization of the tubes/layers and of the resulting zeta potential of the suspended particles. Using combinations of oppositely charged 1D and 2D nanomaterials, 3D composites were built and electrocatalytic studies towards the oxygen reactions were carried as a proof-of-concept. The strategy pursued and the results obtained allowed us to establish a methodology to build 3D structures, which can then be explored for the optimization of electrocatalysts and further applications.

Keywords: Nanocomposites & Hybrid materials; Carbon nanomaterials; Surfactants & Polymers; Non-covalent functionalization; Exfoliation; Carbon nanotubes; Graphene & Inorganic graphene analogues; Electrocatalysis

Resumo

A construção de estruturas automontadas através da combinação de nanotubos de carbono (CNTs) e nanomateriais 2D estratificados (por exemplo, grafeno e análogos inorgânicos de grafeno) é uma área emergente na ciência de materiais e nanotecnologia, apresentando desafios científicos e técnicos consideráveis. Paralelamente, o uso de interfaces rígidas e moles para a fabricação deste tipo de nanocompósitos - pela funcionalização das superfícies duras por adsorção de tensioativos (ou outras moléculas anfifílicas) - permite maior versatilidade nas interações, organização hierárquica e, como resultado, nas propriedades químicas, elétricas, térmicas, óticas e mecânicas dos compósitos. Consequentemente, inúmeras possibilidades de aplicações podem surgir, como em eletrónica, energia, sensores e catálise. Tendo em conta os desafios e possibilidades em jogo, este trabalho assentou em três objetivos fundamentais: (i) preparação e funcionalização não covalente dos nanomateriais 1D e 2D; (ii) montagem de compósitos 3D mediada por tensioativos e polímeros; e (iii) estudos de aplicação das estruturas obtidas como eletrocatalisadores para as reações de oxigénio (relevantes, por ex., para pilhas de combustível), nomeadamente a reação de redução do oxigénio (ORR) e a reação de evolução do oxigénio (OER).

Na primeira parte do projeto, realizou-se um estudo sistemático da dispersibilidade de nanotubos de carbono de parede múltipla (MWNTs) usando tensioativos *gemini* de estrutura *n*-*s*-*n*, variando espaçador (*s*) e comprimento de cadeia alquílica (n), e comparando o desempenho com os seus homólogos monoméricos. Utilizando um procedimento experimental rigorosamente controlado, foram obtidas curvas de dispersibilidade (concentração de MWNTs dispersos vs. concentração de tensioativo) permitindo a determinação quantitativa de métricas de dispersibilidade e uma interpretação de base molecular sobre as características dos tensioativos que influenciam a capacidade dos nanotubos em serem bem separados e bem dispersos em meio aquoso.

Numa outra parte do trabalho, efetuaram-se estudos comparativos da dispersibilidade de nanotubos de carbono,1D, e nanoplaquetas de grafeno (GnPs), 2D, usando dois tensioativos - colato de sódio e TritonX-100. Duas abordagens foram adotadas relativamente às dispersões dos nanomateriais 2D: exfoliação de GnPs a partir de grafite e exfoliação de GnPs adquiridos comercialmente. Um dos aspetos mais significativos deste estudo foi a obtenção de uma curva genérica de dispersibilidade, implicando características comuns no processo de dispersão, independentemente do

nanomaterial utilizado (1D ou 2D). As imagens SEM e AFM confirmaram que a metodologia aplicada permitiu obter MWNTs bem dispersos e GnPs de poucas camadas. Além disso, este estudo permitiu racionalizar a dispersibilidade dos diferentes nanomateriais de carbono em soluções aquosas de tensioativo em termos de energia fornecida ao sistema no processo de exfoliação.

Com base no conjunto de resultados na dispersão e funcionalização de nanotubos de carbono e nanoplaquetas de grafeno, e visando a aplicação desses materiais como blocos de construção para compósitos, partiu-se para o estudo do efeito de misturas polímero/tensioativo em dispersões de MWNTs. Quatro combinações de dispersantes não iónico + iónico foram selecionadas, tendo em consideração a carga do polímero e do tensioativo: PVP+SDBS, PVP+CTAB, TX-100+PDDA e TX-100+PAS. A aplicação destas misturas de polímero/tensioativo como dispersantes para MWNTs revelou efeitos interessantes, tendo alguns sistemas apresentado forte sinergismo relativamente à concentração máxima de nanotubos dispersos. A separação dos MWNTs dos aglomerados iniciais foi avaliada por SEM, e a funcionalização não covalente foi confirmada por potencial zeta, permitindo a posterior aplicação desses sistemas para a construção dos compósitos.

Os nanomateriais 2D da família dos dicalcogenetos de metais de transição (TMD), análogos ao grafeno, têm sido alvo de enorme interesse nos últimos anos, substituindo o grafeno em algumas aplicações. No entanto, estudos sistemáticos sobre a preparação desses materiais na sua forma individualizada (ou com poucas camadas) encontram-se escassamente reportados. Para colmatar esta lacuna, foram selecionados três TMDs, MoS_2, WS_2 e $MoSe_2$, para dispersar com dois tensioativos, CTAB, catiónico, e SC, aniónico, os quais se haviam mostrado eficazes nos trabalhos anteriores. Os resultados obtidos neste estudo revelaram efeitos semelhantes aos observados na dispersão de nanomateriais de carbono assistida por tensioativos. O metal e calcogénio do TMD mostraram ter influência na dispersibilidade, dependendo da concentração de tensioativo. As dispersões de TMDs obtidas foram caracterizadas, demonstrando que nanomateriais altamente exfoliados (e não-covalentemente funcionalizados) podem ser eficazmente obtidos através da metodologia de sonicação/centrifugação desenvolvida.

O trabalho descrito permitiu selecionar adequadamente os blocos de construção para fabricar nanocompósitos 1D/2D. Numa primeira abordagem, foram combinados MWNTs com GnPs, usando dispersantes de carga oposta para funcionalizar cada superfície, sendo as interações eletrostáticas a força motriz para automontagem da estrutura compósita. Para isso, três sistemas de nanomateriais funcionalizados não-covalentemente foram selecionados para construir duas combinações 1D/2D:

MWNT/TTAB, MWNT/(PVP+CTAB) e GnP/SC. Duas metodologias de construção foram estudadas: (i) um método *bulk*, em que os blocos de construção foram combinados através da mistura das dispersões individuais e, posteriormente, se aplicou sonicação; e (ii) um método de camada-a-camada adaptado, onde os blocos de construção foram adicionados sequencialmente em camadas alternadas. A organização estrutural dos materiais obtidos foi avaliada por SEM, Raman e BET, e os efeitos da metodologia de construção e composição do dispersante no desempenho eletrocatalítico dos compósitos foram estudados como uma prova de conceito. Apesar de apresentarem um desempenho modesto como catalisadores da reação de redução de oxigénio, o estudo comparativo entre os materiais fabricados abre caminho para uma maior otimização dos compósitos para aplicações nesta área.

A metodologia *bulk*, apesar de originar compósitos com estrutura não organizada, revelou-se simples, rápida e económica para construir compósitos em condições experimentais "suaves". Assim, aplicou-se esta metodologia e substituiu-se o grafeno pelos TMDs WS_2 e MoS_2, comparando o efeito do metal no desempenho eletrocatalítico dos compósitos. O compósito MoS_2/MWNT apresentou um desempenho razoável como catalisador para a reação de evolução de oxigénio, contrastando com o compósito WS_2/MWNT, e demonstrando assim o papel determinante do metal nas propriedades estudadas.

Este trabalho compreendeu estudos rigorosos e sistemáticos sobre a dispersibilidade e funcionalização não covalente de MWNTs, GnPs e TMDs, permitindo considerações moleculares relativamente às características dos dispersantes e dos nanomateriais que influenciam a capacidade de o material ser bem exfoliado e bem disperso. As dispersões obtidas foram caracterizadas em termos de individualização dos tubos/camadas e potencial zeta resultante dos nanomateriais dispersos. Usando combinações de nanomateriais 1D e 2D de carga oposta, construíram-se compósitos 3D e realizaram-se estudos eletrocatalíticos para as reações de oxigénio, como prova de conceito. Os resultados permitem estabelecer uma metodologia para construção de estruturas 3D que podem ser otimizadas como eletrocatalisadores ou estudadas para outro tipo de aplicações.

Palavras-chave: Nanocompósitos & Materiais híbridos; Nanomateriais de carbono; Tensioativos & Polímeros; Funcionalização não covalente; Exfoliação; Nanotubos de carbono; Grafeno & Análogos 2D de grafeno; Eletrocatálise.

Table of Contents

List of Figures

List of Tables

List of Acronyms and Symbols

Acronyms

AFM	Atomic Force Microscopy
BET	Brunauer–Emmett–Teller theory
cac	Critical aggregation concentration
cdc	Critical dispersibility concentration
cmc	Critical micelle concentration
CNT	Carbon Nanotube
CTAB	Cetyltrimethylammonium Bromide
CV	Cyclic Voltammetry
CVD	Chemical Vapor Deposition
DTAB	Dodecyltrimethylammonium Bromide
FLG	Few-Layer Graphene
IGA	Inorganic Graphene Analogue
IR	Infrared
G	Graphene
GCE	Glassy Carbon Electrode
GnP	Graphene Nanoplatelet
GO	Graphene Oxide
HER	Hydrogen Evolution Reaction
IGA	Inorganic Graphene Analogue
K-L	Koutecky-Levich
LbL	Layer-by-layer assembly
LPE	Liquid-Phase Exfoliation
LSV	Linear Sweep Voltammetry
MLD	Mean Lateral Dimensions
MWNT	Multiwalled Carbon Nanotube
MX_2	Generic structure of transition metal dichalcogenides
OER	Oxygen Evolution Reaction
ORR	Oxygen Reduction Reaction
PAS	Polyacrylate Sodium Salt
PDDA	Poly(diallyl dimethylammonium) chloride
PS	Polymer/surfactant mixture
PVP	Polyvinylpyrrolidone
RDE	Rotating Disk Electrode
RHE	Reversible Hydrogen Electrode
RRDE	Rotating Ring Disk Electrode
Ru	Uncompensated resistance
SC	Sodium Cholate
SEM	Scanning Electron Microscopy
SDBS	Sodium Dodecyl Benzene Sulfonate
SDS	Sodium Dodecyl Sulfate

SSA	Specific Surface Area
SWNT	Singlewalled Carbon Nanotube
TGA	Thermogravimetric Analysis
TMD	Transition Metal Dichalcogenide
TTAB	Tetradecyltrimethylammonium Bromide
TX-100	Triton X-100
UV-vis	Ultraviolet-visible Spectroscopy
vdW	van der Waals
wt %	Concentration expressed as weight percent

Symbols

A	Absorbance
d	Diameter
ε	Extinction coefficient
E	Electric potential
E_{onset}	Onset potential
E^d	Energy delivered to the system
γ	Surface tension
i_0	Exchange current density
j	Current density
j_0	Exchange current density
j_k	Kinetic current density
j_L	Diffusion limiting current density
λ	Wavelength
L	Length
n_{O_2}	Number of electrons transferred per O_2 molecule
η	Overpotential
η	Dispersibility effectiveness
η^*	Dispersibility efficiency
n	Number of carbon atoms in alkyl chain
n-s-n	General structure of dicationic gemini surfactants
P_s	Surfactant critical packing parameter
s	Number of carbon atoms in the gemini spacer
S	Synergism
T_{Kr}	Krafft temperature
t	Time
ω	Angular velocity
ζ	Zeta potential

List of papers

I. **Gemini surfactants as efficient dispersants of multiwalled carbon nanotubes: Interplay of molecular parameters on nanotube dispersibility and debundling**
Bárbara Abreu, Jessica Rocha, Ricardo M. F. Fernandes, Oren Regev, István Furó, and Eduardo F. Marques
Journal of Colloid and Interface Science **2019**, 547, 69-77.

II. **Comparative trends and molecular analysis on the surfactant-assisted dispersibility of 1D and 2D carbon materials: multiwalled nanotubes vs graphene nanoplatelets**
Bárbara Abreu, Jorge Montero, Matat Buzaglo, Oren Regev, and Eduardo F. Marques
Manuscript submitted for publication.

III. **Dispersibility and noncovalent functionalization of multiwalled carbon nanotubes by polymer/surfactant mixtures of assorted composition: synergistic vs antagonistic effects**
Bárbara Abreu, Ana Sofia Pires, Andreia Guimarães, Ricardo M. F. Fernandes, and Eduardo F. Marques
Manuscript.

IV. **On the role of ionic surfactants in the liquid-phase exfoliation of 2D graphene analogues: the case of transition metal dichalcogenides MoS_2, WS_2 and $MoSe_2$**
Bárbara Abreu, Pedro Ferreira, Bernardo Almeida, Ricardo M. F. Fernandes, Diana Fernandes, and Eduardo F. Marques
Manuscript.

V. **Carbon nanotube/graphene nanocomposites built via surfactant-mediated colloid assembly as metal-free catalysts for the oxygen reduction reaction**
Bárbara Abreu, Marcos Rocha, Marta Nunes, Cristina Freire, and Eduardo F. Marques
Manuscript submitted for publication.

VI. **Nanocomposites prepared from carbon nanotubes and the transition metal dichalcogenides WS_2 and MoS_2 via surfactant-assisted dispersions as electrocatalysts for oxygen reactions**
Pedro Ferreira, Bárbara Abreu, Cristina Freire, Diana Fernandes, and Eduardo F. Marques
Materials **2021**, 14, 896-912.

Structure and Organization of this Thesis

This thesis is composed of four chapters, as summarized below.

Chapter 1: Introduction

The first chapter comprises an overview on 1D and 2D nanomaterials, focusing on those materials relevant to this work, on amphiphiles and their role as dispersing agents, and on the assembly methods of the described materials. The applications of the resulting composite structures are also addressed. The topic of energy conversion is further introduced, to provide context on one of the possible applications of the type of nanomaterial/amphiphile hybrids explored in this thesis.

Chapter 2: Experimental section

In this chapter, relevant information regarding the materials and reagents used in this work are presented. Chapter 2 also broadly covers the experimental methodologies used. The characterization techniques and procedures are briefly described.

Chapter 3: Results and Discussion

This chapter comprises the results obtained in this work and their discussion, in the form of published papers and manuscripts, organized according to the unfolding of the work: 1) preparation of the building blocks (Papers I - IV); 2) building of 3D composite materials and application-related studies (Papers V and VI).

Chapter 4: Conclusions and Future Perspectives

The thesis ends with an overview of the main conclusions, and future perspectives regarding the building of new composite materials *via* surfactant-mediated interactions, for advanced applications.

Chapter 1 Introduction

1.1. 1D and 2D nanomaterials

New allotropic forms of carbon, in particular 1D carbon nanotubes (CNTs) and 2D graphene (G), have been at the forefront of nanotechnology during the last years, especially due to their novel and unique electrical, mechanical, thermal and optical properties.[1] More recently, other families of 2D nanomaterials, comparable to graphene in structure – inorganic graphene analogues (IGA) – emerged as a viable alternative for specific applications (e.g. electrocatalysis, electronic devices).[2]

In this section, the structure and properties of carbon nanotubes, graphene and inorganic graphene analogues will be addressed. The functionalization approaches will be described, focusing on the non-covalent methods. Finally, an outline on the applications of the introduced 1D and 2D nanomaterials will be presented.

1.1.1 Carbon nanotubes

Structure

Carbon nanotubes are extremely long and narrow cylinders made of graphene sheets, which possess unique mechanical, thermal, optical, and electrical properties.[3, 4] Since their discovery by Iijima's group in 1991,[5] CNTs have been on the spotlight of research in a wide range of fields, from material science to nanotechnology.[1, 6]

The simplest way to visualize a CNT is by the roll up of a graphene sheet, resulting in a hollow cylinder (Fig.1.1). Each carbon atom in the graphene monolayer is connected to three other carbons by σ bonds, in a sp^2 hybridized hexagonal network.[7] The electrons in the non-hybridized p orbitals of adjacent carbon atoms create a conjugated π system, making CNTs electrically conductive.[8]

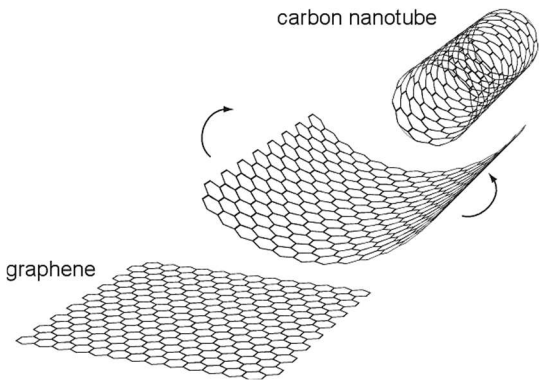

Fig. 1.1. Construction of a carbon nanotube from a graphene sheet.[9]

The type of CNT can be classified as i) singlewalled carbon nanotube (SWNT), if it is composed by one graphene sheet; or ii) multiwalled carbon nanotube (MWNT), if it results from the roll-up of two or more layers. The typical diameter, *d*, of a SWNT stands in the range of 0.4-3 nm.[7] For a MWNT, *d* depends on the number of concentric tubes, typically separated from each other by 0.34 nm.[8] Regarding length, *L*, both SWNTs and MWNTs can reach hundreds of micrometers. This high *L/d* aspect ratio warrants CNTs the designation of quasi-one-dimensional materials.

Considering a SWNT, the roll up of the graphene sheet may produce different types of nanotube, with different diameters. The angle of formation of the cylinder allows three different structures, identified by a pair of integers (*n, m*) of the chiral vector C_h: armchair, where *n* = *m* (*n, n*), zigzag (*n,* 0) and chiral, where *n* > *m* > 0 (*n, m*) (Fig. 1.2). The electronic properties of the CNT are thus defined by their structure.[10, 11]

Properties

The combination of the *L/d* aspect ratio with the conjugated π system turns CNTs into singular materials regarding electronic, optical, mechanical, and thermal properties.[12]

Concerning the electronic properties, metallic conduction occurs when:

$$n - m = 3q \tag{1.1}$$

where q is an integer. Therefore, according to Eq. 1.1, armchair tubes are metallic, while zigzag and chiral nanotubes can present metallic or semiconducting properties. The curvature of the nanotube (i.e. diameter) also plays a role in the electronic properties, since conduction bands are more affected than the valence bands in the rolling-up of the graphene sheet. The curvature presents a major effect in non-armchair nanotubes, which can shift from metallic to semiconducting.[10]

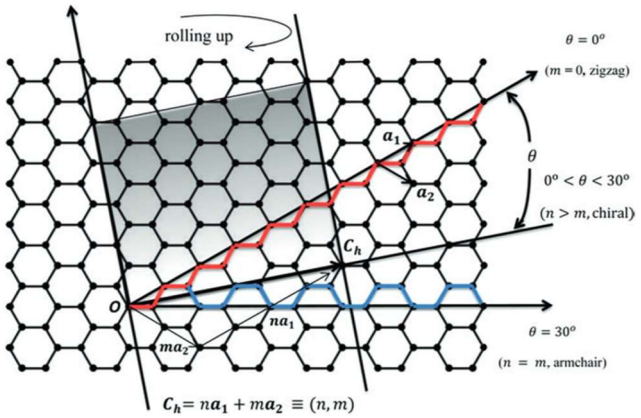

Fig. 1.2. Schematic of a graphene sheet roll-up and definition of geometrical parameters that describe a CNT. Adapted.[13]

The sp^2 network of carbon nanotubes is not only responsible for the electronic properties, but also for their black color, since π-electrons are capable of absorbing light at a wide range of wavelengths, from UV to near-infrared. Going from the macroscale to the nanoscale, however, nanotubes can be transparent due to the high radiation penetration depth (i.e. the distance electromagnetic radiation of a specific wavelength can penetrate the material).[14] The absorption of discrete radiation wavelengths by SWNTs is determined by the van Hove singularities, corresponding to electronic transitions between different states. The peaks in the absorption spectra are related to the band gap energies in the nanotubes, and, since both are connected to the density of electronic states (dictated by nanotube structure), the optical absorption information could be used to structurally characterize the CNTs. However, when analyzing a sample with a high number of nanotubes, the absorption features from CNTs with different structures often overlap, making a rigorous structural identification difficult.[12, 14]

Adding to their electronic and optical properties, carbon nanotubes present remarkable mechanical properties. CNTs are the stiffest and strongest material ever created, with SWNTs presenting Young's modulus of 1000 GPa (approximately 5 times higher than steel) and values of tensile strength than can achieve 63 GPa (50 times higher than steel). Regarding MWNTs, the Young's modulus estimated experimentally yields an average value of 1.8 TPa, and no apparent effect of diameter is seen.[14,15] Additionally, one observes that, following deformation, MWNTs can release the stress and return to the original straight form. This feature makes this nanomaterial a promising candidate for composites, increasing the fracture resistance.[15]

Among all known materials, crystalline carbons display the highest measured values of thermal conductivity, k. For SWNTs, at room temperature, k = 6600 $W \cdot m^{-1} \cdot K^{-1}$ was obtained for an isolated (10, 10) nanotube, a k value around 17 times superior to that of copper. For MWNTs, a value of k = 3000 $W \cdot m^{-1} \cdot K^{-1}$ was estimated. The high k values obtained for CNTs refer, however, to thermal conductivity along the tube axis, since the radial conductivity is significantly lower.[14]

Despite the remarkable properties and wide applicability of both SWNTs and MWNTs, it is essential to recognize that in practice not all CNTs possess outstanding characteristics. The production method, as well as the further preparation of the nanotubes to be applied, may increase the defects in the CNT structure, significantly affecting their properties. Consequently, irrespective of the type of tube or the application, it is crucial to apply reproducible methodologies that allow to preserve the remarkable features of pristine carbon nanotubes.

1.1.2 Graphene and Inorganic Graphene Analogues

In recent years, the dimensionality of materials, besides their composition and chemical structure, was found to play a pivotal role in their fundamental properties, as was emphasized by the discovery of free-standing graphene.[16] The focus of research on graphene, its properties and potential applications, led to the fast progress on methodologies to prepare this nanomaterial at large scale. However, the strong dependence of the as-produced graphene's properties with the number of layers unveiled a drawback in the large-scale production of this material. As an alternative, the exploration of other 2D materials with remarkable properties,[17, 18] analogue to graphene, emerged.[19, 20]

1.1.2.1 Graphene

Structure

Graphene is the definition given to a single layer of a hexagonal network of carbon atoms with sp^2 hybridization, creating a 2D nanosheet. In theory, graphene has been studied for several decades, as it is the basic building block of bulk graphite.[16] However, the monolayer was not presumed to exist as a free-standing material, until it was found in 2004 by Geim and Novoselov.[21] Once separated from bulk graphite, graphene was found to acquire an unique electronic structure with very unusual characteristics, with some experimental measurements reaching their theoretically predicted limits.[22]

Properties

Graphene is a zero-gap semiconductor. An uncommon electronic feature of this material are its massless charge carriers, also known as Dirac fermions.[22, 23] In neutral graphene, the chemical potential crosses exactly the Dirac point. This phenomenon mimics the physics of quantum electrodynamics (QED) for massless particles; however, in graphene the Dirac fermions move with a speed 300 times smaller than the speed of light, meaning the unusual properties of QED can appear in graphene but at lower speeds.[23] Dirac fermions behave in unusual ways when compared to ordinary electrons if subjected to magnetic fields, leading to new physical phenomena such as the anomalous integer quantum Hall effect. The quantum Hall effect at room temperature and an electron mobility value of $2.5 \times 10^{-5}\ cm^2\ V^{-1}\ s^{-1}$ [24] are indicative of the great electronic properties of graphene.[22, 23, 25, 26]

Like carbon nanotubes, graphene also shows remarkable mechanical, optical, and thermal properties. In addition to the high flexibility and specific surface area (SSA) of graphene, a Young's modulus of 1 TPa and intrinsic strength of 130 GPa were experimentally obtained[27]; the monolayer has an optical absorption of $\pi\alpha \approx 2.3\%$ (in the infrared limit, where α is the fine structure constant)[28]; and thermal conductivity values can reach 3000 W m K^{-1}, an order of magnitude higher than copper.[29] Graphene also possesses the ability to sustain extremely high densities of electric current.[30]

The combination of all these properties in one material explains the "gold-rush" towards graphene in the last decade. However, one important concept is the number of layers in the material, for it is known that the electronic structure rapidly evolves with the increasing sheet number. In the case of graphene materials, the properties approach the 3D limit of graphite at 10 layers. For the graphene monolayer and bilayer, the electronic spectra are simple since both are zero-gap semiconductors. For three or more layers, several charge carriers and the conduction and valence bands start notably overlapping in the spectra.[16]

Classification

During the last years, the focus of graphene research shifted from fundamental studies to applications.[20] Considering the importance of the structure and defects of the material in the final properties, some efforts have been made to bring the definition of graphene materials to a common ground (Fig.1.3), since the literature can be confusing regarding these concepts. The basic principles for the graphene classification rely on i) lateral dimensions; 2) number of layers; and 3) whether the particle is isolated or is a unit of the material.[31] Thus, "graphene" refers to the isolated monolayer, while "graphene layer" is the designation attributed to the structure unit within the carbon material. Multi-layer graphene (MLG) and few-layer graphene (FLG) are some of the most used concepts, but sometimes they overlap. Bianco et al. defined MLG as a sheet-like material consisting of a small number (2-10) of well-defined, countable, stacked graphene layers of extended lateral dimension. FLG is a subclass of MLG, differing in the layer number (2-5). When graphene is chemically modified and becomes highly oxidized, the term "graphene oxide" (GO) is applied.[31-33]

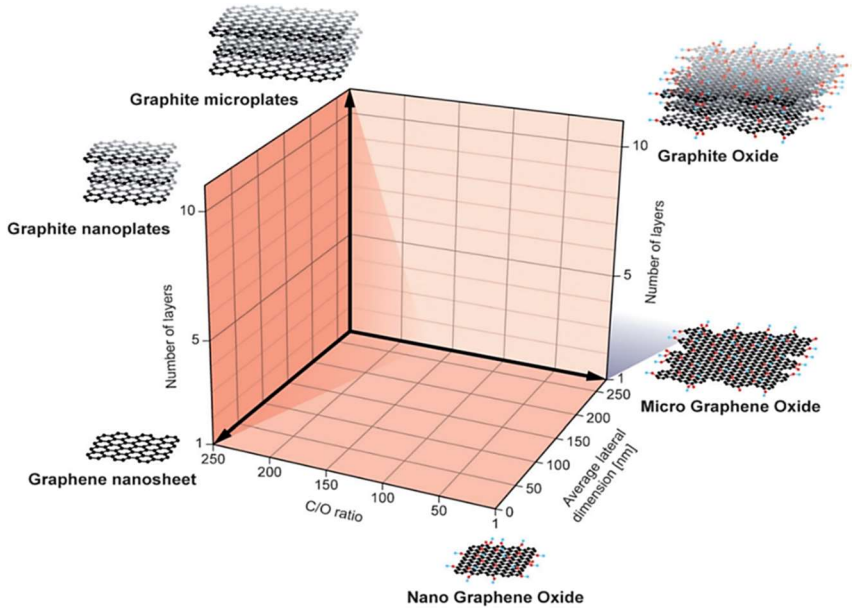

Fig. 1.3. Classification grid proposed by Wick et al. for the categorization of different graphene types according to three fundamental properties: number of graphene layers, average lateral dimension, and atomic carbon/oxygen ratio. The different materials drawn at the six corners of the box represent the ideal cases according to the lateral dimensions and the number of layers reported in the literature. The values of the three axes are related to the graphene based materials at the nanoscale, but it is feasible to expand the values to the microscale.[32]

Although the "graphene" designation should only be attributed to the monolayer, the concept is more complex, and it is common to find authors classifying as "graphene" materials that are not the isolated 2D monolayer. Since the properties vary significantly with the number of layers, a rigorous characterization is imperative to correctly define the graphene material, allowing proper comparisons between different works to be made.

1.1.2.2 Inorganic graphene analogues: transition metal dichalcogenides

Structure

The importance of layered materials and their individualization into monolayers was put forth by Richard P. Feynman more than 60 years ago.[34] The real potential of these sheets was not found, however, until the discovery of free-standing graphene.[21] Like the 2D allotrope of carbon, there are many families of layered materials of different elements or compounds. Great efforts have been put both in academia and industry on the research of these two-dimensional materials, focusing on their distinct bulk and monolayer properties.[2, 35]

One of the most important classes of inorganic graphene analogues is that of transition metal dichalcogenides (TMDs). The chemistry of TMDs allows to take a step forward to new fundamental and technological applications beyond graphene, which is

chemically inert.[19] These materials have a MX_2 structure, with M being a transition metal atom (e.g. Mo, W) and X a chalcogen atom (e.g. S, Se), and can be visualized as one layer of M atoms "sandwiched" between two layers of X atoms. Like graphene, MX_2 compounds are characterized by weak, non-covalent bonding (van der Waals interactions) between layers, and strong in-plane covalent bonding.[36] The exfoliation of these materials into mono- or few-layer particles not only preserves their bulk properties, but also leads to additional features due to confinement effects.[19]

The metal coordination of layered TMDs can be either trigonal prismatic (H) or octahedral (T) - typically distorted and sometimes referred to as trigonal-antiprismatic - as represented in Fig. 1.4.[19] Since an individual MX_2 layer can be in either one of the two possible phases, the stacking of sheets of different phases confers TMDs a specific case of polymorphism, called polytypism. The most common polymorphs are 1T, 2H and 3R: the letters stand for trigonal, hexagonal, and rhombohedral, respectively, and the digit indicates the number of layer (i.e. X-M-X) units in the unit cell. Further, there are different possible polytypes (i.e. different stacking sequences) for each polymorph.[19]

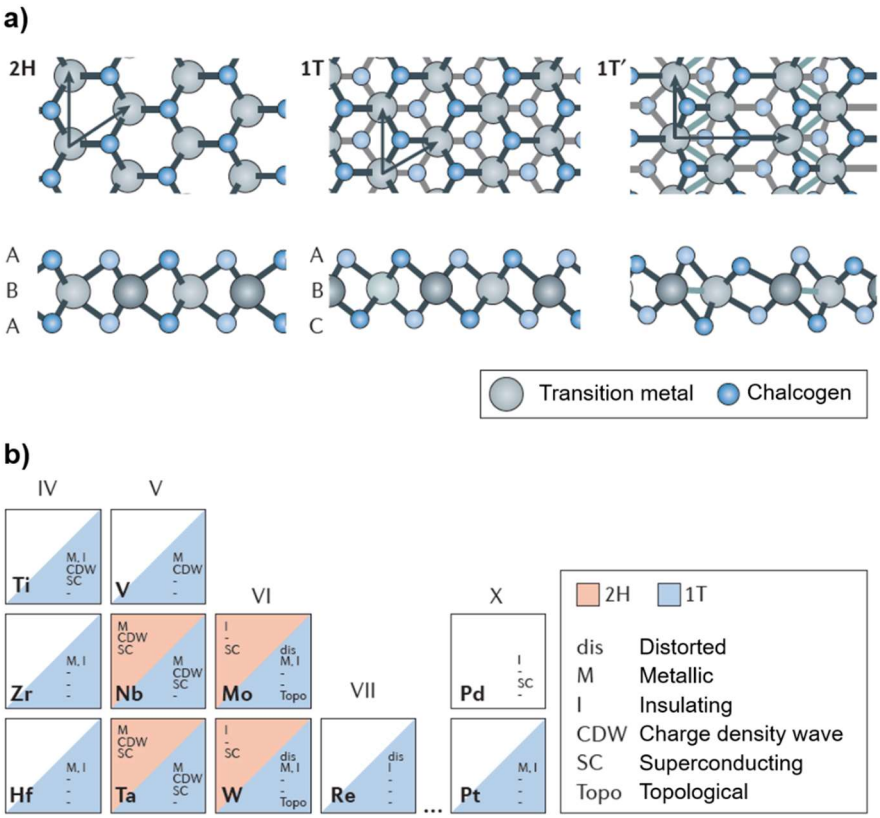

Fig. 1.4. Structure and electronic properties of TMDs: a) Atomic structure of single layers of TMDs in their trigonal prismatic (2H), distorted octahedral (1T) and dimerized (1T') phases. Arrows indicate lattice vectors and the stacking of atomic planes; b) "Periodic table" of known layered TMDs, summarizing their existing structural phases (2H, 1T or other, as in the case of Pd-based TMDs) and indicating the presence of distorted structural phases and observed electronic phases.[37]

Properties

The electronic properties are the most prominent feature of TMDs, since they can be tuned depending on the elements involved and structural arrangement. Bulk TMDs properties range from insulators (e.g. HfS_2), semiconductors (e.g. MoS_2 and WS_2), semimetals (e.g. WTe_2 and $TiSe_2$) to true metals (e.g. NbS_2 and VSe_2). Many TMDs exhibit band structures that are similar in their general features. However, since there are so many compounds in this family, this subsection will focus mainly on the materials used in the project, namely MoS_2, WS_2 and $MoSe_2$.

As referred above, group VI TMDs, such as MoX_2 and WX_2, are semiconductors. The direct excitonic transitions at the K-point (i.e. at the middle of an edge joining two similar faces) of the Brillouin zone remain relatively unchanged with layer number (Fig. 1.4).[38 39] In particular, density functional theory (DFT) calculations for MoS_2 have shown that localized *d* orbitals on the Mo atoms (located in the middle of the X-M-X "sandwiches") are responsible for the conduction-band states at the K-point and are almost unaffected by interlayer coupling. Near the Γ-point (i.e. center of the Brillouin zone), however, the states are due to combinations of the antibonding p_z-orbitals on the S atoms and the *d* orbitals on Mo atoms, having a strong interlayer coupling effect. Consequently, the direct excitonic states near the K-point are relatively unchanged by increasing layer number, while the transition at the Γ-point shifts from indirect for the bulk material to direct for the monolayer.[39] This effect is expected for all MoX_2 and WX_2 compounds, covering the bandgap energy range 1.1–1.9 eV from bulk to monolayer structures.[38, 40]

The electronic structure of semiconductors has a key effect in their optical properties: for semiconductors with direct bandgap, photons with higher energy than the bandgap energy can be immediately absorbed or emitted; for indirect bandgap, the process is less efficient, requiring an additional photon to be absorbed or emitted. Consequently, the change from indirect to direct bandgap for MoX_2 and WS_2 can be monitored by photoconductivity, absorption spectroscopy or photoluminescence.[38]

The mechanical properties of MoX_2 and WX_2 TMDs have been studied for flexible electronics applications.[41] In particular, MoS_2 was found to be 30 times stronger than steel and can be deformed up to 11% before breaking, which makes this material one of the strongest semiconducting materials known and enhances its applicability.[42]

1.1.3 Synthesis and functionalization of nanomaterials

The nanomaterials described in the previous sections can be obtained by different methods; some can occur naturally, and all can be synthetized using bottom-up approaches. Usually, the synthesis produces highly aggregated and heterogeneous powders, and therefore additional preparation steps are required to obtain the 1D and 2D objects in well-separated and manageable forms.

1.1.3.1 Synthesis of carbon nanotubes, graphene, and inorganic graphene analogues

Carbon nanotubes

Carbon nanotubes do not occur naturally – as observed to this date – therefore, the 1D allotrope of carbon must be synthetized. The most frequent techniques applied to synthetize CNTs are visible light vaporization, electric arc-discharge, and chemical vapor deposition (CVD).[43]

In the visible light vaporization, a solid graphite target is irradiated by a laser or submitted to continuous multiwavelength light (from a solar furnace), under high temperature (around 1200 °C) and using He or Ar atmosphere. As a result, graphite is converted into vaporized particles. The gas flow inside the chamber provides a temperature gradient that recombines the particles into nanotubes, ultimately collected in a cold finger. A catalyst can be used in the process, in which the type of CNT formed depends. If pure graphite is used, MWNTs are collected; if an appropriate metal-filled graphite is vaporized, SWNTs are formed. The main disadvantages of this technique are the cost and the scale-up difficulties. However, it is possible to obtain nanotubes with low defect density.[8]

The arch discharge method is carried under reduced pressure, in a chamber filled with inert gases, like in the light vaporization procedure. The ends of graphite rods are placed close to one another, with a potential set at around 20 V. The distance between the two ends is shortened until an electric arc occurs, increasing the temperature in the surface to 2000 °C – 3000 °C, enough to sublimate carbon. The combination of electric current, reduced pressure and high temperature forms a plasma, that should be kept as stable as possible to produce high quality nanotubes. The deposit formed in the cathode will contain the CNTs: if no catalyst is used, MWNTs are formed; if a proper catalyst is selected, SWNTs are obtained. The main drawback of this process is the amount of non-nanotube material that is formed – typically around 90%. The advantages are,

nevertheless, considerable, since the equipment is inexpensive and easily operated, and low-defect nanotubes are produced.[8]

Chemical vapor deposition can be defined as a thermal reaction in which a transition metal catalyst (e.g. Ni, Co) is applied to reduce the temperature down to the value required to break down the carbon source molecules, separating the carbon atoms. Typically, the temperature involved dictates the type of CNT produced: at lower temperatures, the formation of MWNTs is favored, while higher temperatures origin SWNTs. The gaseous precursor adsorbs on a substrate, with a consequent phase transition to condensed nanotubes through a nucleation and growth process.[44] This procedure permits not only the tunability of the reaction conditions, but also the carbon source to be rather diverse (e.g hydrocarbons and carbon monoxide), hence opening the range of possible reaction conditions and making CVD the most studied technique for CNT production.[8] Over recent years, some processes have been optimized and registered, such as the HiPCO® (High-Pressure Carbon Monoxide), involving a gaseous catalyst, and CoMoCat® (Cobalt-Molybdenum Catalysis), that uses a supported catalyst.[45] The output of CVD usually consists on a high yield of CNTs (reaching 99% of the produced material), but MWNTs tend to display higher defect density than the SWNTs produced by this technique.[8]

The synthesis of CNTs typically produces a powder consisting of tubes agglomerated in bundles and ropes. For this reason, several methods have been developed to obtain homogeneous samples of individualized tubes, as addressed in section 1.1.3.2.

Graphene

The low-cost and scalability of CVD as a thin-film deposition procedure makes it applicable also for bottom-up production of graphene. The main parameter in the control of graphene synthesis by CVD is the choice of substrate material, since the growth mechanism of the nanomaterial appears to be strongly dependent on the type of substrate (i.e. Ni, Cu). Although large, high-quality monolayers have been synthetized using CVD, the combination of reproducible results and large-scale production has not been accomplished yet.[44] Other methods reported to fabricate graphene range from un-zipping of carbon nanotubes, solvothermal synthesis, or organic synthesis. However, the most promising procedures to obtain high-quality monolayer or few-layer graphene that can be produced at industrial scale are the top-down methods, using graphite as the starting bulk material.[46]

Graphite consists of stacked graphene layers, held together by van der Waals interactions. Consequently, the use of forces that exceed the vdW allows to exfoliate the graphene sheets from bulk graphite. Three procedures stand-out regarding the obtention of graphene from graphite: micromechanical cleavage, graphene via graphene oxide and liquid-phase exfoliation (Fig. 1.5). The first is commonly known as the “scotch tape” method, and, as implied, consists of the peeling of graphene flakes from graphite using adhesive tape. Graphene is then deposited on a substrate and the tape can be dissolved in acetone. Despite the high quality of the obtained material and versatility of micromechanical cleavage, scalability remains the major drawback.[46]

The fabrication of graphene via graphene (or graphite) oxide is one of the most used procedures. This method relies on the intercalation of graphite with an oxidant, introducing oxygen groups that help to disperse and stabilize the oxidized material in water, when subjected to sonication. The most applied protocol to oxidize graphite is the Hummers method – an aggressive chemical treatment that, while helping to obtain homogeneous graphene dispersions in water, destroys the sp^2 structure. The defects generated by the oxidation can be partially reverted by an additional reduction step, however, no methodology developed to date has been able to fully restore the pristine graphene structure. The chemicals used in this treatment (such as sodium nitrate and concentrated sulfuric acid) and the high temperatures required make the Hummers method unsuitable for industrial production.[46]

Liquid-phase exfoliation (LPE) appears as an alternative to obtain scalable graphene dispersions without the use of severe treatments. This methodology uses ultrasound or shear forces to exfoliate graphene sheets from graphite. The liquid medium is usually selected considering the interfacial tension between the solvent and the graphene layers, which should be minimized. Among the solvents reported to be effective are N-methylpyrrolidone (NMP) and N,N-dimethylformamide (DMF). In this fact lies the first challenge of LPE: suitable solvents should have a surface energy around 40 $mN \cdot m^{-1}$, a value usually obtained in liquids that are expensive, corrosive, and toxic, with high boiling points. Thus, several efforts have been applied to exfoliate graphite in a large number of alternative solvents, such as acetone, ethanol or even water. While extremely convenient, exfoliation in water requires the modification of the hard material, due to the high surface tension of the solvent and hydrophobic nature of graphite and graphene. Amphiphilic molecules (e.g. surfactants, proteins, and some synthetic polymers) can be used to overcome this drawback, by functionalizing the hydrophobic surface without disrupting the sp^2 structure. This topic will be described in more detail in

section 1.1.3.2. The challenge in LPE is to find the experimental conditions that lead to high-quality graphene dispersions, with controllable size and number of graphene layers.

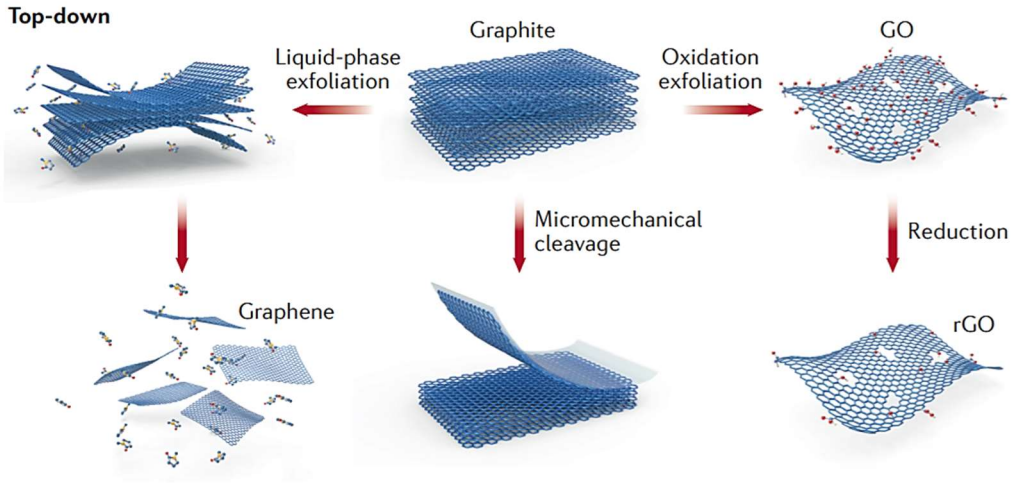

Fig. 1.5. Major top-down fabrication methods to obtain graphene from graphite. Adapted.[47]

Transition metal dichalcogenides

The methodologies described to obtain graphene dispersions (e.g. mechanical cleavage, liquid-phase exfoliation) can be applied to other inorganic 2D analogues, such as transition metal dichalcogenides, using the bulk crystals as thin-layer reservoirs.[48] However, the only TMDs known to occur naturally in the form of a layered crystal are MoS_2 and WS_2. Consequently, bulk crystals of other TMDs must be synthetized. The chemical vapor transport method can be defined as a crystal growth process in which the starting materials (i.e. the high purity metal and chalcogen) are placed, in stoichiometric proportions, in a quartz ampoule with the addition transport agent (e.g. I_2, Br_2) and heated in a furnace under a temperature gradient. The crystal growth takes place in the colder part of the ampoule, to where the material is transported. Similar to the graphite-to-graphene process, monolayers of TMDs can be obtained from the growth crystals.[37] Other widespread process to exfoliate layered materials, that has been applied with TMDs, is the Li-ion intercalation. This method consists in the intercalation of lithium ions into the interlayer space of bulk TMDs, and consequent sonication of the Li-intercalated compounds in water. However, this process still needs optimization, since typically the intercalated compounds present risk of self-ignition, self-heating or self-explosion in air.[48]

1.1.3.2 Functionalization of 1D and 2D nanomaterials

As described in the previous sections, the high aspect ratio and strong van der Waals cohesive forces between tubes or sheets result in tight agglomeration into bundles or stacking of the sheets. Since many applications rely on isolated tubes/ sheets where the properties (e.g. mechanical strength, electrical mobility, thermal conductivity) are optimized, bundling and stacking represent a drawback for the applicability of CNTs, graphene and TMDs. The main procedures to disperse 1D and 2D nanomaterials in liquid medium are i) in organic solvents; 2) by covalent functionalization and 3) by non-covalent functionalization. The first procedure was assessed in section 1.1.3.1, regarding the liquid phase exfoliation of graphene. In this section, the functionalization procedures will be reviewed. In the case of CNTs and TMDs, the relevance of functionalization to individualize the produced materials, hence weakening the interaction between adjacent tubes/sheets, is simple to understand. However, in the case of graphene this concept may overlap with the synthesis of the material since the top-down approaches use exfoliation and/or functionalization to produce graphene from graphite. It is important, then, to recognize that while the functionalization of CNTs and TMDs takes place after their synthesis (typically in the form of bundles or stacked layers), the functionalization of graphene can either be intrinsic to the synthesis process, when exfoliating graphene directly from graphite, or take place after an additional preparation step, when obtaining mono- or few-layer graphene from previously exfoliated materials, such as graphene nanoplatelets, GnPs (i.e. small stacks of graphene layers having a platelet shape, that can be synthetized from graphite exfoliation).

Covalent functionalization

Covalent functionalization relies on chemical modification by adding functional groups to a surface. The attached groups will interact with the solvent, enhancing the dispersibility of the material in the liquid media and the repulsions between tubes/sheets, improving the stabilization of the dispersed particles. The most common procedure to chemically functionalize carbon nanotubes and graphene is oxidation by strong acids (e.g. H_2SO_4 or HNO_3), or mixture of acids, resulting in the formation of carboxylic groups and increasing the affinity of these hydrophobic materials towards polar solvents.[49] Covalent modification of TMDs (in particular MoS_2, the most studied material of the family) has been carried out using several approaches, such as the addition of thiol, dibenzene thiophene, aryl diazonium molecules and organohalides.[50] Although the covalent functionalization methods have been widely studied and optimized, the introduction of

covalently-bonded functional groups to the hard surfaces introduces structural defects that affect the electronic, optical, mechanical and thermal properties of the 1D and 2D nanomaterials. In addition, the use of strong acids and high temperatures is not appealing for large-scale applications, due to the increased risk and environmental cost.[51]

Non-covalent functionalization

The non-covalent functionalization of carbon surfaces can be achieved through the physical adsorption of molecules (e.g. surfactants, polymers) on the hard nanomaterial surface, which changes some of its interfacial properties like hydrophilicity, wettability and surface charge. The colloidal kinetic stability of the dispersed particles is also enhanced due to steric or electrostatic repulsions between the coated surfaces. Since no chemical reactions occur, and the process can be carried out in mild conditions (i.e. aqueous media, low temperature), non-covalent functionalization provides a path to tune the physical properties of carbon nanotubes, graphene or TMD without compromising the material's structure.[49-52] The aspects regarding the mechanism of surfactant and/or polymer adsorption on the hard nanomaterials will be discussed further in section 1.2.4.

1.1.4 Applications of CNTs, graphene and TMDs

The remarkable electrical, optical, mechanical, and thermal properties that carbon nanotubes, graphene, and transition metal dichalcogenides encompass make these nanomaterials suitable for countless applications.

The potential of carbon nanomaterials for electronic devices is widely recognized, from energy conversion (e.g. solar cells, fuel cells) to energy storage (e.g. batteries, supercapacitors).[53] These nanocarbons can be applied in the form of inks, pastes, colloidal dispersions or as free-standing materials. The first CNT film reported, also known as "bucky paper", was fabricated by Rinzler et al.[54] Later, the free-standing carbon film was studied for applications in supercapacitors, presenting electrical conductivity values of 20 S/cm and thermal conductivity reaching 153 W/mK, besides being light and flexible.[55] However, the high manufacturing cost represented a drawback for large-scale production. Graphene oxide paper appeared as an alternative, showing even better electronic properties than the original bucky paper, but was found to be affected by humidity.[53]

Due to the difficulty of processing carbon nanotubes and graphene nanoplatelets as isolated materials, they have been applied as fillers for composite materials and coatings, and studied in microelectronics, energy storage, tribology and biotechnology.[56-58] Keshri et al. found that coatings reinforced with MWNTs exhibit both reduced friction and wear due to the excellent self-lubricating and load bearing effects of the nanotubes.[59] Graphene shows outstanding friction and wear behaviors as well. Interestingly, few-layer and multi-layer graphene experimentally showed a decrease in friction force with increasing number of layers, enhancing the applicability of these materials for lubrication.[60 61, 62] Graphene nanoplatelets have also been studied as polymer nanofillers, modifying the properties of the matrix due to their low mass density and high electrical and thermal conductivities.[63] Other properties, such as the decrease of water vapor permeability, have emerged from this combination.[64]

Regarding the other class of 2D materials studied, theoretical and experimental results suggested single- and few-layer TMDs of the MoX_2 and WX_2 families are promising for applications in electronic devices, since they are semiconductors and the band gaps can be tuned by controlling the number of stacked layers.[2, 36] Furthermore, while the optical properties of TMDs are remarkably affected by the number of layers, the electronic properties of semiconductor TMDs vary relatively weakly with the layer number, contrasting with graphene.[36, 65] The combination of these features, adding to their mechanical properties and chemical stability, boosted the research on applications of MoX_2 and WX_2 materials (e.g. flexible transistors,[38] transparent opticalelectronics,[66] nanoelectronics[67]). The abundance of Mo and W lowers the manufacturing cost, presenting a strong advantage comparing to carbon nanomaterials and making these materials viable for industrial applications.[66] However, while the applicability of 2D materials beyond graphene has been widely studied, fundamental and systematic studies regarding the preparation of reproducible few-layer materials has not been following a comparable growth, remaining scarcely explored or lacking in detail.

1.2. Dispersing and functionalizing agents

As described in section 1.1.3.2, non-covalent functionalization stands as one of the main routes to prepare stable and individualized carbon nanomaterials. This process is based on the use of amphiphilic molecules to adsorb on the hard material, conferring functionalization without disruption of the surface. In this section, the main dispersing and non-covalent functionalizing agents used through the work – surfactants and

polymers – will be described, focusing on their interfacial behavior and self-assembly in aqueous systems.

1.2.1. Surfactants

Surfactants (abbreviation for surface active agents) can be defined as amphiphilic molecules that have a strong tendency to adsorb at interfaces, lowering the interfacial tension between them. The amphiphilic character of these compounds means that they are formed by a hydrophobic portion, usually a hydrocarbon chain (typically referred as "tail"), attached to a hydrophilic group ("head"), as depicted in Fig. 1.6. The type of charge of the hydrophilic portion is one of the most common ways of distinguishing different surfactant classes. Thus, surfactants can be classified according to their hydrophilic group charge as: anionic, cationic, nonionic, zwitterionic and catanionic.[68] Another classification is related to the number of chains (e.g. single-, double-chained). Adding to these classes there are some different families, such as dimeric surfactants (e.g. gemini surfactants). Gemini surfactants present two hydrophobic chains linked by a spacer and two polar head groups; these features confer different properties than their monomeric analogues.[69]

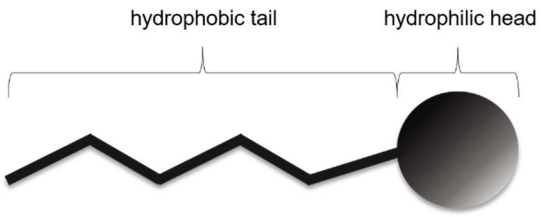

Fig. 1.6. Schematic representation of a surfactant molecule.

The duality of their nature is the key feature for surfactant behavior in water and the reason behind the hydrophobic effect. The low solubility in water (or polar solvents) drives both surfactant adsorption at interfaces, significantly reducing the interfacial tension, and self-assembly – the most prominent feature of these soft materials.[68, 70] At high dilutions, surfactants exist as unimers, and the molecular interactions between the hydrophobic tail and the water dipoles are highly unfavorable. To minimize this effect, surfactants tend to adsorb at the air-water interface, forming a monolayer and consequently reducing the surface tension. When the interface is saturated, above a specific temperature – Krafft temperature, T_{Kr} - and after a determined surfactant concentration – defined as critical micellar concentration, *cmc* – the surfactant molecules

self-assemble in solution in typically spherical aggregates, called micelles, where the surfactant tails are in close contact and the hydrophilic heads point towards the solvent. This phenomenon results in a lower Gibbs energy of the system.[68, 70, 71] The concentration range where micellization occurs can be determined by several techniques, being surface tension and conductometry the most common. Fig. 1.7 represents the variation in surface tension and conductivity as a function of surfactant concentration.

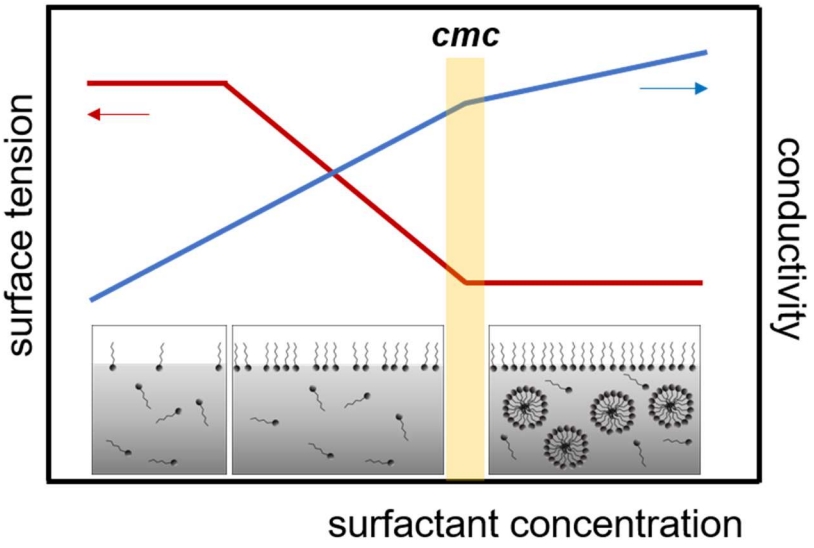

Fig. 1.7. Schematic representation of surface tension and conductivity as function of surfactant concentration.

The hydrophobic effect defines the onset of aggregation (micellization), but the repulsions between the headgroups define the formation of aggregates (micelles) with well-defined sizes. Thus, the hydration of the headgroups and the steric and electrostatic repulsions (depending on the charge of the polar head) between them are the main reason that surfactants do not phase-separate in water. The thermodynamic models can provide a more quantitative view of the micellization process. Two main approaches are considered: the pseudo phase separation model and the mass action model.[68]

The pseudo phase separation model assumes that micellization can be treated as a phase separation process and hence that it is cooperative: after the onset of micelle formation, adding another molecule (in the case of micellization, another unimer) to the assembled structures is more and more favorable as the number of unimers in the micellar phase increases. The standard molar Gibbs energy of micellization, $\Delta_{\mathrm{mic}}G_{\mathrm{m}}^{\mathrm{o}}$, can be determined from the difference between the chemical potential of the surfactant in the micelle and its standard chemical potential at infinite dilution, per mole:

$$\Delta_{\mathrm{mic}}G_{\mathrm{m}}^{\mathrm{o}} = \mu_{\mathrm{mic}}^{\mathrm{o}} - \mu_{\mathrm{S}}^{\mathrm{o}} = RT \ln x_{\mathrm{cmc}} \quad (1.2)$$

where $\mu_{\mathrm{mic}}^{\mathrm{o}}$ is the standard chemical potential of the micelle, $\mu_{\mathrm{S}}^{\mathrm{o}}$ is the unimer standard chemical potential, *R* is the gas constant, *T* is the absolute temperature and x_{cmc} is the *cmc* expressed in surfactant molar fraction.[68]

The pseudo phase separation model, although providing an approximation for $\Delta_{\mathrm{mic}}G_{\mathrm{m}}^{\mathrm{o}}$, assumes that micelles are unlimited assemblies, when in fact they have a finite aggregation number. Thus, mass-action (or equilibrium) model is an alternative way of modeling the micellization process. In this model, the micellization process is considered as a chemical equilibrium between the free unimers and the micelles.[68] This model relates the aggregation number with the Gibbs energy of micellization, describing the micellization process more accurately. For monomeric surfactants with monovalent counterions, in the absence of salt, the mass-action model states $\Delta_{\mathrm{mic}}G_{\mathrm{m}}^{\mathrm{o}}$ as:

$$\Delta_{\mathrm{mic}}\mathrm{G}_{\mathrm{m}}^{\mathrm{o}} = (2-\alpha)RT \ln x_{\mathrm{cmc}} \quad (1.3)$$

where α is the degree of counterion dissociation (or degree of micelle ionization). For totally charged micelles, $\alpha = 1$; for neutral micelles, $\alpha = 0$. Further expressions are applied in the presence of salt or other types of surfactants, such as gemini.[72]

Micelles are not the only structure formed by self-assembled surfactant molecules. In fact, the type of aggregate formed by the assembly of surfactant molecules can be rationalized in terms the surfactant packing parameter (P_s) defined as the ratio:

$$P_s = \frac{V_{hc}}{a_{hg}\, l_{hc}} \quad (1.4)$$

where V_{hc} is the volume of the hydrocarbon chain of the surfactant and $a_{hg}\, l_{hc}$ represents the volume of a hypothetical cylinder defined by the effective area of the polar head group (a_{hg}) and the length of the extended hydrocarbon chain (l_{hc}).[68] If the volume of the alkyl chain is equal to the cylinder volume, $P_s = 1$, and a bilayer is favored. The most favorable packing will result in curved aggregates like spherical micelles, when $P_s = 1/3$ (corresponding to a surfactant with shape similar to a cone), or cylindrical micelles ($P_s = 1/3 - 1/2$). When $P_s > 1$, reverse structures are preferably formed.[68]

The concentration of surfactant molecules affects the type of structures formed. With increasing concentration, inter-aggregate interactions occur and some

rearrangements to more favorable structures can take place. An ideal phase sequence for a surfactant, regarding the gradual increase in the surfactant concentration in solution, is given by the Fontell diagram (Fig.1.8).[73]

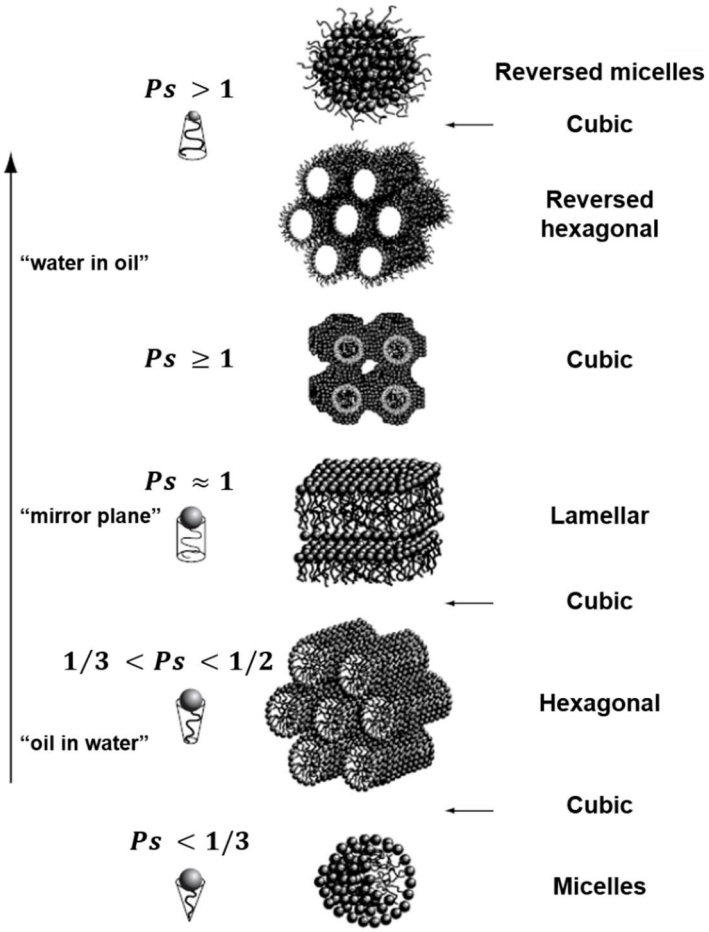

Fig. 1.8. Phase sequence of surfactant structures with increasing concentration according to the packing parameter. Adapted. [70]

1.2.2. Polymers

Polymer science is a broad field of science, where chemistry, physics and material science intersect. In this section, we will cover more specifically the topics relevant to the work developed, namely the properties of water-soluble polymers. Polymers can be defined as macromolecules constituted by a repetition of smaller chemical units - monomers – that are covalently linked in a process designated as polymerization.[74] Polymers can be broadly divided into two major families: natural or biological polymers (e.g. proteins, polysaccharides and nucleic acids), and synthetic or man-made polymers.[70]

Synthetic polymers are classified regarding their structure - linear, branched, or cross-linked - or composition. If the polymer is synthetized using more than one type of monomer, it is designated as copolymer. The monomer units can distribute i) randomly; ii) in blocks; or iii) one of the monomers is grafted in chains onto the backbone of other chain.[70] If the monomers in a polymer bear a charged group, the polymer can be designated as a polyelectrolyte.[71] Alongside these definitions, a polymer will have surface active properties if it shows i) hydrophobic chains grafted to a hydrophilic backbone; ii) hydrophilic chains grafted to a hydrophobic backbone or iii) hydrophilic and hydrophobic segments.

The configuration of a polymer in solution depends on the balance between segment-segment interactions and segment-solvent interactions, which in turn often depend on the type of solvent used and/or the temperature. Hence different conformations can be adopted by a polymer chain in solution (Fig. 1.9), with the most common ones for synthetic polymers being: the globule or collapsed coil (in poor solvents) and the random coil (in a good solvent). In polyelectrolytes, the typical conformations are the expanded coil and the rigid rod, depending on the charge density.[70]

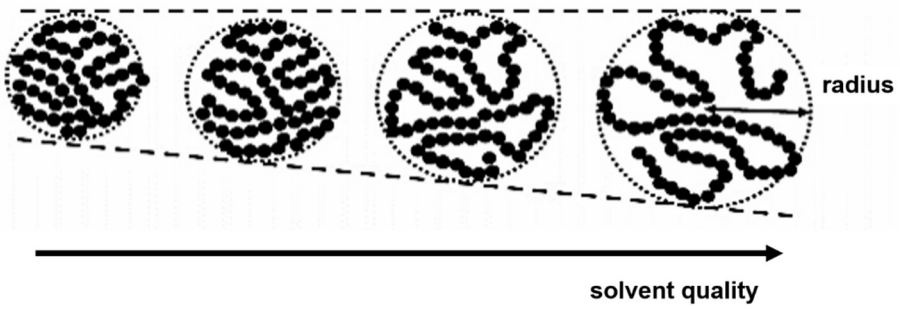

Fig. 1.9. Polymer chain conformation, from the globule or collapsed coil (left) to the random coil (right), according to segment-solvent interaction. Adapted.[75]

Some of the most studied water-soluble polymers include polyvinylpyrrolidone (PVP) and polyacrylic acid (PAA). The first, a non-ionic polymer, is highly soluble in water and other polar solvents due to its polarity. PVP associates with anionic surfactants in aqueous solution, forming complex structures.[70] These features, associated to its low toxicity, confer PVP high applicability in pharmaceuticals,[76] biosensors[77] and synthesis of nanoparticles for drug delivery.[78] PAA is an anionic polyelectrolyte (or polyanion). Polyelectrolytes, due to their typical conformation in extended chains or rigid rods, are widely used as thickeners, dispersants and to build composite films or coatings.[70, 79, 80]

PAA can also be found neutralized with sodium, in the form of sodium polyacrylate (PAS). PAS, due to its increased sodium content, is a super-absorbent polymer. This class of polymers has applicability in a wide range of areas, from hygiene products[81] to water treatment.[82]

1.2.3. Polymer/surfactant mixtures

Regarding their applicability in carbon science, surfactants have been widely used not only as dispersants for CNTs and graphene but also to produce composites with carbon nanomaterials, since they can be easily fabricated and are considered a group of relatively inexpensive materials for many engineering applications.[83-85] The interfacial and aggregation behavior of surfactants, however, can be modified by the presence of a polymer in the solution. Polymer/surfactant systems are extremely interesting from a fundamental colloidal point of view and so they have been extensively studied over time.[79, 86-92] Besides, they bear a crucial importance in many products and industrial processes, namely in detergents,[93] pharmaceutical and cosmetics,[94] food industry,[95] enhanced oil recovery[96] and wastewater treatment.[97]

There are two main pictures of polymer/surfactant solutions: i) interaction in terms of a strongly cooperative association (i.e. binding of the surfactant to the polymer) and ii) micellization of surfactant on or in the surrounding area of the polymer chain. Usually, the first approach is preferred for polymers with hydrophobic groups, while for hydrophilic homopolymers the second approach is favorable. Regarding the aggregate structure, one of the most accepted models for homopolymer/ionic surfactant systems is the “pearl necklace model” (Fig. 1.10), with the surfactant forming micellar-like clusters along the polymer chain.[70]

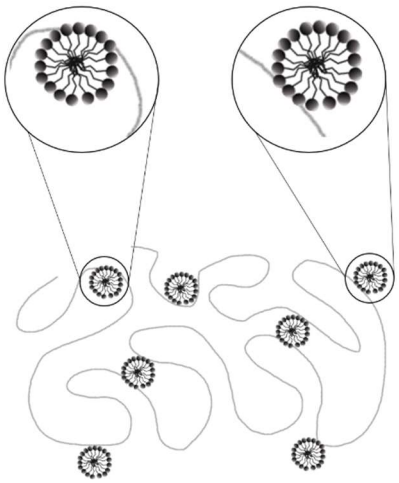

Fig. 1.10. The "pearl-necklace model" of polymer-surfactant association. Adapted.[70]

We will now analyze in more detail the interactions in solution between ionic surfactants and polymers, a subset of polymer/surfactant systems. The concentration and charge of the surfactant and polymer in the mixture play a pivotal role in the interactions of the complex formed. Similar to the micellization process of the individual surfactant, the hydrophobic interaction is a dominating contribution to the Gibbs energy of association in PS systems; however, strong associative phase behavior can be expected if the two co-solutes (surfactant and polymer) are oppositely charged, and, conversely, repulsive interactions that occur between charged polymer and similarly charged surfactant lead often to segregation behavior.[70, 92]

When there is associative phase behavior, over a range of surfactant concentrations, the surfactant and polymer form molecular complexes due to the net attractive interaction between surfactant and polymer. This behavior is illustrated in Fig. 1.11, which shows the dependance of surface tension as a function of surfactant concentration when mixed with polymer (at fixed polymer concentration) and compares this behavior with that of the individual surfactant. At low surfactant concentrations, depending on the surface activity of the polymer, there may be already a decreased surface tension compared to that of the neat surfactant system. Increasing the surfactant concentration, a first break in the surface tension curve occurs and a nearly constant surface tension value is attained (*cac*), remaining stable over a concentration range. This point represents an onset of interaction between the surfactant unimers and the polymer, whereby micelles form along the polymer chains, in close interaction. Once the polymer chains become saturated with surfactant micelles, the surfactant unimer concentration and the activity increase again. Consequently, there is a lowering of surface tension until the unimer concentration reaches the formation of surfactant-only micelles in the bulk, that is the *cmc* in the presence of polymer (*cmc*'), after which the surface tension value becomes constant again.[70] Therefore, *cac* is lower than neat surfactant *cmc*, and the latter is lower than *cmc*'.

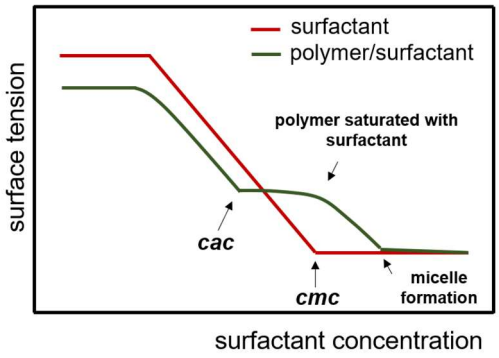

Fig. 1.11. Schematic representation of surface tension as a function of surfactant concentration in water with no polymer present (red) and in an aqueous solution containing polymer at fixed concentration (green).

The charge effect was studied for polyions and surfactants of opposite charge, where strong interactions are at play due to electrostatic forces[98]: neutral polymer/ionic surfactant systems have also been investigated, with the general conclusion that anionic surfactants (e.g. SDBS) interact strongly with non-ionic polymers (e.g. PVP). Conversely, cationic surfactants (e.g. CTAB) have been found to interact very weakly (or not interact at all) with neutral polymers. The interaction was found to improve when more hydrophobic polymers, such as poly(vinyl alcohol) were used.[86, 87, 91] Furthermore, Minati et al. reported that PVP/SDS systems form negatively charged aggregates, consisting of SDS molecules associated with individual polymeric chains, at low concentrations. Above the critical aggregation concentration, *cac*, the aggregates are formed by PVP chains with multiple SDS micelles attached. Interestingly, these aggregates exhibited similar properties as linear polyelectrolytes.[99] Similar behavior was reported for PVP/AOT systems by Kamli et al.[100]

The possible industrial and technological applications of polymer/surfactant systems are immense, due to the tunability of the system properties and innumerable combination possibilities. Therefore, an understanding of the behavior of these systems is an important issue for both scientific and technological purposes. Despite the extensive study of PS mixtures in the last decades, the knowledge on their interaction with hydrophobic surfaces, such as carbon nanotubes or other hard nanomaterials, is still being consolidated, making it difficult to establish general rules for describing the adsorption behavior for these systems.[101]

1.2.4. Non-covalent functionalization: mechanisms and dynamics

The production of well-dispersed nanotubes,[102, 103] graphene,[104, 105] and inorganic graphene analogues[65, 106, 107] in various organic solvents has been widely explored over the years. For most applications and due to environmental restrictions, however, obtaining aqueous dispersions of these nanomaterials is of great practical interest.[108, 109] One of the most common approaches for dispersion (and stabilization) of nanomaterials in aqueous solvents is to employ amphiphilic dispersants, as described in previous sections. Among the dispersants used are surfactants,[49, 110-112] synthetic polymers[113] and proteins[114, 115] - which bind to the hard surface via their hydrophobic moieties, providing wettability and colloidal kinetic stability through their polar regions. The electrostatic repulsions (when ionic dispersants are used) or steric repulsions (when nonionic dispersants are used) are responsible for the long term colloidal stability of the dispersed particles, even though it is a metastability and not true thermodynamic stability.[103]

The mechanism of amphiphile-assisted dispersion proposed for carbon nanotubes is schematically depicted in Fig. 1.12.[116] The general dispersant behavior on the exfoliation of 2D layered materials, such as graphene and transition metal dichalcogenides, is expected to be similar, although fundamental studies are still scarce. Three stages should be distinguished in the dispersing process: i) cleavage (Fig. 1.12b); ii) amphiphile adsorption (Fig. 1.12c); and iii) stabilization (Fig. 1.12d).

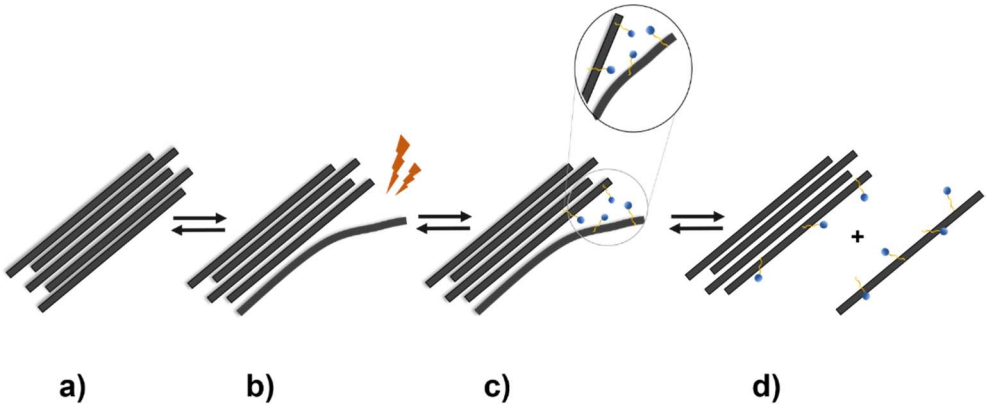

Fig. 1.12. Representation of the dispersant-assisted exfoliation proposed for carbon nanotubes and 2D layered materials: a) bulk reservoir; b) applied forces create cavities in the bundle end; c) amphiphilic molecules adsorb on the freshly exposed surface; d) individualized particles separate from the bulk and remain dispersed due to non-covalent functionalization.

The first part of the process consists in the mechanical separation of the sheets or tubes from the bulk reservoir. This separation occurs through an 'unzipping' mechanism: the energy source produces clefts between adjacent tubes/sheets, allowing surfactant (or polymer) molecules to adsorb (essentially via hydrophobic interactions)

onto the newly exposed surface. Surfactant adsorption propagates along the fissure, separating the tube/sheet beyond the short van der Waals distance and eventually splitting it from the bundle/ aggregate.[110, 117] Finally, after removing the non-dispersed particles and large aggregates using a centrifugation step, the dispersed materials remain stabilized by steric or electrostatic repulsions that provide a kinetic barrier to reaggregation. This procedure allows to obtain kinetically (not thermodynamically) stabilized suspensions of the 1D and 2D nanomaterials.

Regarding CNT dispersion via surfactant adsorption, the mechanism has not been unequivocally determined. It has been previously hypothesized that the SWNTs form the core of cylindrical micelles of surfactants (Fig. 1.13a) or are coated by adsorbed hemimicellar surfactants (Fig. 1.13b).[118, 119] Yurekeli et al. presented structural data that refute the formation of cylindrical micelles in aqueous dispersions of sodium dodecyl sulfate (SDS)-SWNT and suggest that structureless random adsorption with no preferential arrangement of the head and tail of the surfactants is responsible for the stabilization of the dispersions (Fig. 1.13c).[112, 119-121]

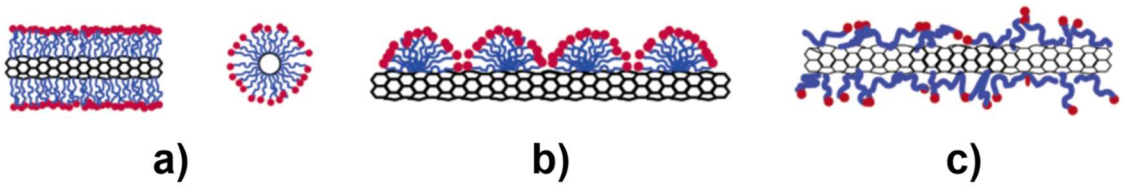

Fig. 1.13. Schematic representations of proposed mechanisms of surfactant adsorption on a SWNT hydrophobic surface. a) CNT encapsulated in a cylindrical surfactant micelle: side view (left) and cross section (right); b) surfactant adsorbed in the form of hemimicelles; c) random adsorption of surfactant molecules on a SWNT. Adapted from [119]

To describe polymer-nanotube interactions, two configurations stand out among the proposed models: polymer wrapping[122] and loose adsorption.[123, 124] O'Connel et al. discussed a general thermodynamic drive for CNT wrapping, whereby the polymer disrupts both the hydrophobic interface with water and the tube-tube interactions in the aggregates; nanotubes can be unwrapped by changing the solvent system.[122] In this model, the polymer forms a helical structure in close contact with the CNT surface, suggesting strong a polymer-nanotube interaction. Alternatively, the loose adsorption model considers that the original configuration of the polymer does not change significantly, suggesting a weaker polymer-nanotube interaction. The latter is believed to be adopted by polymers consisting of hydrophilic and hydrophobic moieties, wherein the hydrophobic part is (supposedly) attached to the CNT surface by a "non-wrapping" interaction, while the hydrophilic part provides a barrier to prevent reaggregation.[125-128]

The general aspects of amphiphile-CNT interaction can be extrapolated, to a certain extent, to the exfoliation of graphene and other 2D inorganic graphene analogues. Sun et al. simulated the adsorption of the anionic surfactant sodium dodecylbenzene sulfonate (SDBS) on graphene sheets, finding that, at high concentrations, surfactant tends to form micelles that encapsulate the graphene.[129] Studies regarding the surfactant-aided exfoliation of TMDs, although fewer when compared to those on CNTs and graphene, suggest a similar mechanism to CNTs, and are gaining importance.[18, 48, 130]

Literature covers a wide range of dispersants, assessing different molecular properties.[49, 51, 110, 112, 131-133] However, the distinct processing conditions, nanomaterial batches and non-systematic variation of the dispersant features make comparisons difficult - which is crucial to select the best system for further applications (e.g. composite building). Therefore, studies comparing surfactants in a significative concentration range, using controlled experimental conditions and with a systematic variation of the surfactant or material features are both necessary from a fundamental viewpoint and useful from a practical perspective.[112, 120]

1.3. Nanocomposites of 1D and 2D nanomaterials

1.3.1. Aims and challenges

The applications of carbon nanotubes, graphene, and transition metal dichalcogenides have been widely studied in the past years, and the performance of the different materials has been compared.[134-136]

Following the growth of research on 1D and 2D nanomaterials per se, the interest on the combination of the basic forms into more complex 3D architectures also emerged, projecting the individual properties of CNTs, graphene and TMDs into new or enhanced fucntionalities.[1] Countless applications have arisen from the combination of these nanomaterials, such as energy storage, sensors, coatings, mechanical reinforcement, or catalysis.[137] One particular combination is the synergistic combination of graphene sheets with carbon nanotubes (CNT). For instance, the vertical interposition of CNTs between 2D sheets would avoid aggregation of the layers and hence electronic transport,[138] thermal transport,[139] and hydrogen storage[140] properties could be enhanced. Conversely, CNTs could also be horizontally organized within large-area sheets, and the mechanical strength of the latter could be significantly reinforced due to the excellent

flexibility and strength of CNTs.[1] The main challenge lies in building assembled, reproducible and scalable structures with synergistic properties.

It is important to clarify the definitions of composite, nanocomposite, and hybrid material, when assessing the combination of 1D and 2D nanomaterials to create 3D structures. According to IUPAC, a composite is a multicomponent material comprising multiple, different (non-gaseous) phase domains in which at least one type of phase domain is a continuous phase; when at least one of the phase domains has at least one dimension of the order of nanometers, the term “nanocomposite” can be applied. Hybrid materials are defined as mixtures of inorganic components, organic components, or both types of component, in which the components interpenetrate on scales of less than 1 μm.[141] Therefore, materials obtained from the combination of 1D and 2D nanomaterials can be considered as nanocomposites or hybrids, and it is common to see both these designations used interchangeably in literature. Regarding this work, typically the built 3D structures will be designated as composites or nanocomposites, since the 1D and 2D nanomaterial building blocks are non-covalently functionalized with surfactant and/or polymer and hence are, by themselves, hybrids.

1.3.2. Fabrication methods and applications of 1D/2D composites

Recent studies in the carbon nanomaterials area have focused on the building of hybrid materials by covalent functionalization of one or both of the carbon nanomaterials involved, and frequently using graphene oxide as building block or adding the graphene reduction step to the building procedure.[142-147] Faisal et al. developed a nitrogen-doped graphene/carbon nanotube composite material via thermal annealing treatment at 800 °C, using graphene oxide and oxidized CNTs as starting materials. The resulting 3D structure showed excellent capacitive properties when incorporated in a solid-state capacitor device and electrocatalytic performance towards ORR and OER.[148] Graphene oxide/carbon nanotube hybrid materials were fabricated using surfactant-dispersed CNTs. The mixture of GO/CNTs was sonicated, followed by filtration and annealing at 800 °C. The final free-standing material presented promising results as collector and binder-free anode for lithium batteries.[149] Pham et al. reported the building of a CNT/graphene hybrid with outstanding performance for supercapacitors. The building of the assembled structure relied on the intercalation of the GO sheets with the surfactant-dispersed CNTs, through KOH activation.[150]

A common procedure to build composite structures is the layer-by-layer assembly (LbL), which consists in the deposition of alternating layers of oppositely charged

materials (Fig.1.14). The deposition can be by dip-coating (Fig.1.14a), if a substrate is alternately submerged in oppositely charged building block solutions, with a rinsing and a drying step between each deposited layer; or by spin-coating, where a small amount of material is deposited on the center of the substrate, followed by rotation to spread the coating material under the centrifugal force (Fig. 1.14b).[151]

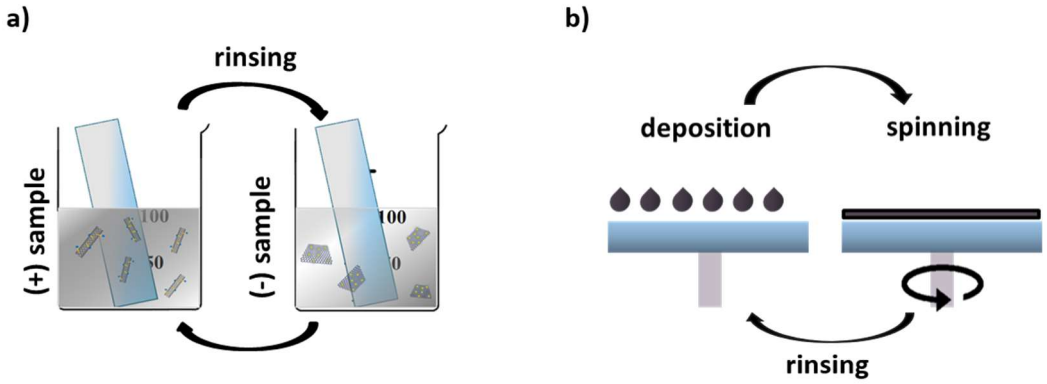

Fig. 1.14. Schematic representation of the layer-by-layer assembly methodologies: a) dip-coating and b) spin-coating.

Covalently functionalized carbon nanotubes and reduced graphene oxide have also been used to build composites by LbL, showing increased electronic conductivity and potential for supercapacitors and flexible electrodes.[142, 152]

Regarding the use of TMDs to fabricate composite materials, a new research field has recently emerged, based on the combination of 2D layers to build heterostructures and devices. The resulting structures consist of stacks of monolayer or few-layer materials assembled in a chosen sequence.[20] The combination of these 2D materials with carbon nanotubes has been recently reported, but this area remains unexplored. Wang et al. used MWNTs to prevent MoS_2 stacking and to bridge isolated MoS_2 nanosheets, improving the interfacial interaction in an epoxy matrix. The MWNT/MoS_2 composite was built using electrostatic interactions, mixing negatively charged MWNTs (prepared by strong acid oxidization) and positively charged MoS_2 sheets (exfoliated by sonication in a chitosan aqueous solution). This combination resulted in increased tensile modulus, improved strength and enhanced elongation at break of the composite, compared to pure epoxy.[153] Kim et al. have also applied CNTs to prevent the TMD restacking, by mixing non-covalently functionalized SWNTs with lithium-intercalated WS_2. The obtained multi-dimensional nanocomposite exhibited enhanced thermoelectric power and mechanical stretchability, to be applied in wearable power sources.[154]

While chemical functionalization may change the carbon surface and its properties, physical adsorption (i.e. surfactant binding to the surface) is suitable if one wants to preserve the original properties of CNTs. However, studies regarding the design and building of CNT/graphene or CNT/TMD composite materials via non-covalent functionalization only are still very scarce, indicating that this area of research remains largely unexplored. The applications for 1D/2D assembled structures are infinite. However, the building method of the 3D materials has an influence in the final properties and needs to be tuned according to the chosen application. Even with the intense research on this area, the building of scalable, reproducible materials fabricated using carbon nanotubes and graphene/transition metal dichalcogenides remains a challenge.

1.4. Nanomaterials as electrocatalysts for energy conversion reactions

1.4.1. Energy conversion

The pursuit of a clean and sustainable future has increased the demand for alternative energy conversion technologies. The basis for promising energy conversion systems is the hydrogen cycle (i.e. water cycle). It involves the hydrogen and oxygen reactions and the use of electricity for the water splitting reaction to generate H_2 (fuel) and O_2 in an electrolytic cell, through the hydrogen evolution reaction (HER) at the cathode and the oxygen evolution reaction (OER) at the anode. In the reverse direction, in hydrogen-based fuel cells, the produced H_2 can be oxidized at the anode (hydrogen oxidation reaction, HOR) while at the cathode occurs the reduction of oxygen (oxygen reduction reaction, ORR), with water as the major product.[155, 156]

Recent years have witnessed the exponential growing of research in fuel cells and metal-air batteries as promising alternatives for energy conversion. In a fuel cell, electricity is generated from the conversion of electrochemical energy through the oxidation of fuel (often hydrogen, as mentioned above) at the anode and ORR at the cathode. However, the slow kinetics of oxygen reduction makes the use of an electrocatalyst mandatory for these devices.[157, 158] According to the electrolyte used and operation temperatures, fuel cells can be divided in classes, as depicted in Fig. 1.15. The metal-air batteries combine a metal anode and an air cathode with open structure to draw cathode-active materials (i.e. oxygen) from air; in short, these devices generate electricity through a redox reaction between metal and oxygen in air. Since cathode oxygen reactions are generally irreversible with slow kinetics, to implement the cycling

of an air electrode it is necessary to use a catalyst capable of accelerating the ORR upon discharging and mediating the OER on charging.[159]

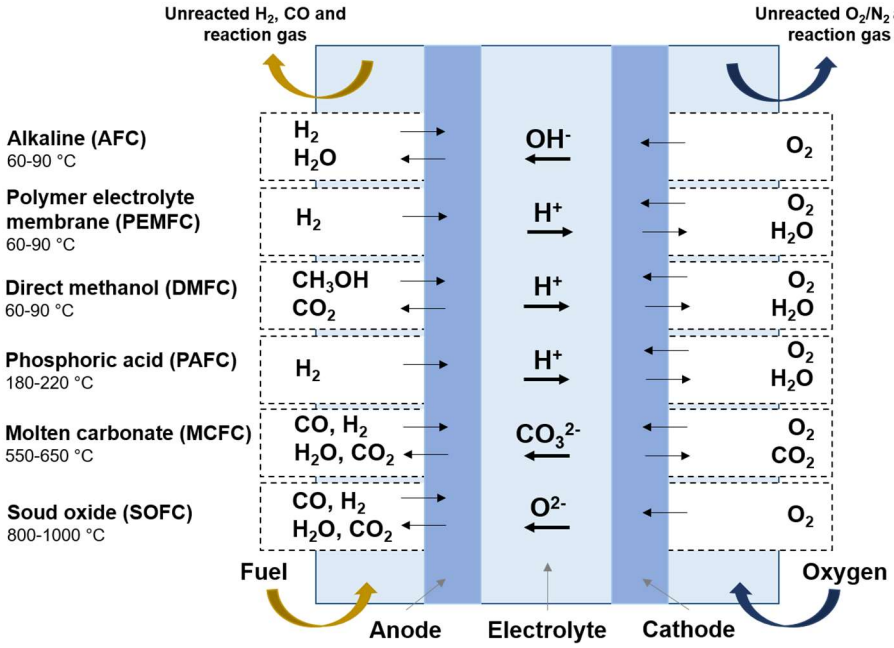

Fig. 1.15. Summary of fuel cell classes, with respective reactions and processes that occur in the various systems. Adapted.[160]

Alongside the development of the described electrochemical devices, the optimization of chemical processes to meet the sustainability requirements for industry represents a considerable research challenge. One of these processes is the generation of hydrogen peroxide, H_2O_2, considered one of the 100 most important chemicals. Hydrogen peroxide is a versatile and environmentally friendly oxidant, possessing wide applicability (e.g. bleaching, synthesis of organic compounds, water treatment, environmental remediation).[161, 162] The majority of H_2O_2 is produced through the anthraquinone oxidation process (i.e. auto-oxidation process), that requires massive infrastructure and significant energy input. The production is thus centralized, with consequent need for transport, storage and handling of high-concentration H_2O_2, which involves hazards and high costs.[163, 164] However, several applications, such as disinfection, cosmetics, wastewater treatment or chemical synthesis, require H_2O_2 at low concentrations, which makes other production processes candidates to replace the anthraquinone oxidation.[165] Hydrogen peroxide production via 2-electron O_2 electroreduction pathway is one of the most attractive alternatives, enabling *in situ* H_2O_2 production at moderate temperature and atmospheric pressure.

In the next subsections, the fundamental aspects of oxygen reduction reaction (ORR) and oxygen evolution reaction (OER) will be presented, and the application of carbon-based materials as electrocatalysts will be introduced.

1.4.1.1. Oxygen Reduction Reaction (ORR)

The oxygen reduction reaction plays a crucial role in energy converting systems. In aqueous solutions, oxygen can be reduced through two different pathways: i) the direct pathway, or four-electron process; ii) the indirect pathway, or two-electron process. In the first, the oxygen molecule gains four electrons, generating water (in acidic media) or hydroxyl group (in alkaline media). In the indirect process, intermediate hydrogen peroxide (in acidic media) or peroxide ion (in alkaline media) is generated. The two processes are summarized in Table 1.1.[166, 167]

Table 1.1. Reaction pathways of ORR in aqueous electrolyte solutions, at 25 °C (potentials vs. SHE).

Electrolyte	Reaction pathway
Alkaline	*4-electron* $O_2 + 4e^- + 2H_2O \rightarrow 4OH^-$ (E^o = 0.401 V) *2-electron* $O_2 + 2e^- + H_2O \rightarrow HO_2^- + OH^-$ (E^o = -0.065 V) $HO_2^- + 2e^- + H_2O \rightarrow 3OH^-$ (E^o = 0.867 V)
Acidic	*4-electron* $O_2 + 4e^- + 4H^+ \rightarrow 2H_2O$ (E^o = 1.229 V) *2-electron* $O_2 + 2e^- + 2H^+ \rightarrow H_2O_2$ (E^o = 0.695 V) $H_2O_2 + 2e^- + 2H^+ \rightarrow 2H_2O$ (E^o = 1.763 V)

The ORR has slow kinetics, due to the high energy of O=O bond, which makes the use of an electrocatalyst crucial for practical applications. The state-of-the-art ORR electrocatalyst consists of platinum nanoparticles immobilized on carbon nanomaterials (Pt/C), showing high current densities and selectivity for the 4-electron reduction pathway.[168] Electrochemical parameters are used to compare ORR electrocatalysts with the Pt/C, namely: i) the onset potential (E_{onset}), defined as the potential at which the reaction starts; ii) the diffusion-limited current density (j_L), reached when the reaction at the electrode is fully controlled by mass transport, and visualized as a *plateau* in the voltammogram; iii) the kinetic current density (j_k), the current in the absence of mass-transfer limitations; iv) the number of electrons transferred per O_2 molecule (n_{O2}), usually obtained through the Koutecky–Levich (K–L) equation (as described in section 2.5), and

v) the Tafel slope, that provides information on the mechanism of reaction of the electrocatalyst. An electrocatalyst with good ORR performance shows a less negative E_{onset}, high j_L value and low Tafel slope.[155, 169, 170] The ideal n_{O2} depends on the desired application.

Despite the outstanding performance as an ORR electrocatalyst, Pt/C does not have a significative tolerance to methanol, which is a drawback for the application in the cathode of fuel cells, where fuel poisoning can occur. This feature, adding to the high-cost and scarcity of the noble metal, makes the research for alternative, sustainable electrocatalysts imperative.[155, 171, 172]

1.4.1.2. Oxygen Evolution Reaction (OER)

The oxygen evolution is a four electron-proton coupled reaction, involving the electrochemical oxidation of water to produce O_2 (Table 1.2). Despite the importance of OER in the anode of energy conversion systems (e.g. fuel cells, metal-air batteries), the high energy (i.e. high overpotential) required to overcome the kinetic barrier of OER is a drawback for the practical use of this reaction.[173]

Table 1.2. OER reaction mechanism in aqueous electrolyte solutions.

Electrolyte	Reaction pathway
Alkaline	$4OH^- \rightarrow 2H_2O\ (l) + O_2\ (g) + 4e^-$
Acidic	$2H_2O\ (l) \rightarrow 4H^+ + O_2\ (g) + 4e^-$

As described for ORR, the performance of OER electrocatalysts can be evaluated through some parameters: i) overpotential (η), defined as the difference between the applied potential (E) and potential under equilibrium conditions (E_{eq}), and also referred to as the value that has to be applied to achieve a specific current density (i.e. a lower overpotential indicates a superior electrocatalytic activity of the electrocatalyst); ii) exchange current density (i_0), that reflects the intrinsic bonding/charge transferring interactions between electrocatalyst and reactant (meaning a high i_0 is typically indication of a good electrocatalyst), and iii) Tafel slope, that, as in ORR, provides information towards the mechanism of the reaction, specifically the rate-determining step.[155, 173]

The state-of-the-art electrocatalysts for OER are ruthenium and iridium oxides (RuO_2 and IrO_2), with the latter showing the best relation between electrocatalytic

performance and stability. However, similar to Pt/C, the scarcity and cost of these materials is a shortcoming for applications.[170]

1.4.2. Carbon-based materials as electrocatalysts for ORR and OER

As addressed in the previous sections, ORR and OER are fundamental in electrochemical devices and processes. ORR is the cathode reaction of fuel cells and metal-air batteries, which require the reaction to occur through 4-electron pathway. The capacity to catalyze both ORR and OER would be a significant improvement of electrocatalysts for metal-air batteries since the current benchmark catalysts only exhibit superior performance for one of the reactions. In parallel, the ORR 2-electron pathway is gaining attention as a sustainable alternative for the electrochemical production of hydrogen peroxide. The major problems that limit the commercialization of electrochemical devices rely on the cost and durability, attributed to the use of expensive materials as catalysts, that present relatively low durability in the device operating conditions. Thus, the optimization of these devices relies on finding cost-effective materials to substitute the benchmark electrocatalysts.[159, 165, 174-176]

The wide availability and tunability of carbon nanomaterials (e.g. carbon nanotubes, graphene nanoplatelets), combined with their remarkable electronic, mechanical, and thermal properties, lead the research of their individualized forms or composites as electrocatalysts. Due to their high conductivities, carbon nanomaterials have also been applied as support materials, increasing the stability of the catalyst particles, and improving the catalytic activity. Carbon-based nanocomposites, being metal-free, have been found to perform as efficient, selective, and stable electrocatalysts toward 2-electron O_2 reduction.[165, 177, 178]

The activity (or reaction rate) of an electrocatalyst can be improved by two strategies: i) increasing the number of active sites on a given electrode (e.g. by changes in the electrode structuration, or through increased loading); or ii) increasing the intrinsic activity of each active site (e.g. through alloys or the use of adsorbates). These strategies can ideally be addressed simultaneously, aiming at critical improvements in electrocatalyst activity.[167, 179] Considering these approaches, heteroatom doping has been widely used to improve the electrochemical activity of carbon nanomaterials, resulting in promising catalysts for ORR and OER under alkaline conditions.[180, 181] The doping of carbon with more electronegative atoms (e.g. nitrogen) creates a net positive charge on adjacent carbon atoms, facilitating oxygen adsorption and charge transfer, and consequently increasing ORR/OER activity.[180] When dopant atoms that are less

electronegative than carbon are used (e.g. boron), similar charge sites are created to facilitate the catalytic process.[167, 175, 181] Doped carbon nanotubes and doped graphene have been widely applied as electrocatalysts for ORR and OER, in their individual forms[181-184] or in composites (typically combined with metals and/or a different carbon nanomaterial).[185-189] However, the ORR performance significantly depends on level of doping, which is hard to control and reproduce.[190]

The doping of carbon nanotubes and graphene relies on intramolecular charge-transfer, creating a net charge. This principle has been further applied to develop carbon-based electrocatalysts without the doping requirement, by using physical functionalization of the carbon surface to create the net charge through intermolecular charge-transfer. In particular, Wang et al. reported that the use of polyelectrolytes with electron-withdrawing ability was able to enhance the electrocatalytic activity of graphene[191] and carbon nanotubes[192] towards ORR (Fig. 1.16).

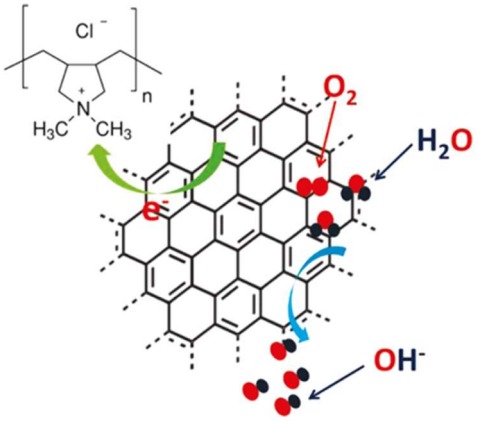

Fig. 1.16. Schematic illustration of the electron-withdrawing from graphene by PDDA, to facilitate the ORR process, as proposed by Wang et al.[191]

The use of adsorbed molecules to enhance the intrinsic electrocatalytic activity of carbon nanomaterials opens the path to the development of catalysts with reproducible performance. The variety of polyelectrolytes – or charged polymer/surfactant mixtures – that can be applied provides further tunability and opens the possibility for large-scale applications. Different physically functionalized materials (e.g. carbon nanotube/graphene nanoplatelets; carbon nanotube/transition metal dichalcogenide) can be combined into more complex structures, aiming at maximum improvement of electrocatalytic activity.

1.5. Scope and goals of this work

This work was conducted in the *Surfactants, Colloids and Soft Nanomaterials* group, within the RG3- Nanostructures & Self-organization R&D Group, Centro de Investigação em Química da Universidade do Porto (CIQUP), in collaboration with the Materials for Sustainability and Wellness Group, Associated Laboratory for Green Chemistry (LAQV) of the Network of Chemistry and Technology (REQUIMTE), at the Department of Chemistry and Biochemistry of Faculty of Sciences of University of Porto (DQB-FCUP).

The project aimed at the exfoliation, functionalization, and characterization of 1D and 2D nanomaterials, focusing on their use as building blocks for developing functional 3D composites for electrocatalytic applications. The strategy involved the selection of the most suitable nanomaterial blocks, regarding quality, preparation, reproducibility, and cost, for the fabrication and characterization of the 3D composites. Electrocatalytic studies were then performed to evaluate the applicability of the prepared nanocomposites as catalysts for ORR and OER.

This project encompassed the following more specific goals:

- to understand the role of surfactants in the exfoliation and non-covalent functionalization of carbon nanotubes, graphene, and inorganic graphene analogues, starting from bulk materials (Papers I, II, IV);

- to assess the effect of polymer/surfactant mixtures as dispersants for carbon nanotubes, and their role in the organization of 3D hybrids (Papers III and V);

- to build 3D composites from non-covalently functionalized 1D and 2D nanomaterials, establishing a simple and reproducible methodology (Papers V and VI);

- to study the electrocatalytic performance of the new 3D materials for ORR and OER and compare them with the building blocks (Papers V and VI).

References

1. Zhang, J.; Terrones, M.; Park, C. R.; Mukherjee, R.; Monthioux, M.; Koratkar, N.; Kim, Y. S.; Hurt, R.; Frackowiak, E.; Enoki, T.; Chen, Y.; Chen, Y. S.; Bianco, A., Carbon science in 2016: Status, challenges and perspectives. *Carbon* **2016,** *98* (70), 708-732.
2. Tan, C.; Cao, X.; Wu, X. J.; He, Q.; Yang, J.; Zhang, X.; Chen, J.; Zhao, W.; Han, S.; Nam, G. H.; Sindoro, M.; Zhang, H., Recent advances in ultrathin two-dimensional nanomaterials. *Chem. Rev.* **2017,** *117* (9), 6225-6331.
3. Hecht, D. S.; Hu, L.; Irvin, G., Emerging transparent electrodes based on thin films of carbon nanotubes, graphene, and metallic nanostructures. *Adv. Mater.* **2011,** *23* (13), 1482-513.
4. Breuer, O.; Sundararaj, U., Big returns from small fibers: A review of polymer/carbon nanotube composites. *Polym Composite* **2004,** *25* (6), 630-645.
5. Iijima, S., Helical microtubules of graphitic carbon. *Nature* **1991,** *354* (6348), 56-58.
6. Baughman, R. H.; Zakhidov, A. A.; De Heer, W. A., Carbon nanotubes--the route toward applications. *Science* **2002,** *297* (5582), 787-792.
7. Britz, D. A.; Khlobystov, A. N., Noncovalent interactions of molecules with single walled carbon nanotubes. *Chem. Soc. Rev.* **2006,** *35* (7), 637-59.
8. Grady, B. P., *Carbon nanotube-polymer composites: manufacture, properties, and applications*. John Wiley & Sons: 2011.
9. Noé, J. Environmental effects in the photophysics of cryogenic carbon nanotubes. lmu, 2019.
10. Harris, P. J. F., Physical properties I: electronic. In *Carbon nanotube science: Synthesis, properties and applications*, Harris, P. J. F., Ed. Cambridge University Press: Cambridge, 2009; pp 146-178.
11. Thostenson, E. T.; Li, C.; Chou, T. W., Nanocomposites in context. *Compos. Sci. Technol.* **2005,** *65* (3), 491-516.
12. Reich, S.; Thomsen, C.; Maultzsch, J., *Carbon nanotubes: basic concepts and physical properties*. John Wiley & Sons: 2008.
13. Yengejeh, S. I.; Kazemi, S. A.; Öchsner, A., *A primer on the geometry of carbon nanotubes and their modifications*. Springer: 2015.
14. Harris, P. J. F., Physical properties II: mechanical, optical and thermal. In *Carbon nanotube science: Synthesis, properties and applications*, Harris, P. J. F., Ed. Cambridge University Press: Cambridge, 2009; pp 179-203.
15. Yakobson, B. I.; Avouris, P., Mechanical properties of carbon nanotubes. In *Carbon nanotubes*, Springer: 2001; pp 287-327.
16. Geim, A. K.; Novoselov, K. S., The rise of graphene. In *Nanoscience and technology: a collection of reviews from nature journals*, World Scientific: 2010; pp 11-19.
17. Zhou, K. G.; Mao, N. N.; Wang, H. X.; Peng, Y.; Zhang, H. L., A mixed-solvent strategy for efficient exfoliation of inorganic graphene analogues. *Angew. Chem. Int. Ed.* **2011,** *50* (46), 10839-42.
18. Guardia, L.; Paredes, J. I.; Rozada, R.; Villar-Rodil, S.; Martinez-Alonso, A.; Tascon, J. M. D., Production of aqueous dispersions of inorganic graphene analogues by exfoliation and stabilization with non-ionic surfactants. *RSC Adv.* **2014,** *4* (27), 14115-14127.
19. Chhowalla, M.; Shin, H. S.; Eda, G.; Li, L. J.; Loh, K. P.; Zhang, H., The chemistry of two-dimensional layered transition metal dichalcogenide nanosheets. *Nat. Chem.* **2013,** *5* (4), 263-275.

20. Geim, A. K.; Grigorieva, I. V., Van der Waals heterostructures. *Nature* **2013,** *499* (7459), 419-425.
21. Novoselov, K. S.; Jiang, D.; Schedin, F.; Booth, T. J.; Khotkevich, V. V.; Morozov, S. V.; Geim, A. K., Two-dimensional atomic crystals. *Proc. Natl. Acad. Sci. U.S.A* **2005,** *102* (30), 10451-10453.
22. Flynn, G. W., Perspective: The dawning of the age of graphene. *J. Chem. Phys* **2011,** *135* (5).
23. Castro Neto, A. H.; Guinea, F.; Peres, N. M. R.; Novoselov, K. S.; Geim, A. K., The electronic properties of graphene. *Rev. Mod. Phys.* **2009,** *81* (1), 109-162.
24. Mayorov, A. S.; Gorbachev, R. V.; Morozov, S. V.; Britnell, L.; Jalil, R.; Ponomarenko, L. A.; Blake, P.; Novoselov, K. S.; Watanabe, K.; Taniguchi, T., Micrometer-scale ballistic transport in encapsulated graphene at room temperature. *Nano Lett.* **2011,** *11* (6), 2396-2399.
25. Katsnelson, M. I., Graphene: carbon in two dimensions. *Mater. Today* **2007,** *10* (1-2), 20-27.
26. Biró, L. P.; Nemes-Incze, P.; Lambin, P., Graphene: nanoscale processing and recent applications. *Nanoscale* **2012,** *4* (6), 1824-1839.
27. Lee, C.; Wei, X.; Kysar, J. W.; Hone, J., Measurement of the elastic properties and intrinsic strength of monolayer graphene. *Science* **2008,** *321* (5887), 385-388.
28. Nair, R. R.; Blake, P.; Grigorenko, A. N.; Novoselov, K. S.; Booth, T. J.; Stauber, T.; Peres, N. M. R.; Geim, A. K., Fine structure constant defines visual transparency of graphene. *Science* **2008,** *320* (5881), 1308-1308.
29. Balandin, A. A., Thermal properties of graphene and nanostructured carbon materials. *Nat. Mater.* **2011,** *10* (8), 569-581.
30. Moser, J.; Barreiro, A.; Bachtold, A., Current-induced cleaning of graphene. *Appl. Phys. Lett.* **2007,** *91* (16), 163513.
31. Bianco, A.; Cheng, H. M.; Enoki, T.; Gogotsi, Y.; Hurt, R. H.; Koratkar, N.; Kyotani, T.; Monthioux, M.; Park, C. R.; Tascon, J. M. D.; Zhang, J., All in the graphene family - A recommended nomenclature for two-dimensional carbon materials. *Carbon* **2013,** *65*, 1-6.
32. Wick, P.; Louw-Gaume, A. E.; Kucki, M.; Krug, H. F.; Kostarelos, K.; Fadeel, B.; Dawson, K. A.; Salvati, A.; Vazquez, E.; Ballerini, L.; Tretiach, M.; Benfenati, F.; Flahaut, E.; Gauthier, L.; Prato, M.; Bianco, A., Classification framework for graphene-based materials. *Angew. Chem. Int. Ed.* **2014,** *53* (30), 7714-8.
33. Mogera, U.; Dhanya, R.; Pujar, R.; Narayana, C.; Kulkarni, G. U., Highly decoupled graphene multilayers: turbostraticity at its best. *J. Phys. Chem. Lett.* **2015,** *6* (21), 4437-4443.
34. Feynman, R. P., There's plenty of room at the bottom. *California Institute of Technology, Engineering and Science magazine* **1960**.
35. Kumar, P.; Li, Z.; Wong, S. L., Functionalized transition metal dichalcogenide-based nanomaterials for biomedical applications. In *Biomedical Applications of Functionalized Nanomaterials*, Elsevier: 2018; pp 289-314.
36. Lv, R.; Robinson, J. A.; Schaak, R. E.; Sun, D.; Sun, Y.; Mallouk, T. E.; Terrones, M., Transitionmetal dichalcogenides and beyond: Synthesis, properties, and applications of single- and few-layer nanosheets. *Acc. Chem. Res.* **2015,** *48* (1), 56-64.
37. Manzeli, S.; Ovchinnikov, D.; Pasquier, D.; Yazyev, O. V.; Kis, A., 2D transition metal dichalcogenides. *Nat. Rev. Mater.* **2017,** *2* (8), 17033.
38. Wang, Q. H.; Kalantar-Zadeh, K.; Kis, A.; Coleman, J. N.; Strano, M. S., Electronics and optoelectronics of two-dimensional transition metal dichalcogenides. *Nat. Nanotechnol.* **2012,** *7* (11), 699-712.
39. Splendiani, A.; Sun, L.; Zhang, Y.; Li, T.; Kim, J.; Chim, C. Y.; Galli, G.; Wang, F., Emerging photoluminescence in monolayer MoS2. *Nano Lett.* **2010,** *10* (4), 1271-1275.

40. Ding, Y.; Wang, Y.; Ni, J.; Shi, L.; Shi, S.; Tang, W., First principles study of structural, vibrational and electronic properties of graphene-like MX2 (M= Mo, Nb, W, Ta; X= S, Se, Te) monolayers. *Physica B Condens. Matter* **2011,** *406* (11), 2254-2260.
41. Xu, M.; Liang, T.; Shi, M.; Chen, H., Graphene-like two-dimensional materials. *Chem. Rev.* **2013,** *113* (5), 3766-3798.
42. Bertolazzi, S.; Brivio, J.; Kis, A., Stretching and breaking of ultrathin MoS2. *ACS Nano* **2011,** *5* (12), 9703-9709.
43. Ding, R.; Lu, G.; Yan, Z.; Wilson, M., Recent advances in the preparation and utilization of carbon nanotubes for hydrogen storage. *J. Nanosci. Nanotechnol.* **2001,** *1* (1), 7-29.
44. Tanaka, K.; Iijima, S., *Carbon nanotubes and graphene*. Newnes: 2014.
45. Backes, C.; Mundloch, U.; Ebel, A.; Hauke, F.; Hirsch, A., Dispersion of HiPco® and CoMoCAT®single-walled nanotubes (SWNTs) by water soluble pyrene derivatives-depletion of small diameter SWNTs. *Chem. Eur. J.* **2010,** *16* (11), 3314-3317.
46. Phiri, J.; Gane, P.; Maloney, T. C., General overview of graphene: Production, properties and application in polymer composites. *Mater. Sci. Eng. B* **2017,** *215*, 9-28.
47. Wang, X.-Y.; Narita, A.; Müllen, K., Precision synthesis versus bulk-scale fabrication of graphenes. *Nat. Rev. Chem.* **2017,** *2*, 0100.
48. Zhang, X.; Lai, Z.; Tan, C.; Zhang, H., Solution-processed two-dimensional MoS2 nanosheets: preparation, hybridization, and applications. *Angew. Chem. Int. Ed.* **2016,** *55* (31), 8816-8838.
49. Vaisman, L.; Wagner, H. D.; Marom, G., The role of surfactants in dispersion of carbon nanotubes. *Adv. Colloid Interface Sci.* **2006,** *128-130*, 37-46.
50. Daukiya, L.; Seibel, J.; De Feyter, S., Chemical modification of 2D materials using molecules and assemblies of molecules. *Advances in Physics: X* **2019,** *4* (1), 1625723.
51. Wang, H., Dispersing carbon nanotubes using surfactants. *Curr. Opin. Colloid Interface Sci.* **2009,** *14* (5), 364-371.
52. Lotya, M.; Hernandez, Y.; King, P. J.; Smith, R. J.; Nicolosi, V.; Karlsson, L. S.; Blighe, F. M.; De, S.; Wang, Z.; McGovern, I. T.; Duesberg, G. S.; Coleman, J. N., Liquid phase production of graphene by exfoliation of graphite in surfactant/water solutions. *J. Am. Chem. Soc.* **2009,** *131* (10), 3611-20.
53. Karthick, R.; Chen, F., Free-standing graphene paper for energy application: Progress and future scenarios. *Carbon* **2019,** *150*, 292-310.
54. Rinzler, A.; Liu, J.; Dai, H.; Nikolaev, P.; Huffman, C.; Rodriguez-Macias, F.; Boul, P.; Lu, A. H.; Heymann, D.; Colbert, D., Large-scale purification of single-wall carbon nanotubes: process, product, and characterization. *Appl. Phys. A* **1998,** *67* (1).
55. Wang, D.; Song, P.; Liu, C.; Wu, W.; Fan, S., Highly oriented carbon nanotube papers made of aligned carbon nanotubes. *Nanotechnology* **2008,** *19* (7), 075609.
56. Rao, R.; Pint, C. L.; Islam, A. E.; Weatherup, R. S.; Hofmann, S.; Meshot, E. R.; Wu, F.; Zhou, C.; Dee, N.; Amama, P. B.; Carpena-Nuñez, J.; Shi, W.; Plata, D. L.; Penev, E. S.; Yakobson, B. I.; Balbuena, P. B.; Bichara, C.; Futaba, D. N.; Noda, S.; Shin, H.; Kim, K. S.; Simard, B.; Mirri, F.; Pasquali, M.; Fornasiero, F.; Kauppinen, E. I.; Arnold, M.; Cola, B. A.; Nikolaev, P.; Arepalli, S.; Cheng, H.-M.; Zakharov, D. N.; Stach, E. A.; Zhang, J.; Wei, F.; Terrones, M.; Geohegan, D. B.; Maruyama, B.; Maruyama, S.; Li, Y.; Adams, W. W.; Hart, A. J., Carbon nanotubes and related nanomaterials: Critical advances and challenges for synthesis toward mainstream commercial applications. *Acs Nano* **2018,** *12* (12), 11756-11784.
57. De Volder, M. F. L.; Tawfick, S. H.; Baughman, R. H.; Hart, A. J., Carbon nanotubes: Present and future commercial applications. *Science* **2013,** *339* (6119), 535-539.

58. Mohan, V. B.; Lau, K.; Hui, D.; Bhattacharyya, D., Graphene-based materials and their composites: A review on production, applications and product limitations. *Compos. B Eng.* **2018,** *142*, 200-220.
59. Keshri, A. K.; Singh, V.; Huang, J.; Seal, S.; Choi, W.; Agarwal, A., Intermediate temperature tribological behavior of carbon nanotube reinforced plasma sprayed aluminum oxide coating. *Surf. Coat. Tech.* **2010,** *204* (11), 1847-1855.
60. Filleter, T.; McChesney, J. L.; Bostwick, A.; Rotenberg, E.; Emtsev, K. V.; Seyller, T.; Horn, K.; Bennewitz, R., Friction and dissipation in epitaxial graphene films. *Phys. Rev. Lett* **2009,** *102* (8), 086102.
61. Lee, C.; Li, Q.; Kalb, W.; Liu, X.-Z.; Berger, H.; Carpick, R. W.; Hone, J., Frictional characteristics of atomically thin sheets. *Science* **2010,** *328* (5974), 76-80.
62. Zhai, W.; Srikanth, N.; Kong, L. B.; Zhou, K., Carbon nanomaterials in tribology. *Carbon* **2017,** *119*, 150-171.
63. Li, B.; Zhong, W.-H., Review on polymer/graphite nanoplatelet nanocomposites. *J. Mater. Sci.* **2011,** *46* (17), 5595-5614.
64. Damari, S. P.; Cullari, L.; Nadiv, R.; Nir, Y.; Laredo, D.; Grunlan, J.; Regev, O., Graphene-induced enhancement of water vapor barrier in polymer nanocomposites. *Compos. B. Eng.* **2018,** *134*, 218-224.
65. Smith, R. J.; King, P. J.; Lotya, M.; Wirtz, C.; Khan, U.; De, S.; O'Neill, A.; Duesberg, G. S.; Grunlan, J. C.; Moriarty, G.; Chen, J.; Wang, J.; Minett, A. I.; Nicolosi, V.; Coleman, J. N., Large-scale exfoliation of inorganic layered compounds in aqueous surfactant solutions. *Adv. Mater.* **2011,** *23* (34), 3944-8.
66. Gupta, A.; Sakthivel, T.; Seal, S., Recent development in 2D materials beyond graphene. *Prog. Mater. Sci.* **2015,** *73*, 44-126.
67. Miró, P.; Audiffred, M.; Heine, T., An atlas of two-dimensional materials. *Chem. Soc. Rev.* **2014,** *43* (18), 6537-6554.
68. Marques, E. F.; Silva, B. F. B., Surfactant Self-Assembly. In *Encyclopedia of Colloid and Interface Science*, Springer: 2013; pp 1202-1241.
69. Zana, R., Dimeric and oligomeric surfactants. Behavior at interfaces and in aqueous solution: a review. *Adv. Colloid Interface Sci.* **2002,** *97* (1-3), 205-253.
70. Kronberg, B.; Lindman, B., *Surfactants and polymers in aqueous solution*. John Wiley & Sons Ltd., Chichester: 2003.
71. Evans, D. F.; Wennerstrom, H., *The Colloidal Domain: where physics, chemistry,biology, and technology meet*. 2nd ed.; Wiley-Vch: New York, 1999.
72. Zana, R., Critical micellization concentration of surfactants in aqueous solution and free energy of micellization. *Langmuir* **1996,** *12* (5), 1208-1211.
73. Fontell, K., Cubic phases in surfactant and surfactant-like lipid systems. *Colloid Polym. Sci.* **1990,** *268* (3), 264-285.
74. Challa, G., *Polymer chemistry: an introduction*. Prentice Hall: 1993.
75. Covitch, M. J.; Trickett, K., How polymers behave as viscosity index improvers in lubricating oils. *Adv. Chem. Engineer. Sci.* **2015,** *5*, 134-151.
76. Guo, J.-H.; Skinner, G. W.; Harcum, W. W.; Barnum, P. E., Pharmaceutical applications of naturally occurring water-soluble polymers. *Pharmaceut. Sci. Tech. Today* **1998,** *1* (6), 254-261.
77. Ruecha, N.; Rangkupan, R.; Rodthongkum, N.; Chailapakul, O., Novel paper-based cholesterol biosensor using graphene/polyvinylpyrrolidone/polyaniline nanocomposite. *Biosens. Bioelectron.* **2014,** *52*, 13-19.
78. Koczkur, K. M.; Mourdikoudis, S.; Polavarapu, L.; Skrabalak, S. E., Polyvinylpyrrolidone (PVP) in nanoparticle synthesis. *Dalton Trans.* **2015,** *44* (41), 17883-17905.
79. La Mesa, C., Polymer-surfactant and protein-surfactant interactions. *J. Colloid Interface Sci.* **2005,** *286* (1), 148-157.

80. Shen, J.; Hu, Y.; Qin, C.; Ye, M., Layer-by-layer self-assembly of multiwalled carbon nanotube polyelectrolytes prepared by in situ radical polymerization. *Langmuir* **2008,** *24* (8), 3993-3997.
81. Nizam El-Din, H. M., Surface coating on cotton fabrics of new multilayer formulations based on superabsorbent hydrogels synthesized by gamma radiation designed for diapers. *J. Appl. Polym. Sci.* **2012,** *125* (S2), E180-E186.
82. Paulino, A. T.; Guilherme, M. R.; Reis, A. V.; Campese, G. M.; Muniz, E. C.; Nozaki, J., Removal of methylene blue dye from an aqueous media using superabsorbent hydrogel supported on modified polysaccharide. *J. Colloid Interface Sci.* **2006,** *301* (1), 55-62.
83. Ma, P.-C.; Siddiqui, N. A.; Marom, G.; Kim, J.-K., Dispersion and functionalization of carbon nanotubes for polymer-based nanocomposites: A review. *Compos. Part A Appl. Sci. Manuf.* **2010,** *41* (10), 1345-1367.
84. Regev, O.; ElKati, P. N. B.; Loos, J.; Koning, C. E., Preparation of conductive nanotube-polymer composites using latex technology. *Adv. Mater.* **2004,** *16* (3), 248-+.
85. Moniruzzaman, M.; Winey, K. I., Polymer nanocomposites containing carbon nanotubes. *Macromolecules* **2006,** *39* (16), 5194-5205.
86. Anthony, O.; Zana, R., Effect of temperature on the interactions between neutral polymers and a cationic and a nonionic surfactant in aqueous solutions. *Langmuir* **1994,** *10* (11), 4048-4052.
87. Piculell, L.; Lindman, B., Association and segregation in aqueous polymer/polymer, polymer surfactant, and surfactant surfactant mixtures - Similarities and differences. *Adv. Colloid Interface Sci.* **1992,** *41*, 149-178.
88. Somasundaran, P.; Krishnakumar, S., Adsorption of surfactants and polymers at the solid-liquid interface. *Colloids Surf. A Physicochem. Eng. Asp.* **1997,** *123*, 491-513.
89. Kötz, J.; Kosmella, S.; Beitz, T., Self-assembled polyelectrolyte systems. *Prog. Polym. Sci.* **2001,** *26* (8), 1199-1232.
90. Gilányi, T.; Wolfram, E., Interaction of ionic surfactants with polymers in acqueous solution. *Colloids Surf.* **1981,** *3* (2), 181-198.
91. Goddard, E. D., Polymer/surfactant interaction: Interfacial aspects. *J. Colloid Interface Sci.* **2002,** *256* (1), 228-235.
92. Jamieson, E. J.; Fewkes, C. J.; Berry, J. D.; Dagastine, R. R., Forces between oil drops in polymer-surfactant systems: Linking direct force measurements to microfluidic observations. *J. Colloid Interface Sci.* **2019,** *544*, 130-143.
93. Goddard, E. D., Polymer/surfactant interaction—Its relevance to detergent systems. *J. Am. Oil Chem.' Soc.* **1994,** *71* (1), 1-16.
94. Arzhavitina, A.; Steckel, H., Foams for pharmaceutical and cosmetic application. *Int. J. Pharm.* **2010,** *394* (1-2), 1-17.
95. Bureiko, A.; Trybala, A.; Kovalchuk, N.; Starov, V., Current applications of foams formed from mixed surfactant-polymer solutions. *Adv. Colloid Interface Sci.* **2015,** *222*, 670-677.
96. Wever, D. A. Z.; Picchioni, F.; Broekhuis, A. A., Polymers for enhanced oil recovery: A paradigm for structure–property relationship in aqueous solution. *Prog. Polym. Sci.* **2011,** *36* (11), 1558-1628.
97. Al-Hetlani, E.; Amin, M. O.; Bezzu, C. G.; Carta, M., Spirobifluorene-based polymers of intrinsic microporosity for the adsorption of methylene blue from wastewater: effect of surfactants. *R. Soc. Open Sci.* **2020,** *7* (9), 200741.
98. Hansson, P.; Schneider, S.; Lindman, B., Phase separation in polyelectrolyte gels interacting with surfactants of opposite charge. *J. Phys. Chem. B* **2002,** *106* (38), 9777-9793.
99. Minatti, E.; Norwood, D. P.; Reed, W. F., Surfactant/polymer assemblies. 2. Polyelectrolyte properties. *Macromolecules* **1998,** *31* (9), 2966-2971.

100. Kamli, M.; Guettari, M.; Tajouri, T., Structure of polyvinylpyrrolidone aqueous solution in semi-dilute regime: Roles of polymer-surfactant complexation. *J. Mol. Struct.* **2019,** *1196*, 176-185.
101. Guzmán, E.; Llamas, S.; Maestro, A.; Fernández-Peña, L.; Akanno, A.; Miller, R.; Ortega, F.; Rubio, R. G., Polymer-surfactant systems in bulk and at fluid interfaces. *Adv. Colloid Interface Sci.* **2016,** *233*, 38-64.
102. Kharissova, O. V.; Kharisov, B. I.; Ortiz, E. G. D., Dispersion of carbon nanotubes in water and non-aqueous solvents. *Rsc Adv* **2013,** *3* (47), 24812-24852.
103. Premkumar, T.; Mezzenga, R.; Geckeler, K. E., Carbon nanotubes in the liquid phase: addressing the issue of dispersion. *Small* **2012,** *8* (9), 1299-313.
104. Coleman, J. N., Liquid-phase exfoliation of nanotubes and graphene. *Adv. Funct. Mater.* **2009,** *19* (23), 3680-3695.
105. Khan, U.; Porwal, H.; O'Neill, A.; Nawaz, K.; May, P.; Coleman, J. N., Solvent-exfoliated graphene at extremely high concentration. *Langmuir* **2011,** *27* (15), 9077-9082.
106. Grayfer, E. D.; Kozlova, M. N.; Fedorov, V. E., Colloidal 2D nanosheets of MoS2 and other transition metal dichalcogenides through liquid-phase exfoliation. *Adv. Colloid Interface Sci.* **2017,** *245*, 40-61.
107. Synnatschke, K.; Cieslik, P. A.; Harvey, A.; Castellanos-Gomez, A.; Tian, T.; Shih, C. J.; Chernikov, A.; Santos, E. J. G.; Coleman, J. N.; Backes, C., Length- and thickness-dependent optical response of liquid-exfoliated Transition Metal Dichalcogenides. *Chem. Mater.* **2019,** *31* (24), 10049-10062.
108. Zhang, L.; Huang, Y.; Zhang, Y.; Fan, W.; Liu, T., Three-dimensional nanoporous graphene-carbon nanotube hybrid frameworks for confinement of SnS2 nanosheets: flexible and binder-free papers with highly reversible lithium storage. *ACS Appl. Mater. Interfaces* **2015,** *7* (50), 27823-30.
109. Compton, O. C.; Nguyen, S. T., Graphene oxide, highly reduced graphene oxide, and graphene: versatile building blocks for carbon-based materials. *Small* **2010,** *6* (6), 711-23.
110. Blanch, A. J.; Lenehan, C. E.; Quinton, J. S., Parametric analysis of sonication and centrifugation variables for dispersion of single walled carbon nanotubes in aqueous solutions of sodium dodecylbenzene sulfonate. *Carbon* **2011,** *49* (15), 5213-5228.
111. Angelikopoulos, P.; Bock, H., The science of dispersing carbon nanotubes with surfactants. *Phys. Chem. Chem. Phys* **2012,** *14* (27), 9546-57.
112. Fernandes, R. M.; Abreu, B.; Claro, B.; Buzaglo, M.; Regev, O.; Furo, I.; Marques, E. F., Dispersing carbon nanotubes with ionic surfactants under controlled conditions: Comparisons and insight. *Langmuir* **2015,** *31* (40), 10955-65.
113. Fernandes, D. M.; Costa, M.; Pereira, C.; Bachiller-Baeza, B.; Rodriguez-Ramos, I.; Guerrero-Ruiz, A.; Freire, C., Novel electrochemical sensor based on N-doped carbon nanotubes and Fe3O4 nanoparticles: simultaneous voltammetric determination of ascorbic acid, dopamine and uric acid. *J. Colloid Interface Sci.* **2014,** *432*, 207-13.
114. Frise, A. E.; Edri, E.; Furo, I.; Regev, O., Protein dispersant binding on nanotubes studied by NMR self-diffusion and Cryo-TEM techniques. *J. Phys. Chem. Lett.* **2010,** *1* (9), 1414-1419.
115. Horn, D. W.; Tracy, K.; Easley, C. J.; Davis, V. A., Lysozyme dispersed single-walled carbon nanotubes: Interaction and activity. *J. Phys. Chem. C* **2012,** *116* (18), 10341-10348.
116. Strano, M. S.; Moore, V. C.; Miller, M. K.; Allen, M. J.; Haroz, E. H.; Kittrell, C.; Hauge, R. H.; Smalley, R., The role of surfactant adsorption during ultrasonication in the dispersion of single-walled carbon nanotubes. *J. Nanosci. Nanotechnol.* **2003,** *3* (1-2), 81-86.

117. Buzaglo, M.; Shtein, M.; Kober, S.; Lovrincic, R.; Vilan, A.; Regev, O., Critical parameters in exfoliating graphite into graphene. *Phys. Chem. Chem. Phys* **2013,** *15* (12), 4428-4435.
118. Islam, M.; Rojas, E.; Bergey, D.; Johnson, A.; Yodh, A., High weight fraction surfactant solubilization of single-wall carbon nanotubes in water. *Nano Lett.* **2003,** *3* (2), 269-273.
119. Yurekli, K.; Mitchell, C. A.; Krishnamoorti, R., Small-angle neutron scattering from surfactant-assisted aqueous dispersions of carbon nanotubes. *J. Am. Chem. Soc.* **2004,** *126* (32), 9902-9903.
120. Abreu, B.; Rocha, J.; Fernandes, R. M. F.; Regev, O.; Furó, I.; Marques, E. F., Gemini surfactants as efficient dispersants of multiwalled carbon nanotubes: Interplay of molecular parameters on nanotube dispersibility and debundling. *J. Colloid Interface Sci.* **2019,** *547*, 69-77.
121. Dai, J.; Fernandes, R. M.; Regev, O.; Marques, E. F.; Furó, I. n., Dispersing carbon nanotubes in water with amphiphiles: Dispersant adsorption, kinetics, and bundle size distribution as defining factors. *J. Phys. Chem. C* **2018,** *122* (42), 24386-24393.
122. O'Connell, M. J.; Boul, P.; Ericson, L. M.; Huffman, C.; Wang, Y.; Haroz, E.; Kuper, C.; Tour, J.; Ausman, K. D.; Smalley, R. E., Reversible water-solubilization of single-walled carbon nanotubes by polymer wrapping. *Chem. Phys. Lett.* **2001,** *342* (3-4), 265-271.
123. Tallury, S. S.; Pasquinelli, M. A., Molecular dynamics simulations of flexible polymer chains wrapping single-walled carbon nanotubes. *J. Phys. Chem. B* **2010,** *114* (12), 4122-4129.
124. Tallury, S. S.; Pasquinelli, M. A., Molecular dynamics simulations of polymers with stiff backbones interacting with single-walled carbon nanotubes. *J. Phys. Chem. B* **2010,** *114* (29), 9349-9355.
125. Frise, A. E.; Pages, G.; Shtein, M.; Pri Bar, I.; Regev, O.; Furo, I., Polymer binding to carbon nanotubes in aqueous dispersions: residence time on the nanotube surface as obtained by NMR diffusometry. *J. Phys. Chem. B* **2012,** *116* (9), 2635-42.
126. Fernandes, R. M. F.; Dai, J.; Regev, O.; Marques, E. F.; Furó, I., Block copolymers as dispersants for single-walled carbon nanotubes: Modes of surface attachment and role of block polydispersity. *Langmuir* **2018,** *34* (45), 13672-13679.
127. Fernandes, R. M. F.; Buzaglo, M.; Shtein, M.; Pri Bar, I.; Regev, O.; Marques, E. F.; Furó, I., Lateral diffusion of dispersing molecules on nanotubes as probed by NMR. *J. Phys. Chem. C* **2014,** *118* (1), 582-589.
128. Fernandes, R. M. F.; Buzaglo, M.; Regev, O.; Marques, E. F.; Furó, I., Surface coverage and competitive adsorption on carbon nanotubes. *J. Phys. Chem. C* **2015,** *119* (38), 22190-22197.
129. Sun, H.; Yang, X., Molecular simulation of self-assembly structure and interfacial interaction for SDBS adsorption on graphene. *Colloids Surf. A Physicochem. Eng. Asp.* **2014,** *462*, 82-89.
130. Howe, R. C.; Woodward, R. I.; Hu, G.; Yang, Z.; Kelleher, E. J.; Hasan, T., Surfactant-aided exfoliation of molybdenum disulfide for ultrafast pulse generation through edge-state saturable absorption. *Phys. Status Solidi* **2016,** *253* (5), 911-917.
131. Sun, Z.; Nicolosi, V.; Rickard, D.; Bergin, S. D.; Aherne, D.; Coleman, J. N., Quantitative evaluation of surfactant-stabilized single-walled carbon nanotubes: dispersion quality and its correlation with zeta potential. *J. Phys. Chem. C* **2008,** *112* (29), 10692-10699.
132. Clark, M. D.; Subramanian, S.; Krishnamoorti, R., Understanding surfactant aided aqueous dispersion of multi-walled carbon nanotubes. *J. Colloid Interface Sci.* **2011,** *354* (1), 144-51.

133. Oh, H.; Sim, J.; Ju, S. Y., Binding affinities and thermodynamics of noncovalent functionalization of carbon nanotubes with surfactants. *Langmuir* **2013,** *29* (35), 11154-62.
134. Rafiee, M. A.; Rafiee, J.; Wang, Z.; Song, H.; Yu, Z. Z.; Koratkar, N., Enhanced mechanical properties of nanocomposites at low graphene content. *Acs Nano* **2009,** *3* (12), 3884-3890.
135. Stankovich, S.; Dikin, D. A.; Dommett, G. H. B.; Kohlhaas, K. M.; Zimney, E. J.; Stach, E. A.; Piner, R. D.; Nguyen, S. T.; Ruoff, R. S., Graphene-based composite materials. *Nature* **2006,** *442* (7100), 282-286.
136. Guo, S.; Dong, S., Graphene nanosheet: synthesis, molecular engineering, thin film, hybrids, and energy and analytical applications. *Chem. Soc. Rev.* **2011,** *40* (5), 2644-2672.
137. Huang, J. R.; Her, S. C.; Yang, X. X.; Zhi, M. N., Synthesis and characterization of multi-walled carbon nanotube/graphene nanoplatelet hybrid film for flexible strain sensors. *Nanomaterials* **2018,** *8* (10), 786.
138. Novaes, F. D.; Rurali, R.; Ordejon, P., Electronic transport between graphene layers covalently connected by carbon nanotubes. *Acs Nano* **2010,** *4* (12), 7596-7602.
139. Varshney, V.; Patnaik, S. S.; Roy, A. K.; Froudakis, G.; Farmer, B. L., Modeling of thermal transport in pillared-graphene architectures. *Acs Nano* **2010,** *4* (2), 1153-61.
140. Dimitrakakis, G. K.; Tylianakis, E.; Froudakis, G. E., Pillared graphene: a new 3-D network nanostructure for enhanced hydrogen storage. *Nano Lett.* **2008,** *8* (10), 3166-70.
141. IUPAC, *Compendium of Chemical Terminology, 2nd ed. (the "Gold Book"). Compiled by A. D. McNaught and A. Wilkinson*. Blackwell Scientific Publications: Oxford, 1997; Vol. 1669.
142. Hong, T. K.; Lee, D. W.; Choi, H. J.; Shin, H. S.; Kim, B. S., Transparent, flexible conducting hybrid multilayer thin films of multiwalled carbon nanotubes with graphene nanosheets. *Acs Nano* **2010,** *4* (7), 3861-3868.
143. Park, J. S.; Cho, S. M.; Kim, W. J.; Park, J.; Yoo, P. J., Fabrication of graphene thin films based on layer-by-layer self-assembly of functionalized graphene nanosheets. *ACS Appl. Mater. Interfaces* **2011,** *3* (2), 360-8.
144. Cheng, Q.; Tang, J.; Ma, J.; Zhang, H.; Shinya, N.; Qin, L. C., Graphene and carbon nanotube composite electrodes for supercapacitors with ultra-high energy density. *Phys. Chem. Chem. Phys.* **2011,** *13* (39), 17615-17624.
145. Yang, S. Y.; Chang, K. H.; Tien, H. W.; Lee, Y. F.; Li, S. M.; Wang, Y. S.; Wang, J. Y.; Ma, C. C. M.; Hu, C. C., Design and tailoring of a hierarchical graphene-carbon nanotube architecture for supercapacitors. *J. Mater. Chem.* **2011,** *21* (7), 2374-2380.
146. Lei, Z. B.; Shi, F. H.; Lu, L., Incorporation of MnO2-coated carbon canotubes between graphene sheets as supercapacitor electrode. *ACS Appl. Mater. Interfaces* **2012,** *4* (2), 1058-1064.
147. Oh, J. Y.; Kim, Y. S.; Jung, Y.; Yang, S. J.; Park, C. R., Preparation and exceptional mechanical properties of bone-mimicking size-tuned graphene oxide@carbon nanotube hybrid paper. *Acs Nano* **2016,** *10* (2), 2184-92.
148. Faisal, S. N.; Subramaniyam, C. M.; Haque, E.; Islam, M. M.; Noorbehesht, N.; Roy, A. K.; Islam, M. S.; Liu, H. K.; Dou, S. X.; Harris, A. T., Nanoarchitectured nitrogen-doped graphene/carbon nanotube as high performance electrodes for solid state supercapacitors, capacitive deionization, Li-ion battery, and metal-free bifunctional electrocatalysis. *ACS Appl. Energy Mater.* **2018,** *1* (10), 5211-5223.
149. Hu, Y.; Li, X.; Wang, J.; Li, R.; Sun, X., Free-standing graphene–carbon nanotube hybrid papers used as current collector and binder free anodes for lithium ion batteries. *J. Power Sources* **2013,** *237*, 41-46.

150. Pham, D. T.; Lee, T. H.; Luong, D. H.; Yao, F.; Ghosh, A.; Le, V. T.; Kim, T. H.; Li, B.; Chang, J.; Lee, Y. H., Carbon nanotube-bridged graphene 3D building blocks for ultrafast compact supercapacitors. *Acs Nano* **2015,** *9* (2), 2018-2027.
151. Scriven, L., Physics and applications of dip coating and spin coating. *MRS Online Proceedings Library Archive* **1988,** *121*.
152. Pansri, S.; Noothongkaew, S., MWCNTs/r-GO hybrid films fabricated by layer by layer assembly for supercapacitor electrodes. *J. Energy Storage* **2019,** *22*, 153-156.
153. Wang, D.; Mu, X.; Cai, W.; Zhou, X.; Song, L.; Ma, C.; Hu, Y., Nano-bridge effects of carbon nanotubes on the properties reinforcement of two-dimensional molybdenum disulfide/polymer composites. *Compos. Part A Appl. Sci. Manuf.* **2019,** *121*, 36-44.
154. Kim, J. Y.; Oh, J. Y.; Lee, T. I., Multi-dimensional nanocomposites for stretchable thermoelectric applications. *Appl. Phys. Lett.* **2019,** *114* (4), 043902.
155. Freire, C.; Fernandes, D. M.; Nunes, M.; Abdelkader, V. K., POM & MOF-based electrocatalysts for energy-related reactions. *ChemCatChem* **2018,** *10* (8), 1703-1730.
156. Tao, H.; Gao, Y.; Talreja, N.; Guo, F.; Texter, J.; Yan, C.; Sun, Z., Two-dimensional nanosheets for electrocatalysis in energy generation and conversion. *J. Mater. Chem. A* **2017,** *5* (16), 7257-7284.
157. Steele, B. C. H.; Heinzel, A., Materials for fuel-cell technologies. *Nature* **2001,** *414* (6861), 345-352.
158. Ray, A.; Mukhopadhyay, I.; Pati, R. K., *Electrocatalysts for Fuel Cells and Hydrogen Evolution: Theory to Design*. BoD–Books on Demand: 2018.
159. Cheng, F.; Chen, J., Metal–air batteries: from oxygen reduction electrochemistry to cathode catalysts. *Chem. Soc. Rev.* **2012,** *41* (6), 2172-2192.
160. Winter, M.; Brodd, R. J., What Are Batteries, Fuel Cells, and Supercapacitors? *Chem. Rev.* **2004,** *104* (10), 4245-4270.
161. Qiang, Z.; Chang, J. H.; Huang, C. P., Electrochemical generation of hydrogen peroxide from dissolved oxygen in acidic solutions. *Water Res.* **2002,** *36* (1), 85-94.
162. Yang, S.; Verdaguer-Casadevall, A.; Arnarson, L.; Silvioli, L.; Čolić, V.; Frydendal, R.; Rossmeisl, J.; Chorkendorff, I.; Stephens, I. E. L., Toward the decentralized electrochemical production of H2O2: A focus on the catalysis. *ACS Catal.* **2018,** *8* (5), 4064-4081.
163. Campos-Martin, J. M.; Blanco-Brieva, G.; Fierro, J. L. G., Hydrogen peroxide synthesis: An outlook beyond the anthraquinone process. *Angew. Chem. Int. Ed.* **2006,** *45* (42), 6962-6984.
164. Yi, Y.; Wang, L.; Li, G.; Guo, H., A review on research progress in the direct synthesis of hydrogen peroxide from hydrogen and oxygen: Noble-metal catalytic method, fuel-cell method and plasma method. *Catal. Sci. Technol.* **2016,** *6* (6), 1593-1610.
165. Zhou, W.; Meng, X.; Gao, J.; Alshawabkeh, A. N., Hydrogen peroxide generation from O2 electroreduction for environmental remediation: A state-of-the-art review. *Chemosphere* **2019,** *225*, 588-607.
166. Si, F.; Zhang, Y.; Yan, L.; Zhu, J.; Xiao, M.; Liu, C.; Xing, W.; Zhang, J., Electrochemical Oxygen Reduction Reaction. In *Rotating Electrode Methods and Oxygen Reduction Electrocatalysts*, Xing, W.; Yin, G.; Zhang, J., Eds. Elsevier: Amsterdam, 2014; pp 133-170.
167. Seh, Z. W.; Kibsgaard, J.; Dickens, C. F.; Chorkendorff, I.; Nørskov, J. K.; Jaramillo, T. F., Combining theory and experiment in electrocatalysis: Insights into materials design. *Science* **2017,** *355* (6321).
168. Tao, H.; Zhang, Y.; Gao, Y.; Sun, Z.; Yan, C.; Texter, J., Scalable exfoliation and dispersion of two-dimensional materials – an update. *Phys. Chem. Chem. Phys.* **2017,** *19* (2), 921-960.

169. Gao, S.; Fan, H.; Zhang, S., Nitrogen-enriched carbon from bamboo fungus with superior oxygen reduction reaction activity. *J. Mater. Chem. A* **2014,** *2* (43), 18263-18270.
170. Ghosh, S. K.; Rahaman, H., Noble Metal–Manganese Oxide Hybrid Nanocatalysts. In *Noble Metal-Metal Oxide Hybrid Nanoparticles*, Elsevier: 2019; pp 313-340.
171. Fernandes, D. M.; Mathumba, P.; Fernandes, A. J.; Iwuoha, E. I.; Freire, C., Towards efficient oxygen reduction reaction electrocatalysts through graphene doping. *Electrochim. Acta* **2019,** *319*, 72-81.
172. Delmondo, L.; Salvador, G. P.; Muñoz-Tabares, J. A.; Sacco, A.; Garino, N.; Castellino, M.; Gerosa, M.; Massaglia, G.; Chiodoni, A.; Quaglio, M., Nanostructured MnxOy for oxygen reduction reaction (ORR) catalysts. *Appl. Surf. Sci.* **2016,** *388*, 631-639.
173. Suen, N.-T.; Hung, S.-F.; Quan, Q.; Zhang, N.; Xu, Y.-J.; Chen, H. M., Electrocatalysis for the oxygen evolution reaction: recent development and future perspectives. *Chem. Soc. Rev.* **2017,** *46* (2), 337-365.
174. Gorlin, Y.; Jaramillo, T. F., A bifunctional nonprecious metal catalyst for oxygen reduction and water oxidation. *J. Am. Chem. Soc.* **2010,** *132* (39), 13612-13614.
175. Zhang, J.; Zhao, Z.; Xia, Z.; Dai, L., A metal-free bifunctional electrocatalyst for oxygen reduction and oxygen evolution reactions. *Nat. Nanotechnol.* **2015,** *10* (5), 444-452.
176. Daems, N.; Sheng, X.; Vankelecom, I. F. J.; Pescarmona, P. P., Metal-free doped carbon materials as electrocatalysts for the oxygen reduction reaction. *J. Mater. Chem. A* **2014,** *2* (12), 4085-4110.
177. Chen, S.; Chen, Z.; Siahrostami, S.; Higgins, D.; Nordlund, D.; Sokaras, D.; Kim, T. R.; Liu, Y.; Yan, X.; Nilsson, E.; Sinclair, R.; Nørskov, J. K.; Jaramillo, T. F.; Bao, Z., Designing boron nitride islands in carbon materials for efficient electrochemical synthesis of hydrogen peroxide. *J. Am. Chem. Soc.* **2018,** *140* (25), 7851-7859.
178. Chen, L.; Lei, C.; Li, Z.; Yang, B.; Zhang, X.; Lei, L., Electrochemical activation of sulfate by BDD anode in basic medium for efficient removal of organic pollutants. *Chemosphere* **2018,** *210*, 516-523.
179. Benck, J. D.; Hellstern, T. R.; Kibsgaard, J.; Chakthranont, P.; Jaramillo, T. F., Catalyzing the hydrogen evolution reaction (HER) with molybdenum sulfide nanomaterials. *ACS Catal.* **2014,** *4* (11), 3957-3971.
180. Gong, K.; Du, F.; Xia, Z.; Durstock, M.; Dai, L., Nitrogen-doped carbon nanotube arrays with high electrocatalytic activity for oxygen reduction. *Science* **2009,** *323* (5915), 760-764.
181. Yang, L.; Jiang, S.; Zhao, Y.; Zhu, L.; Chen, S.; Wang, X.; Wu, Q.; Ma, J.; Ma, Y.; Hu, Z., Boron-doped carbon nanotubes as metal-free electrocatalysts for the oxygen reduction reaction. *Angew. Chem. Int. Ed. Engl.* **2011,** *50* (31), 7132-7135.
182. Qu, L.; Liu, Y.; Baek, J. B.; Dai, L., Nitrogen-doped graphene as efficient metal-free electrocatalyst for oxygen reduction in fuel cells. *Acs Nano* **2010,** *4* (3), 1321-1326.
183. Yang, Z.; Yao, Z.; Li, G.; Fang, G.; Nie, H.; Liu, Z.; Zhou, X.; Chen, X.; Huang, S., Sulfur-doped graphene as an efficient metal-free cathode catalyst for oxygen reduction. *Acs Nano* **2012,** *6* (1), 205-211.
184. Yang, H. B.; Miao, J.; Hung, S. F.; Chen, J.; Tao, H. B.; Wang, X.; Zhang, L.; Chen, R.; Gao, J.; Chen, H. M.; Dai, L.; Liu, B., Identification of catalytic sites for oxygen reduction and oxygen evolution in N-doped graphene materials: Development of highly efficient metal-free bifunctional electrocatalyst. *Sci. Adv.* **2016,** *2* (4).
185. Xie, Y.; Feng, C.; Guo, Y.; Li, S.; Guo, C.; Zhang, Y.; Wang, J., MOFs derived carbon nanotubes coated CoNi alloy nanocomposites with N-doped rich-defect and abundant cavity structure as efficient trifunctional electrocatalyst. *Appl. Surf. Sci.* **2021,** *536*.

186. Lu, Z.; Yao, S.; Dong, Y.; Wu, D.; Pan, H.; Huang, X.; Wang, T.; Sun, Z.; Chen, X., Earth-abundant coal-derived carbon nanotube/carbon composites as efficient bifunctional oxygen electrocatalysts for rechargeable zinc-air batteries. *J. Energy Chem.* **2021,** *56*, 87-97.
187. Yan, L.; Wang, H.; Shen, J.; Ning, J.; Zhong, Y.; Hu, Y., Formation of mesoporous Co/CoS/Metal-N-C@S, N-codoped hairy carbon polyhedrons as an efficient trifunctional electrocatalyst for Zn-air batteries and water splitting. *Chem. Eng. J.* **2021,** *403*.
188. Park, B. J.; Kim, J.; Park, H. S., Bifunctional electrocatalysts based on hierarchical graphene/iron hybrid architectures branched by N-doped CNT. *J. Alloys Compd.* **2020,** *846*.
189. Tian, G. L.; Zhao, M. Q.; Yu, D.; Kong, X. Y.; Huang, J. Q.; Zhang, Q.; Wei, F., Nitrogen-doped graphene/carbon nanotube hybrids: In situ formation on bifunctional catalysts and their superior electrocatalytic activity for oxygen evolution/reduction reaction. *Small* **2014,** *10* (11), 2251-2259.
190. Tao, L.; Wang, Q.; Dou, S.; Ma, Z.; Huo, J.; Wang, S.; Dai, L., Edge-rich and dopant-free graphene as a highly efficient metal-free electrocatalyst for the oxygen reduction reaction. *ChemComm* **2016,** *52* (13), 2764-2767.
191. Wang, S.; Yu, D.; Dai, L.; Chang, D. W.; Baek, J.-B., Polyelectrolyte-functionalized graphene as metal-free electrocatalysts for oxygen reduction. *Acs Nano* **2011,** *5* (8), 6202-6209.
192. Wang, S.; Yu, D.; Dai, L., Polyelectrolyte functionalized carbon nanotubes as efficient metal-free electrocatalysts for oxygen reduction. *J. Am. Chem. Soc.* **2011,** *133* (14), 5182-5185.

Chapter 2 Experimental section

2.1. Materials

The following nanomaterials were purchased from the suppliers and used as received: i) MWNTs, produced by catalytic chemical vapor deposition, from Cheaptubes, with diameter *d* = 8-15 nm and length *L* = 10-50 μm; ii) graphene nanoplatelets, from xGnP® grade M-5, xGSciences; iii) graphite flakes from Sigma Aldrich, CAS 7782-42-5; iv) transition metal dichalcogenides molybdenum (IV) disulfide, MoS_2, tungsten (IV) disulfide, WS_2, and molybdenum diselenide, $MoSe_2$, all from Sigma-Aldrich, purities ≥ 99.

All the alkanediyl-α,ω-bis(alkyldimethylammonium bromide) gemini surfactants used in this work (Paper I), and abbreviated as 12-s-12 (s = 2, 6 and 12), 14-s-14 (s = 2, 6 and 12) and 16-s-16 (s = 2 and 12), were synthesized in our group at CIQUP according to the method described by Menger and Littau[1] and purified by recrystallization. The purity of the compounds was evaluated by NMR and mass spectrometry and further confirmed by the *cmc* values, obtained by conductivity measurements (cf. also Fig. S1, Paper I), and are in agreement with previous reports.[2] The following surfactants and polymers were acquired from Sigma Aldrich (purities ≥ 99 %) and used as received: dodecyltrimethylammonium bromide, DTAB; tetradecyltrimethylammonium bromide, TTAB; cetyltrimethylammonium bromide, CTAB; sodium cholate hydrate, SC; Triton™ X-100 (t-Octylphenoxypolyethoxyethanol); polyvinylpyrrolidone, PVP; sodium polyacrylate, PAS; and poly(diallyldimethyl ammonium chloride), PDDA. The data for the dispersants used in this work are shown in Tables 2.1 and 2.2: surfactants – Table 2.1; polymers – Table 2.2.

Reagents used for electrocatalysis preparation, potassium hydroxide (KOH, Riedel-de-Häen), Nafion (Aldrich, 5 wt% solution in lower aliphatic alcohols and water), 2-propanol (Aldrich, 99.5%), methanol (Fisher Scientific, > 99.99 %) and 20 wt% Pt/C (HiSPEC® 3000, Alfa Aesar) were also used as received.

All solutions were prepared using ultra-pure water (resistivity 18.2 MΩ cm at 25 °C,) from a Millipore system.

Table 2.1. Acronyms, IUPAC designation and molecular mass of the surfactants studied.

Surfactants	IUPAC designation	M_W/ g·mol^{-1}	Molecular Structure	Paper
DTAB	Dodecyltrimethylammonium bromide	308.3	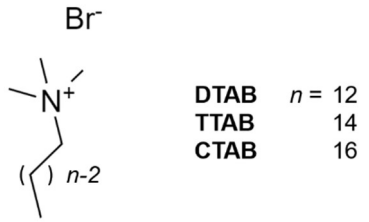	I
TTAB	Tetradecyltrimethylammonium bromide	336.4		I, V, VI
CTAB	Cetyltrimethylammonium bromide	364.5		I, III-V
12-2-12	*N,N'*-didodecyl-*N,N,N',N'*-tetramethylethane-1,2-diammonium dibromide	421.5		
12-6-12	*N,N'*-didodecyl-*N,N,N',N'*-tetramethylhexane-1,2-diammonium dibromide	554.9		I
12-12-12	*N,N'*-didodecyl-*N,N,N',N'*-tetramethyldodecane-1,2-diammonium dibromide	754.9	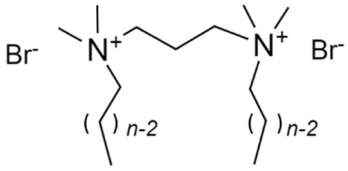	
14-2-14	*N,N'*-ditetradecyl-*N,N,N',N'*-tetramethylethane-1,2-diammonium dibromide	670.8		
14-6-14	*N,N'*-ditetradecyl-*N,N,N',N'*-tetramethyhexane-1,2-diammonium dibromide	804.2	**12-*s*-12** *n* = 12 *s* = 2, 6, 12	I
14-12-14	*N,N'*-ditetradecyl-*N,N,N',N'*-tetramethyldodecane-1,2-diammonium dibromide	1004	**14-*s*-14** *n* = 14 *s* = 2, 6, 12	
16-2-16	*N,N'*-dihexadecyl-*N,N,N',N'*-tetramethylethane-1,2-diammonium dibromide	726.9	**16-*s*-16** *n* = 16 *s* = 2, 12	
16-12-16	*N,N'*-dihexadecyl-*N,N,N',N'*-tetramethyldodecane-1,2-diammonium dibromide	1060		I
TX-100	2-[4-(2,4,4-trimethylpentan-2-yl)phenoxy]ethanol	647.0	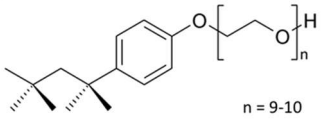	II
SC	3α,7α,12α-Trihydroxy-5β-cholan-24-oic acid sodium salt	430.6	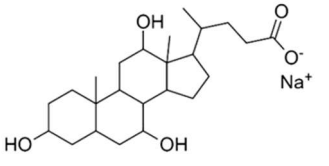	II, IV-VI
SDBS	Sodiumdodecylbenzene sulphonate	342.4	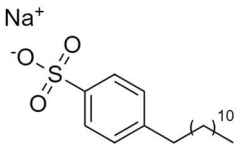	III

Table 2.2. Acronyms, name and molecular mass of the polymers studied.

Polymers	Name	Mw/ g·mol^{-1}	Molecular Structure	Paper
PVP	Polyvinylpyrrolidone	40 000	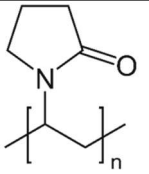	III, V
PAS	Sodium polyacrylate	15 000	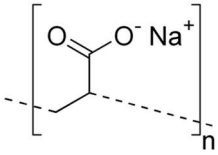	III
PDDA	Poly(diallyldimethyl ammonium chloride)	200 000–350 000	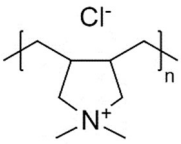	III

2.2. Preparation of the building blocks

All the building blocks for 3D composites were prepared using the same well-controlled and stringent procedure.[3] The nanomaterial powder was added to the desired dispersant aqueous solution yielding an initial loading concentration of 3 mg·mL^{-1} for MWNTs, GnPs and TMDs and 10 mg·mL^{-1} for graphite suspensions. These mixtures were tip-sonicated and centrifuged (Centurion Scientific Centrifuge Model K241R) and the top of the supernatant was carefully removed, extracting the most exfoliated materials for quantification. The sonication and centrifugation parameters were tuned for each of the studies regarding the exfoliation of MWNTs, graphite, GnPs and TMDs, and are detailed in each article. After preparation, the nanomaterial concentration was determined by UV-Vis spectrophotometry, using previously determined TGA/UV-Vis calibration curves, according to the procedures described below.

Sonication

The 1D and 2D nanomaterials were exfoliated from their powders (bulk reservoirs) through an ultrasonic procedure. The ultrasonic wavelengths vary from roughly 100 μm up to 10 cm (depending on the frequency of the ultrasonic equipment), highly above the molecular size scale. Thus, the chemical and physical effects of ultrasounds arise from the physical phenomenon of acoustic cavitation. As an ultrasonic wave propagates through a liquid medium, the liquid is under dynamic tensile stress and the density

changes with alternating expansive and compressive waves, creating cavitation bubbles. Above a critical size, the bubbles collapse and generate hot spots that can achieve temperatures above 5000 K and pressures exceeding 1000 atm. Near a surface, if the bubble collapses, a hydrodynamic microjet is created; however, if the bubble is unperturbed by a surface, the compression of the surrounding liquid propagates as a shock wave from the rebounding bubble. The combination of these two physical effects is determinant in nanomaterial preparation, resulting in the exfoliation of the nanotubes or nanosheets through an "unzipping" mechanism.[4]

The dispersibility of nanomaterials is highly dependent on sonication. Delivering a certain amount of energy, high-concentration dispersions of *quasi*-individually dispersed nanomaterials can be obtained. However, excessive sonication can result in undesired fragmentation of the 1D and 2D exfoliated species.[5-7] Therefore, it is of extreme importance to control sonication conditions when preparing the building blocks and the composites, to guaranty reproducible results. In this work, the total energy transferred to the system was approximately estimated by a calorimetric experiment, assuming the heat generated through the ultrasonic experiment is proportional to the acoustic energy dissipated. Thus, the power, *P*, transferred to the liquid medium was estimated according to Eq. 2.1:

$$P = m\, c_{\mathrm{p}} \left(\frac{dT}{dt}\right) \tag{2.1}$$

where m is the mass of water in the vial, c_{p} is the specific heat capacity of water at constant pressure and (dT/dt) is the rate of temperature increase as function of sonication time. Tip sonication was carried using two different equipment, considering the nature of the experiment. For smaller volumes, a Bandelin Sonopuls 3 mm microtip (70 W, 20 kHz) was used. The building blocks for composites were prepared using a VCX500 13 mm tip (500 W, 20 kHz). The tips were frequently polished and calorimetric measurements were carried after each polishing, assuring reproducibility of the sonication conditions. Amplitude of vibration was set below 30 % for the 70 W microtip and below 60 % for the 500 W tip, to minimize surface erosion. Sonication times were set to keep a constant delivered energy density in all systems, as described in each paper. An external bath was used to dissipate the heat generated by the sonication procedure, stabilizing the temperature of the sample.

Centrifugation

Centrifugation is used to sediment any non-dispersed material. Typically, after sonication the nanomaterials are individualized, in small, or non-dispersed bundles. The contrast in the *L*/*d* aspect ratios allows nanomaterial separation based on g force and/or centrifugation time.[5, 8]

In this thesis the centrifugation step was adjusted for the 1D and 2D nanomaterials. The g forces used lied between 1000 and 4000 g, and centrifugation times between 10 and 20 minutes (except for the GnPs exfoliation from graphite, where 150 minutes of centrifugation were required to obtain stable dispersions). To build the dispersibility curves, after the centrifugation step ≈ 30% of the supernatant was collected with a pipette and used in subsequent experiments. For composite building, ≈ 90% of the MWNT supernatant was used.

Nanomaterial quantification

The quantification of nanomaterial dispersed in water is based on a thermogravimetric-spectroscopic approach.[9] In this methodology the exact concentration of nanomaterial dispersed in the liquid is quantified by thermogravimetric analysis (TGA) and related to the optical density of the dispersion.

To quantify the nanomaterial concentration, an accurate volume, V_s, of the supernatant was freeze-dried for 24 hours resulting in a dry powder of mass, m_s, composed by nanomaterial and dispersant. Thermogravimetric measurements were then used to determine the mass loss fraction in the dry supernatant, Φ_s, and the mass loss fraction in neat dry surfactant, Φ_d. The obtained data was related with nanomaterial concentration according to Eq. 2.2:

$$c_{nmat} = \frac{m_s}{V_s} \times \left(1 - \frac{\Phi_s}{\Phi_d}\right) \quad (2.2)$$

where the ratio Φ_s/Φ_d represents incomplete surfactant decomposition in TGA. Apparent extinction coefficient, ε, can be estimated for a wavelength, λ, by measuring the optical density for the same stock dispersion. Once ε is determined, the nanomaterial concentration in each dispersion can be easily determined from the absorbance through the Beer-Lambert equation (Eq. 2.3), as shown in section 2.4.3.

The apparent extinction coefficient for each nanomaterial used - MWNT, GnPs, MoS_2, WS_2 and $MoSe_2$ – was determined at specific wavelengths, as depicted in section 2.4.3.

2.3. Composite assembly

To build the 3D materials, the surfactants were chosen according to previous studies[3, 10] considering the aspects described below.

i) The building blocks were functionalized with oppositely charged surfactants, since electrostatic interactions are the driving force for the composite assembly;

ii) Surfactant TTAB was selected to functionalize MWNT, since it has similar effectiveness to CTAB (the cationic surfactant with best performance) but lower Kraft temperature. [3] SC was used to functionalize the GnPs, since it shows good effectiveness and efficiency (Paper II) and it is oppositely charged to TTAB;

iii) Considering the importance of the use of polymers to obtain more structured composite materials,[11, 12] in Paper V polymer/surfactant mixtures were used to functionalize the MWNTs. For this, the system PVP/CTAB was selected, due to the effectiveness of this mixture and its positive charge;

iv) The surfactant concentration for each system was selected from the surfactant's dispersibility curve, at the maximum dispersibility.[3, 10]

After surfactant selection, the preparation steps were carefully monitored. As described above, the nanocarbon powder was weighted, followed by addition of the desired surfactant solution. The samples were then tip-sonicated, delivering the same energy per volume as in the preparation of the building blocks. Centrifugation causes the larger aggregates (e.g. bundles of CNTs and impurities) to precipitate, including the graphene nanosheets with higher lateral dimensions. In the latter case, the starting graphene nanoplatelets were thus characterized before and after centrifugation by SEM (Fig. 2.1). The results showed a significant decrease in the sheet dimensions. Since this characteristic is crucial for the 3D building, the centrifugation of the 2D building block was eliminated in the composite fabrication procedure, as described in Papers V and VI. Therefore, the final concentration of 2D nanomaterial corresponds to its initial loading on the dispersions.

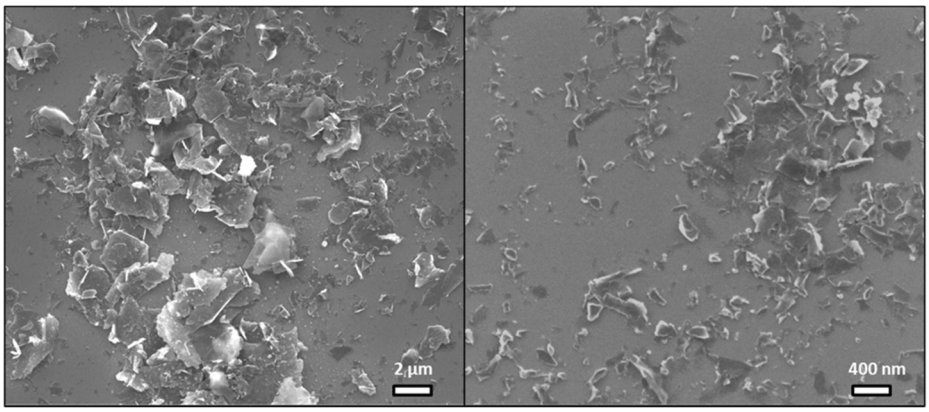

Fig. 2.1. Representative micrographs of GnP dispersions without centrifugation (left) and after centrifugation (right).

Following the building block preparation, conventional layer-by-layer assembly[13 14] (described in section 1.3.2) by dip-coating and spin-coating, using MWNTs and GnPs, was tested to build the 3D structures. SEM analysis showed domains of GnPs with MWNTs – no continuity in the film (Fig. 2.2 a and b); however, the results suggested interaction between the materials in these domains (Fig. 2.2c).

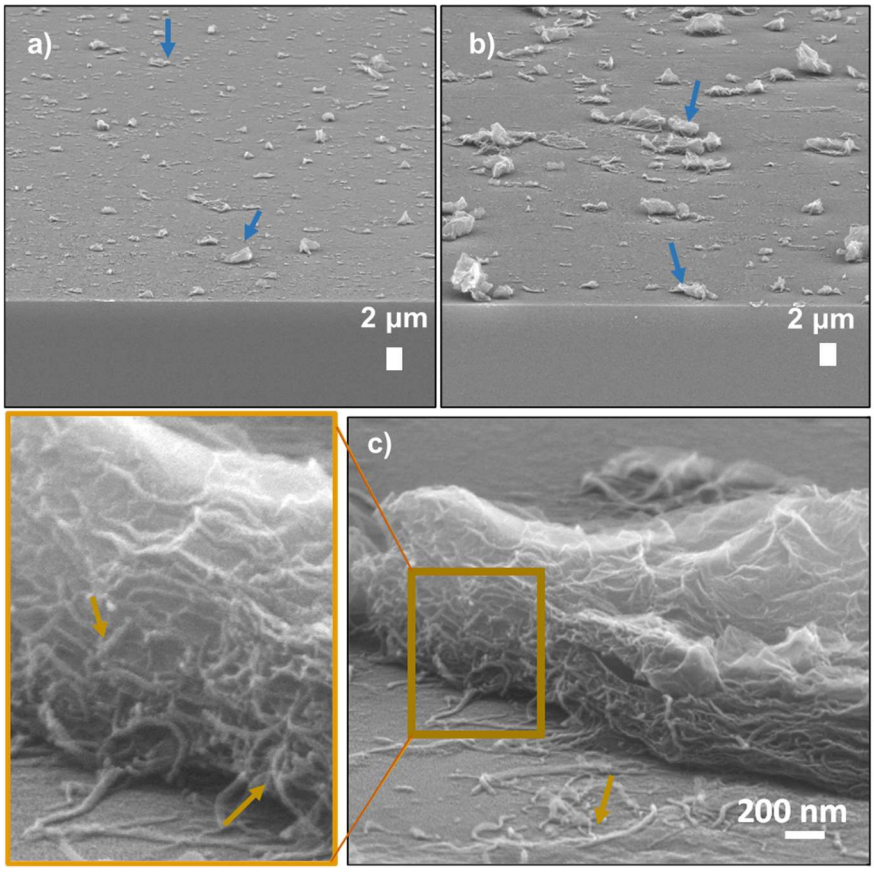

Fig. 2.2. Representative SEM micrographs of (top) the domains of MWNT/GnP built by conventional layer-by-layer assembly using: a) dip-coating method; b) spin-coating method. c) interaction of MWNTs and GnPs. MWNT/GnP domains are pointed by blue arrows; yellow arrows point MWNTs interacting with the GnPs.

Considering these results, two approaches were followed: i) *bulk mixture* (B-method) and ii) *adapted layer-by-layer* (L-method), as described below and depicted in Fig. 2.3:

i) *Bulk mixture films* (B-method): identical volumes of 2D/SC dispersion (without centrifugation) and MWNT/TTAB (or MWNT/PVP+CTAB) supernatant were added to a vial and tip-sonicated using the same energy density applied to the starting dispersions, as described in section 2.2. The obtained dispersion was vacuum filtered using a cellulose acetate membrane, rinsed with ethanol to remove the excess surfactant, and dried overnight.

ii) *Adapted layer-by-layer films* (L-method): identical aliquots of 2D/SC dispersion and MWNT/TTAB (or MWNT/PVP+CTAB) supernatant were added alternately to a cellulose acetate membrane, inserted in a vacuum filtration system.[15] Each layer was deposited after the previous one was apparently dry. In the end, the film was rinsed with ethanol and dried overnight.

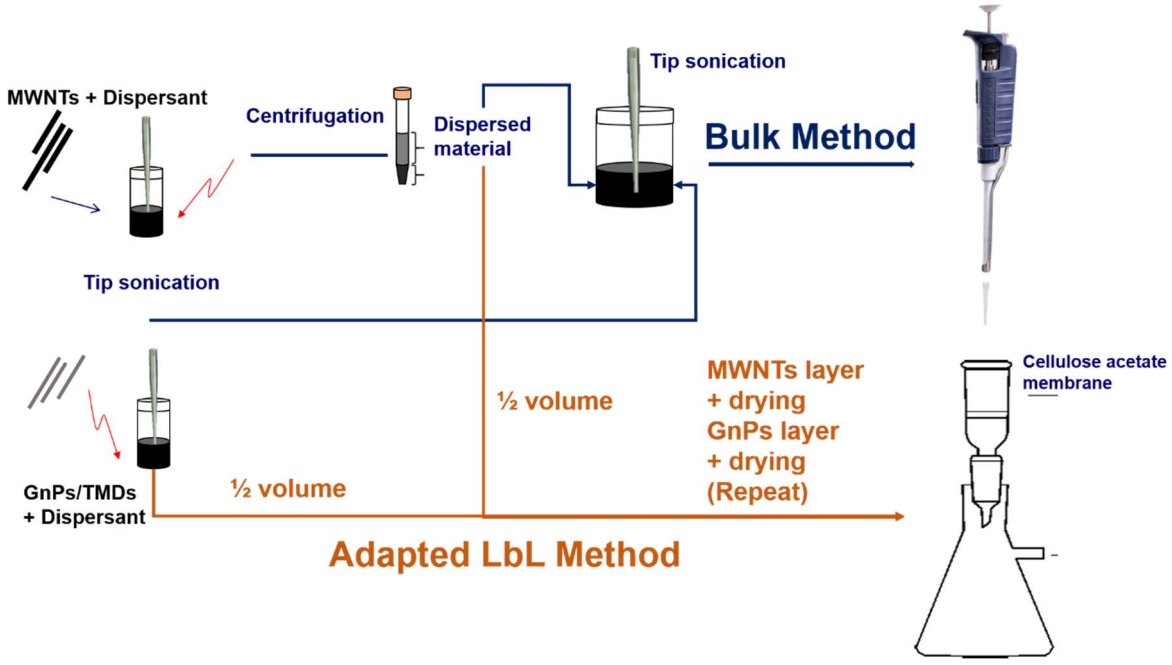

Fig. 2.3. Schematic representation of the assembly methodologies: *bulk* (blue) and *adapted layer-by-layer* (yellow).

The described methodologies aimed at the building of reproducible materials under optimized conditions. In Paper V, two systems were selected for each procedure: 1) MWNT/TTAB + GnPs/SC and 2) MWNT/(PVP+CTAB) + GnPs/SC. The choice of these systems allowed further comparisons, namely:

i) the influence of the preparation method and dispersant composition on the final structure and electrochemical activity of the obtained composites;

ii) the effect of the presence of polymer in the structural organization of the material;

iii) the applicability of the experimental methodology to build structures with reproducible electrocatalytic performance.

Following this study, the bulk procedure was applied to build MWNT/TMDs structures (Paper VI).

2.4. Characterization methods

In this section, the most relevant characterization methods used throughout the work are depicted. The fundamental principles of each technique are addressed, followed by a description of the experimental procedure.

2.4.1. Scanning Electron Microscopy (SEM)

Scanning Electron Microscopy (SEM) creates magnified images by scanning a sample with a focused beam of high-energy electrons. The beam is emitted from an electron source and modified by apertures, magnetic and/or electrostatic lenses, and electromagnetic coils which act to successively reduce the beam diameter. The interaction of the beam with the sample produces two outgoing electron products: i) backscattered electrons (BSEs), defined as beam electrons that remain with a large fraction of their energy intact, after scattering and deflection by the electric fields of the atoms in the sample; and ii) secondary electrons (SEs), which are electrons that escape the specimen surface after that beam electrons have ejected them from atoms in the sample. These outgoing electron signals are detected and measured at each specific location, and are subsequently converted to a gray level, forming a single picture element (pixel). The scanning of the surface will result in the full picture of the sample.[16]

To minimize the unwanted scattering of the beam electrons, BSEs and SEs, that would happen if those electrons interacted with atoms and molecules of atmospheric gases, the electron-optical column and the specimen chamber must operate under high vacuum conditions ($< 10^{-4}$ Pa). Furthermore, any insulating specimens that would develop surface electrical charge because of the impact of the beam electrons must be given a conductive coating.[16]

SEM is extremely useful in the characterization of nanomaterials. The ability to focus large depths of field at one time (producing 3D-like images) combined with the sample area scanned (from micrometers to millimeters) allows to obtain statistically representative micrographs of the morphology of the sample in a time-efficient analysis.[17]

Experimental aspects

To analyze the morphology of the nanomaterials in the dispersions, evaluate the organization of the composites and compare the prepared samples with the starting bulk materials, SEM was performed. Dispersion samples were prepared by drop casting 10 µL of the supernatant dispersion on a pre-heated (> 100 ºC, for fast solvent evaporation) silicon wafer and then rinse in ethanol to remove surfactant excess. Composite samples of MWNT/GnPs were prepared by placing the film in epoxy resin and break it in liquid nitrogen, after curing, to obtain the cross-section of the material. Due to the nature of the 2D building blocks, for the composites of MWNT/TMDs the immersion in epoxy resin was not required. The cross-section of these materials was obtained by breaking the films in liquid nitrogen.

SEM images were obtained at Centro de Materiais da Universidade do Porto (CEMUP), on a FEI Quanta 400FE microscope with an electron beam of 25 kV, in secondary electrons (SE) mode, at different magnifications.

2.4.2. Atomic force microscopy

AFM is a form of scanning probe microscopy (SPM) that allows imaging of surfaces with atomic resolution. The AFM works by scanning a probe over the sample surface, the result being a map of the height or topography of the surface, providing information on the X, Y and Z dimensions of the sample. Thus, this technique completes the information obtained with SEM, elucidating on the diameter of carbon nanotubes and number of layers in the graphene nanoplatelets.

Regarding AFM instrumentation, three main concepts should be considered to understand the operation of the microscope: i) piezoelectric transducers (i.e. piezoelectric scanners); ii) force transducers (i.e. force sensors) and iii) feedback control. The first converts electrical potential into mechanical motion, moving the tip over the sample surface. The force transducer measures the force between the AFM probe and the surface, and the feedback control feeds the signal from the force transducer back in to the piezoelectric, to maintain a fixed force between the tip and the sample. The signals

are then processed to compute a digital image of the topographical aspect of the surface sample with accurate measurement in height and lateral displacement, at the nanometer range (Fig. 2.4).[18]

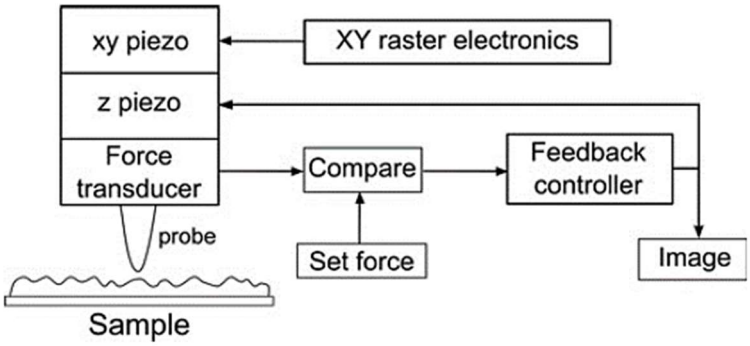

Fig. 2.4. Block diagram of AFM operation. Adapted.[18]

Tapping is the recommended operation mode when characterizing carbon nanotubes or graphene. The tip is first set to oscillate at a fixed frequency and amplitude in air, and then approached to the surface. The oscillation frequency of the tip allows contact with the surface at discrete points, mapping a small area (few micrometers). In tapping mode, the AFM uses two types of data output: height (the change in altitude of the piezo) and amplitude (representation of the change in amplitude of the tip which more accurately represents edges on the substrate instead of the actual height). Together, the two types of data provide an accurate representation of the surface geometry.[19]

Experimental aspects

Atomic Force Microscopy (AFM) was performed to characterize the quality and thickness of exfoliated graphene nanoplatelets. The samples were prepared by casting 10 µL of the supernatant on a pre-heated silicon wafer at 100 ºC. The samples were then rinsed in ethanol to remove the excess of surfactant. AFM images were taken using a Veeco Multimode NanoScope IV under ambient conditions with silicon tip (RTESP).

2.4.3. UV-Vis spectroscopy

Ultraviolet-visible (UV-Vis) spectroscopy quantifies the absorption of electromagnetic radiation in the UV-Vis range absorbed by a sample. The absorbance, *A*, corresponds to the excitation of valence electrons from ground state to higher energetic levels. Since the energy difference between states is discrete, wavelengths with matching energy can

promote the electrons to higher energetic levels. Beer-Lambert law states that the absorbance is proportional to the concentration of the sample (for low values of absorbance), described by the following equation:

$$A = \varepsilon l c \quad (2.3)$$

where ε is the extinction coefficient and l the optical path (i.e. length of the cuvette). The extinction coefficient is an intrinsic property of the sample and its value can be determined from an absorbance calibration curve.

The amount of nanomaterial dispersed in a sample can thus be determined by measuring the absorbance relatively to an aqueous dispersion of known nanomaterial concentration. The apparent extinction coefficient for each nanomaterial used in this work was determined by combining TGA results with UV-Vis.

Experimental aspects

The spectra were obtained using a single beam Agilent 8453 spectrometer. The dispersions were properly diluted to keep the apparent absorbance in a measurable range. Absorbance was recorded at λ = 660 nm for carbon nanomaterials and $MoSe_2$ (to eliminate the surfactant absorbance contribution),[20, 21] and at the absorption peak for MoS_2 and WS_2, λ = 678 nm for MoS_2 and λ = 630 nm for WS_2, in line with previous reports.[22, 23]

2.4.4. Zeta potential measurements

The electrical charge (or potential) at the surface of a dispersed particle affects most of the properties of a colloidal system.[24] Charged colloid particles possess an electric double layer: the Stern layer is the inner layer, with counterions strongly bound to the surface of the particle; the outer diffuse layer is an ionic cloud around the Stern layer. The boundary region between the diffuse cloud and the medium is called slipping plane. The electric potential at this boundary (i.e. at the surface between a stationary solution and a moving charged colloid particle) is defined as zeta potential, ζ-potential (Fig. 2.5).

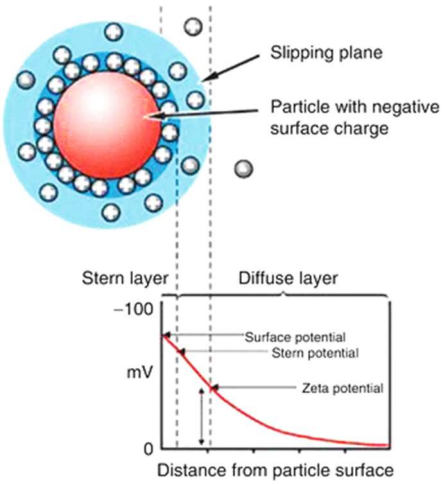

Fig. 2.5. Representation of the zeta potential definition in the charged particle. Adapted.[25]

The measurement of zeta potential of a system is an indirect calculus, from the determination of the electrophoretic mobility of a particle immersed in a liquid under an electrical field. The electrophoretic mobility can be measured by laser Doppler velocimetry, by relating the particle velocity with the frequency measured by the variation in the intensity of scattered light. The ζ-potential of a particle is determined by applying Henry's equation:

$$U_E = \frac{2\,\varepsilon\,\zeta\,f(ka)}{3\eta} \tag{2.3}$$

where U_E is the electrophoretic mobility, ε is the dielectric constant, $f(ka)$ represents Henry´s function and η is the viscosity of the medium. Henry's function is related to the ratio of the particle radius and the thickness of the double layer, and two values are usually applied: 1.5 is generally used for systems that fit the Smoluchowski model (larger than 0.2 μm), for aqueous media and moderate electrolyte concentration; the value of 1 is used for small particles with low dielectric constant and also for samples in nonaqueous media.[25]

The colloidal kinetic stability of suspensions is often inferred from the zeta potential modulus, |ζ-potential|, of the particles. Generally, colloidal dispersions with |ζ-potential| between 0-5 mV will coagulate or flocculate; in the 10-30 mV range, the suspensions have incipient stability; from 30-40 mV, have moderate stability; from 40-60 mV good stability is achieved; finally, when |ζ-potential| is greater than 60 mV the system shows excellent stability.

The surface charge of the nanotubes and the 2D nanomaterials has implications not only on the stability of the colloidal dispersions, but also on their assembly in composite structures.[26] Thus, it is highly important to determine this parameter not only for the study of dispersibility behavior, but also for the use of the building blocks for composite preparation, since the assembly process is driven by electrostatic interactions.

Experimental aspects

Zeta potential measurements were performed in a Zetasizer NANO ZS, from Malvern Instruments and Anton Paar Litesizer™ 500. In zeta potential determinations samples were placed in a disposable capillary polycarbonate U-shaped cuvette, with gold coated electrodes. Samples were left inside the instrument to reach thermal equilibrium 120 seconds at temperatures above the Krafft temperature of each surfactant.

2.4.5. Thermogravimetric analysis (TGA)

Thermogravimetric analysis (TGA) is a technique that measures mass variation of a sample as a function of temperature or time, in controlled atmosphere. This atmosphere can be inert or reactive (e.g. air, nitrogen or other gases). The equipment uses the combination of a microbalance with a furnace, that allows the sample to be simultaneously weighted and heated (or cooled). The output obtained is a thermogram, where the variation of mass is plotted as a function of temperature or time, allowing the mass loss to be determined. In the case of a mixture of different components, if each component decomposes at a well-defined temperature, then the mass composition of the mixture can be determined.[27-29]

Experimental aspects

Thermogravimetric analysis (TGA) was performed using a Netzsch TG 209 F1-Iris and a Hitachi STA STA7200RV under N_2 atmosphere (flow rate of 50 $mL \cdot min^{-1}$). Aluminum crucibles of 100 µL of volume were used.

2.4.6. Raman spectroscopy

The vibrational modes of the molecules provide a “fingerprint” of the molecular structure. Vibrational spectroscopy includes several techniques, such as infrared (IR) and Raman spectroscopy. Although these two techniques are complementary when studying completely the vibrational modes of a molecule, the use of both IR and Raman is not always necessary.

Raman spectroscopy is a two-photon inelastic light scattering phenomenon. In a typical Raman analysis, the sample is irradiated by a laser with monochromatic radiation, usually from the visible, near infrared or near ultraviolet range. The incident photon is of higher energy than the vibrational quantum energy, losing part of the energy to the molecular vibration. The remaining energy is scattered as a photon with reduced frequency. The interaction between light and matter in Raman spectroscopy is an off-resonance condition (i.e. results from a signal which has a frequency different from that expected for the system) involving the polarization of the molecule. The Raman bands are characterized by their frequency (energy), intensity (polarizability) and shape (environment of bonds). The frequencies of the molecular vibrations depend on the masses of the atoms, geometric arrangement, and strength of the chemical bonds.[30] Thus, Raman spectra provides useful information and can be used to characterize the lattice structure and electronic, optical, and phonon properties of nanomaterials.[31] Among the strengths of Raman spectroscopy are also the simple sample preparation and versatility to analyze both liquids and solids.[30]

Experimental aspects

Raman spectra of the GnP dispersions (Paper II) were recorded on a LabRam HR800 model of Jobin-Yvon Horiba spectrometer using a He-Ne laser at 514 nm on quartz cuvette, at room temperature. Accumulations of 120 s were recorded. Raman spectra of the TMD dispersions (Paper IV) and the built composites (Papers V) were recorded on a RAMOS RA532 Raman Analyzer using a laser emitting at 532 nm on glass cuvette, at room temperature.

2.4.7. Additional techniques

Complementary techniques were used for additional characterization of the carbon nanotubes and the MWNT/GnP composites built in this work. The experimental aspects

and details on instrumentation are described in the experimental sections of papers V and VI.

The Brunauer-Emmett-Teller (BET) method is a widely used procedure to determine the surface area of porous materials. The theory is based on an extension of the Langmuir theory, used to describe the equilibrium between an adsorbate (gas molecules) and adsorbent (solid surface) at constant temperature. The Langmuir theory applies to monolayers, while the BET theory extends to multilayer adsorption.[32] In a typical BET analysis, known amounts of adsorbate (commonly nitrogen) are released to the sample cell while the pressure is varied. At a certain point, no more adsorption occurs irrespective of any increase in pressure. The sample is then removed from the nitrogen atmosphere and heated to cause the adsorbed gas to be released from the material and quantified. The data is collected in the form of a BET isotherm (amount of gas adsorbed vs. relative pressure). The porous nature of the sample can be then identified through the profile of the BET isotherm and the surface area can be evaluated.[33] In this work, BET analysis was applied to evaluate the surface area of the MWNT/GnP composites built. Further details can be found in Paper V.

Transmission electron microscopy (TEM) is an imaging technique that, similar to SEM, is based on the interaction of an electron beam with a specimen; however, in TEM the image results of the transmission of the electrons through the sample. Due to diffraction contrast, TEM allows to identify particles with different densities within the analyzed specimen.[34] In this work, TEM was used to evaluate the purity of the MWNT used regarding the existence of metallic particles (Paper VI).

2.5. Electrocatalytic studies

The electrocatalytic performance of the obtained materials was evaluated at room temperature in a three-electrode compartment cell. The electrochemical measurements were carried out using an Autolab PGSTAT 302N potentiostat/galvanostat (EcoChimie B.V.), controlled by NOVA 2.0 software. A rotating disk electrode (RDE) of glassy carbon (3 mm of diameter, Metrohm) was used as working electrode, an Ag/AgCl (3 mol dm^{-3} KCl, Metrohm) as reference electrode and a glassy carbon rod (2 mm of diameter, Metrohm) as auxiliary electrode for ORR; this electrode was substituted by a platinum wire purchased by Goodfellow (with d = diameter of 0.6 mm, l = 0.5 m, > 99.99%) for OER experiments.

The modified electrodes were prepared by the following procedure: 1 mg of material was dispersed ultrasonically (for 15 min) in 250 µL of a mixture of

isopropanol/water (1:1 v/v) and Nafion (20 µL) to form a homogeneous ink. Details on the modification of the electrode can be found on the experimental section of the papers (V and VI). The electrocatalytical tests were accomplished in N_2- or O_2-saturated (purged for 30 min before the measurements) 0.1 mol dm^{-3} KOH solution.

2.5.1. ORR electrocatalytic activity evaluation

To evaluate the material's electrocatalytic activity for ORR, cyclic voltammetry (CV) experiments were conducted at the scan rate of 0.005 V·s^{-1} and the linear sweep voltammetry (LSV) measurements at 0.005 V·s^{-1} for several rotation speeds from 400 to 3000 rpm. The ORR current was obtained by subtracting the current measured in N_2-saturated electrolyte from the current measured in O_2-saturated electrolyte. The onset potential (E_{onset}), defined as the potential at which the O_2 reduction reaction starts, was calculated as the potential at which the slope of the voltammogram exceeds a threshold value (e.g. 0.1 mA cm^{-2} V^{-1}), as described in literature.[35]

LSV data was analyzed though Koutecky-Levich (K-L) equation (Eq. 2.4). The number of electrons transferred per O_2 molecule (n_{O_2}) in the ORR process was calculated from the slopes of the K-L plot [36, 37]:

$$\frac{1}{j} = \frac{1}{j_L} + \frac{1}{j_k} = \frac{1}{B\omega^{1/2}} + \frac{1}{j_k} \quad (2.4)$$

where j is the experimentally measured current density, j_L is the diffusion-limiting current density, j_k is the kinetic current density and ω is the angular velocity; B is related to the diffusion limiting current density expressed by the Eq. 2.5:

$$B = 0.2 n_{O_2} F (D_{O_2})^{2/3} v^{-1/6} C_{O_2} \quad (2.5)$$

where F is the Faraday constant (96 485 C·mol^{-1}), C_{O_2} is the bulk concentration of O_2 (1.15×10^{-3} mol·dm^{-3} in 0.1 mol·dm^{-3} KOH), v is the kinematic viscosity of the electrolyte (0.008977 cm^2·s^{-1} for 0.1 mol·dm^{-3} KOH) and D_{O_2} is the diffusion coefficient of O_2 (1.95×10^{-5} cm^2·s^{-1} in 0.1 mol·dm^{-3} KOH). The constant 0.2 was adopted, once the rotating speed is in rpm.[38] The Tafel plots (E_{RHE} $vs.$ $\log i_k$) for oxygen reduction kinetics were obtained after the measured currents in LSV were corrected for diffusion to give the kinetic currents. The mass transport correction was made using the diffusion-limiting current density j_L, calculated by combination of equations (2.4) and (2.5).[39]

For the bipotentiostat measurements, a rotating ring-disk electrode (RRDE) of glassy carbon disk (d = 5 mm) with a platinum ring (d = 375 µm, Metrohm) was used as working electrode. The modified disk-electrode was swept cathodically at the scan rate of 0.005 V·s^{-1} and 1600 rpm in O_2-saturated 0.1 mol·dm^{-3} KOH solution, while the potential of the Pt ring was kept constant at E = 0.2 V vs. Ag/AgCl to assure the oxidation of the peroxide species formed during the ORR. The peroxide percentage (%H_2O_2) was calculated based on Equation 2.6[40]:

$$\%\mathrm{H_2O_2} = 200 \times \frac{i_\mathrm{g}/N}{i_D + i_\mathrm{g}/N} \tag{2.6}$$

where i_D and i_g are the disk and ring currents, respectively, and N is the current collection efficiency of the Pt ring (calculated as N = 0.25).[41]

The evaluation of the electrochemical stability was performed by chronoamperometry in O_2-saturated 0.1 mol·dm^{-3} KOH solution. Details can be found in the experimental section of Papers V and VI.

Another important parameter in fuel-cells is the tolerance of the catalyst to methanol, since it is commonly used as fuel and may pass across the membrane from the anode to the cathode, poisoning the catalyst.[36] Thus, in Paper VI, methanol tolerance tests were performed by cyclic voltammetry, with MWNT/TMD modified electrodes and standard Pt/C for comparison. The CVs were obtained in O_2-saturated 0.1 mol dm^{-3} KOH solutions, in the presence and absence of methanol (1.0 mol·dm^{-3}).

To facilitate the comparison with the literature, the E values determined vs. Ag/AgCl were converted to the reversible hydrogen electrode (RHE) scale according to the Nernst equation:

$$E_\mathrm{RHE} = E_\mathrm{Ag/AgCl} + 0.059\mathrm{pH} + E^\circ_\mathrm{Ag/AgCl} \tag{2.7}$$

where E_RHE is the converted potential vs. RHE, $E^\circ_\mathrm{Ag/AgCl}$ = 0.1976 at 25 ºC and $E_\mathrm{Ag/AgCl}$ is the experimentally measured potential against Ag/AgCl reference.[42]

2.5.2. OER electrochemical performance

The performance of the materials used in Paper VI for the oxygen evolution reaction was evaluated through LSV in KOH 0.1 M solution purged with O_2. The potential was swept from 0.96 to 1.86 V vs. RHE at 1600 rpm and 5 mV·s^{-1}. The iR-compensated LSV tests

were performed by calculating the uncompensated resistance (Ru) of the circuit through i-interrupt approach. Following, the value of 0.90×Ru was applied for iR-compensation in the LSV measurements. The Tafel plots were acquired from the LSV data at 1600 rpm, according to Eq. 2.8:

$$\eta = \mathrm{b} \times \log|j| \tag{2.8}$$

where η is the overpotential, b is the Tafel slope and j is the current density.

References

1. Menger, F. M.; Littau, C. A., Gemini-surfactants: synthesis and properties. *J. Am. Chem. Soc.* **1991,** *113* (4), 1451-1452.
2. Zana, R., Dimeric and oligomeric surfactants. Behavior at interfaces and in aqueous solution: a review. *Adv. Colloid Interface Sci.* **2002,** *97* (1-3), 205-253.
3. Fernandes, R. M.; Abreu, B.; Claro, B.; Buzaglo, M.; Regev, O.; Furo, I.; Marques, E. F., Dispersing carbon nanotubes with ionic surfactants under controlled conditions: Comparisons and insight. *Langmuir* **2015,** *31* (40), 10955-65.
4. Xu, H.; Zeiger, B. W.; Suslick, K. S., Sonochemical synthesis of nanomaterials. *Chem. Soc. Rev.* **2013,** *42* (7), 2555-2567.
5. Blanch, A. J.; Lenehan, C. E.; Quinton, J. S., Parametric analysis of sonication and centrifugation variables for dispersion of single walled carbon nanotubes in aqueous solutions of sodium dodecylbenzene sulfonate. *Carbon* **2011,** *49* (15), 5213-5228.
6. Coleman, J. N., Liquid exfoliation of defect-free graphene. *Acc. Chem. Res.* **2013,** *46* (1), 14-22.
7. Guardia, L.; Paredes, J. I.; Rozada, R.; Villar-Rodil, S.; Martinez-Alonso, A.; Tascon, J. M. D., Production of aqueous dispersions of inorganic graphene analogues by exfoliation and stabilization with non-ionic surfactants. *RSC Adv.* **2014,** *4* (27), 14115-14127.
8. Khan, U.; O'Neill, A.; Porwal, H.; May, P.; Nawaz, K.; Coleman, J. N., Size selection of dispersed, exfoliated graphene flakes by controlled centrifugation. *Carbon* **2012,** *50* (2), 470-475.
9. Shtein, M.; Pri-bar, I.; Regev, O., A simple solution for the determination of pristine carbon nanotube concentration. *Analyst* **2013,** *138* (5), 1490-6.
10. Abreu, B.; Rocha, J.; Fernandes, R. M. F.; Regev, O.; Furó, I.; Marques, E. F., Gemini surfactants as efficient dispersants of multiwalled carbon nanotubes: Interplay of molecular parameters on nanotube dispersibility and debundling. *J. Colloid Interface Sci.* **2019,** *547*, 69-77.
11. Shen, J.; Hu, Y.; Qin, C.; Ye, M., Layer-by-layer self-assembly of multiwalled carbon nanotube polyelectrolytes prepared by in situ radical polymerization. *Langmuir* **2008,** *24* (8), 3993-3997.
12. Marmisollé, W. A.; Azzaroni, O., Recent developments in the layer-by-layer assembly of polyaniline and carbon nanomaterials for energy storage and sensing applications. from synthetic aspects to structural and functional characterization. *Nanoscale* **2016,** *8* (19), 9890-9918.
13. Elosua, C.; Lopez-Torres, D.; Hernaez, M.; Matias, I. R.; Arregui, F. J., Comparative study of layer-by-layer deposition techniques for poly(sodium phosphate) and poly(allylamine hydrochloride). *Nanoscale Res. Lett.* **2013,** *8* (1), 539-539.
14. Xiao, F. X.; Pagliaro, M.; Xu, Y. J.; Liu, B., Layer-by-layer assembly of versatile nanoarchitectures with diverse dimensionality: a new perspective for rational construction of multilayer assemblies. *Chem. Soc. Rev.* **2016,** *45* (11), 3088-3121.
15. Pansri, S.; Noothongkaew, S., MWCNTs/r-GO hybrid films fabricated by layer by layer assembly for supercapacitor electrodes. *J. Energy Storage* **2019,** *22*, 153-156.
16. Goldstein, J. I.; Newbury, D. E.; Michael, J. R.; Ritchie, N. W. M.; Scott, J. H. J.; Joy, D. C., *Scanning electron microscopy and X-ray microanalysis*. Springer: 2017.
17. Ul-Hamid, A., *A Beginners' Guide to Scanning Electron Microscopy*. Springer: 2018.
18. Eaton, P.; West, P., *Atomic Force Microscopy*. Oxford University Press: 2010.
19. Kimberlin, K. *Basic SPM Training Course*; 2000.

20. Zhang, K.; Zhang, X.; Li, H.; Xing, X.; Jin, L. e.; Cao, Q.; Li, P., Direct exfoliation of graphite into graphene in aqueous solution using a novel surfactant obtained from used engine oil. *J. Mater. Sci.* **2018,** *53* (4), 2484-2496.
21. Narayan, R.; Lim, J.; Jeon, T.; Li, D. J.; Kim, S. O., Perylene tetracarboxylate surfactant assisted liquid phase exfoliation of graphite into graphene nanosheets with facile re-dispersibility in aqueous/organic polar solvents. *Carbon* **2017,** *119*, 555-568.
22. Smith, R. J.; King, P. J.; Lotya, M.; Wirtz, C.; Khan, U.; De, S.; O'Neill, A.; Duesberg, G. S.; Grunlan, J. C.; Moriarty, G.; Chen, J.; Wang, J.; Minett, A. I.; Nicolosi, V.; Coleman, J. N., Large-scale exfoliation of inorganic layered compounds in aqueous surfactant solutions. *Adv. Mater.* **2011,** *23* (34), 3944-8.
23. Liu, H.-L.; Shen, C.-C.; Su, S.-H.; Hsu, C.-L.; Li, M.-Y.; Li, L.-J., Optical properties of monolayer transition metal dichalcogenides probed by spectroscopic ellipsometry. *Appl. Phys. Lett.* **2014,** *105* (20), 201905.
24. Hunter, R. J., *Zeta potential in colloid science: principles and applications*. Academic press: 2013; Vol. 2.
25. Williams, P. M., Zeta Potential. In *Encyclopedia of Membranes*, Drioli, E.; Giorno, L., Eds. Springer Berlin Heidelberg: Berlin, Heidelberg, 2016; pp 2063-2064.
26. White, B.; Banerjee, S.; O'Brien, S.; Turro, N. J.; Herman, I. P., Zeta-potential measurements of surfactant-wrapped individual single-walled carbon nanotubes. *J. Phys. Chem. C* **2007,** *111* (37), 13684-13690.
27. Gabbott, P., *Principles and applications of thermal analysis*. John Wiley & Sons: 2008.
28. Menczel, J. D.; Prime, R. B., *Thermal analysis of polymers: fundamentals and applications*. John Wiley & Sons: 2009.
29. Brown, M. E., *Introduction to thermal analysis: techniques and applications*. Springer Science & Business Media: 2001; Vol. 1.
30. Larkin, P., *Infrared and Raman spectroscopy: principles and spectral interpretation*. Elsevier: 2017.
31. Wu, J. B.; Lin, M. L.; Cong, X.; Liu, H. N.; Tan, P. H., Raman spectroscopy of graphene-based materials and its applications in related devices. *Chem. Soc. Rev.* **2018,** *47* (5), 1822-1873.
32. Brunauer, S.; Emmett, P. H.; Teller, E., Adsorption of Gases in Multimolecular Layers. *J. Am. Chem. Soc.* **1938,** *60* (2), 309-319.
33. Barron, A. R., Physical methods in chemistry and nano science. **2015**.
34. Loos, J.; Grossiord, N.; Koning, C. E.; Regev, O., On the fate of carbon nanotubes: Morphological characterisations. *Compos. Sci. Technol.* **2007,** *67* (5), 783-788.
35. Daems, N.; Sheng, X.; Vankelecom, I. F. J.; Pescarmona, P. P., Metal-free doped carbon materials as electrocatalysts for the oxygen reduction reaction. *J. Mater. Chem. A* **2014,** *2* (12), 4085-4110.
36. Nunes, M.; Rocha, I. M.; Fernandes, D. M.; Mestre, A. S.; Moura, C. N.; Carvalho, A. P.; Pereira, M. F. R.; Freire, C., Sucrose-derived activated carbons: Electron transfer properties and application as oxygen reduction electrocatalysts. *RSC Adv.* **2015,** *5* (124), 102919-102931.
37. Liu, F.; Peng, H. J.; You, C.; Fu, Z.; Huang, P.; Song, H.; Liao, S., High-performance doped carbon catalyst derived from nori biomass with melamine promoter. *Electrochim. Acta* **2014,** *138*, 353-359.
38. Mani, A.; Birss, V. I., Dependence of the oxygen reduction reaction at sol–gel derived Co-based catalysts on acidic solution pH and temperature. *J. Electroanal. Chem.* **2012,** *687*, 102-110.
39. Gao, S.; Fan, H.; Zhang, S., Nitrogen-enriched carbon from bamboo fungus with superior oxygen reduction reaction activity. *J. Mater. Chem. A* **2014,** *2* (43), 18263-18270.

40. Delmondo, L.; Salvador, G. P.; Muñoz-Tabares, J. A.; Sacco, A.; Garino, N.; Castellino, M.; Gerosa, M.; Massaglia, G.; Chiodoni, A.; Quaglio, M., Nanostructured MnxOy for oxygen reduction reaction (ORR) catalysts. *Appl. Surf. Sci.* **2016,** *388*, 631-639.
41. Swesi, A. T.; Masud, J.; Nath, M., Nickel selenide as a high-efficiency catalyst for oxygen evolution reaction. *Energy Environ. Sci.* **2016,** *9* (5), 1771-1782.
42. Hoang, S.; Guo, S.; Hahn, N. T.; Bard, A. J.; Mullins, C. B., Visible light driven photoelectrochemical water oxidation on nitrogen-modified TiO2 nanowires. *Nano Lett.* **2012,** *12* (1), 26-32.

Chapter 3 Results and Discussion

I. Gemini surfactants as efficient dispersants of multiwalled carbon nanotubes: Interplay of molecular parameters on nanotube dispersibility and debundling

II. Comparative trends and molecular analysis on the surfactant-assisted dispersibility of 1D and 2D carbon materials: multiwalled nanotubes vs graphene nanoplatelets

III. Dispersibility and noncovalent functionalization of multiwalled carbon nanotubes by polymer/surfactant mixtures of assorted composition: synergistic vs antagonistic effects

IV. On the role of ionic surfactants in the liquid-phase exfoliation of 2D graphene analogues: the case of transition metal dichalcogenides MoS_2, WS_2 and $MoSe_2$

V. Carbon nanotube/graphene nanocomposites built via surfactant-mediated colloid assembly as metal-free catalysts for the oxygen reduction reaction

VI. Nanocomposites prepared from carbon nanotubes and the transition metal dichalcogenides WS_2 and MoS_2 via surfactant-assisted dispersions as electrocatalysts for oxygen reactions

I

Gemini surfactants as efficient dispersants of multiwalled carbon nanotubes: Interplay of molecular parameters on nanotube dispersibility and debundling

Journal of Colloid and Interface Science 547 (2019) 69–77

Contents lists available at ScienceDirect

Journal of Colloid and Interface Science

journal homepage: www.elsevier.com/locate/jcis

Regular Article

Gemini surfactants as efficient dispersants of multiwalled carbon nanotubes: Interplay of molecular parameters on nanotube dispersibility and debundling

Bárbara Abreu [a], Jessica Rocha [a], Ricardo M.F. Fernandes [a,b], Oren Regev [c,d], István Furó [b], Eduardo F. Marques [a,*]

[a] CIQUP, Department of Chemistry and Biochemistry, Faculty of Sciences, University of Porto, Rua do Campo Alegre, 4169-007 Porto, Portugal
[b] Division of Applied Physical Chemistry, Department of Chemistry, KTH Royal Institute of Technology, SE-10044 Stockholm, Sweden
[c] Department of Chemical Engineering, Ben-Gurion University of the Negev, 84105 Beer-Sheva, Israel
[d] Ilse Katz Institute for Nanotechnology, Ben-Gurion University of the Negev, 84105 Beer-Sheva, Israel

GRAPHICAL ABSTRACT

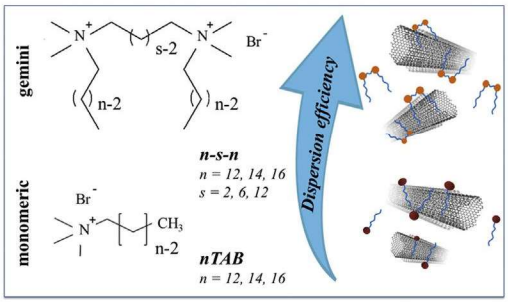

ARTICLE INFO

Article history:
Received 11 February 2019
Revised 18 March 2019
Accepted 24 March 2019
Available online 25 March 2019

Keywords:
Gemini surfactant
Carbon nanotube
Exfoliation
Dispersion efficiency
Molecular structure
Spacer length
Tail length
Adsorption
Hydrophobicity

ABSTRACT

Surfactants have been widely employed to debundle, disperse and stabilize carbon nanotubes in aqueous solvents. Yet, a thorough understanding of the dispersing mechanisms at molecular level is still warranted. Herein, we investigated the influence of the molecular structure of gemini surfactants on the dispersibility of multiwalled carbon nanotubes (MWNTs). We used dicationic *n-s-n* gemini surfactants, varying *n* and *s*, the number of alkyl tail and alkyl spacer carbons, respectively; for comparisons, single-tailed surfactant homologues were also studied. Detailed curves of dispersed MWNT concentration vs. surfactant concentration were obtained through a stringently controlled experimental procedure, allowing for molecular insight. The gemini are found to be much more efficient dispersants than their single-tailed homologues, i.e. lower surfactant concentration is needed to attain the maximum dispersed MWNT concentration. In general, the spacer length has a comparatively higher influence on the dispersing efficiency than the tail length. Further, scanning electron microscopy imaging shows a sizeable degree of MWNT debundling by the gemini surfactants in the obtained dispersions. Our observations also point to an adsorption process that does not entail the formation of micelle-like aggregates on the nanotube surface, but rather coverage by individual molecules, among which the ones that seem to be able to adapt best to the nanotube surface provide the highest efficiency. These studies are relevant for the rational design and choice of optimal dispersants for carbon nanomaterials and other similarly water-insoluble materials.

* Corresponding author.
E-mail address: efmarque@fc.up.pt (E.F. Marques).

https://doi.org/10.1016/j.jcis.2019.03.082
0021-9797/

1. Introduction

Carbon nanotubes (CNTs) are extremely long, narrow and hollow cylinders made of graphene sheets possessing unique mechanical, thermal, optical and electrical properties [1,2]. Their high aspect ratio and strong inter-tube van der Waals cohesive forces ($\sim$40 $kT\,nm^{-1}$) result in tight agglomeration into bundles, specifically so in their as-prepared, pristine state. Since many applications rely on isolated tubes where the properties (e.g. mechanical strength) are optimized, bundling is a major hurdle towards applications. Significant efforts have been made over the years to produce well-dispersed nanotubes in various solvents [3,4]. One of the most common approaches for aqueous solvents is to employ amphiphilic dispersants—surfactants [5–12], synthetic polymers [13–18], nucleic acids [19,20] or proteins [21–25]—which bind to the CNT surface via their hydrophobic moieties, and provide wettability and colloidal kinetic stability via their polar regions. The produced dispersions (not solutions) [4] remain metastable owing to double-layer electrostatic repulsions when ionic dispersants are used or to steric repulsions in the case of nonionic ones.

A large number of studies dealing with low molecular-weight dispersants, ranging from ionic to nonionic, and covering assorted molecular properties has been reported [5–11,26–30]. The wide diversity of surfactant structures (namely headgroup and tail composition), coupled to big differences between carbon nanotube batches and processing conditions used, often makes comparisons very difficult. Further, it obscures a more fundamental understanding of the dispersing process. For these reasons, studies where molecular features are methodically varied, protocols are strictly controlled and the experimental data are both accurate and precise, are warranted [7–11,31].

One of the key issues still awaiting clarification is the type of arrangement of the surfactant molecules on the curved surface of the CNTs. Randomly adsorbed molecules, monolayers, or aggregates like spherical micelles and hemimicelles, or even fully wrapping coverage, have been proposed despite that experimental evidence is scarce [32,33]. Molecular simulations have also provided somewhat disparate views [10,34]. Other key issues pertaining the adsorption process include the fraction of bound surfactant and surface coverage. Recently, we have shown that the amount of dispersant bound to the CNT surface is surprisingly small (only a few percent of the dispersant demanded to achieve high CNT concentrations) and that there is a limiting surface coverage [17,18]. It was also proposed that the surfactant concentration required for dispersibility seems to basically constitute a kinetic factor: high CNT dispersibility is found if the dispersant concentration is high enough to be able to rapidly cover the freshly cleaved nanotube surfaces [35].

While the dispersing of MWNTs based on various types of single-tailed surfactants has been extensively reported [3,4,7,36], double-tailed dispersants and in particular gemini surfactants have been much less explored in that respect. And yet, gemini surfactants are an important class of surfactants because of their unconventional structure, related amphiphilic properties and widespread applications. They possess two polar headgroups linked by a covalent spacer, whose length and flexibility/rigidity can be tailor-made [37–39]. These compounds are often abbreviated by *n-s-n* where the *n* is number of carbon atoms of the alkyl tail and *s* that of the spacer chain. Hydrophobicity can thus be controlled both through the two tails and the headgroup spacer, with the latter also influencing the headgroup charge-to-charge distance. These surfactants present lower *cmc* values, higher surface activity and more versatile self-assembly than their single-tailed homologues [37–41]. The spacer length, in particular, has been found to be crucial in such diverse phenomena as the melting behavior of bilayers [42], thermotropic mesomorphism [43], binding onto polyelectrolytes [44] and stabilization of nanoparticles [45]. Hence, gemini surfactants have been successfully employed *inter alia* as emulsifiers, gelators, wetting agents and gene transfection agents [46–50].

In this work, it was anticipated that the interplay of spacer and tail effects of gemini surfactants could also have important consequences for their ability to disperse MWNTs.

Previous studies on gemini surfactants as dispersants for carbon nanotubes are scarce [28,51–59] and deal with a small number of compounds. Some reports deal with the dispersibility of MWNTs in water by conventional *bis*-quat gemini [51,52] and molecular dynamics simulations of their adsorption on SWNTs [53], looking in general for spacer effects. Other studies report on the dispersibility of MWNTs with gemini of assorted chemistry either in water [28,54–58] or in organic solvents [59]. However, a wide-ranging investigation of the dispersing behavior of gemini with varying spacer and tail lengths, allowing for deeper molecular insight, is not available and this is the gap we wish to fill with the current work.

For that, we resorted to a series of dicationic gemini surfactants of general structure $[C_nH_{2n+1}(CH_3)_2N^+(CH_2)_sN^+(CH_3)_2C_nH_{2n+1}]Br_2$, abbreviated as *n-s-n* (Fig. 1). Thus, 12-*s*-12 gemini with $s = 2$, 6, and 12 were studied alongside 14-*s*-14 with $s = 2$, 6 and 12 and 16-*s*-16, with $s = 2$ and 12. The single-tailed conventional homologues dodecyltrimethylammonium bromide, DTAB ($n = 12$), tetradecyltrimethylammonium bromide, TTAB ($n = 14$) and cetyltrimethylammonium bromide, CTAB ($n = 16$) were also employed for direct comparison. Our main goal was therefore to explore on a consistent basis how the variation in molecular architecture of the gemini affects their ability to disperse MWNTs.

Sonication and centrifugation parameters are known to have considerable influence on the concentration of dispersed CNTs, and on the bundle length and width distributions [9,29,35,36]. Thus, a rigorous experimental protocol was used to prepare the dispersions [11]. A strict control of the processing parameters, repeated measurements and accurate MWNT quantification—combining thermogravimetric analysis (TGA) and UV–visible absorption spectroscopy—were employed to obtain highly precise dispersibility curves and hence extract reliable comparative metrics. The main findings and key conclusions are presented, and critically discussed under the light of previous work on surfactant-assisted dispersions of CNTs.

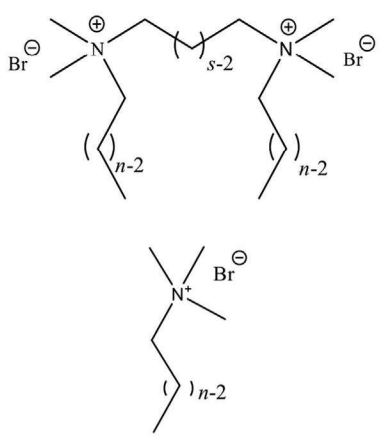

Fig. 1. Chemical structure of the surfactants herein used: gemini bis(quaternary ammonium) surfactants, 12-*s*-12, 14-*s*-14 and 16-*s*-16; DTAB, dodecyltrimethylammonium bromide; TTAB, tetradecyltrimethylammonium bromide; and CTAB, cetyltrimethylammonium bromide.

2. Experimental section

2.1. Materials

MWNTs (d = 8–15 nm and L = 10–50 μm) were used as received from CheapTubes. All the alkanediyl-α,ω-bis(alkyldimethylammonium bromide) dimeric surfactants used here, and abbreviated as 12-s-12 (s = 2, 6 and 12), 14-s-14 (s = 2, 6 and 12) and 16-s-16 (s = 2 and 12), were synthesized according to established procedures [37] and purified by recrystallization. The purity of the compounds was evaluated by nuclear magnetic resonance (NMR), mass spectrometry and further confirmed by the *cmc* values, obtained by conductivity measurements (see Fig. S1 and Table S2, supplementary data); they are in good agreement with previous reports [38]. DTAB, TTAB and CTAB were acquired from Sigma Aldrich (purities ≥ 99%) and used as received, with the *cmc* values also in line with those typically reported [60].

2.2. Preparation of CNT dispersions

The CNT/surfactant mixtures were initially prepared by weighing the carbon material, 9 mg, followed by addition of the desired aqueous surfactant solution, 3 mL, resulting in approx. 0.3 wt% CNT mixtures. All stock surfactant solutions were prepared in ultrapure water, at temperatures lying above the Krafft temperature of the surfactant to ensure its full dissolution (set to 25 °C for all surfactants, except CTAB, 30 °C, 14-2-14, 35 ºC, and 16-2-16, 46 °C). For sonication, a Bandelin Sonoplus Vb 2070 probe (70 W output power; 20 kHz processing frequency) with a freshly polished 3 mm microtip was used, with a vibration amplitude set to 30% and a sonication time to 8.5 min. In order to ensure identical sample treatment, a rigorous procedure, previously established [11], was followed: (i) the sonication energy density transferred to the sample was kept constant ($\approx 5.3 \times 10^2$ J mL^{-1}, estimated from calorimetric measurements) resulting in an average power density of 1.0 W mL^{-1}; (ii) the tip was always placed in the same position inside the same type of vial (1 cm from the bottom); (iii) temperature was controlled with an external thermostated bath and set above the Krafft temperature of the surfactants. Under these mild sonication conditions, there is insignificant nanotube damage [9,17]. After sonication, the samples were centrifuged during 20 min at 4000 g. After centrifugation, the top 1 mL of the supernatant was separated from the precipitate by decantation to determine the MWNT concentration.

2.3. Quantification of CNT concentration

The absolute carbon nanotube concentration in the supernatant, c_{MWNT}, was determined using a previously published method [61]. An accurately measured aliquot of each dispersion was lyophilized during 24–48 h. In order to quantify the mass fraction of surfactant present in the solid residue, TGA was performed using a Netzsch TG 209 F1-Iris under N_2 atmosphere (flow rate of 50 mL min^{-1}). Simple mass balance yields the dispersed mass of MWNTs in the aliquot [61]. Calibration curves (TGA + UV–vis spectroscopy) [61] were then obtained for each surfactant, by measuring absorbance versus c_{CNT} at λ = 660 nm (ensuring null absorption from the neat surfactant solution), using dilutions from a stock dispersion with known MWNT mass concentration. A double-beam spectrophotometer Agilent 8453 was used, with a plastic cuvette with optical path length of 1 cm. For each dispersion composition, 3 to 5 independent preparations were made, and on average 3 sampling spectrophotometric measurements done.

On the basis of Beer-Lambert law and the linear regimes observed [11,61], the apparent extinction coefficients, ε_{660}, were determined for each surfactant (see Table S1, s.d.), yielding a mean value 40 ± 2 mL mg^{-1} cm^{-1}, in line with previous reports [9,11]. The c_{MWNT} values were determined from the apparent absorbance using the mean extinction coefficient value.

2.4. Dispersibility curves

The dispersibility curves obtained for the gemini surfactants follow a sigmoidal profile, as depicted in Fig. 2, similar to those previously obtained for single-tailed surfactants [11,35]. Thus, appropriate statistical metrics can be withdrawn from the plots: *cdc*, critical dispersibility concentration, the initial concentration of surfactant needed for dispersibility to take off; $c_{s,max}$, the minimum surfactant concentration at which the maximum value of c_{MWNT}, denoted as $c_{CNT,max}$, is attained.

For comparative purposes, the dispersibility effectiveness, η, and efficiency, η^*, are also introduced. The effectiveness η at a particular sonication/centrifugation regime [35] is defined as the ratio $c_{MWNT,max}/c_{MWNT,initial} \times 100$ and it measures the ability of the surfactant to disperse MWNTs with respect to the initial loading (herein, $c_{MWNT,initial}$ = 3 mg mL^{-1}). The efficiency η^* is defined as the $\eta/c_{s,max}$ ratio and is expressed in units of % kg mmol^{-1}; for a highly efficient dispersant, maximal dispersibility (high η) should be attained at the lowest possible $c_{s,max}$.

2.5. Zeta potential measurements

The zeta potential, ζ, of the dispersed particles was measured at 25 °C using a zeta sizer Nano ZS, ZN 3500, with a 4 mW He-Ne laser (633 nm) and DTS 1060C disposable zeta cells. The electrophoretic mobility, μ, was measured using a combination of electrophoresis and laser Doppler velocimetry techniques and ζ was calculated from μ using the known Henry equation [6,62]. A dielectric constant of 78.5, a medium viscosity of 0.89 cP and a $f(\kappa a)$ function value of 1.5 were used, following previously reported assumptions, namely that MWNT/MWNT interactions are negligible [6,62]. All ζ values are mean values based on at least 2 independent dispersions and 5 measurements per dispersion.

2.6. Characterization of CNT debundling by scanning electron microscopy (SEM)

Samples for SEM were prepared by casting a droplet of CNTs dispersion (diluted 100 times) on a pre-heated (~110 °C) silicon wafer, followed by fast solvent evaporation. Subsequently,

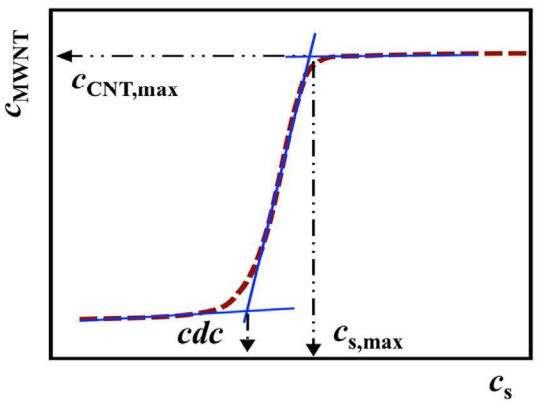

Fig. 2. Representative dispersibility curve (concentration of dispersed nanotubes vs. surfactant concentration), with the graphical definition of the different parameters, *cdc*, $c_{s,max}$ and $c_{CNT,max}$. The surfactant concentration c_s is typically expressed in a logarithmic scale.

the silicon wafer was rinsed with ethanol to remove the excess of surfactant. SEM images were obtained on a FEI Quanta 400FE operated at 25 kV. A distribution of MWNTs (individual ones or thin bundles) was recorded and statistically analyzed. To ensure meaningful statistics, more than 100 objects were measured for each sample (except for DTAB, as detailed in Section 3.3).

3. Results and discussion

3.1. General features of the dispersibility curves

The dispersibility curves obtained for the 12-*s*-12, 14-*s*-14 and 16-*s*-16 surfactants are shown in Fig. 3(a)-(c), respectively, allowing to monitor the influence of *increasing spacer length* for fixed tail length. In Fig. 3(d)-(e), the curves are grouped with respect to *increasing tail length* for fixed spacer length. In addition, curves for the single-tailed homologous surfactants, DTAB, TTAB and CTAB are shown in Fig. 3(f).

Before analyzing Fig. 3, a few points are noteworthy. (1) The initial concentration of MWNT powder is constant in all systems, 3 mg mL^{-1}. (2) The surfactant concentration, c_s, was varied typically in the range (0.1–10) × *cmc* for each surfactant and it is expressed in molality (surfactant amount per water mass in kg); the values are practically identical in mmol L^{-1} and can also be easily converted to mg mL^{-1} (Table S2, s.d.). (3) c_s is the value for the *initial* mixture (i.e. before sonication), not the final one in the as-produced dispersion (i.e., the supernatant obtained after centrifugation) [35,63]; the latter quantity was not investigated here. Since some surfactant exits by the precipitate [35], the surfactant concentration in the supernatant is estimated to be roughly 60–70% of c_s (Table S3, s.d.). (4) For comparisons, the *cmc* of each neat surfactant solution is indicated by arrows in the graphs. In a dispersion, the surfactant concentration at which free micelles may form is somewhat higher than the neat *cmc*, due to the uptake of surfactants by the dispersed tubes [64].

From the curves in Fig. 3, the parameters *cdc*, $c_{s,max}$ and $c_{CNT,max}$ were extracted using appropriate linear regression statistics (Table S2, s.d.), and thereafter η and η^* were determined.

Two main trends already are apparent in Fig. 3(a)-(c) and Fig. 4(a). First, the gemini surfactants in each family (12-*s*-12, 14-*s*-14 and 16-*s*-16) are typically less (or at most, similarly) effective (Fig. 4(a), middle) in dispersing MWNTs compared to the respective single-tailed homologues. Second, they are nevertheless much more efficient (Fig. 4(a), bottom) than the latter, primarily because of their much lower $c_{s,max}$ values (Fig. 4(a), top). Overall, the data indicate that the gemini surfactants in general can disperse the same amount of MWNTs as conventional single-tailed surfactants but do so at much lower surfactant concentration.

3.2. Role of molecular properties

The effect of varying the spacer length, *s*, in the dispersion metrics is plotted in Fig. 4(a). For all the gemini, there is a decrease in $c_{s,max}$ as *s* increases, a trend that is particularly strong for the

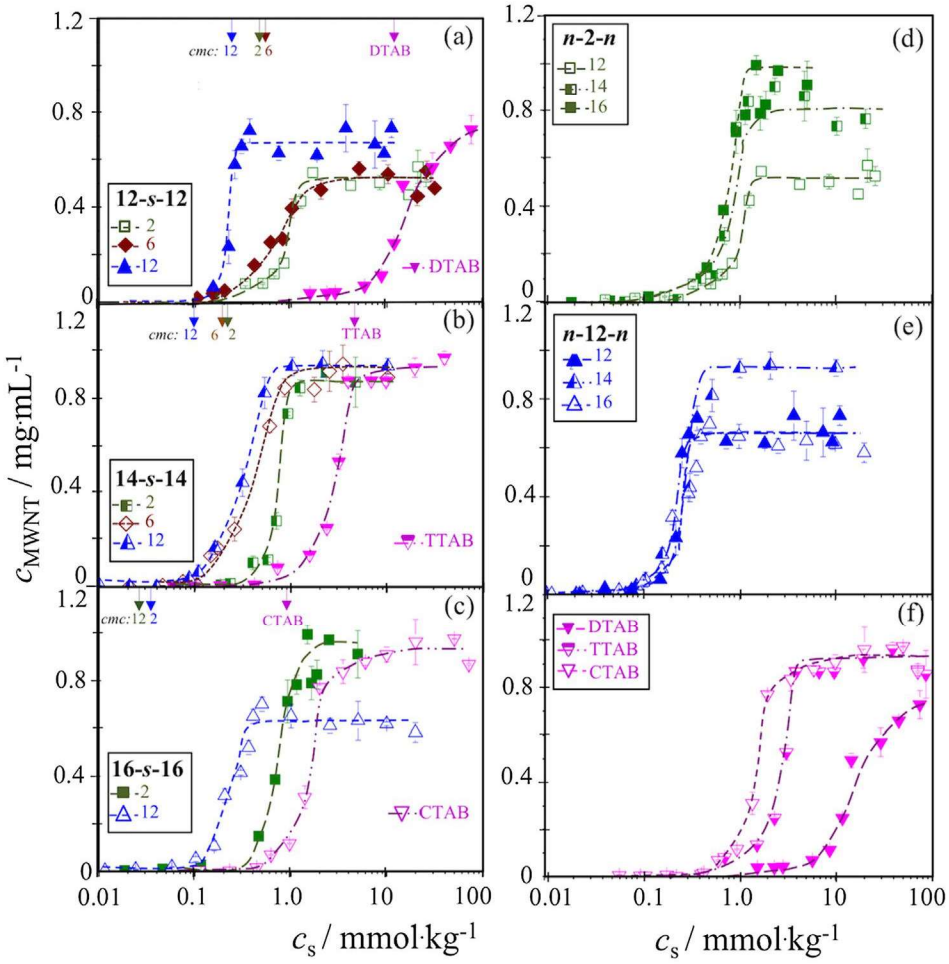

Fig. 3. Concentration of dispersed MWNTs vs. surfactant concentration (in log scale to enhance features at low c_s) for the different gemini series and single-tailed homologues: (a) 12-*s*-12 and DTAB; (b) 14-*s*-14 and TTAB; (c) 16-*s*-16 and CTAB; (d) *n*-2-*n*; (e) *n*-12-*n* and (f) single-tailed series. Lines are for visual guidance. The arrows on top of Fig. 3(a)-(c) indicate the *cmc* of each surfactant.

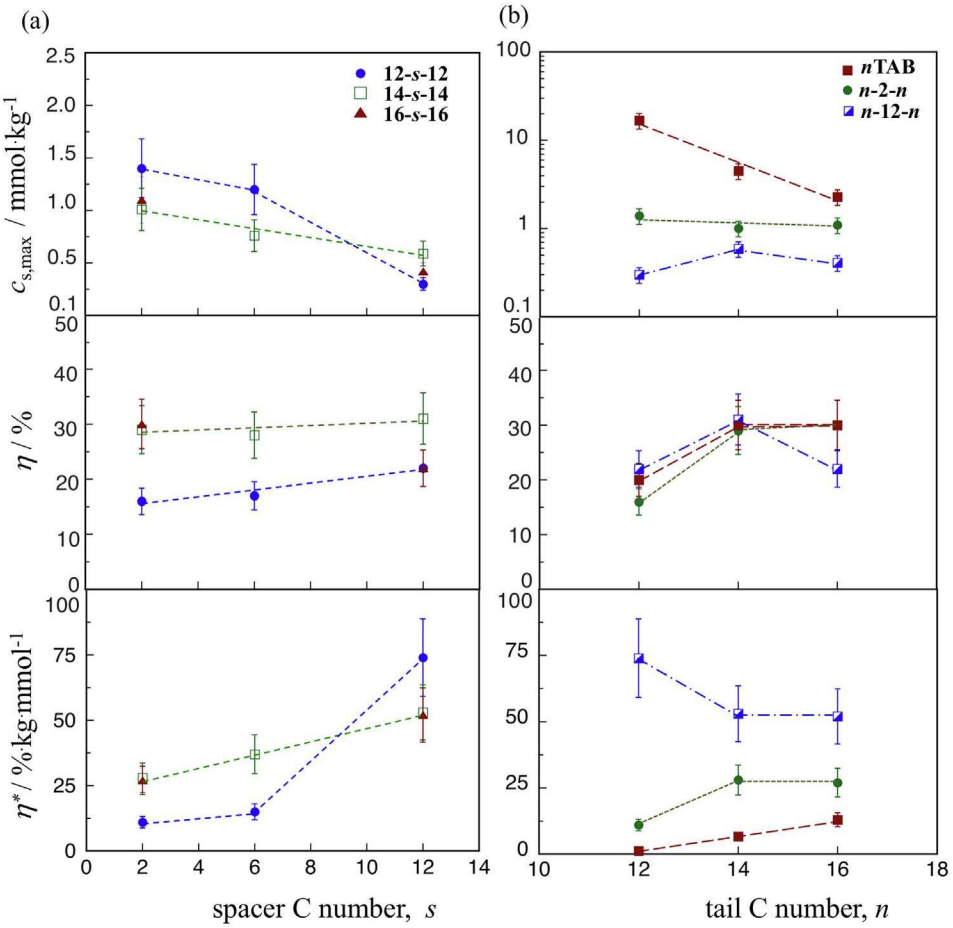

Fig. 4. The concentration of surfactant needed for maximum dispersibility, $c_{s,max}$, the effectiveness, η, and efficiency, η^*, as function of (a) spacer length for 12-*s*-12 (●), 14-*s*-14 (□) and 16-*s*-16 (▲) families; (b) tail length, for a short spacer, *n*-2-*n* (●), and long spacer *n*-12-*n* (◪), and no spacer, *n*TAB, single-tailed surfactants (■).

12-*s*-12 family where that decrease approaches one order of magnitude. In turn, $c_{CNT,max}$ does not vary much with *s,* lying between 0.5 and 0.9 mg mL^{-1} (Table S2, s.d.). This means also that the effectiveness remains essentially constant though slightly different for each single family. From the combined trends of $c_{s,max}$ and η, however, it is clear that the efficiency η^* must increase sizably with spacer length, as shown in Fig. 4(a) bottom.

With respect to tail length effects on $c_{s,max}$ for *n*-2-*n* and *n*-12-*n* families, Fig. 4(b) top (log scale used for easier visualization), the clear and strong variation of $c_{s,max}$ with *n* for single-tailed surfactants benchmarks the effect of increasing hydrophobicity. This must be connected to the higher affinity of longer chains to the nanotube surface. While the hydrophilic/hydrophobic balance in the *n*-2-*n* gemini is roughly similar to that in the single-tailed surfactants, the former display a completely different behavior: a much smaller variation of $c_{s,max}$ with the tail length. In addition, there is an interesting dichotomy: gemini – which individually display a hydrophobic component much larger than that of any *n*TAB – exhibit lower $c_{s,max}$ values than the *n*TABs, but they show no variation with their own increasing hydrophobicity (indicating that some molecular features in gemini may have to each other opposing effects).

Effectiveness shows a moderate variation (on average, an increase) with tail length. Recently, it was stated that, in the presence of sufficiently high dispersant concentration, the amount of dispersed CNT is mainly dependent on the sonication energy and centrifugation regime used [35]. Considering that $c_{s,max}$ is a measure of having sufficient dispersant and that effectiveness benchmarks the dispersing behavior in that particular regime for any dispersants investigated, the lack of strong variation comes of no surprise.

Finally, we note that on an absolute basis, of all the gemini the most effective ones are the longest tail/shortest spacer compound, 16-2-16 and the 14-s-14 family, with η values in the order of 30%, similar to those of CTAB and TTAB (see also Table S2, s.d.). Conversely, the most efficient is clearly the shortest tail/longest spacer compound, 12-12-12, about 3 times more efficient than 16-2-16 and only slightly less effective. Further analysis of the performance in terms of ability to separate the MWNTs is presented in the next section.

3.3. MWNT debundling: morphological characterization

Besides the dispersion efficiency and effectiveness of a surfactant to disperse CNTs, another important feature is the aggregation state of the dispersed nanotubes. An ideal surfactant disperses to the maximum concentration of individual CNTs with the lowest amount of surfactant (highest η^*) [11]. Thus, to assess the actual surfactant debundling, the dispersions were analyzed by SEM, and the size of the bundles was measured and critically compared among surfactants, choosing MWNT concentrations at the respective plateau regions of the dispersibility curves (Fig. 3).

SEM representative micrographs and respective distribution of the bundle diameters are presented in Fig. 5 for four surfactants with different behavior: 12-12-12, the most efficient surfactant; 16-2-16 and its single-tailed homologue, CTAB, the most effective

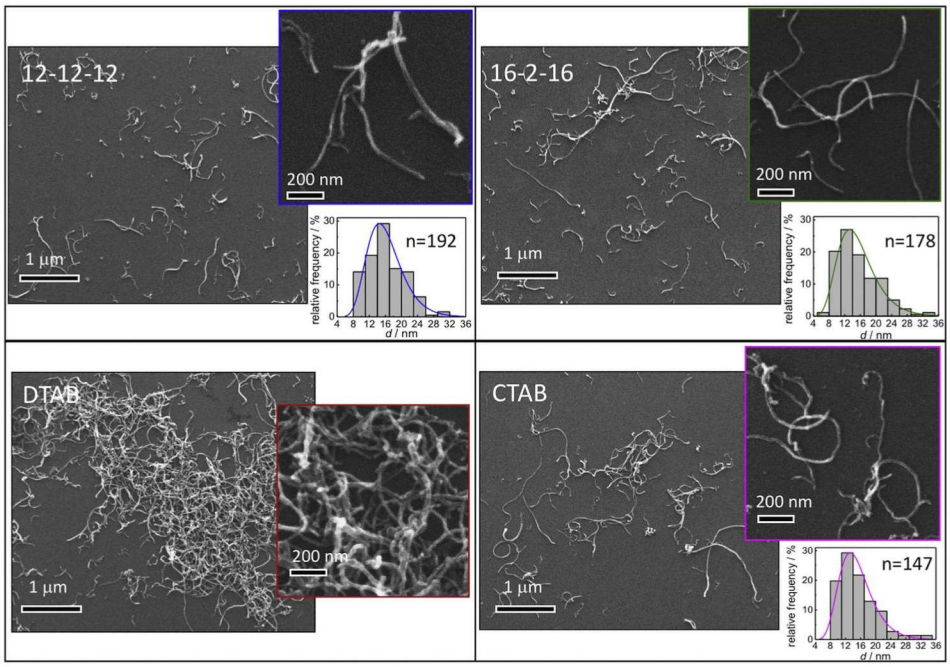

Fig. 5. SEM imaging and respective histograms of the CNT bundle diameter distributions in dispersions obtained with different surfactants. The insets represent images with a higher magnification. The histograms were fitted to a log-normal distribution (see Table S4, s.d., for the fitting parameters).

surfactants; and DTAB, the least efficient surfactant. Close inspection of SEM images indicate striking differences between DTAB and the remaining compounds. While the gemini surfactants and CTAB show a big fraction of thin bundles (<10 CNTs) and also individual tubes, DTAB shows CNTs aggregated into bundles and mesh-like structures. The entanglement observed for the latter dispersions does not allow to get a measure of size for a statistically representative number (>100) of distinctly dispersed MWNTs. When comparing a larger group of surfactants (Fig. S2, s.d.), the average particle diameter obtained through a log-normal fitting to the values lies in the range of 15–18 nm (see Table S4, s.d.). These values are close to the supplier's specifications for the individual MWNT diameter (8–15 nm). Hence, we can safely infer that a high degree of debundling was achieved for both gemini surfactants and CTAB.

Detailed analysis of the histograms further suggests that (i) for single-tailed surfactants, tail length plays an important role on the dispersion quality, adding to its effect on the quantitative parameters (see Table S2, s.d.); (ii) for longer spacers ($s = 12$), tail length does not seem to influence the quality of the dispersions. Finally, the results point to an ordering of the degree of CNT separation as follows: DTAB $\ll$ gemini $\leq$ CTAB. For DTAB, the observed mesh structure (and thereby the actual lack of *de facto* debundling in terms of small bundles and individual CNTs) may be the result of re-aggregation [12].

3.4. Molecular aspects of the dispersing process

One parameter worth to look at in this context is the *cmc*. It both provides a measure of the hydrophobicity and permits us to decide the role of the surfactant state (unimer vs. micelle) in the dispersing process. Regarding the latter point, the ratios *cdc*/*cmc* and $c_{s,max}$/*cmc* are displayed in Fig. 6 for all surfactants. The dashed line marks unity and thus allow us to assess the relative importance of *cmc*, and hence the presence of micelles, in the initial stage of the dispersing process, i.e. upon sonication of the CNT/surfactant mixtures. For 8 out of 11 surfactants studied, *cdc*/*cmc* is sizably smaller than 1 (the exceptions being 14-2-14, 16-2-16 and 16-12-16). Regarding the $c_{s,max}$/*cmc* ratio, values are typically around 1 to 2 for the 12-*s*-12 series and the single-tailed surfactants, but significantly higher (5 to 25) for the C14 and C16 gemini. Since for the latter compounds, the *cmc* values are also rather low (in the range of 5–50 µmol.kg^{-1}, Table S2, s.d.), it is unsurprising that the surfactant concentrations needed for meaningful dispersibility lie necessarily well above *cmc*.

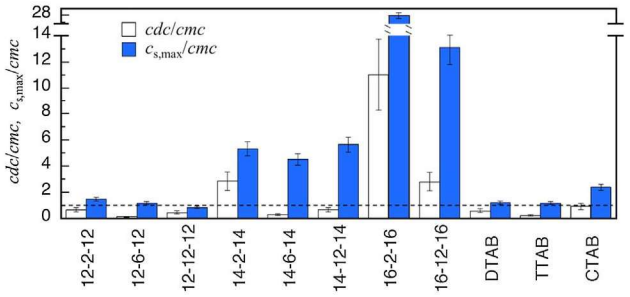

Fig. 6. The ratios of *cdc* and $c_{s,max}$ relative to *cmc* for the 12-*s*-12, 14-*s*-14 and 16-*s*-16 gemini surfactants and their single-tailed homologues DTAB, TTAB and CTAB. The dashed horizontal line marks the unity value.

It has previously been inferred for various single-tailed surfactants [11] that it is the dispersant overall concentration, irrespective of it being in unimer or micelle form, that matters for the exfoliation process. Our current observations, for a family of very different (double-tailed gemini) surfactants, are in line with those conclusions.

Further molecular information is provided by zeta potential measurements performed in the dispersions. Fig. 7(a) shows the ζ values for neat gemini surfactant solution ($c_s = 2$ mmol kg^{-1}) and Fig. 7(b) the ζ values for dispersions with identical surfactant concentration, $c_s = 2$ mmol kg^{-1}, and identical mass of dispersed MWNTs, $c_{CNT} = 0.1$ mg mL^{-1} (such dispersions require special preparation; see Section 5 and Table S5 in s.d. for details).

In the case of neat gemini micelles ($c_s > cmc$ for all surfactants), the ζ – potential decreases with increasing spacer length for all three series (12-*s*-12, 14-*s*-14 and 16-*s*-16), covering a range of

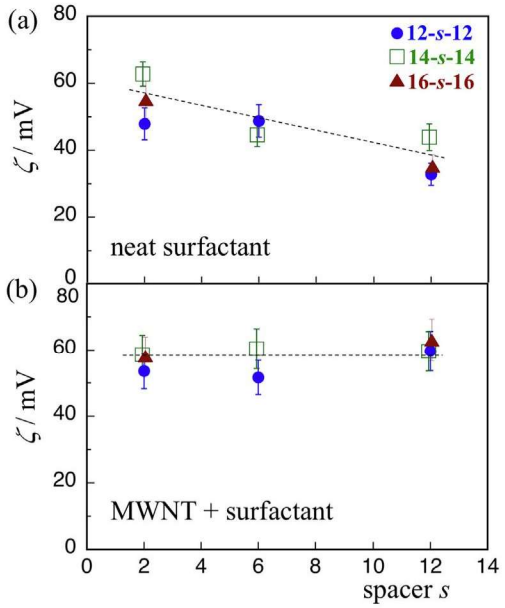

Fig. 7. Zeta potential vs. the number of carbons in the spacer, *s*, for the 12-*s*-12 (●), 14-*s*-14 (□) and 16-*s*-16 (▲) families: (a) neat gemini micelles, c_s = 2 mmol kg^{-1}; (b) MWNT/gemini dispersions, c_s = 2 mmol kg^{-1} and c_{CNT} = 0.1 mg mL^{-1}. Lines are visual guides.

values between roughly +60 to +30 mV. In contrast, when nanotubes are present, ζ remains essentially constant at ca. +60 mV with increasing *s*.

These results warrant two major considerations. (1) From previous work by Zana and co-workers [38,65] on *n*-*s*-*n* surfactants, it can be concluded that at the low concentrations herein used (2 mmol kg^{-1}, which lies between 2 and 10 times the *cmc* depending on surfactant), micelle size and shape do not vary meaningfully with spacer length, with the micelles remaining essentially spheroidal (implying also the strict validity of Henry's equation to calculate ζ [6]). Therefore, an explanation for the variation seen in Fig. 7 (a) cannot be found in changes of aggregate shape, but likely in the increasing charge-to-charge distance in the same gemini molecule and hence decreased charge density of the micellar surface, as the spacer becomes bigger (polymethylene spacers of $s \leq 12$ lie essentially stretched at the surface [65]). For the surfactant-coated MWNTs, Fig. 7(b), such variation is not observed. This suggests that the different gemini surfactants (i) *attach at the nanotube surface in a similar arrangement among them*, and (ii) *may do so not in the form of micelle-like aggregates but rather in an individually and randomly distributed way*. If so, this is in line with inferences made in previous work by us concerning the mode of adsorption of single-tailed surfactants on CNTs [11] and also consistent with molecular dynamics simulations by other groups on 12-*s*-12 gemini adsorbed on the surfaces of single-walled nanotubes [53] and graphene nanosheets [66].

(2) Since the same mass of MWNTs is present, and the analyzed dispersions correspond to the *plateau* (i.e. to the maximum dispersibility, under the set sonication/centrifugation conditions), the virtually constant value of ζ – potential in Fig. 7(b) reflects a similar eletrophoretic mobility of the charged particles and, as can be reasonably inferred, a constant surface charge density for the surfactant-coated MWNTs [6] irrespective of *s* or *n*. In turn, this implicitly suggests that the *attained surface charge density is at its maximum available value*. This inference is again consistent with our previous observations made on CNT dispersions—using a very different dispersant, a polymeric surfactant (F127), and NMR diffusion as probing technique—that pointed to a limiting surface coverage of dispersant at the plateau level [18,35].

The most dramatic and clear-cut effect demonstrated by our data is that $c_{s,max}$ (and, thereby, efficiency) reaches its minimum value at longest spacer lengths, i.e. for the *n*-12-*n* molecules. High spacer length provides, besides extra hydrophobicity, maximum conformational adaptability of the gemini molecule to the MWNT surface. Among the *n*-12-*n* surfactants, it is 12-12-12 (surprisingly yet rather clearly) that has the highest $c_{s,max}$ and not 16-12-16, the most hydrophobic molecule. We have recently presented evidence that the dispersant in solution (remaining after the sonication/centrifugation process) is more than one order of magnitude higher than what is needed to cover all freshly exposed surface of the dispersed CNTs created by sonication [35]. Based on that observation and related results (such as having a complete surface coverage in a wide range of dispersant concentration) we argued that the surfactant concentration required for dispersibility is primarily a demand related to *fast enough microscopic kinetics of dispersants transferring from their bulk solution into a surface-attached state*. If so, it could be that 12-12-12 molecules may transfer more quickly from bulk to freshly cleaved CNT surfaces than the other s = 12 gemini. We can hypothesize two reasons for this. First, having a very low *cmc* and thereby very low unimer concentration in the case of 14-12-14 and 16-12-16 (compared to 12-12-12) will limit the rate at which their respective unimers attach to the surface. Second, the adsorption of a long C16 tail to the CNT parallel to the surface [53] is expected to provide quite tight anchoring; however, the adsorption of the second tail and 12-carbon spacer of the same molecule may take comparatively longer time (than for 12-12-12) as they seek to adapt their conformation to the CNT surface due to a less-than-optimal tail/spacer relative size (and hence hydrophobicity).

3.5. Comparisons with previous work

With respect to the few previous studies on the dispersion of CNTs by gemini surfactants, our results present both similarities and clear contrasts. Wang *et al.* have used 12-6-12 and DTAB to disperse MWNTs [51], starting with a nanotube load of 2.0 mg mL^{-1}, and found that 12-6-12 disperses twice as much as DTAB for concentrations well below *cmc*. In contrast, here we do not find significant differences in effectiveness between DTAB and all the other gemini surfactants (effectiveness lying in the range of 20–30%), and, in fact, 12-6-12 disperses slightly worse than DTAB. In another study, Chen *et al.* investigated the thermal conductivity of MWNTs stabilized in water by 12-*s*-12, with s = 3, 4 and 6 and concluded that both dispersibility and conductivity were higher for short spacers [52]. Herein, and even though their range of *s* differs from ours, the effectiveness of spacer 6 (16%) is similar to that of 2 (17%), but a longer spacer like 12 disperses a bit more (22%) and, especially, it is much more efficient. Zheng *et al.* used imidazolium-based gemini to investigate the effect of tail length, concluding that [14-4-14im]Br_2 dispersed much more than [12-4-12im]Br_2 [54], and similar results were obtained with pyrrolidinium-based homologues [57]. We did not find comparable tail length effects. Interestingly, and as pointed out above, recent molecular dynamics simulation studies on the binding of 12-2-12 and 12-6-12 to SWNTs [53] and graphene nanosheets [66], at low surface coverage, showed no indication of micelle-like aggregates on the nanomaterial surface, and our results for MWNTs support the same molecular view.

4. Conclusions

In this work, by using rigorously controlled experimental procedure and statistical sampling, high quality dispersibility curves of MWNTs in water were obtained for 12-*s*-12, 14-*s*-14 and 16-*s*-16

gemini surfactants (s = 2, 6, 12 for the C12 and C14 tails; s = 2, 12 for the C16 tail) and their single-tailed homologues DTAB, TTAB and CTAB. This systematic analysis allowed to extract reliable quantitative metrics for each surfactant—namely the critical dispersibility concentration, *cdc;* the maximum dispersed CNT concentration, $c_{CNT,max}$, and the minimum surfactant concentration necessary to achieve it, $c_{s,max}$; the dispersibility effectiveness, η, and efficiency η^*. These results altogether provide then a sound basis for withdrawing trends, comparisons and molecular-level interpretations for the CNT/dispersants systems investigated, hence advancing the understanding of these systems in relation to previous work [51–57].

A first key finding is that the efficiency of gemini surfactants in dispersing MWNTs is clearly higher than that of single-tailed surfactants, though the effectiveness is similar. Secondly, comparing only the gemini compounds, while the effectiveness is basically insensitive to both spacer and tail variation, $c_{s,max}$ clearly decreases and the efficiency thereby increases as the spacer length increases. Therefore, the spacer length is deemed as the key structural feature for enhancing the dispersing performance of this family of compounds. Characterization by scanning electron microscopy demonstrate that gemini surfactants provide well-dispersed, individual tubes in water, an important requirement for practical purposes. Furthermore, the data allow to infer that for the initial process of dispersion (i.e. during sonication), whether the dispersant is in unimer or micellar form is not relevant for its dispersing ability. Finally, based on the zeta potential data herein obtained, we posit that the gemini dispersants adsorb at the MWNT surface similarly and in the form of randomly distributed molecules, and that this adsorption is primarily controlled by a kinetic demand (i.e. by how fast dispersant molecules transfer from the bulk to the adsorbed state).

In summary, the results herein presented provide an insight on the influence of the surfactant molecular structure on CNTs dispersibility and allow meaningful comparisons between families of dispersants. This approach can be extended to other types of dispersants and, concurrently, to various types of water-insoluble nanomaterials. The high efficiency values obtained by the n-12-n surfactants besides offering an interesting molecular picture also have practical implications for the search of high-performance dispersants, as ultimately one aims at achieving maximum MWNT dispersibility and individualization at the lowest possible dispersant concentration.

Acknowledgements

CIQUP acknowledges financial support from FEDER/COMPETE and FCT through projects NORTE-01-0145-FEDER-000028, UID/QUI/00081/2013 and POCI-01-0145-FEDER-006980; RMFF acknowledges a post-doctoral grant financed under these projects; BA acknowledges the PhD grant PD/BD/128129/2016 from FCT. IF thanks the Swedish Research Council VR for support.

Appendix A. Supplementary material

Fig. S1 (conductimetric curves for the determination of the *cmc* of the surfactants); Fig. S2 (SEM imaging characterization of MWNT dispersions). Table S1 (apparent extinction coefficients of MWNTs for the different surfactant dispersions); Table S2 (parameters obtained from the MWNT dispersibility curves); Table S3 (parameters for supernatant characterization); Table S4 (parameters obtained from the statistical analysis of the SEM micrographs); Table S5 (zeta potential measurements). Supplementary data to this article can be found online at https://doi.org/10.1016/j.jcis.2019.03.082.

References

[1] D.S. Hecht, L. Hu, G. Irvin, Emerging transparent electrodes based on thin films of carbon nanotubes, graphene, and metallic nanostructures, Adv. Mater. 23 (2011) 1482–1513.
[2] O. Breuer, U. Sundararaj, Big returns from small fibers: A review of polymer/carbon nanotube composites, Polym. Compos. 25 (2004) 630–645.
[3] O.V. Kharissova, B.I. Kharisov, E.G. de Casas Ortiz, Dispersion of carbon nanotubes in water and non-aqueous solvents, RSC Adv. 3 (2013) 24812–24852.
[4] T. Premkumar, R. Mezzenga, K.E. Geckeler, Carbon nanotubes in the liquid phase: addressing the issue of dispersion, Small 8 (2012) 1299–1313.
[5] L. Vaisman, H.D. Wagner, G. Marom, The role of surfactants in dispersion of carbon nanotubes, Adv. Colloid Interface Sci. 128 (2006) 37–46.
[6] Z. Sun, V. Nicolosi, D. Rickard, S.D. Bergin, D. Aherne, J.N. Coleman, Quantitative evaluation of surfactant-stabilized single-walled carbon nanotubes: Dispersion quality and its correlation with zeta potential, J. Phys. Chem. C 112 (2008) 10692–10699.
[7] H. Wang, Dispersing carbon nanotubes using surfactants, Curr. Opin. Colloid Interface Sci. 14 (2009) 364–371.
[8] M.D. Clark, S. Subramanian, R. Krishnamoorti, Understanding surfactant aided aqueous dispersion of multi-walled carbon nanotubes, J. Colloid Interface Sci. 354 (2011) 144–151.
[9] A.J. Blanch, C.E. Lenehan, J.S. Quinton, Parametric analysis of sonication and centrifugation variables for dispersion of single walled carbon nanotubes in aqueous solutions of sodium dodecylbenzene sulfonate, Carbon 49 (2011) 5213–5228.
[10] P. Angelikopoulos, H. Bock, The science of dispersing carbon nanotubes with surfactants, PCCP 14 (2012) 9546–9557.
[11] R.M.F. Fernandes, B. Abreu, B. Claro, M. Buzaglo, O. Regev, I. Furó, E.F. Marques, Dispersing carbon nanotubes with ionic surfactants under controlled conditions: comparisons and insight, Langmuir 31 (2015) 10955–10965.
[12] R.M.F. Fernandes, M. Buzaglo, O. Regev, I. Furó, E.F. Marques, Mechanical agitation induces counterintuitive aggregation of pre-dispersed carbon nanotubes, J. Colloid Interface Sci. 493 (2017) 398–404.
[13] N. Grossiord, J. Loos, O. Regev, C.E. Koning, Toolbox for dispersing carbon nanotubes into polymers to get conductive nanocomposites, Chem. Mater. 18 (2006) 1089–1099.
[14] R. Shvartzman-Cohen, M. Florent, D. Goldfarb, I. Szleifer, R. Yerushalmi-Rozen, Aggregation and self-assembly of amphiphilic block copolymers in aqueous dispersions of carbon nanotubes, Langmuir 24 (2008) 4625–4632.
[15] A.E. Frise, G. Pages, M. Shtein, I. Pri Bar, O. Regev, I. Furó, Polymer binding to carbon nanotubes in aqueous dispersions: residence time on the nanotube surface as obtained by NMR diffusometry, J. Phys. Chem. B 116 (2012) 2635–2642.
[16] K. Saint-Aubin, P. Poulin, H. Saadaoui, M. Maugey, C. Zakri, Dispersion and film-forming properties of poly(acrylic acid)-stabilized carbon nanotubes, Langmuir 25 (2009) 13206–13211.
[17] R.M.F. Fernandes, M. Buzaglo, M. Shtein, I. Pri Bar, O. Regev, E.F. Marques, I. Furó, Lateral diffusion of dispersing molecules on nanotubes as probed by NMR, J. Phys. Chem. C 118 (2014) 582–589.
[18] R.M.F. Fernandes, M. Buzaglo, O. Regev, E.F. Marques, I. Furó, Surface coverage and competitive adsorption on carbon nanotubes, J. Phys. Chem. C 119 (2015) 22190–22197.
[19] S. Badaire, C. Zakri, M. Maugey, A. Derre, J.N. Barisci, G. Wallace, P. Poulin, Liquid crystals of DNA-stabilized carbon nanotubes, Adv. Mater. 17 (2005) 1673–1676.
[20] F. Tardani, C. La Mesa, P. Poulin, M. Maugey, Phase behavior of DNA-based dispersions containing carbon nanotubes: effects of added polymers and ionic strength on excluded volume, J. Phys. Chem. C 116 (2012) 9888–9894.
[21] S.S. Karajanagi, H.C. Yang, P. Asuri, E. Sellitto, J.S. Dordick, R.S. Kane, Protein-assisted solubilization of single-walled carbon nanotubes, Langmuir 22 (2006) 1392–1395.
[22] E. Edri, O. Regev, "Shaken, not stable": dispersion mechanism and dynamics of protein-dispersed nanotubes studied via spectroscopy, Langmuir 25 (2009) 10459–10465.
[23] A.E. Frise, E. Edri, I. Furó, O. Regev, Protein dispersant binding on nanotubes studied by NMR self-diffusion and cryo-TEM techniques, J. Phys. Chem. Lett. 1 (2010) 1414–1419.
[24] D.W. Horn, K. Tracy, C.J. Easley, V.A. Davis, Lysozyme dispersed single-walled carbon nanotubes: interaction and activity, J. Phys. Chem. C 116 (2012) 10341–10348.
[25] F. Karchemsky, E. Drug, E. Mashiach-Farkash, L. Fadeev, H.J. Wolfson, M. Gozin, O. Regev, Diameter-selective dispersion of carbon nanotubes by beta-lactoglobulin whey protein, Colloids Surf. B 112 (2013) 16–22.
[26] H. Oh, J. Sim, S.Y. Ju, Binding affinities and thermodynamics of noncovalent functionalization of carbon nanotubes with surfactants, Langmuir 29 (2013) 11154–11162.
[27] F. Ernst, T. Heek, A. Setaro, R. Haag, S. Reich, Functional surfactants for carbon nanotubes: effects of design, J. Phys. Chem. C 117 (2013) 1157–1162.
[28] A. Di Crescenzo, S. Cambre, R. Germani, P. Di Profio, A. Fontana, Dispersion of SWCNTs with imidazolium-rich surfactants, Langmuir 30 (2014) 3979–3987.
[29] K.G. Dassios, P. Alafogianni, S.K. Antiohos, C. Leptokaridis, N.-M. Barkoula, T.E. Matikas, Optimization of sonication parameters for homogeneous surfactant-assisted dispersion of multiwalled carbon nanotubes in aqueous solutions, J. Phys. Chem. C 119 (2015) 7506–7516.

[30] N. Grossiord, O. Regev, J. Loos, J. Meuldijk, C.E. Koning, Time-dependent study of the exfoliation process of carbon nanotubes in aqueous dispersions by using UV-visible spectroscopy, Anal. Chem. 77 (2005) 5135–5139.
[31] W.H. Duan, Q. Wang, F. Collins, Dispersion of carbon nanotubes with SDS surfactants: a study from a binding energy perspective, Chem. Sci. 2 (2011) 1407–1413.
[32] C. Richard, F. Balavoine, P. Schultz, T.W. Ebbesen, C. Mioskowski, Supramolecular self-assembly of lipid derivatives on carbon nanotubes, Science 300 (2003) 775–778.
[33] E. Nativ-Roth, R.J. Nap, I. Szleifer, R. Yerushalmi-Rozen, Order-disorder transition induced by surfactant micelles in single-walled carbon nanotubes dispersions, Soft Matter 6 (2010) 5289–5292.
[34] N. Poorgholami-Bejarpasi, B. Sohrabi, Self-assembly of cationic surfactants on the carbon nanotube surface: insights from molecular dynamics simulations, J. Mol. Model. 19 (2013) 4319–4335.
[35] J. Dai, R.M.F. Fernandes, O. Regev, E.F. Marques, I. Furó, Dispersing Carbon Nanotubes in Water with Amphiphiles: dispersant adsorption, kinetics, and bundle size distribution as defining factors, J. Phys. Chem. C 122 (2018) 24386–24393.
[36] Y.Y. Huang, E.M. Terentjev, Dispersion of carbon nanotubes: mixing, sonication, stabilization, and composite properties, Polymers 4 (2012) 275–295.
[37] F.M. Menger, J.S. Keiper, Gemini surfactants, Angew. Chem. Int. Ed. 39 (2000) 1906–1920.
[38] R. Zana, Dimeric and oligomeric surfactants. Behavior at interfaces and in aqueous solution: A review, Adv. Colloid Interface Sci. 97 (2002) 205–253.
[39] E.O. Alami, K. Holmberg, Heterogemini surfactants, Adv. Colloid Interface Sci. 100 (2003) 13–46.
[40] D. Berthier, T. Buffeteau, J.M. Leger, R. Oda, I. Huc, From chiral counterions to twisted membranes, J. Am. Chem. Soc. 124 (2002) 13486–13494.
[41] S.G. Silva, C. Alves, A.M.S. Cardoso, A.S. Jurado, M.C. Pedroso De Lima, M.L.C. Vale, E.F. Marques, Synthesis of gemini surfactants and evaluation of their interfacial and cytotoxic properties: Exploring the multifunctionality of serine as headgroup, Eur. J. Org. Chem. (2013) 1758–1769.
[42] J.A.S. Almeida, S.P.R. Pinto, Y. Wang, E.F. Marques, A.A.C.C. Pais, Structure and order of DODAB bilayers modulated by dicationic gemini surfactants, PCCP 13 (2011) 13772–13782.
[43] R.M.F. Fernandes, Y.J. Wang, P.B. Tavares, S.C.C. Nunes, A. Pais, E.F. Marques, Critical role of the spacer length of gemini surfactants on the formation of ionic liquid crystals and thermotropic behavior, J. Phys. Chem. B 121 (2017) 10583–10592.
[44] H.D. Burrows, M.J. Tapia, C.L. Silva, A.A.C.C. Pais, S.M. Fonseca, J. Pina, J.S. de Melo, Y. Wang, E.F. Marques, M. Knaapila, A.P. Monkman, V.M. Garamus, S. Pradhan, U. Scherf, Interplay of electrostatic and hydrophobic effects with binding of cationic gemini surfactants and a conjugated polyanion: Experimental and molecular modeling studies, J. Phys. Chem. B 111 (2007) 4401–4410.
[45] S. Datta, J. Biswas, S. Bhattacharya, How does spacer length of imidazolium gemini surfactants control the fabrication of 2D-Langmuir films of silver-nanoparticles at the air-water interface?, J Colloid Interface Sci. 430 (2014) 85–92.
[46] R. Oda, I. Huc, S.J. Candau, Gemini surfactants as new, low molecular weight gelators of organic solvents and water, Angew. Chem. Int. Ed. 37 (1998) 2689–2691.
[47] S.D. Wettig, R.E. Verrall, M. Foldvari, Gemini surfactants: A new family of building blocks for non-viral gene delivery systems, Curr. Gene Ther. 8 (2008) 9–23.
[48] L. Mivehi, R. Bordes, K. Holmberg, Adsorption of cationic gemini surfactants at solid surfaces studied by QCM-D and SPR: effect of the rigidity of the spacer, Langmuir 27 (2011) 7549–7557.
[49] A.M. Cardoso, C.M. Morais, S.G. Silva, E.F. Marques, M.C. Pedroso de Lima, M.A. S. Jurado, Bis-quaternary gemini surfactants as components of nonviral gene delivery systems: A comprehensive study from physicochemical properties to membrane interactions, Int. J. Pharm. 474 (2014) 57–69.
[50] A.R. Tehrani-Bagha, K. Holmberg, C.G. van Ginkel, M. Kean, Cationic gemini surfactants with cleavable spacer: chemical hydrolysis, biodegradation, and toxicity, J. Colloid Interface Sci. 449 (2015) 72–79.
[51] Q. Wang, Y. Han, Y. Wang, Y. Qin, Z.-X. Guo, Effect of surfactant structure on the stability of carbon nanotubes in aqueous solution, J. Phys. Chem. B 112 (2008) 7227–7233.
[52] L. Chen, H. Xie, Y. Li, W. Yu, Applications of cationic gemini surfactant in preparing multi-walled carbon nanotube contained nanofluids, Colloids Surf. A 330 (2008) 176–179.
[53] N. Poorgholami-Bejarpasi, B. Sohrabi, Role of surfactant structure in aqueous dispersions of carbon nanotubes, Fluid Phase Equilib. 394 (2015) 19–28.
[54] Y. Liu, L. Yu, S. Zhang, J. Yuan, L. Shi, L. Zheng, Dispersion of multiwalled carbon nanotubes by ionic liquid-type Gemini imidazolium surfactants in aqueous solution, Colloids Surf. A 359 (2010) 66–70.
[55] A. Di Crescenzo, R. Germani, E. Del Canto, S. Giordani, G. Savelli, A. Fontana, Effect of surfactant structure on carbon nanotube sidewall adsorption, Eur. J. Org. Chem. (2011) 5641–5648.
[56] H. Xie, L. Chen, Review on the preparation and thermal performances of carbon nanotube contained nanofluids, J. Chem. Eng. Data 56 (2011) 1030–1041.
[57] S. Zhang, F. Lu, L. Zheng, Dispersion of multiwalled carbon nanotubes (MWCNTs) by ionic liquid-based Gemini pyrrolidinium surfactants in aqueous solution, Colloid Polym. Sci. 289 (2011) 1815–1819.
[58] J.T. Hou, W.B. Du, F.J. Meng, C.C. Zhao, X. Du, Effective dispersion of multi-walled carbon nanotubes in aqueous solution using an ionic-gemini dispersant, J. Colloid Interface Sci. 512 (2018) 750–757.
[59] G. Sun, G. Chen, J. Liu, J. Yang, J. Xie, Z. Liu, R. Li, X. Li, A facile gemini surfactant-improved dispersion of carbon nanotubes in polystyrene, Polym. 50 (2009) 5787–5793.
[60] K. Holmberg, B. Jönsson, B. Kronberg, B. Lindman, Surfactant and Polymers in Aqueous Solution, John Wiley & Sons, Chichester, 2002.
[61] M. Shtein, I. Pri-bar, O. Regev, A simple solution for the determination of pristine carbon nanotube concentration, Analyst 138 (2013) 1490–1496.
[62] B. White, S. Banerjee, S. O'Brien, N.J. Turro, I.P. Herman, Zeta-potential measurements of surfactant-wrapped individual single-walled carbon nanotubes, J. Phys. Chem. C 111 (2007) 13684–13690.
[63] R.M.F. Fernandes, J. Dai, O. Regev, E.F. Marques, I. Furó, Block copolymers as dispersants for single-walled carbon nanotubes: modes of surface attachment and role of block polydispersity, Langmuir 34 (2018) 13672–13679.
[64] V. Sa, K.G. Kornev, Analysis of stability of nanotube dispersions using surface tension isotherms, Langmuir 27 (2011) 13451–13460.
[65] D. Danino, Y. Talmon, R. Zana, Alkanediyl-alpha,omega-bis (dimethylalkylammonium bromide) surfactants (dimeric surfactants). 5. Aggregation and microstructure in aqueous-solutions, Langmuir 11 (1995) 1448–1456.
[66] M. Poorsargol, B. Sohrabi, M. Dehestani, Study of the gemini surfactants' self-assembly on graphene nanosheets: insights from molecular dynamics simulation, J. Phys. Chem. A 122 (2018) 3873–3885.

Supplementary Data

Gemini surfactants as efficient dispersants of multiwalled carbon nanotubes: interplay of molecular parameters on nanotube dispersibility and debundling

B. Abreu, J. Rocha, R. M. F. Fernandes, O. Regev, I. Furó and E. F. Marques

1. Determination of the critical micelle concentration of the surfactants

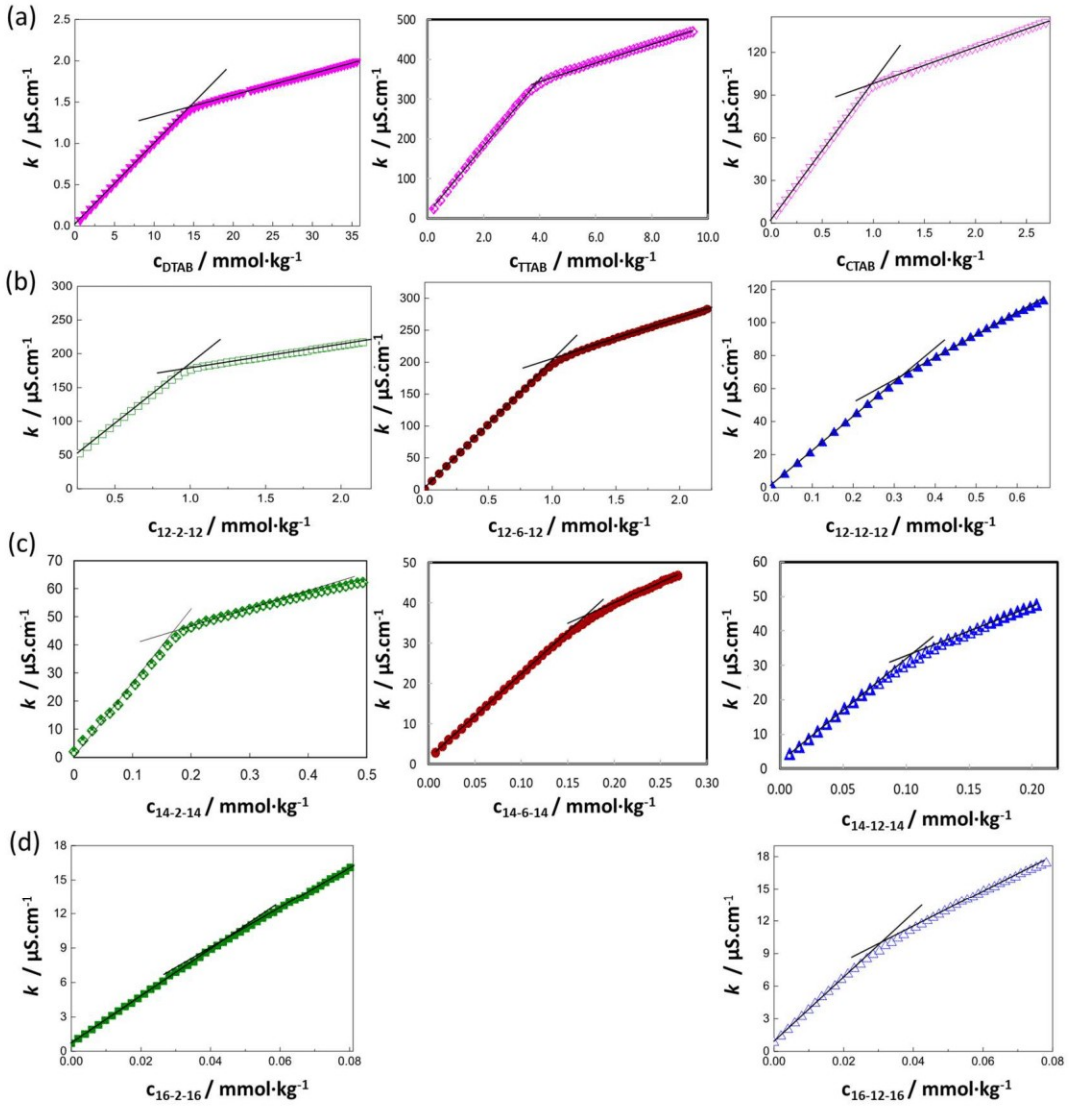

Fig. S1 – Conductivity plots of: (a) DTAB, TTAB and CTAB; (b) 12-*s*-12, (c) 14-*s*-14, and (d) 16-*s*-16 gemini surfactants. The obtained *cmc* values (intersection points of linear fits) are shown in Table S2.

2. Apparent extinction coefficients for c_{MWNT} quantification

Table S1. Apparent extinction coefficients, ε_{660}, of MWNTs for the different surfactants as obtained from the linear dependence of the apparent absorbance on MWNT concentration.

Surfactant	ε_{660}[(1)] / **mL·mg^{-1}·cm^{-1}**
12-2-12	39
12-6-12	43
12-12-12	41
14-2-14	38
14-6-14	39
14-12-14	38
16-2-16	41
16-12-16	42
DTAB	39
TTAB	40
CTAB	42
mean ± s.d.	40 ± 2

[(1)]The typical uncertainty of each value is ± 2%.

3. Characteristic parameters for the dispersibility curves

Table S2. Values of the dispersibility parameters obtained from the curves in Fig. 3 through the fitting procedure depicted in Fig. 2. Each point in the curves is the average value obtained for at least five independent dispersions. The estimated errors of the parameters are the following: for *cdc* and $c_{s,max}$, ca ± 20% (they depend strongly on the availability of enough and clearly assignable points in the quickly ascending parts of the respective dispersibility curves); for $c_{CNT,max}$, ca. ± 10%; for η, ca. ± 15% and η^*, ca. ± 20%. The surfactant *cmc* values obtained from conductivity (Fig. S1) are within an error of ± 5%, based on three independents curves.

Surfactant	***cmc*[(1),(2)]**	***cdc*[(1)]**	**$c_{s,max}$[(1)]**	**$c_{CNT,max}$ / mg·mL^{-1}**	**η / %**	**η^* / (%·kg·mmol^{-1})**
12-2-12	0.95 (0.58)	0.63 (0.39)	1.4 (0.86)	0.44	15	11
12-6-12	1.0 (0.69)	0.14 (0.094)	1.2 (0.80)	0.52	17	15
12-12-12	0.35 (0.26)	0.16 (0.12)	0.30 (0.23)	0.67	22	74
14-2-14	0.19 (0.13)	0.54 (0.36)	1.0 (0.67)	0.86	29	28
14-6-14	0.17 (0.12)	0.053 (0.036)	0.76 (0.55)	0.87	29	38
14-12-14	0.11 (0.085)	0.072 (0.058)	0.59 (0.48)	0.93	31	53
16-2-16	0.040 (0.029)	0.44 (0.32)	1.1 (0.80)	0.88	29	28
16-12-16	0.032 (0.029)	0.093 (0.078)	0.42 (0.36)	0.66	22	52
DTAB	14 (4.3)	8.2 (2.5)	17 (5.2)	0.61	20	1.2
TTAB	3.9 (1.3)	0.89 (0.30)	4.5 (1.5)	0.90	30	6.7
CTAB	0.97 (0.35)	0.89 (0.32)	2.3 (0.84)	0.90	30	13

[(1)]Values in mmol·kg^{-1} (top) and in mg·mL^{-1} (in parentheses).

[(2)]The Krafft temperatures are (approx. values): 12-2-12, 15 ºC; 12-6-12, < 0 ºC; 12-12-12, 14 ºC; 14-2-14, 32 ºC; 14-6-14, 8 ºC; 14-12-14, < 20 ºC; 16-2-16, 45 ºC; 16-12-16, 14 ºC; DTAB, < 0 ºC; TTAB, 13 ºC; CTAB, 26 ºC.

Definition of parameters: *cdc,* critical dispersibility concentration, the initial concentration of surfactant needed for dispersibility to take off; $c_{s,max}$, the minimum surfactant concentration at which the maximum value of dispersed c_{MWNT}, denoted as $c_{CNT,max}$, is attained; effectiveness η, the ratio $c_{MWNT,max}/c_{MWNT,initial}$ x 100 (herein, $c_{MWNT,initial}$ = 3 mg·mL^{-1}); and efficiency η^*, the ratio $\eta/c_{s,max}$, expressed in units of %·kg·mmol^{-1}.

Table S3. Parameters for the supernatant characterization: TGA mass loss fraction of dry supernatant (Φ_s) and neat surfactant (Φ_d), c_{MWNT} in the supernatant, surfactant concentration in the supernatant before ($c_{s,\,initial}$) and after ($c_{s,\,final}$) centrifugation, and fraction of surfactant lost to the precipitate (Δc_s).

Surfactant	Φ_s	Φ_d	$c_{MWNT,\,supernatant}$ / mg·mL^{-1}	$c_{s,\,initial}$ / mg·mL^{-1}	$c_{s,\,final}$ / mg·mL^{-1}	Δc_s[(1)] / %
12-2-12	0.73	0.97	0.61	3.0	1.8	40
12-6-12	0.89	0.97	0.57	7.0	6.0	14
12-12-12	0.43	0.93	0.73	1.0	0.6	40
14-2-14	0.57	0.98	0.75	1.5	1.0	33
14-6-14	0.71	0.99	0.79	2.4	2.0	17
14-12-14	0.59	0.97	0.79	1.7	1.2	29
16-2-16	0.48	0.96	0.71	1.3	0.7	46
16-12-16	0.69	0.98	0.57	2.3	2.0	13
DTAB	0.92	1.0	0.80	14.0	8.5	39
TTAB	0.88	0.99	1.43	13.1	9.4	28
CTAB	0.81	1.0	0.67	3.6	2.8	22

[(1)] $\Delta c_s = (c_{s,initial} - c_{s,final}) / c_{s,initial}$.

The fraction of surfactant lost to the precipitate is rather significant and of the order of (30 ± 10) %.

4. SEM characterization of the dispersions

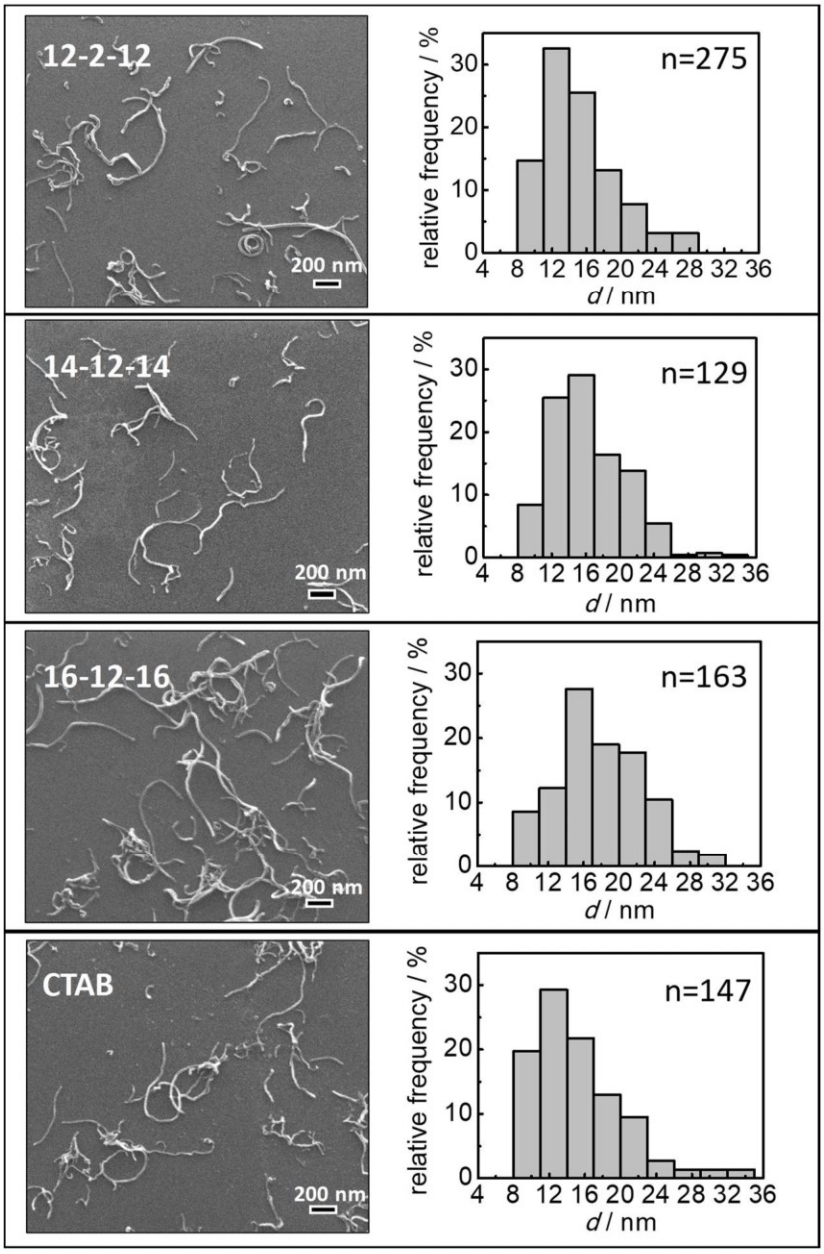

Fig. S2. SEM imaging characterization of MWNT and the respective histograms with CNT/bundle diameters distributions dispersed by the double-tailed gemini surfactants 12-2-12, 14-12-14 and 16-12-16, and single-tailed CTAB.

Table S4. Parameters obtained from the fitting of a log-normal distribution to the CNTs diameter, based on SEM micrographs: median, d; width of log-normal distribution, w; the mean diameter $\langle d \rangle$ obtained by $\langle d \rangle = d \exp(w^2/2)$.

surfactant	d_{median} / nm	w	$\langle d \rangle$/ nm
CTAB	14	0.32	15
12-12-12	16	0.36	17
14-12-14	14	0.24	14
16-2-16	14	0.35	15
16-12-16	18	0.26	18

5. Zeta potential measurements

For these measurements, because the curves in Fig.3 show that the dispersed c_{MWNT} varies differently with c_s for different surfactants, a careful procedure was followed. All dispersions were prepared in the usual manner using c_s = 2 mmol·kg^{-1} which yielded different c_{MWNT} values between surfactants, but all above 0.1 mg·mL^{-1} (Figure 3); then, the samples were diluted with its respective neat surfactant solution (c_s = 2 mmol·kg^{-1}) to the final desired c_{MWNT} (0.1 mg·mL^{-1}). The zeta potential for F127-coated MWNTs was also measured as a baseline value (yielding – 11 mV).

Table S5. ζ-potential values for neat surfactant micelles and for surfactant-assisted MWNT dispersions with c_{MWNT} = 0.1 mg·mL^{-1} and c_s = 2 mmol·kg^{-1} for all gemini surfactants (for F127 the concentration was c_{F127} = 3 mg·mL^{-1}). Observed distributions are unimodal and meet quality criteria; typical uncertainties in ζ-potential are ± 5 % (5 runs on average).

surfactant	ζ / mV	
	neat micelles	MWNT/surfactant dispersions
F-127	not measurable	– 11
12-2-12	+48	+54
12-6-12	+49	+52
12-12-12	+33	+60
14-2-14	+63	+59
14-6-14	+45	+60
14-12-14	+44	+60
16-2-16	+55	+58
16-12-16	+35	+63

II

Comparative trends and molecular analysis on the surfactant-assisted dispersibility of 1D and 2D carbon materials: multiwalled nanotubes vs graphene nanoplatelets

Comparative trends and molecular analysis on the surfactant-assisted dispersibility of 1D and 2D carbon materials: multiwalled nanotubes vs graphene nanoplatelets

Bárbara Abreu[1], Jorge Montero[1], Matat Buzaglo[2], Oren Regev[2,3] and Eduardo F. Marques[1*]

[1]CIQUP - Departamento de Química e Bioquímica, Faculdade de Ciências, Universidade do Porto, Rua do Campo Alegre P-4169-007 Porto, Portugal.

[2]Department of Chemical Engineering and [3]Ilse Katz Institute for Nanotechnology, Ben-Gurion University of the Negev, 84105 Beer-Sheva, Israel.

*email: efmarque@fc.up.pt

Keywords:

Nanocarbon; multiwalled carbon nanotubes; graphene nanoplatelets; surfactant; dispersion; liquid-phase exfoliation; non-covalent functionalization

Abstract

Most applications of nanocarbons, such as carbon nanotubes and graphene, require that they are well-separated and well-dispersed in a liquid phase. Intensive efforts have been put on exfoliating and dispersing nanocarbons in aqueous solvents, typically using amphiphilic dispersants and sonication/centrifugation procedures, alongside a drive to fundamentally understand and rationally optimize these processes. Herein, we employed a robust method to separate and disperse multiwalled carbon nanotubes (MWNTs), and graphene nanoplatelets (GnPs) either from bulk graphite or from pre-formed GnP powders, using rigorously controlled processing conditions. An ionic (sodium cholate) and a nonionic (Triton X-100) surfactant were used as dispersants. Our aim was to determine high-precision dispersibility curves (concentration of dispersed nanomaterial versus initial surfactant concentration) for the different nanocarbon/dispersant systems, characterize morphologically the dispersed particles and compare the mechanisms of exfoliation of 1D and 2D nanocarbons at molecular level. Typically bell-shaped dispersibility curves with a plateau were obtained and from the latter, several quantitative metrics were extracted that permitted reliable comparisons between nanocarbon/surfactant systems. Scanning electron and atomic force microscopies allowed to characterize the suspended particles in as-obtained dispersions, namely the MWNT bundle width and GnP dimensions (mean lateral size and layer number). Under fixed conditions (in particular, delivered energy per carbon mass), MWNTs are dispersed in much higher yields, by two orders of magnitude, than GnPs. However, and significantly, a master curve for the dispersibility was obtained, implying that common fundamental features underpin the dispersal process, irrespective of nanocarbon (1D or 2D) or surfactant (ionic or nonionic) types.

1. Introduction

New allotropic forms of carbon, in particular 1D carbon nanotubes (CNTs) and 2D graphene have been at the forefront of nanotechnology during the last years, especially due to their novel and unique electrical, mechanical, thermal and optical properties.[1-6] For the majority of applications (e.g. composites, catalysis and electronics), obtaining aqueous dispersions of individualized carbon nanotubes (CNTs) or few-layer graphene (FLG) is of great practical interest.[1-3, 7-9] A common approach is liquid-phase exfoliation of the carbon materials, like exfoliation in water of CNTs or graphite using amphiphilic dispersants (namely surfactants[10-17] or polymers[18-22], including proteins[23, 24]), and sonication-centrifugation procedures. Three stages can be broadly distinguished in the amphiphile-assisted dispersing process: exfoliation, adsorption and stabilization. The first consists in the mechanical separation (typically using sonication, either bath or tip, or ball milling) of the tubes or 2D sheets from their respective bulk reservoirs. The second entails amphiphile binding via essentially hydrophobic interactions in the as-exposed carbon surface. Finally, after a centrifugation step that removes the larger undispersed particles, the smaller ones remain in suspension stabilized by steric or electrostatic repulsions that provide a kinetic barrier to reaggregation. Hence, in the end, kinetically (not thermodynamically) stabilized suspensions of the nanocarbons are produced.

For CNTs, exfoliation of individual nanotubes from their bundles by a surfactant is thought to occur through an ‘unzipping’ mechanism, whereby the energy source produces clefts between adjacent nanotubes at the end of a bundle, allowing surfactant molecules to adsorb onto the newly exposed surface.[25-28] Surfactant adsorption propagates along the fissure, eventually splitting the bundle or separating an individual nanotube from the aggregate. Graphene nanoplatelets (GnPs), with as few layers as possible, can be obtained from similar unzipping mechanisms, by the top-down exfoliation of graphite into GnPs rather than the bottom-up growth of single graphene films (which requires intensive synthetic efforts and challenging scale-up process).[29, 30] Indeed, despite that bottom-up processes produce un-matched electronic quality and uniformity of graphene, they also yield smaller amount of material at a much higher energy-cost compared to bottom-up exfoliation.[27, 31] Exfoliation of graphite into a GnP dispersion can be induced by either chemical or physical forces to overcome the van der Waals forces holding the graphene layers in solid graphite. Chemical exfoliation could be also based on oxidation of graphite and dissolution of graphene-oxide (GO),[31] while physical exfoliation is driven by energy injection, e.g. sonication,[27] high shear mixing[32] or ball milling.[33] The latter processes, as mentioned above, unzip the graphene layers

beyond the short van der Waals distance, filling the gaps with adsorbed surfactant and solvent molecules, eventually leading to their detachment and dispersion as single to few-layer graphene.[27, 34]

Few studies have recently explored the nanocarbon dispersibility, i.e., the dispersed concentration as a function of surfactant concentration,[13, 35-41] showing that it reaches a maximum at an optimum surfactant concentration; beyond that point, the dispersibility typically decreases significantly. However, most of the dispersibility curves reported lack in profile detail and sufficient precision, e.g. lacking in indication of reproducibility or providing no error bars for the data. To address this problem, in this work we developed high-precision dispersibility curves for MWNTs and GnPs using two surfactants, sodium cholate (SC) and Triton™ X-100 (TX-100), shown in Fig. 1. SC is an anionic surfactant (a bile acid salt), with a hydrophobic region consisting of a rigid cholic acid ring system (with the three OH groups facing the same side of the ring) and a carboxylate headgroup. TX-100 is a nonionic surfactant with a hydrophobic section composed of a short alkyl tail plus a benzene ring, and a bulky hydrophilic headgroup with several oxyethylene moieties. These surfactants were selected because they are deemed as good dispersants of carbon nanomaterials,[42, 43] and because they differ in molecular properties, namely headgroup charge, and flexibility/rigidity of the hydrophobic section, allowing thus for interesting comparisons to be made. Three types of starting materials were studied: MWNTs, graphite, and commercially available graphene nanoplatelets (designated herein as cGNPs). This allows insight on the features that lead to the separation and dispersal of carbon nanomaterials either from their aggregated forms (powders of entangled MWNT or stacked cGNPs) or from a crystalline bulk reservoir (graphite). The processing sonication/centrifugation conditions for exfoliating and dispersing these nanocarbons were carefully controlled and the total energy delivered per mass of nanocarbon was selected as a fixed parameter (≈ 0.20 $kJ \cdot mg^{-1}$) for all systems to provide comparisons.

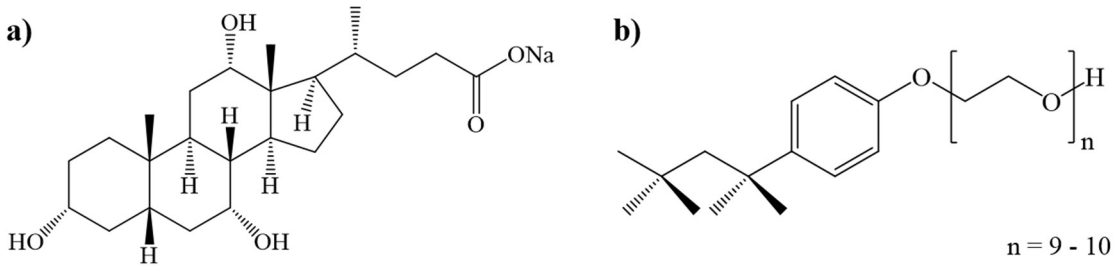

Fig. 1. Chemical structure of the surfactants used in this work: a) anionic surfactant sodium cholate (SC); b) nonionic surfactant Triton X-100 (TX100).

As will be shown, the initial sigmoidal profile of the obtained dispersibility curves (concentration of dispersed nanocarbon vs. surfactant concentration) permits us to extract quantitative parameters such as the maximum concentration of dispersed nanocarbon ($c_{nc,max}$), the surfactant concentration needed to achieve that value ($c_{s,max}$), and the effectiveness and efficiency of the dispersing process. Significantly, it also allows us to present a type of dispersibility master curve, that highlights some common features of the dispersing process irrespective of carbon source and surfactant used. Structural characterization of the as-obtained dispersions is also presented based on SEM, AFM and Raman data. Finally, an overall qualitative molecular-level discussion of the results is put forth.

2. Experimental Section

2.1 Materials and sample preparation

Multiwalled carbon nanotubes (from Cheaptubes, d = 8 -15 nm and length L = 10 - 50 μm), commercial graphene nanoplatelets (from xGnP® Graphene Nanoplatelets Grade M-5, xGSciences) and graphite flakes (from Sigma Aldrich) were used as received. The surfactants sodium cholate hydrate (> 99%) and Triton™ X-100, t-octylphenoxypolyethoxyethanol were purchased from Sigma-Aldrich and used as obtained.

Sample preparation combines tip sonication and centrifugation.[13, 17] The carbon source powder (9.0 mg for MWNTs and cGnPs, and 100.0 mg for graphite) was added to the desired surfactant aqueous solution yielding an initial loading concentration of 3.0 mg·mL^{-1} for MWNTs and cGnPs, and 10.0 mg·mL^{-1} for graphite suspensions. These mixtures were tip-sonicated using a Bandelin Sonoplus Vb 2070 Ultrasonic Homogenizer with a 3 mm probe (70 W, 20 kHz), at 25-30% amplitude, in water bath circulation yielding a constant energy delivered per carbon mass of ≈ 0.20 kJ·mg^{-1}. After sonication, the dispersions were centrifuged (Centurion Scientific Centrifuge Model K241R) and the top 30% of the supernatant was carefully removed. The sonication and centrifugation parameters for dispersing the MWNTs, graphite, and cGnPs are provided in detail in Table S1, in the Supplementary Data file.

2.2 Quantification of CNT and graphene concentration

A previously published method was applied to determine the absolute carbon nanomaterial concentration in the supernatant.[44] To quantify the mass fraction of surfactant present on the solid, thermogravimetric analysis (TGA) was performed in a

Hitachi STA7200RV equipment, under N_2 atmosphere (flow rate of 200 mL·min^{-1}). Calibration curves from TGA and UV-Vis spectroscopy were then obtained, using dilutions from a stock dispersion with known nanomaterial mass concentration, by measuring UV absorbance versus concentration of nanocarbon. A single-beam UV spectrophotometer Agilent 8453 operating at λ = 660 nm (to eliminate the contribution from surfactant absorption) was used.[45, 46] Application of the Beer-Lambert law allowed to determine the apparent extinction coefficient, ε, for the different systems, which yielded a value of 40 mL·mg^{1}·cm^{-1} for MWNTs and 31 mL·mg^{1}·cm^{-1} for graphene systems, in line with previous reports.[13, 17, 25, 27]

2.3 Dispersibility curves

The dispersibility curves for all nanocarbons studied here show a bell-shape profile (Fig. 2), with an initial sigmoidal shape and a plateau level (stages I-III), similar to those previously obtained for both single and multiwalled carbon nanotubes dispersed by common single-tailed surfactants.[13] After the *plateau,* the dispersibility decreases with further added surfactant (stage IV). Appropriate statistical metrics can be withdrawn from the sigmoidal part of the curve until the plateau: *cdc,* the critical dispersibility concentration, i.e. the concentration of surfactant needed for the dispersibility to take off; $c_{nc,max}$, the maximum concentration of dispersed nanocarbon attained; $c_{s,max}$, the surfactant concentration at which $c_{nc,max}$ is attained. For comparative purposes, the dispersibility effectiveness, η, and efficiency, η^* are also introduced. The effectiveness is given by the ratio ($c_{nc,max}/c_{nc,initial}$) x 100 and is thus a measure of the ability of the surfactant to disperse nanomaterial with respect to its initial loading. The efficiency, η^*, is defined as $\eta/c_{s,max}$ and is a measure of the capacity of the surfactant to disperse vs its concentration used, and is expressed in units of %·kg·mmol^{-1}; hence, for a highly efficient dispersant, maximal dispersibility (high η) is attained at the lowest possible $c_{s,max}$.

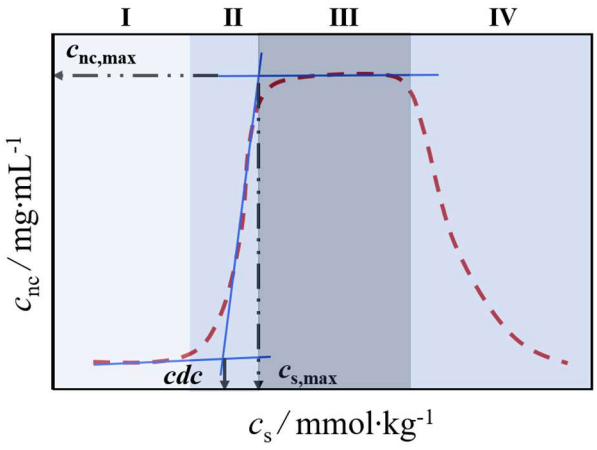

Fig. 2. Representative dispersibility curve with the definition of the metrics herein used: *cdc,* critical dispersibility concentration; $c_{nc,max}$, maximum concentration of dispersed nanocarbon i; $c_{s,max}$, surfactant concentration at which $c_{nc,max}$ is attained.

2.4 Characterization of dispersed nanocarbon

The surface morphology and dimensions (i.e., diameter, *d*, of tubes and mean lateral dimension, *MLD*, of graphene particles) of the dispersed materials were determined using SEM and AFM. Both the SEM and AFM samples were prepared by drop casting 10 µL of the supernatant on a pre-heated silicon wafer (111) at 100 °C. The wafers were then rinsed in ethanol to remove the excess surfactant. MWNT dispersions were previously diluted by a factor of 100.

SEM images were obtained on a FEI Quanta 400FE microscope, with an acceleration voltage of 25 kV, and SE detector. The distributions of diameter, *d,* for MWNTs and mean lateral dimension, *MLD,* for GnPs were recorded (for a number of particles, $n > 200$). Log normal distributions were obtained and average values, $\bar{d}$ and $\overline{MLD}$, and other statistical data were extracted. It should be noted that only the apparently individualized CNTs (small bundles are essentially impossible to distinguish from individual objects) were measured in the SEM images. Tapping mode AFM was performed on each sample, with a Veeco Multimode Nanoscope IV, under ambient conditions with RTESP silicon tip. For the GnPs, the height and *MLD* of each flake were measured and correlated.

The zeta potential, ζ, of the dispersed particles was measured at 25 ºC using a Malvern Nano ZS, ZN 3500, with a 4 mW He-Ne laser (633 nm) and DTS 1060C disposable zeta cells. The electrophoretic mobility, μ, was measured using a combination of electrophoresis and laser Doppler velocimetry techniques and ζ was calculated from μ using the known Henry equation. A dielectric constant of 78.5, a medium viscosity of

0.89 cP and a $f(\kappa a)$ function value of 1.5 were used, following previously reported assumptions, namely that tube-tube interactions are negligible.[47, 48] All ζ values are average values based on at least 3 independent dispersions.

Raman spectra of the GnP aqueous dispersions were recorded on a LabRam HR800 model of Jobin-Yvon Horiba spectrometer using a He-Ne laser at 514 nm on quartz cuvette, at room temperature, for an accumulation time of 120 s.

3. Results and Discussion

3.1 General features of the dispersibility curves

The surfactant molecular structure is an important parameter in the exfoliation and dispersal of carbon nanomaterials, alongside with the experimental conditions used in processing the materials (namely sonication energy, centrifugation rpm and time, and initial dispersant concentration).[25, 40] For the obtained dispersibility curves shown in Fig. 3 a)-c), and as detailed in the experimental section, the processing conditions and reproducibility were carefully controlled and this allows some reliable comparisons to be made.

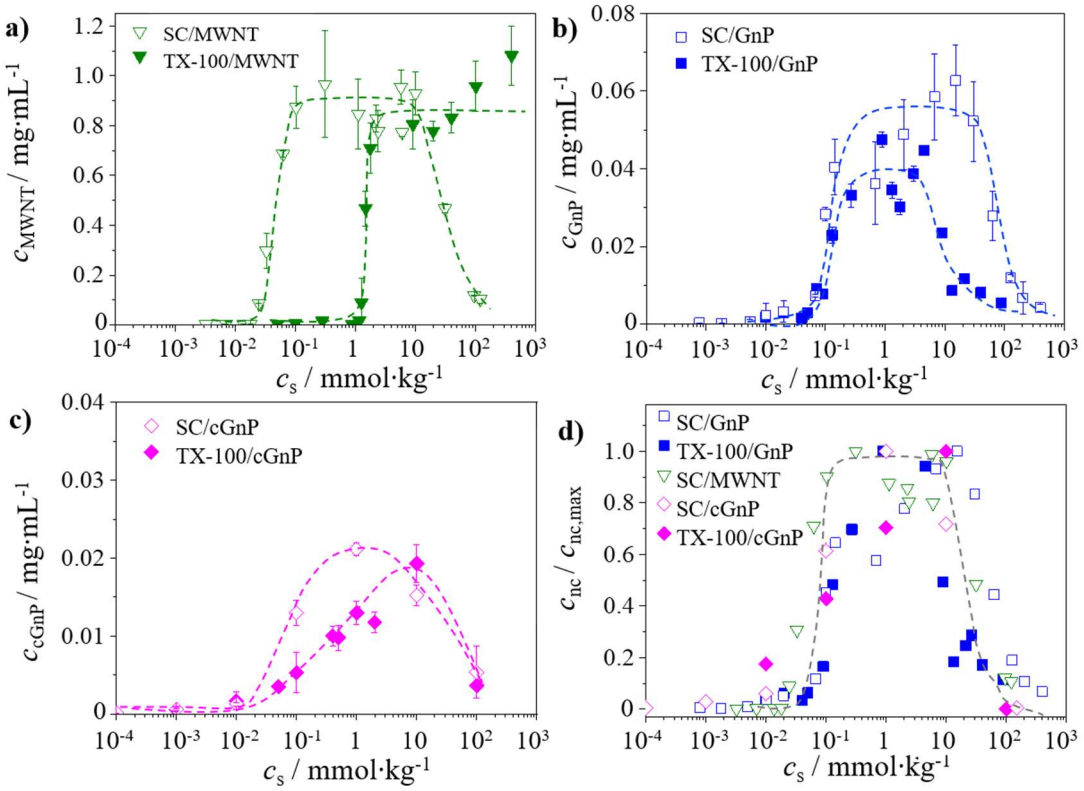

Fig. 3. Concentration of dispersed nanocarbon vs. surfactant concentration (in log scale to enhance features at low c_s) for the different surfactants. a) MWNT b) GnP c) cGNP and d) master curve. Lines are for visual guidance. Initial carbon material concentration was 3.0 mg·mL^{-1} for MWNTs and cGnPs, and 10.0 mg·mL^{-1} for graphite suspensions.

Table 1. Parameters obtained from the dispersibility curves for MWNTs, GnPs and cGnP using surfactants sodium cholate (SC) and TX-100.[a)]

Dispersibility parameter	SC/ MWNT	TX-100/ MWNT	SC/ GnP	TX-100/ GnP	SC/ cGnP	TX-100/ cGnP
$c_{nc,max}$ / mg·mL^{-1}	0.91	0. 77	0.055	0.036	0.017	0.012
cdc / mmol·kg^{-1}	0.017	1.2	0.024	0.047	0.005	0.028
$c_{s,max}$ / mmol·kg^{-1}	0.077	1.8	0.21	0.19	0.13	0.58
η / %	30	26	0.55	0.36	0.56	0.39
η* / %	395	14	2.7	1.9	4.3	0.67

[a)]The precision is estimated as ca. ±10% for $c_{nc,max,}$ while higher, ca. ±20% for the other two parameters, *cdc* and $c_{s,max}$, since the latter depends strongly on the availability of many enough and clearly assignable points in the quickly ascending parts of the respective dispersion curves.

Firstly, it is apparent that all the curves follow approximately the described bell-shape profile, with the exception of the system TX100/MWNT, where the final decay stage (IV, in Fig. 2) could not be attained even at very high surfactant concentrations. Secondly, from the initial sigmoidal profiles, and the dispersibility metrics obtained using appropriate statistics (described elsewhere [13] and shown in Table 1, it is clear that for all the systems studied (MWNTs, graphite-exfoliated GnPs and cGNPs), the ionic surfactant, SC, is a better dispersant than the nonionic one, TX100. In fact, SC disperses higher concentrations of nanocarbon (higher values of $c_{MWNT,max}$, $c_{GnP,max}$ and $c_{cGnP,max}$), starts dispersing at lower concentrations (lower *cdc*), and is both more effective and more efficient than TX-100.

Thirdly, at fixed delivered energy per carbon mass (≈ 0.20 kJ·mg^{-1}), it is clear that the process is dramatically more effective for the 1D nanotubes than for the 2D graphene nanoplatelets, either obtained from graphite or from cGnPs. In fact, for MWNTs, final yields (η) of the order of 26-30% are obtained (Table 1), where are as for GnPs (irrespective of type), the values are in the range of 0.4-0.6%. Further, Fig. 2b) and 2c), as well as Table 1 values, show that under the set conditions, the preformed cGnPs are dispersed in lower concentrations (by 1/3) that GnPs obtained from exfoliating graphite. The cGNP powder was in fact processed with identical conditions to MWNTs (see Table S1), namely, at identical delivered energy/carbon mass, 0.20 kJ·mg^{-1}, and energy density (delivered energy per volume of dispersion), 0.59 kJ·mL^{-1}, a parameter also deemed pivotal in the exfoliation of carbon materials.[13, 49] The reason for this strict choice of identical parameters lies in that we wanted to investigate the role of particle-particle

interactions in the separation process, since in both materials there are already preformed particles (entangled MWNTs or stacked GnPs). The results thus suggest that under strict equivalence of dispersing conditions, the stacked GnP particles are dramatically less prone to separation than MWNTs. We will defer discussions on this point to section 3.3 below.

Fourthly, and crucially, after normalizing the concentration of nanocarbon dispersed with the maximum dispersed concentration, Fig. 3d), nearly superimposable curves are found for the systems studied, except for the outlying TX-100/MWNT. This common trend is rather significative, indicating that, irrespective of the dimensionality of the nanomaterial and of the surfactant, the dispersing process follows qualitatively similar stages, resulting in a similar bell-shaped curve. We postpone further discussion of this point to section 3.3.

Having investigated the profile of the dispersibility curves for the different materials and surfactants, it was then important to know in detail in which state of separation, the suspended particles are (bundle widths for MWNTs and GnP lateral dimensions and layer number). For this, characterization of the dispersions using SEM, AFM, Raman spectroscopy and zeta potential measurements was undertaken.

3.2 Structural characterization of the dispersions

3.2.1 Dispersed MWNTs

The diameter distribution of the MWNTs dispersions with highest $c_{nc,max}$ was evaluated through microscopic techniques. The MWNT diameter was measured by SEM (Fig. 4) suggesting no significant effect of the surfactant structure on the degree of debundling. The bundles consist of < 10 MWNT units taking into consideration the supplier's diameter specifications (d = 8 - 15 nm); in fact, the biggest d measured by SEM was ~70 nm, implying bundles of 5-9 MWNTs. AFM height values results (Fig. S1), yield similar diameter distribution as the SEM measurements (albeit the much smaller data). These results, in combination with the dispersibility curves, show that for these two surfactants, the molecular structure has an influence on the quantitative parameters (i.e. $c_{nc,max}$, cdc and $c_{s,max}$) but no apparent effect in the debundling degree of the final dispersion. The experimental processing parameters, namely the set sonication energy/carbon mass and centrifugation conditions, seem to play the most critical role for the "quality" of the dispersions, that is, the degree of separation of the nanotubes into homogenous dispersions.[25, 27, 31]

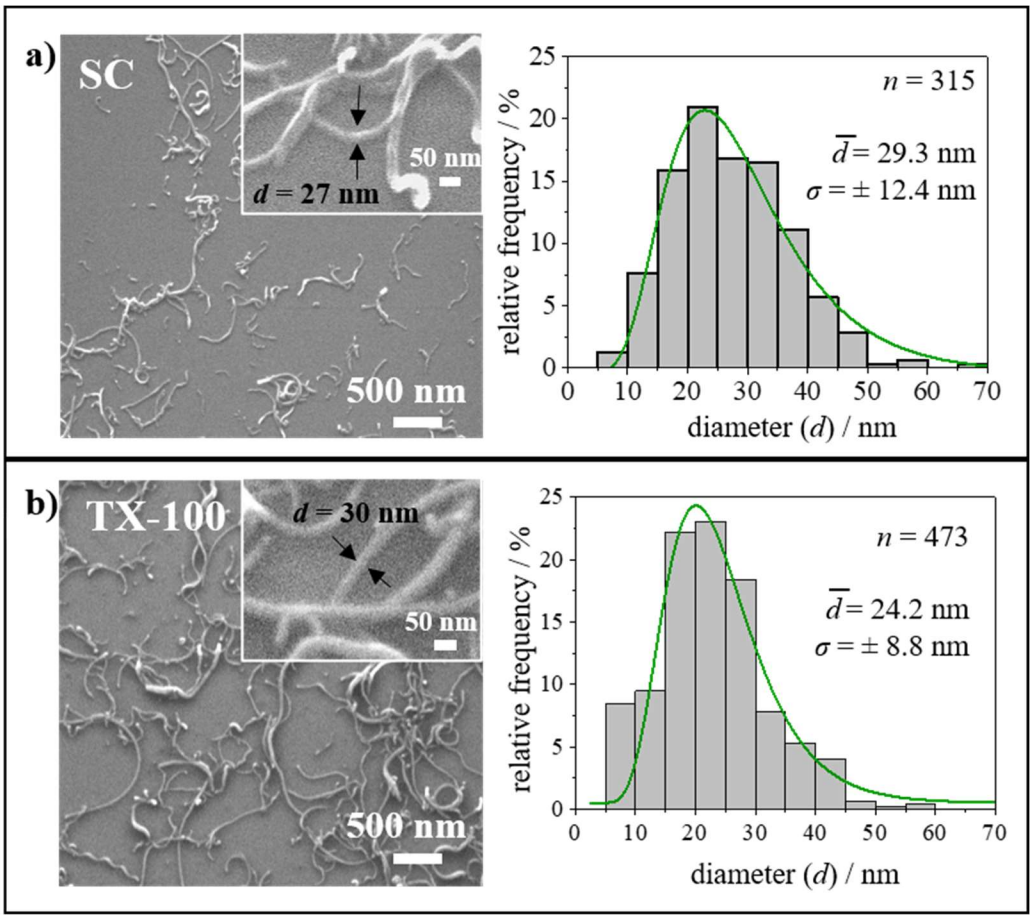

Fig. 4. A typical SEM micrographs and the respective diameter distributions of CNT bundle dispersed by TX-100 20 mmol·kg^{-1} (up) and SC 1.0 mmol·kg^{-1} (down) surfactants. The histograms obtained based on SEM imaging were fitted to a lognormal distribution.

3.2.2 Exfoliated graphene nanoplatelets

The distribution of mean lateral dimensions, *MLD*, of the GnPs was analyzed by AFM (Fig. 5). This *MLD* corresponds to the geometric mean of the length and the width of the flake, measured perpendicularly to each other (see section S3, supplementary data file). The thickness of each flake was also measured using height profiles as shown in Fig. 5a). In previous studies, it has been found that single-layered graphene with surfactant underneath has an apparent AFM height of ~ 2 nm.[35] This value is consistent with our AFM measurements, which showed discrete steps of ~ 2 nm thickness (Fig. 5a).

On the basis of a reported methodology for the characterization of graphene obtained by liquid phase exfoliation,[50] the *MLD* obtained by AFM and the corresponding flake thickness for each flake were plotted (Fig.5b) and a linear fitting, using 95% confidence bands was obtained.

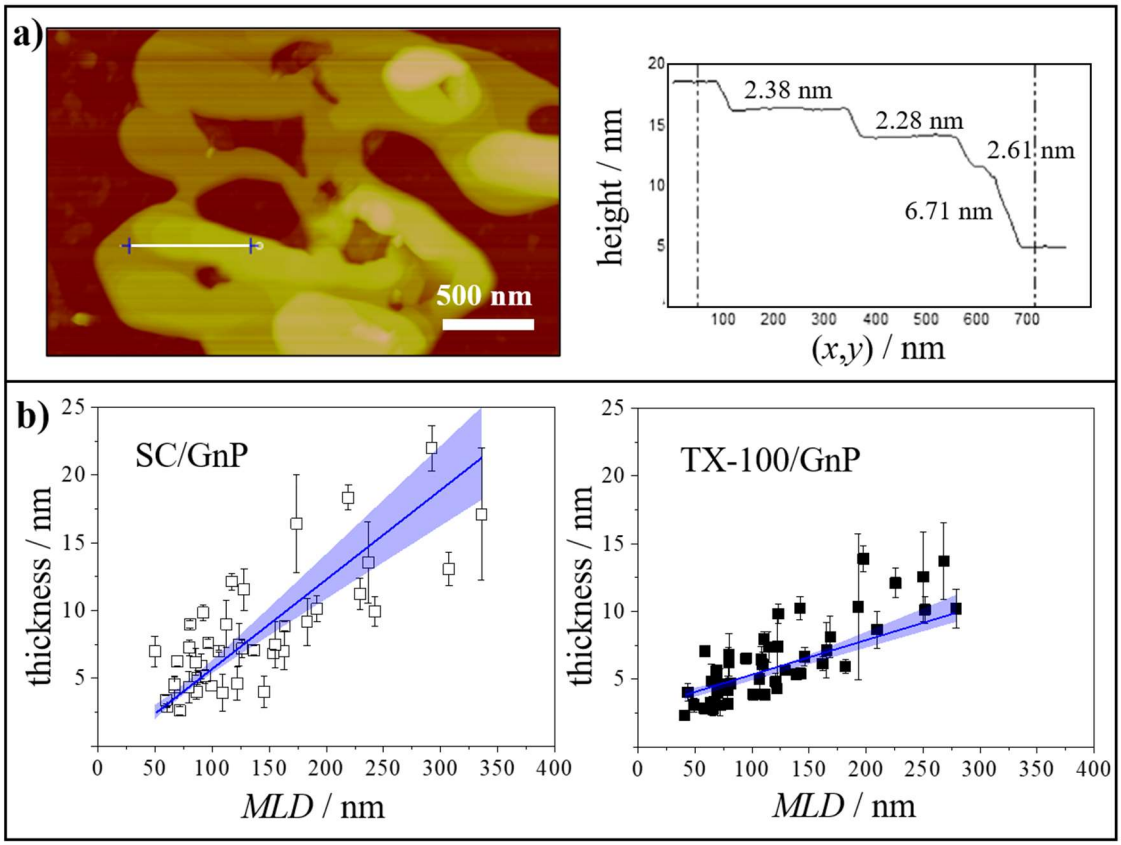

Fig. 5. a) AFM micrographs and height profile of terraces of stacked graphene, for TX-100/GnP and b) *MLD* vs flake thickness plots, determined by AFM measurements.

Since SEM is statistically representative when compared with AFM, the *MLD* of more than 200 flakes was measured using this technique (Fig. 6a). An average *MLD,* $\overline{MLD}$, of 111 ± 3 nm for SC/GnP and 120 ± 5 nm for TX-100/GnP system was obtained. From the plots in Fig. 5b, we extrapolated the flake thickness corresponding to the *MLD* measured by SEM (Fig. 6b), following the aforementioned methodology [50]. The calculations (see section S4, supplementary data file) indicate that approximately 80% and 60% of the dispersed GnPs for the SC and TX-100 systems, respectively, have less than 5 layers [51].

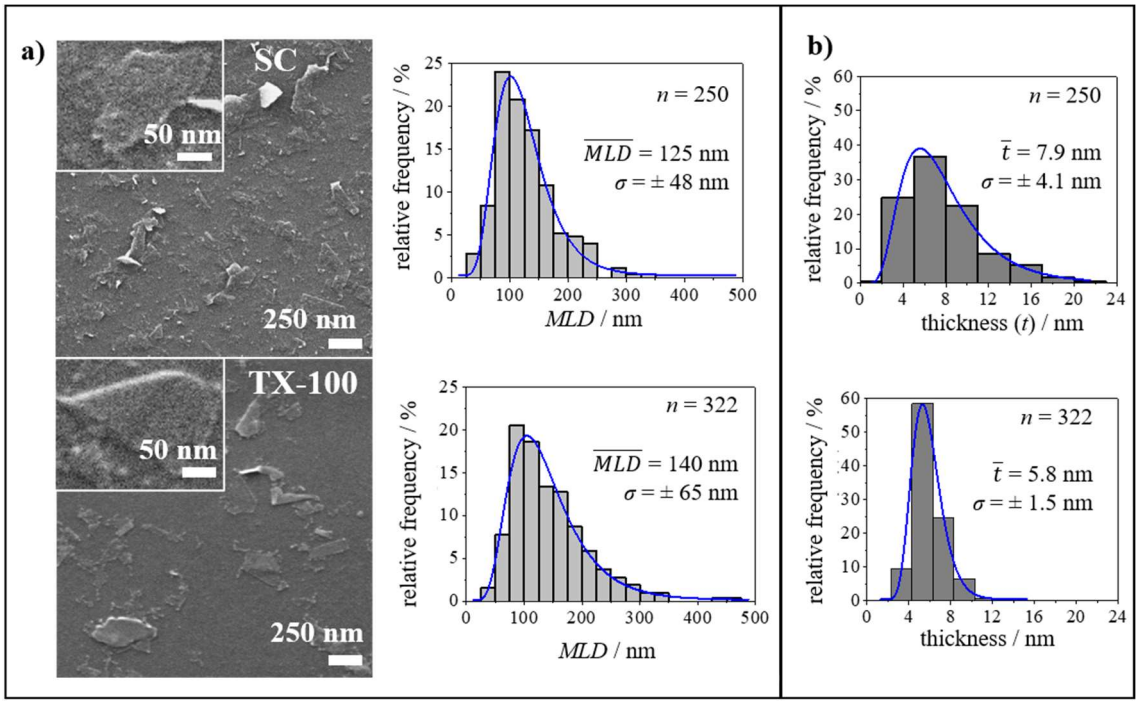

Fig. 6. a) SEM imaging characterization and the respective histograms with GnP flakes MLD distributions dispersed by the surfactants TX-100 0.9 mmol·kg^{-1}(up) and SC 6.7 mmol·kg^{-1} (down). The histograms obtained based on SEM imaging were fitted to a lognormal distribution; b) thickness distribution for TX-100 (up) and SC (down) systems, obtained from the fitting presented in Fig. 5b.

The defect density of the material exfoliated by SC was compared to that of the original graphite using Raman spectroscopy (Fig.7). Even with the superimposition of the surfactant spectra, the main bands typical of graphene are present: D band at ~ 1556 cm^{-1} (indicates the disorder of the flake), G band at ~1588 cm^{-1} (first order Raman scattering process) and the second order 2D band at ~2700 cm^{-1}, due to second order phonons and related to the number of layers (Fig.7) [33, 52]. Moreover, it was possible to subtract the surfactant spectra (Fig. S5) to the one of the GnP/SC system, and its profile allowed to extract information on the defect density of graphene sheets ($I_D/I_{D'}$—defect type and I_D/I_G —total defect density [53, 54]) and number of layers (I_D/I_{2D}).[52, 55] The ratio $I_D/I_{D'}$ = 8.75 implies the existence of vacancy like defects in the exfoliated material [56]. I_D/I_G = 1.3 indicates total defect density, and it is correlated with *MLD*, according to equation (1).[53]

$$MLD = \frac{0.17}{\frac{I_D}{I_G} - \left(\frac{I_D}{I_G}\right)_{GF}} = \frac{0.17}{\frac{I_D}{I_G} - 0.14} \qquad (1)$$

Smaller *MLD* has the effect of increasing the edges contour and consequently the I_D/I_G ratio.[33] The *MLD* value obtained (147 nm) is reasonably close to the value determined by SEM and AFM (120 nm). Additionally, I_D/I_{2D} = 1.4 indicates the presence of FLG (< 10 layers) with more than 2 layers, also in line with the microscopy results.[55]

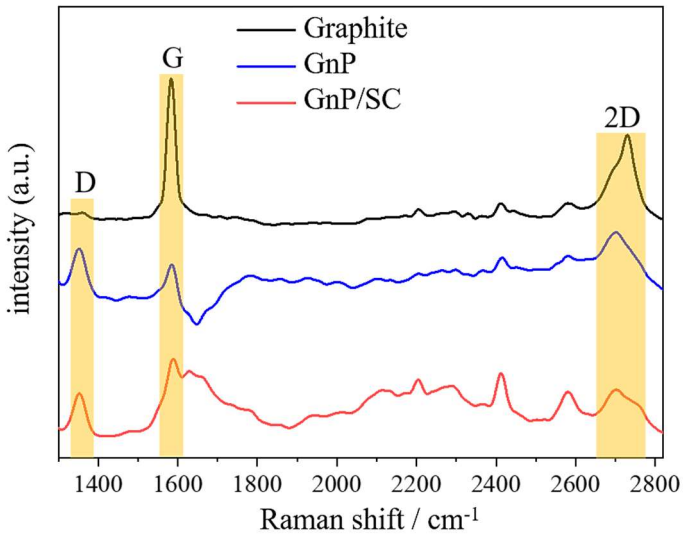

Fig. 7. Raman spectra acquired at 514 nm for graphite (powder) and GnP/SC aqueous dispersion. The spectra referred as GnP is the subtraction of the GnP/SC and SC solution spectra.

3.2.3 Zeta potential studies

Zeta potential, ζ, measurements of SC systems suggest that the dispersed nanomaterials are coated with surfactant molecules, stabilizing the carbon nanomaterial *via* electrostatic interactions (Fig.8).[57] DLVO theory, which relies on the presence of a surface charge, can be used to describe the colloidal particle stabilization mechanism [58]. This can be applied to both MWNTs and GnPs. The adsorption of surfactant molecules *via* their hydrophobic tails on the carbon surface introduces a surface charge that stabilizes the dispersed particles against reaggregation. The sign and magnitude of this surface charge is associated with the zeta potential.[59] For the ionic dispersions, the observed negative zeta potential values (ζ < -30 mV) indicate high particle stability in the dispersion. For the non-ionic surfactant TX-100, stabilization through steric repulsions between the polar headgroups should play the dominant role. Nevertheless, weakly negative ζ values are observed (-10 to -20 mV) in the surfactant-coated nanocarbons, which may be related to residual charge present in the cleaved carbon surface or adsorption of contaminants.[58]

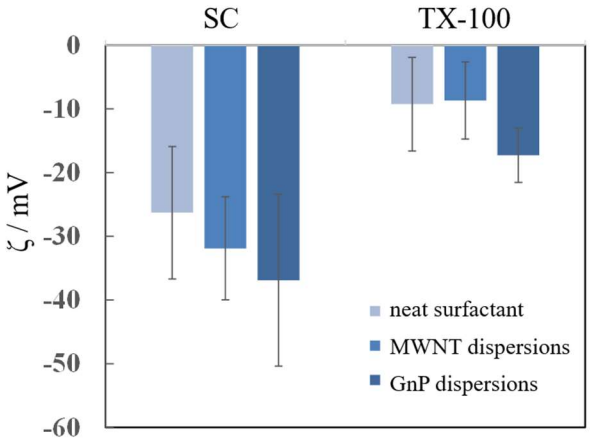

Fig.8. Zeta potential determined for the neat surfactants and dispersions with MWNT and GnPs.

In summary, the processing conditions used allowed not only to obtain high precision dispersibility curves but also well-dispersed nanocarbons, namely relatively high concentrations of suspended individual MWNTs or thin bundles (< 10 tubes), and high percentages of GnPs with < 10 layers and *MLD* mostly around 100-200 nm. Besides, the zeta potential studies indicates that surfactant coating leads to highly negative (for SC) or neutral/weakly negative (for TX100) carbon surfaces.

3.3 Comparison on the dispersibility of 1D and 2D nanocarbons: molecular insight

The first feature that stands out when comparing the exfoliation of MWNTs and graphite-to -GnPs is that the maximum dispersed nanomaterial concentration, $c_{nc,max}$, strikingly superior for the first system (Table 1). The mass ratio of dispersed MWNTs to dispersed GnPs, $m_{disp}^{MWNT}/m_{disp}^{GnP}$, is 17 for SC and 21 for TX-100, implying that at conditions of identical delivered energy/nanocarbon mass, $E_d/m \approx 0.20$ kJ·mg^{-1}, the MWNTs are ca. one order of magnitude more dispersible than GnPs obtained from graphite (and that does not seem to depend significantly on surfactant features). To make sense of these numbers, some approximate calculations can be made. Exfoliating these nanocarbon materials is difficult owing to the strong van der Waals (vdW) binding forces between either the nanotubes or the graphene layers. MWNT powders are highly entangled due to packing to the nanotubes into (thin) bundles and mostly due to formation of network clusters, where strong vdW binding occurs at the contact junctions between inter-crossed MWNTs (or thin bundles thereof).[49] In graphite, even stronger cohesive vdW forces hold the graphene monolayers together. For both materials, complete exfoliation implies overcoming these forces and stabilizing the nanotubes or graphene layers in solution. The $m_{disp}^{MWNT}/m_{disp}^{GnP}$ ratio can be estimated taking into account the surface energy, γ, of

the individual materials their specific surface area, SSA (see Section S1, S.I., for details). Values of $\gamma \approx 45$ mJ·m^{-2} for MWNTs[60] and ≈ 300 mJ·m^{-2} for graphene monolayers[61] have been determined, while SSA for $d \approx 10$ nm MWNTs is estimated as 200 m^2·g^{-1} [62] (consistent herein with the supplier's values) and 2630 m^2·g^{-1} for graphene[63] (about an order of magnitude higher). These values yield $m_{\mathrm{disp}}^{\mathrm{MWNT}}/m_{\mathrm{disp}}^{\mathrm{GnP}} \approx 7$ using the actual delivered sonication energy (see Section S1, S.I.) or ≈ 88, if we consider the normalized energy ($E_d/m \approx 0.20$ kJ·mg^{-1}). Significantly, the observed experimental ratios (≈ 20) fall well within this approx. 10-100 calculated range. Several comments are in place here. First, these calculations, owing to their rather approximate nature, allow to estimate a mass ratio (hence a relative order of magnitude) rather than absolute dispersed mass values. Secondly, the reasonable agreement obtained is consistent with well-separated MWNTs and well-exfoliated graphite (that is, graphite converted into GnPs with few layers) are obtained, in line with the observations in section 3.2.3. Thirdly, the higher binding energy and higher SSA of graphene layers explain, at least partially, that under equivalent E_d/m conditions, MWNTs are more separated in much higher concentration than GnPs.

Regarding the dispersion of cGnPs, the $m_{\mathrm{disp}}^{\mathrm{MWNT}}/m_{\mathrm{disp}}^{\mathrm{cGnP}}$ ratio is 54 for SC and 64 for TX100. It should be kept in mind that all these materials (MWNTs, graphite and cGnPs) were processed at fixed E_d/m, but in the case of MWNTs and cGnPs the total supplied energy density, E_d/V, and initial carbon loading, were additionally fixed, at 0.59 kJ·mL^{-1} and 3.0 mg·mL^{-1}, respectively (see table S1, S.I.). Our aim here was to provide an even more stringent comparison between the separation of 1D and 2D nanocarbons, since the local energy density (equivalent to shear stress) is also deemed as a crucial parameter in the exfoliation of nanocarbons by sonication.[49] Close inspection of Table S1 shows that the supplied energy density for graphite was ≈ 2.0 kJ·mL^{-1}, about an order of magnitude higher than that for the cGnPs. This difference provides an explanation for the higher concentration obtained of exfoliated GnPs compared to that of cGnPs. However, when comparing the respective yield values, η, in Table 1, the values are nearly identical (for each surfactant), which means that in practice, it is equally effective to separate GnPs or to exfoliate them from graphite. Another pivotal point is that both at fixed energy/carbon mass and fixed energy density conditions, the MWNTs are sizably more dispersible than preformed GnPs. The conclusion is that even in the latter, vdW binding forces acting between 2D (FLG) particles are fairly significant and comparable to those in graphite.

Addressing now the master curve shown in Fig. 3d), it is noteworthy the surfactant concentration is presented on absolute scale, indicating that the conditions of surfactant concentration necessary to yield the profile are nearly identical, namely that *cdc* and $c_{s,max}$ do not vary appreciably neither with material nor with surfactant. This master curve thus seems to unveil some fundamental aspects of the dispersing process. Kinetic aspects likely rule the dispersibility behavior when surfactants are used to disperse carbon nanomaterials, as argued in a previous work by us.[64] Therein, we proposed that the bulk concentration and bulk diffusion of the dispersant molecules dictate how rapidly the dispersant is available to adsorb at the carbon surface. Presumably, the master curve of Fig. 3d) reflects such kinetic effects, namely that high enough surfactant concentration is required to allow *high enough surface coverage of freshly cleaved carbon surface to be attained rapidly by the available surfactant*. The surface is either freshly cleaved MWNT surface (along the tubes or in junction points) or freshly exposed graphene layers. The used sonication conditions and surfactant concentration range culminate in dispersibility curves offering a master profile, once the y-axis (dispersed nanocarbon) is normalized. Still, the question of the different plateau levels observed in the individual dispersibility curves remains. This may be the consequence of two things: (i) the differences in tube-tube interaction energy in MWNTs, and layer-layer energy in graphite/GnPs; (ii) the rate of adsorption of the different dispersants, SC and TX100, or even the configuration of adsorbed state configuration (a less favored state may act weaklier to the forced driving the nanocarbon clefts to reclose), both of which stem from molecular differences between the dispersants (see discussion on this point further below).

After the plateau, the master curve in Fig. 3d) also shows a common sharp decrease on the dispersibility of dispersed nanocarbon particles, irrespective of surfactant and material. This decreasing effect is likely due to depletion forces at stake. The dispersed particles in suspension aggregate due to an osmotic pressure difference owing to the high concentration of bulk micelles around the dispersed colloidal particles; the solvent in between the particles tends to flow out causing the particles to flocculate. For the 2D systems, Wang *et al* presented similar results for ionic surfactants as obtained in this work, that is c_{GnP} decreases after reaching its maximum value, when increasing c_s.[40] However, for nonionic surfactants, the author reported that c_{GnP} reaches a maximum value and maintains a plateau. These results were, nevertheless, based on a smaller number of c_s values and covering a shorter range than in our work, hence likely missing the full behavior.[40] Therefore, our results show that depletion effects are common to 1D and 2D nanocarbons, occurring at comparable surfactant concentrations.

It is relevant here to also discuss the differences observed between SC and TX100 as dispersants. The dispersion of CNTs by ionic surfactants was previously studied by us in depth, not only for MWNTs but also for SWNTs, using conventional surfactants.[13, 17] It is clear that the efficiency of the bile salt SC in dispersing MWNTs stands out between all the surfactants so far studied (Table 1). A possible explanation is the large area occupied by the hydrophobic and planar backbone of the bile salt, with high affinity for the carbon surface.[65] Sodium cholate has a hydrophobic face that is particularly amenable to interact hydrophobically with carbon surfaces, while the OH groups and COO^- headgroup provide both wettability and repulsive steric and electrostatic forces, respectively. The outlying behavior presented by the TX-100/MWNT system in Fig. 3b) may be due to a number of reasons. Previous work on adsorption isotherms of Triton X-100 on active carbons and clays[66, 67] already mentioned that the adsorption mechanisms of Triton X-series surfactants on CNTs differed from other adsorbents.[68] The distinct trend observed herein might be due to the smaller hydrophobic section of TX-100 (despite that aromatic ring that can establish π-π interactions, the hydrocarbon tail is fairly short, compared to its large bulk-protruding hydrophilic segment with oxyethylene groups. Overall, this may decrease slightly the surfactant affinity for the nanotube surface. Also, bigger and flexible hydrophilic segments may determine high steric repulsions between neighboring molecules adsorbed at the surface, and this effect may stand out in CNTs because of the surface curvature.[69]

4. Conclusions

Dispersions of MWNTs, GnPs exfoliated from graphite, and commercial GnPs (cGnPs) were prepared by a sonication/centrifugation process using two different surfactants, under rigorously controlled conditions, and for a fixed delivered energy per nanocarbon mass (0.2 $kJ \cdot mg^{-1}$). Sodium cholate (SC) and TritonX-100 (TX100) were selected as ionic and nonionic dispersants, respectively, allowing comparison between two of the most used surfactants to disperse carbon nanomaterials. A common initial sigmoidal profile for the dispersibility curves, followed by a plateau, was observed for all systems allowing to extract quantitative parameters, such as $c_{nc,max}$, *cdc*, $c_{s,max}$. SC presented the best results for both MWNT and GnP dispersions, achieving higher dispersibility values at lower surfactant concentration. Except for the TX-100/MWNT system, all the other complete individual dispersibility curves fall into a common bell-shaped master curve of normalized $c_{nc}/c_{nc,max}$ vs surfactant concentration, indicating that the dispersing process follows common fundamental mechanisms, likely associated with kinetic aspects (*viz*.

surfactant availability and diffusion rate to freshly cleaved carbon surface). SEM and AFM characterization demonstrated that a good debundling/exfoliation degree of the 1D and 2D materials was obtained in the dispersions, and zeta potential studies validate the view that kinetic stabilization of the dispersed particles occurs mainly *via* electrostatic and steric interactions for SC and TX-100, respectively. Results further show that under similar processing conditions, MWNTs are quantitatively dispersed far more significantly than GnPs (by at least an order of magnitude), irrespectively of their origin, and this was critically rationalized in terms of vDW binding forces acting on the systems. In conclusion, the results presented here provide fundamental insight into the dispersing process of nanocarbon materials and may prove useful when designing effective experimental protocols for the exfoliation of other types of 1D and 2D nanomaterials, development of nanocomposites and exploration of their applications.

CRediT authorship contribution statement

B. Abreu: Investigation, Formal analysis, Validation, Writing - original draft. **J. Montero:** Investigation, Formal analysis. **M. Buzaglo:** Methodology. **O. Regev:** Conceptualization, Methodology, Writing - review & editing. **E. F. Marques:** Conceptualization, Methodology, Resources, Supervision, Funding acquisition, Writing - review & editing.

Declaration of competing interest

The authors declare that they have no known competing financial interests or personal relationships that could have appeared to influence the work reported in this paper.

Acknowledgments

The authors acknowledge Fundação para a Ciência e para a Tecnologia (FCT) for financial support through project UIDB/00081/2020. B. Abreu also acknowledges financial support from FCT through the PhD grant PD/BD/128129/2016 from FCT.

References

1. De Volder, M. F. L.; Tawfick, S. H.; Baughman, R. H.; Hart, A. J., Carbon nanotubes: Present and future commercial applications. *Science* **2013,** *339* (6119), 535-539.
2. Zhang, J.; Terrones, M.; Park, C. R.; Mukherjee, R.; Monthioux, M.; Koratkar, N.; Kim, Y. S.; Hurt, R.; Frackowiak, E.; Enoki, T.; Chen, Y.; Chen, Y. S.; Bianco, A., Carbon science in 2016: Status, challenges and perspectives. *Carbon* **2016,** *98* (70), 708-732.
3. Phiri, J.; Gane, P.; Maloney, T. C., General overview of graphene: Production, properties and application in polymer composites. *Mater. Sci. Eng. B-Adv. Funct. Solid-State Mater.* **2017,** *215*, 9-28.
4. Tan, C. L.; Cao, X. H.; Wu, X. J.; He, Q. Y.; Yang, J.; Zhang, X.; Chen, J. Z.; Zhao, W.; Han, S. K.; Nam, G. H.; Sindoro, M.; Zhang, H., Recent advances in ultrathin two-dimensional nanomaterials. *Chem. Rev.* **2017,** *117* (9), 6225-6331.

5. Rao, R.; Pint, C. L.; Islam, A. E.; Weatherup, R. S.; Hofmann, S.; Meshot, E. R.; Wu, F. Q.; Zhou, C. W.; Dee, N.; Amama, P. B.; Carpena-Nunez, J.; Shi, W. B.; Plata, D. L.; Penev, E. S.; Yakobson, B. I.; Balbuena, P. B.; Bichara, C.; Futaba, D. N.; Noda, S.; Shin, H. M.; Kim, K. S.; Simard, B.; Mirri, F.; Pasquali, M.; Fornasiero, F.; Kauppinen, E. I.; Arnold, M.; Cola, B. A.; Nikolaev, P.; Arepalli, S.; Cheng, H. M.; Zakharov, D. N.; Stach, E. A.; Zhang, J.; Wei, F.; Terrones, M.; Geohegan, D. B.; Maruyama, B.; Maruyama, S.; Li, Y.; Adams, W. W.; Hart, A. J., Carbon nanotubes and related nanomaterials: Critical advances and challenges for synthesis toward mainstream commercial applications. *ACS Nano* **2018,** *12* (12), 11756-11784.
6. Mohan, V. B.; Lau, K. T.; Hui, D.; Bhattacharyya, D., Graphene-based materials and their composites: A review on production, applications and product limitations. *Compos. Pt. B-Eng.* **2018,** *142*, 200-220.
7. Monajjemi, M., Liquid-phase exfoliation (LPE) of graphite towards graphene: An ab initio study. *J. Mol. Liq.* **2017,** *230*, 461-472.
8. Hassanloo, H.; Sadeghzadeh, S.; Ahmadi, R., A new approach to dispersing and stabilizing graphene in aqueous nanofluids of enhanced efficiency of energy-systems. *Sci. Rep.* **2020,** *10* (1), 7707.
9. Qiu, M.; Wang, D.; Zhang, L.; Li, M.; Liu, M.; Fu, S., Electrochemical exfoliation of water-dispersible graphene from graphite towards reinforcing the mechanical and flame-retardant properties of poly (vinyl alcohol) composites. *Mater. Chem. Phys* **2020,** *254*, 123430.
10. Wang, H., Dispersing carbon nanotubes using surfactants. *Curr. Opin. Colloid Interface Sci.* **2009,** *14* (5), 364-371.
11. Angelikopoulos, P.; Bock, H., The science of dispersing carbon nanotubes with surfactants. *PCCP* **2012,** *14* (27), 9546-9557.
12. Clark, M. D.; Subramanian, S.; Krishnamoorti, R., Understanding surfactant aided aqueous dispersion of multi-walled carbon nanotubes. *J. Colloid Interface Sci.* **2011,** *354* (1), 144-151.
13. Fernandes, R. M.; Abreu, B.; Claro, B.; Buzaglo, M.; Regev, O.; Furo, I.; Marques, E. F., Dispersing carbon nanotubes with ionic surfactants under controlled conditions: Comparisons and insight. *Langmuir* **2015,** *31* (40), 10955-65.
14. Di Crescenzo, A.; Di Profio, P.; Siani, G.; Zappacosta, R.; Fontana, A., Optimizing the interactions of surfactants with graphitic surfaces and clathrate hydrates. *Langmuir* **2016,** *32* (26), 6559-6570.
15. Cao, M.; Wang, N.; Wang, L.; Zhang, Y.; Chen, Y.; Xie, Z.; Li, Z.; Pambou, E.; Li, R.; Chen, C.; Pan, F.; Xu, H.; Penny, J.; Webster, J. R. P.; Lu, J. R., Direct exfoliation of graphite into graphene in aqueous solutions of amphiphilic peptides. *J. Mater. Chem. B* **2016,** *4* (1), 152-161.
16. Poorsargol, M.; Sohrabi, B.; Dehestani, M., Study of the gemini surfactants' self-assembly on graphene nanosheets: Insights from molecular dynamic simulation. *J. Phys. Chem. A* **2018,** *122* (15), 3873-3885.
17. Abreu, B.; Rocha, J.; Fernandes, R. M. F.; Regev, O.; Furó, I.; Marques, E. F., Gemini surfactants as efficient dispersants of multiwalled carbon nanotubes: Interplay of molecular parameters on nanotube dispersibility and debundling. *J. Colloid Interface Sci.* **2019,** *547*, 69-77.
18. Saint-Aubin, K.; Poulin, P.; Jaillet, C.; Maugey, M.; Zakri, C., Changes of morphology and properties of block copolymers induced by carbon nanotubes. *Polymer* **2013,** *54* (9), 2285-2291.
19. Fernandes, R. M. F.; Buzaglo, M.; Shtein, M.; Pri Bar, I.; Regev, O.; Marques, E. F.; Furó, I., Lateral diffusion of dispersing molecules on nanotubes as probed by NMR. *J. Phys. Chem. C* **2014,** *118* (1), 582-589.
20. Di Crescenzo, A.; Ettorre, V.; Fontana, A., Non-covalent and reversible functionalization of carbon nanotubes. *Beilstein J. Nanotechnol.* **2014,** *5*, 1675-1690.
21. Fernandes, R. M. F.; Dai, J.; Regev, O.; Marques, E. F.; Furó, I., Block copolymers as dispersants for single-walled carbon nanotubes: Modes of surface attachment and role of block polydispersity. *Langmuir* **2018,** *34* (45), 13672-13679.
22. Hamdi, S. S.; Al-Kayiem, H. H.; Muhsan, A. S., Natural polymer non-covalently grafted graphene nanoplatelets for improved oil recovery process: A micromodel evaluation. *J. Mol. Liq.* **2020,** *310*.
23. Frise, A. E.; Edri, E.; Furo, I.; Regev, O., Protein dispersant binding on nanotubes studied by NMR self-diffusion and Cryo-TEM techniques. *J. Phys. Chem. Lett.* **2010,** *1* (9), 1414-1419.

24. Fernandes, R. M. F.; Buzaglo, M.; Regev, O.; Marques, E. F.; Furo, I., Surface coverage and competitive adsorption on carbon nanotubes. *J. Phys. Chem. C* **2015,** *119* (38), 22190-22197.
25. Blanch, A. J.; Lenehan, C. E.; Quinton, J. S., Parametric analysis of sonication and centrifugation variables for dispersion of single walled carbon nanotubes in aqueous solutions of sodium dodecylbenzene sulfonate. *Carbon* **2011,** *49* (15), 5213-5228.
26. Lu, F.; Zhang, S.; Zheng, L., Dispersion of multi-walled carbon nanotubes (MWCNTs) by ionic liquid-based phosphonium surfactants in aqueous solution. *J. Mol. Liq.* **2012,** *173*, 42-46.
27. Buzaglo, M.; Shtein, M.; Kober, S.; Lovrincic, R.; Vilan, A.; Regev, O., Critical parameters in exfoliating graphite into graphene. *Phys. Chem. Chem. Phys* **2013,** *15* (12), 4428-4435.
28. Dassios, K. G.; Alafogianni, P.; Antiohos, S. K.; Leptokaridis, C.; Barkoula, N.-M.; Matikas, T. E., Optimization of sonication parameters for homogeneous surfactant-assisted dispersion of multiwalled carbon nanotubes in aqueous solutions. *J. Phys. Chem. C* **2015,** *119* (13), 7506-7516.
29. Luo, B.; Liu, S.; Zhi, L., Chemical approaches toward graphene-based nanomaterials and their applications in energy-related areas. *Small* **2012,** *8* (5), 630-646.
30. Li, C. Y.; Li, Z.; Zhu, H. W.; Wang, K. L.; Wei, J. Q.; Li, X. A.; Sun, P. Z.; Zhang, H.; Wu, D. H., Graphene nano-"patches" on a carbon nanotube network for highly transparent/conductive thin film applications. *J. Phys. Chem. C* **2010,** *114* (33), 14008-14012.
31. Coleman, J. N., Liquid-phase exfoliation of nanotubes and graphene. *Adv. Funct. Mater.* **2009,** *19* (23), 3680-3695.
32. Paton, K. R.; Varrla, E.; Backes, C.; Smith, R. J.; Khan, U.; O'Neill, A.; Boland, C.; Lotya, M.; Istrate, O. M.; King, P.; Higgins, T.; Barwich, S.; May, P.; Puczkarski, P.; Ahmed, I.; Moebius, M.; Pettersson, H.; Long, E.; Coelho, J.; O'Brien, S. E.; McGuire, E. K.; Sanchez, B. M.; Duesberg, G. S.; McEvoy, N.; Pennycook, T. J.; Downing, C.; Crossley, A.; Nicolosi, V.; Coleman, J. N., Scalable production of large quantities of defect-free few-layer graphene by shear exfoliation in liquids. *Nat. Mater.* **2014,** *13*, 624.
33. Buzaglo, M.; Bar, I. P.; Varenik, M.; Shunak, L.; Pevzner, S.; Regev, O., Graphite-to-graphene: Total conversion. *Adv. Mater.* **2017,** *29* (8).
34. Nazari, B.; Ranjbar, Z.; Hashjin, R. R.; Rezvani Moghaddam, A.; Momen, G.; Ranjbar, B., Dispersing graphene in aqueous media: Investigating the effect of different surfactants. *Colloids Surf. A Physicochem. Eng. Asp.* **2019,** *582*, 123870.
35. Lotya, M.; King, P. J.; Khan, U.; De, S.; Coleman, J. N., High-concentration, surfactant-stabilized graphene dispersions. *ACS Nano* **2010,** *4* (6), 3155-3162.
36. Yeon, C.; Yun, S. J.; Lee, K. S.; Lim, J. W., High-yield graphene exfoliation using sodium dodecyl sulfate accompanied by alcohols as surface-tension-reducing agents in aqueous solution. *Carbon* **2015,** *83*, 136-143.
37. Das, S.; Irin, F.; Ahmed, H. S. T.; Cortinas, A. B.; Wajid, A. S.; Parviz, D.; Jankowski, A. F.; Kato, M.; Green, M. J., Non-covalent functionalization of pristine few-layer graphene using triphenylene derivatives for conductive poly (vinyl alcohol) composites. *Polymer* **2012,** *53* (12), 2485-2494.
38. Parviz, D.; Das, S.; Ahmed, H. S.; Irin, F.; Bhattacharia, S.; Green, M. J., Dispersions of non-covalently functionalized graphene with minimal stabilizer. *ACS Nano* **2012,** *6* (10), 8857-67.
39. Arao, Y.; Kubouchi, M., High-rate production of few-layer graphene by high-power probe sonication. *Carbon* **2015,** *95*, 802-808.
40. Wang, S.; Yi, M.; Shen, Z., The effect of surfactants and their concentration on the liquid exfoliation of graphene. *RSC Adv.* **2016,** *6* (61), 56705-56710.
41. Zhang, F.; Li, S.; Zhang, Q.; Liu, J.; Zeng, S.; Liu, M.; Sun, D., Adsorption of different types of surfactants on graphene oxide. *J. Mol. Liq.* **2019,** *276*, 338-346.
42. Ciesielski, A.; Samorì, P., Graphene via sonication assisted liquid-phase exfoliation. *Chem. Soc. Rev* **2014,** *43* (1), 381-398.
43. Wei, Y.; Sun, Z., Liquid-phase exfoliation of graphite for mass production of pristine few-layer graphene. *Curr. Opin. Colloid Interface Sci.* **2015,** *20* (5), 311-321.
44. Shtein, M.; Pri-bar, I.; Regev, O., A simple solution for the determination of pristine carbon nanotube concentration. *Analyst* **2013,** *138* (5), 1490-6.
45. Zhang, K.; Zhang, X.; Li, H.; Xing, X.; Jin, L.; Cao, Q.; Li, P., Direct exfoliation of graphite into graphene in aqueous solution using a novel surfactant obtained from used engine oil. *J. Mater. Sci* **2018,** *53* (4), 2484-2496.

46. Narayan, R.; Lim, J.; Jeon, T.; Li, D. J.; Kim, S. O., Perylene tetracarboxylate surfactant assisted liquid phase exfoliation of graphite into graphene nanosheets with facile re-dispersibility in aqueous/organic polar solvents. *Carbon* **2017,** *119*, 555-568.
47. White, B.; Banerjee, S.; O'Brien, S.; Turro, N.; Herman, I., Zeta-potential measurements of surfactant-wrapped individual single-walled carbon nanotubes. *J. Phys. Chem. C* **2007,** *111*, 13684-13690.
48. Sun, Z.; Nicolosi, V.; Rickard, D.; Bergin, S.; Aherne, D.; Coleman, J. N., Quantitative evaluation of surfactant-stabilized single-walled carbon nanotubes: dispersion quality and its correlation with zeta potential. *J. Phys. Chem. C* **2008,** *112*, 10692-10699.
49. Huang, Y. Y.; Terentjev, E. M., Dispersion of carbon nanotubes: Mixing, sonication, stabilization, and composite Properties. *Polymers* **2012,** *4* (1), 275-295.
50. Pollard, A. J.; Paton, K. R.; Clifford, C. A.; Legge, E.; Oikonomou, A.; Haigh, S.; Casiraghi, C.; Nguyen, L.; Kelly, D. *Characterisation of the structure of graphene*; 1368-6550; National Physical Laboratory, University of Manchester, 2017.
51. Bianco, A.; Cheng, H. M.; Enoki, T.; Gogotsi, Y.; Hurt, R. H.; Koratkar, N.; Kyotani, T.; Monthioux, M.; Park, C. R.; Tascon, J. M. D.; Zhang, J., All in the graphene family - A recommended nomenclature for two-dimensional carbon materials. *Carbon* **2013,** *65*, 1-6.
52. Ferrari, A. C., Raman spectroscopy of graphene and graphite: Disorder, electron-phonon coupling, doping and nonadiabatic effects. *Solid State Commun.* **2007,** *143* (1-2), 47-57.
53. Khan, U.; O'Neill, A.; Porwal, H.; May, P.; Nawaz, K.; Coleman, J. N., Size selection of dispersed, exfoliated graphene flakes by controlled centrifugation. *Carbon* **2012,** *50* (2), 470-475.
54. Ferrari, A. C.; Meyer, J. C.; Scardaci, V.; Casiraghi, C.; Lazzeri, M.; Mauri, F.; Piscanec, S.; Jiang, D.; Novoselov, K. S.; Roth, S.; Geim, A. K., Raman spectrum of graphene and graphene layers. *Phys. Rev. Lett* **2006,** *97* (18), 187401.
55. Memon, N. K.; Tse, S. D.; Al-Sharab, J. F.; Yamaguchi, H.; Goncalves, A. M. B.; Kear, B. H.; Jaluria, Y.; Andrei, E. Y.; Chhowalla, M., Flame synthesis of graphene films in open environments. *Carbon* **2011,** *49* (15), 5064-5070.
56. Eckmann, A.; Felten, A.; Mishchenko, A.; Britnell, L.; Krupke, R.; Novoselov, K. S.; Casiraghi, C., Probing the nature of defects in graphene by Raman spectroscopy. *Nano Lett.* **2012,** *12* (8), 3925-3930.
57. Coleman, J. N., Liquid exfoliation of defect-free graphene. *Acc. Chem. Res.* **2013,** *46* (1), 14-22.
58. Smith, R. J.; Lotya, M.; Coleman, J. N., The importance of repulsive potential barriers for the dispersion of graphene using surfactants. *New J. Phys* **2010,** *12*.
59. Tkalya, E. E.; Ghislandi, M.; de With, G.; Koning, C. E., The use of surfactants for dispersing carbon nanotubes and graphene to make conductive nanocomposites. *Curr. Opin. Colloid Interface Sci* **2012,** *17* (4), 225-232.
60. Nuriel, S.; Liu, L.; Barber, A. H.; Wagner, H. D., Direct measurement of multiwall nanotube surface tension. *Chem. Phys. Lett.* **2005,** *404* (4-6), 263-266.
61. Zhao, J. H.; Jiang, J. W.; Jia, Y.; Guo, W. L.; Rabczuk, T., A theoretical analysis of cohesive energy between carbon nanotubes, graphene and substrates. *Carbon* **2013,** *57*, 108-119.
62. Peigney, A.; Laurent, C.; Flahaut, E.; Bacsa, R. R.; Rousset, A., Specific surface area of carbon nanotubes and bundles of carbon nanotubes. *Carbon* **2001,** *39* (4), 507-514.
63. Bonaccorso, F.; Colombo, L.; Yu, G.; Stoller, M.; Tozzini, V.; Ferrari, A. C.; Ruoff, R. S.; Pellegrini, V., 2D materials. Graphene, related two-dimensional crystals, and hybrid systems for energy conversion and storage. *Science* **2015,** *347* (6217), 1246501.
64. Dai, J.; Fernandes, R. M.; Regev, O.; Marques, E. F.; Furó, I. n., Dispersing carbon nanotubes in water with amphiphiles: Dispersant adsorption, kinetics, and bundle size distribution as defining factors. *J. Phys. Chem. C* **2018,** *122* (42), 24386-24393.
65. Gubitosi, M.; Trillo, J. V.; Alfaro Vargas, A.; Pavel, N. V.; Gazzoli, D.; Sennato, S.; Jover, A.; Meijide, F.; Galantini, L., Characterization of carbon nanotube dispersions in solutions of bile salts and derivatives containing aromatic substituents. *J. Phys. Chem. B* **2014,** *118* (4), 1012-21.
66. González-García, C. M.; González-Martín, M. L.; González, J. F.; Sabio, E.; Ramiro, A.; Gañán, J., Nonionic surfactants adsorption onto activated carbon. Influence of the polar chain length. *Powder Technol.* **2004,** *148* (1), 32-37.
67. Han, Z.; Zhang, F.; Lin, D.; Xing, B., Clay minerals affect the stability of surfactant-facilitated carbon nanotube suspensions. *Environ. Sci. Technol* **2008,** *42* (18), 6869-6875.

68. Bai, Y.; Lin, D.; Wu, F.; Wang, Z.; Xing, B., Adsorption of Triton X-series surfactants and its role in stabilizing multi-walled carbon nanotube suspensions. *Chemosphere* **2010,** *79* (4), 362-367.
69. Jódar-Reyes, A. B.; Ortega-Vinuesa, J. L.; Martín-Rodríguez, A.; Leermakers, F. A. M., Modeling the effect of structural details of nonionic surfactants on micellization in solution and adsorption onto hydrophobic surfaces. *Langmuir* **2002,** *18* (22), 8706-8713.

Supplementary data

Comparative trends and molecular analysis on the surfactant-assisted dispersibility of 1D and 2D carbon materials: multiwalled nanotubes vs graphene nanoplatelets

Bárbara Abreu, Jorge Montero, Matat Buzaglo, Oren Regev and Eduardo F. Marques*

[1]CIQUP - Departamento de Química e Bioquímica, Faculdade de Ciências, Universidade do Porto, Rua do Campo Alegre P-4169-007 Porto, Portugal.

[2]Department of Chemical Engineering and [3]Ilse Katz Institute for Nanotechnology, Ben-Gurion University of the Negev, 84105 Beer-Sheva, Israel.

*efmarque@fc.up.pt

Table of contents

S1. Experimental processing conditions and parameters

Estimation of energy/carbon mass, energy density and power density delivered by sonication

A procedure to estimate the delivered ultrasound energy during the sonication process using bath and probe was established. Briefly, the temperature increase was recorded over time in a certain mass of water in a properly insulated vial that was irradiated with ultrasounds, at a given output power setting of the sonicator. The delivered energy, E_d, and power, P, for each assay were calculated, respectively, according to expressions:

$$E_d = m\, c_p\, \Delta T \qquad \text{(eq. S1)}$$

$$P_d = E_d/\Delta t \qquad \text{(eq. S2)}$$

where ΔT is the sample temperature variation, Δt is the sonication time, m is the mass of liquid and c_p is the specific heat capacity of the solvent (water). Average values for E and P for at least 3 assays were calculated. The average delivered energy density (delivered energy per volume of dispersion) and average delivered power density were then calculated as E_d/V and where P_d/V is the sample volume (different volumes and sample vials geometries were tested). The final results are shown in Table S1.

Table S1. Experimental conditions used to produce the dispersions.

Parameter	Graphite	MWNTs / cGnPs
Initial mass of carbon material	100 mg	9.0 mg
Volume of dispersant solution, *V*	10.0 mL	3.0 mL
Initial carbon material concentration (loading)	10.0 mg·mL^{-1}	3.0 mg·mL^{-1}
Input power, *P*	2.8 W (25% amplitude)	3.5 W (30% amplitude)
Sonication time, t_{son}	120 min	8.5 min
Delivered energy, E_d	20 kJ	1.8 kJ
Delivered energy/carbon mass, E_d/m	0.20 kJ·mg^{-1}	0.20 kJ·mg^{-1}
Delivered energy density, $\frac{E_d}{V}$ (= shear stress / MPa)	2.0 kJ·mL^{-1}	0.59 kJ·mL^{-1}
Power density, $\frac{P_d}{V}$ (= shear rate / MPa·s^{-1})	0.28 W·mL^{-1}	1.2 W·mL^{-1}
Centrifugal force, F_g	1000 g	4000 g
Centrifugation time	150 min	20 min

Estimation of the mass ratio of dispersed MWNTs to dispersed GnPs

The dispersed mass of nanomaterial can be estimated by

$$m_{disp} = E_d / \left(\frac{E_c}{A} \times \frac{A}{m} \right) \approx E_d / (\gamma \times SSA) \qquad \text{(eq. S3)}$$

where $\frac{E_c}{A}$ is the cohesive energy per area, γ is the surface energy and SSA is the specific surface area of the material. We used here the following values: for graphene monolayers, $\gamma \approx 300$ mJ·m^{-2} [1] and SSA = 2630 m^2·g^{-1} [2]; for MWNTs, $\gamma \approx 45$ mJ·m^{-2} [3] and SSA = 200 m^2·g^{-1} [4] (also in agreement with value supplied from the manufacturer). From the latter values, the values of E_d from Table S1, and equation S3, we can then estimate

$$m_{\text{disp}}^{\text{MWNT}} / m_{\text{disp}}^{\text{GnP}} \approx \frac{(E_d)_{\text{MWNT}} \times \gamma_{\text{graphene}} \times \text{SSA}_{\text{graphene}}}{(E_d)_{\text{GnP}} \times \gamma_{\text{MWNT}} \times SSA_{\text{MWNT}}} \approx 6.9$$

Experimentally, we obtained $m_{\text{disp}}^{\text{MWNT}} / m_{\text{disp}}^{\text{GnP}}$ = 17 and 21, for SC and TX100, and GnPs exfoliated from graphite, which are in fairly reasonable agreement (same order of magnitude) with the estimated value, given the all the approximate values used. Noteworthy, if we consider the “normalized energy” of 0.20 kJ·mg^{-1} (to account for the fact that different initial loadings and solvent volumes were used for MWNTs and GnPs), E_d values cancels and the ratio becomes 88, which is sizeably higher than 7 but still reasonable in comparison with the experimental values.

S2. AFM characterization and obtained size histograms

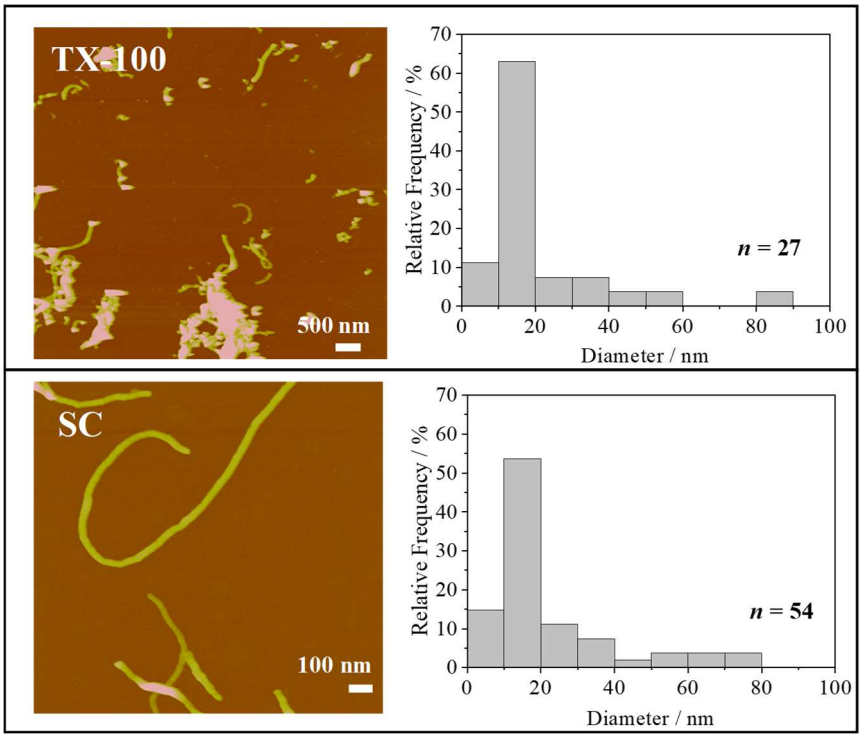

Fig. S1. AFM imaging characterization of MWNT and respective histograms.

S3. Determination of MLD and number of layers for GnPs (SEM and AFM data)

Length and width of the exfoliated flakes were measured in SEM micrographs using the directives of Fig. S2. For each flake, the geometric mean of these values was calculated, corresponding to its *MLD*. The obtained values were plotted in histograms (Fig. 5a), and the mean value for each surfactant system was determined.

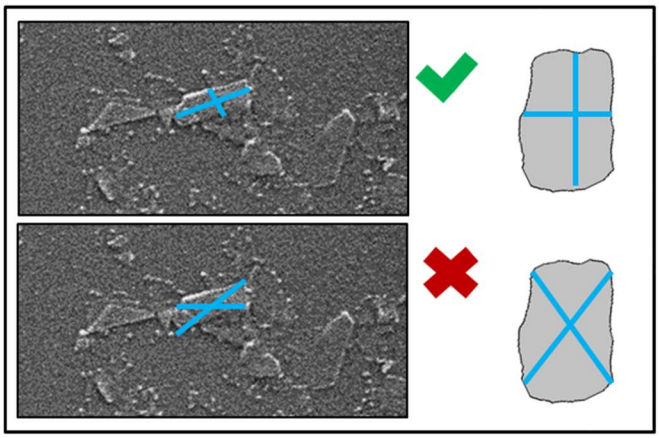

Fig. S2. Examples of correct (up) and incorrect (down) lateral flake size measurements for SEM images.

AFM allowed to measure *MLD* and the corresponding flake thickness for each flake (Fig. S3 and Fig. 5). The obtained values were plotted (Fig.4b) and a linear fitting, using 95% confidence bands (t-student distribution) was obtained in OriginPro 2018 (Fig. S4).

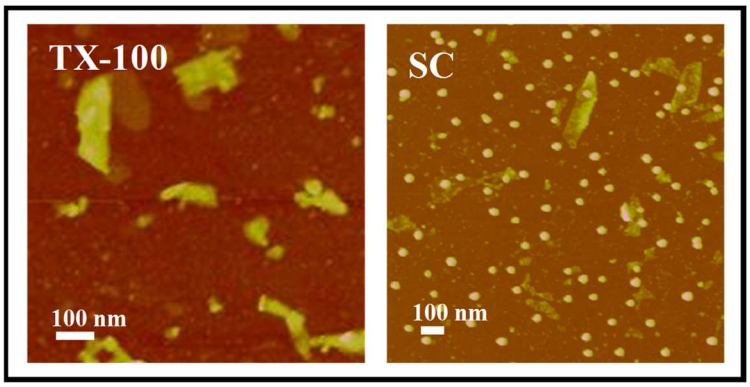

Fig. S3. AFM imaging characterization of exfoliated GnPs. The droplets in micrographs of the SC/G system can be attributed to the surfactant excess.

The obtained slope and intersection values allow to determine the height corresponding to the mean *MLD* extrapolated from the SEM histograms, according to Eq. S4, for both TX-100 (Fig. S4a and Eq. S5) and SC (Fig. S4b and Eq. S6) systems:

$$thickness = m \times MLD + b \quad \text{(Eq. S4)}$$

$$mean\ thickness_{TX-1} = 0.023 \times 111\ nm + 2.52 = 5.14\ nm \quad \text{(Eq. S5)}$$

$$mean\ thickness_{SC} = 0.0667 \times 120\ nm - 0.842 = 7.16\ nm \quad \text{(Eq. S6)}$$

Assuming the distance between 2 graphene sheets as ~2 nm, a mean number of layers of ~3 and ~4 for TX-100 and SC systems, respectively, is obtained. Therefore, the dispersions are composed mainly by FLG.

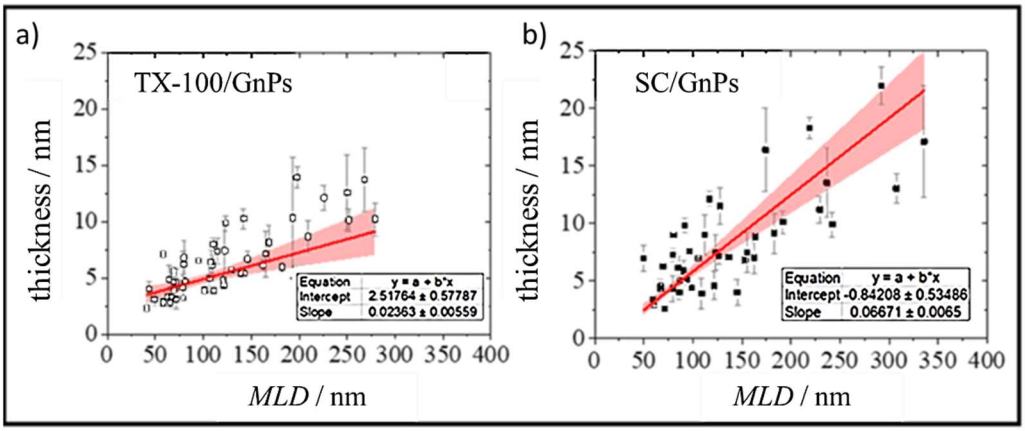

Fig. S4. *MLD* and the corresponding flake thickness for each flake, measured by AFM. Linear fitting, using 95% confidence bands (t-student distribution) was obtained in OriginPro 2018.

S4. Additional Raman data

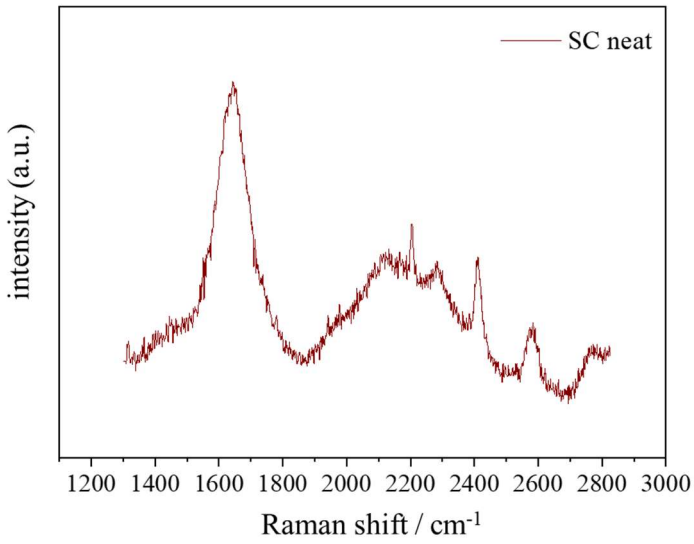

Fig. S5. Raman spectra acquired at 514 nm for SC neat aqueous solution.

References

1. Zhao, J. H.; Jiang, J. W.; Jia, Y.; Guo, W. L.; Rabczuk, T., A theoretical analysis of cohesive energy between carbon nanotubes, graphene and substrates. *Carbon* **2013,** *57*, 108-119.
2. Bonaccorso, F.; Colombo, L.; Yu, G.; Stoller, M.; Tozzini, V.; Ferrari, A. C.; Ruoff, R. S.; Pellegrini, V., 2D materials. Graphene, related two-dimensional crystals, and hybrid systems for energy conversion and storage. *Science* **2015,** *347* (6217), 1246501.
3. Nuriel, S.; Liu, L.; Barber, A. H.; Wagner, H. D., Direct measurement of multiwall nanotube surface tension. *Chem. Phys. Lett.* **2005,** *404* (4-6), 263-266.
4. Peigney, A.; Laurent, C.; Flahaut, E.; Bacsa, R. R.; Rousset, A., Specific surface area of carbon nanotubes and bundles of carbon nanotubes. *Carbon* **2001,** *39* (4), 507-514.

III

Dispersibility and noncovalent functionalization of multiwalled carbon nanotubes by polymer/surfactant mixtures of assorted composition: synergistic vs. antagonistic effects

Dispersibility and noncovalent functionalization of multiwalled carbon nanotubes by polymer/surfactant mixtures of assorted composition: synergistic vs. antagonistic effects

Bárbara Abreu[1,2], Ana Sofia Pires[1], Andreia Guimarães[1], Ricardo M. F. Fernandes[1] and Eduardo F. Marques[1*]

[1]CIQUP, Departamento de Química e Bioquímica, Faculdade de Ciências, Universidade do Porto, Rua do Campo Alegre P-4169-007 Porto, Portugal.

[2]REQUIMTE-LAQV, Departamento de Química e Bioquímica, Faculdade de Ciências da Universidade do Porto, Rua do Campo Alegre P-4169-007 Porto, Portugal.

*email: efmarque@fc.up.pt

Keywords:
Multiwalled carbon nanotubes; surfactant; polymer; polymer/surfactant systems; liquid-phase exfoliation; non-covalent functionalization

Abstract

Many applications of carbon nanotubes (CNTs) require that they are well-separated and well-dispersed in liquid phase. Surfactants or polymers have been extensively employed to disperse, stabilize and non-covalently functionalize CNTs in water, but mixed polymer/surfactant systems have been far less explored for that end. Yet, polymer/surfactant association could potentially enhance dispersibility, provide new features and hence be key to expand the application range of CNTs, for example in composites and coatings. In this work, we have investigated the ability of polymer/surfactant (P/S) mixtures to separate and disperse multiwalled carbon nanotubes (MWNTs) in water, using rigorously controlled processing conditions. Two types of mixtures were studied: i) nonionic polymer and ionic surfactant; and ii) nonionic surfactant and ionic polymer. Detailed and high precision dispersibility curves (concentration of dispersed nanotubes vs. total P + S concentration, at fixed S concentration) were obtained for four different P/S mixtures, and their respective individual components. Several quantitative metrics were extracted, allowing for reliable comparisons between the systems. Depending on the P/S mixture, either beneficial (synergistic) or detrimental (antagonistic) effects in nanotube dispersibility are observed compared to the individual components. Morphological characterization of the as-obtained dispersions by scanning electron microscopy (SEM) shows a significant degree of MWNT separation by the polymer/surfactant dispersants. The results are interpreted in terms of the interactions at play between the polymer/surfactant moieties and the nanotube surface, on one hand, and kinetic aspects related to mechanism of MWNT separation, on the other hand. These studies are of great interest for the choice of optimal conditions to obtain well-dispersed and non-covalently functionalized MWNTs for other applications.

1. Introduction

Carbon nanotubes (CNTs) can be envisaged as hollow cylinders, composed of rolled-up graphene sheets, possessing unique mechanical, thermal, optical, and electrical properties.[1, 2] The high length/diameter ratio of CNTs and the strong van der Waals (vdW) cohesive forces cause them to aggregate into bundles, ropes and entangled networks.[3-5] Single-walled carbon nanotubes (SWNTs) tend to form thick bundles in the as-produced powders, while multiwalled nanotubes (MWNTs) form thinner bundles and highly entangled networks where vdW bindings are particularly strong at the junction points.[5, 6] However, most applications—such as in polymer nanocomposites,[7] sensors[8] and electrocatalysis[9, 10]—require that the nanotubes are well-separated (i.e. individualized or in the form of thin bundles) and well-dispersed in a liquid phase. Amphiphile-mediated dispersion in aqueous solvents is one of the most effective methods to exfoliate and disperse CNTs.[11-14] Typically, this process involves two sequential steps: i) mechanical separation of the tube bundles, through an “unzipping” mechanism, where shear forces from the energy source, usually sonication, induce clefts between adjacent tubes, allowing the amphiphilic molecules to rapidly adsorb onto the exposed surface through its hydrophobic moiety, whereas the hydrophilic faces the solvent; and ii) removal of the undispersed and larger particles via centrifugation. The obtained carbon nanotubes, in the supernatant, remain stabilized due to steric (for non-ionic dispersants) or electrostatic (for ionic ones) repulsive forces.[15, 16]

Surfactants and polymers have been the subject of intense scrutiny, separately, as dispersants for carbon nanomaterials, namely for CNTs. With regard to surfactants, the low molecular-weight dispersants, the dispersibility of SWNTs and MWNTs using molecules with assorted molecular structure has been closely studied in the past 10-15 years.[4, 12, 14, 17-19] In recent work, we have carried out systematic studies under stringently controlled sonication/centrifugation conditions, which provided dispersibility curves (i.e. concentration of dispersed CNT vs. concentration of dispersant) with high precision and detail in profile, allowing for molecular insight on the mechanisms of the dispersing process.[13, 14, 20] As concerning polymers, the high molecular-weight dispersants, they have also been extensively dealt with as CNT dispersants, namely block copolymers,[21] polysaccharides[22] and proteins.[23, 24] The polymer-nanotube interaction is expected to have common features with surfactant-nanotube interaction. However, due to the much larger size of polymer molecules, some differences emerge and are commonly described according to two models: the “polymer wrapping” model[25], that implies strong attachment and low diffusivity of the wrapped polymer coil along the tube, and the “loose adsorption”

model,[26, 27] that suggests polymer-nanotube interactions are limited to the adsorbing block and hence higher mobility of the polymer chains exist. This interaction is particularly interesting, as polymers have also been used to produce composites with carbon nanomaterials, since they can be easily fabricated and are considered a group of relatively inexpensive materials for many engineering applications.[7, 28-31]

In surface and colloid science, polymer/surfactant (P/S) systems are of great fundamental interest and have been comprehensively studied over the last decades.[32-37] Different types of polymer-surfactant interactions (namely hydrophobic, electrostatic, H-bonding and London dispersive) and entropic effects (such as those related to polymer chain configuration or to counterion release when charged molecules are involved) result in rather complex phase behavior in solution. This behavior may assume the form of association or segregation, precipitation or complex coacervation, and formation of different types of P/S complexes or aggregates.[32, 34, 35] Polymer and surfactant often form molecular complexes or mixed aggregates over a wide range of surfactant concentration, starting well below the neat surfactant critical micelle concentration, *cmc*. In fact, the polymer chains often induce aggregation of the surfactant at a critical aggregation concentration, *cac*, which is sizably lower than *cmc*.[32, 33] In some cases, surfactant micelles or vesicles can also act as bridging points when hydrophobically modified polymers are used, resulting in the crosslinking of the systems.[38-40] Because of this versatility of properties and effects, P/S systems have also found a wide range of technical and industrial applications, *inter alia* in encapsulation and emulsification,[41] rheological control of colloidal suspensions[38, 42] and hydrogel formulation for drug delivery.[43, 44]

There is also a high potential of mixed PS systems as dispersants of nanomaterials and for the development of composite materials. However, the interaction between P/S complexes and hydrophobic surfaces and nanoparticles, and the consequent interaction between the coated surfaces (or particles), remains relatively less studied and less understood.[37, 45-48] In the particular case of the interaction of P/S systems with CNTs, this field is basically unexplored in the literature.

Herein, we aim at filling in this gap, contributing to unravel the features of polymer/surfactant mixtures as dispersants for CNTs. To investigate the mechanisms that lead to optimal CNT dispersion using P/S mixtures, a systematic study was carried out, encompassing different polymer/surfactant mixtures and strictly controlled processing conditions. For this purpose, the following molecules were chosen: surfactants sodium dodecylbenzene sulfonate, SDBS, cetyltrimethylammonium bromide, CTAB, and t-octylphenoxypolyethoxyethanol (Triton^{TM}-X 100), TX-100, (Fig.

1a) and the polymers polyvinylpyrrolidone, PVP, poly(diallyldimethyl ammonium chloride), PDDA, and sodium polyacrylate, PAS (Fig. 1b). To probe the role and applicability of the P/S mixtures in the dispersibility of carbon nanotubes, two types of basic systems were selected, in a total of four combinations: 1) non-ionic polymer (PVP) with ionic surfactant (CTAB, cationic, or SDBS, anionic) and 2) ionic polymer (PDDA, cationic, or PAS, anionic) with non-ionic surfactant (TX-100).

This systematic study could be a first set to lay the basis for a proper design of polymer/surfactant mixtures as effective and efficient dispersants for CNTs. Moreover, P/S systems could be used to non-covalently functionalize carbon nanotubes, aiming at the application of these nanomaterials as building blocks for robust hybrid materials, where the polymers could be key to impart adhesion and organization on the CNT surface.

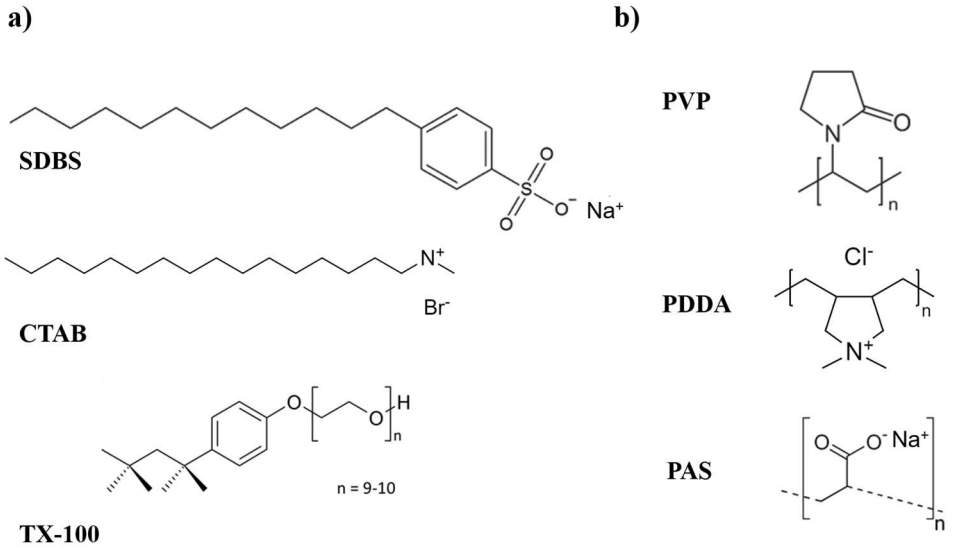

Fig. 1. Chemical structure of the dispersants used in this work: a) surfactants SDBS, sodium dodecylbenzene sulfonate, CTAB, cetyltrimethylammonium bromide and TX-100, t-octylphenoxypolyethoxyethanol; and b) polymers, PVP, polyvinylpyrrolidone, PDDA, poly(diallyldimethyl ammonium chloride) and PAS, sodium polyacrylate.

2. Experimental Section

2.1. Materials

Multiwalled carbon nanotubes (produced by catalytic chemical vapor deposition, purity > 95%) with outer diameter *d* = 8-15 nm and length *L* = 10-50 μm, were purchased from Cheap Tubes Inc. and used as received. All the polymers (PVP, PAS, PDDA) and

surfactants (CTAB, SDBS and TX-100) were acquired from Sigma Aldrich (purities ≥ 99 %) and used as received (see Supporting Information, Table S1, for further information on molecular properties).

2.2. Preparation of MWNT dispersions

Stock surfactant and polymer solutions were prepared in ultrapure water above Krafft temperature (*viz*. set to 25 ºC, except for CTAB, 30 ºC) to ensure full dissolution. Since our aim was to study the P/S interactions with MWNTs, the nanomaterial was dispersed in pre-prepared P/S solutions. Thus, the surfactant and polymer solutions were prepared separately and then mixed together for 24 h to ensure homogeneity in the final solution.

To prepare MWNT-polymer/surfactant dispersions, 9 mg of MWNT powder were weighted, followed by addition of the desired dispersant solution, 3 mL, resulting in a 0.3 wt% MWNT mixture. Sonication was performed using a Bandelin Sonoplus Vb 2070 probe (70 W output power; 20 kHz processing frequency) with a freshly polished 3 mm microtip, with sonication time set to 8.5 min and vibration amplitude to 30 %. A rigorous procedure, previously established,[13] was followed: 1) the sonication probe was always placed in the same position inside the same type of vial (1 cm from the bottom); 2) the sonication average power density transferred to the sample was kept constant at 1.0 $W \cdot mL^{-1}$ (controlled by calorimetric measurements); 3) the temperature of the system was controlled with an external thermostatic bath and set above the Krafft temperature of the surfactants. After sonication, the samples were centrifuged during 20 min at 4000 g. Finally, the top 30% of the supernatant were separated from the precipitate and MWNT concentration in the obtained dispersions was measured.

2.3. Quantification of MWNT concentration and dispersibility studies

The absolute carbon nanotube concentration in the supernatant was determined using a previously published method.[49] First, an accurately measured aliquot of MWNT dispersion was lyophilized during 24-48 h. The mass fraction of dispersant present on the solid was then determined by thermogravimetric analysis (TGA), using a Netzsch TG 209 F1-Iris under N_2 atmosphere (flow rate of 50 $mL \cdot min^{-1}$). The resulting mass balance allows to quantify the concentration of MWNTs in the analyzed sample (therefore, in the supernatant of the dispersion).[49] The absorbance versus c_{CNT} at λ = 660 nm (where the absorption from surfactant is null)[50, 51] of dilutions from a stock dispersion with known MWNT mass concentration was measured, and calibration curves (TGA-UV-vis) were then obtained. A single-beam UV spectrophotometer Agilent 8453 was used, with a plastic cuvette with an optical path of 1 cm.

On the basis of Beer-Lambert law and the linear regimes observed, the apparent extinction coefficient, ε_{660}, was determined yielding a value of 40 ± 2 mL·mg^{-1}·cm^{-1}, in line with previous reports.[13, 14, 52] The MWNT concentration in the final dispersions was then determined through the absorbance values obtained by UV-Vis spectrometry.

The dispersibility curves show the concentration of dispersed MWNTs (in mg·mL^{-1}) versus the dispersant concentration (in weight percent, wt%). The curves obtained typically follow a sigmoidal profile, as depicted in Fig. 2, similar to those previously obtained for monomeric[13] and dimeric (gemini) surfactants.[14] Statistical metrics can be withdrawn from the plots with this profile: *cdc,* critical dispersibility concentration, the concentration of dispersant needed for dispersibility to take off; $c_{MWNT@cdc}$, the concentration of MWNT dispersed at the *cdc*; $c_{disp,max}$, the dispersant (surfactant or polymer) concentration where maximum concentration of dispersed MWNT is attained: and $c_{MWNT,max}$, the latter value. For comparative purposes, the dispersing effectiveness (or yield), η, defined as the ratio (c_{MWNT} /$c_{MWNT,initial}$) x 100, and efficiency, η^*, defined as the ratio ($\eta/c_{disp,max}$), are also introduced. The effectiveness parameter measures the capability of the dispersant to disperse MWNTs with respect to the initial loading concentration, $c_{MWNT,initial}$ (herein, 3 mg·mL^{-1}). The efficiency is related with the dispersant concentration required to attain maximum MWNT dispersibility; an efficient dispersant should attain maximum MWNT dispersibility at the lowest c_{disp} possible.

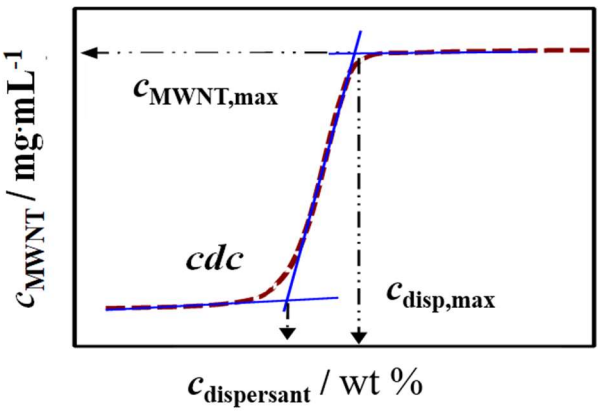

Fig. 2. Representative dispersibility curve with the graphical definition of the dispersion parameters.

2.4 Characterization of dispersed MWNTs by scanning electron microscopy (SEM)

The morphology of the dispersed MWNTs was characterized by scanning electron microscopy (SEM). To prepare the samples, a drop of MWNTs dispersion (diluted 100 times) was casted on a pre-heated (~110 °C) silicon wafer, followed by rinsing with ethanol to remove excess of surfactant. SEM imaging was performed on a FEI Quanta 400FE operated at 25 kV in SE mode, at CEMUP – Centro de Materiais da Universidade do Porto. A distribution of MWNTs (individual or small bundles) was recorded and statistically analyzed for each of the systems characterized. It should be noted that only the apparently individualized MWNTs were measured in the SEM micrographs. To ensure meaningful statistics, more than 100 objects were measured for each sample, except for MWNT/PAS system, where the entanglement of most nanotubes into larger aggregates precluded proper measurement of their width.

2.5 Zeta potential measurements

The zeta potential, ζ, of the dispersed particles (amphiphile-coated MWNTs) was measured using a zeta sizer Nano ZS, ZN 3500, with a 4 mW He-Ne laser (633 nm) and DTS 1060C disposable zeta cells, at 25 ºC. The electrophoretic mobility, μ, was measured using a combination of electrophoresis and laser Doppler velocimetry techniques and ζ was calculated from μ using the known Henry equation.[53, 54] A dielectric constant of 78.5, a medium viscosity of 0.89 cP and a $f(\kappa a)$ function value of 1.5 were used, following previously reported assumptions.[53, 54] All ζ values are average values based on at least 2 independent dispersions.

3. Results and Discussion

3.1 Dispersibility studies

To investigate the effect of surfactants, polymers, and their mixtures as dispersants of MWNTs, dispersibility curves of the selected systems were built using strictly controlled sonication/centrifugation conditions, allowing to compare the performance of individual dispersants with the P/S mixtures. It is worth mentioning that these curves represent the concentration of dispersed MWNTs vs. the initial dispersant concentration, i.e. the concentration prior to the sonication/centrifugation procedure, since during centrifugation some dispersant is lost to the precipitate.[14] As noted in section 2.3, the effect of surfactant concentration in the dispersibility of carbon nanotubes was assessed in previous works by our group.[13, 14, 20] Herein we report high-precision curves not only for surfactants, but

also for polymers and mixtures of these two dispersants. To prepare the polymer/surfactant systems, the approach followed was to fix the surfactant concentration while varying the polymer concentration. The aim was to investigate the influence of the addition of polymer to a small concentration of surfactant, to be more precise, at the minimum surfactant concentration required to take-off the MWNT dispersion, *cdc* (see Fig. 2).

To quantify the effect of the mixture in MWNT dispersibility compared to the individual dispersants (at the same conditions), a parameter *S* is defined:

$$S = \frac{c_{p+s}^{d}}{c_{p}^{d} + c_{s@cdc}^{d}} \quad (1)$$

where c_{p+s}^{d} is the MWNT concentration dispersed by the mixture of P/S mixture, c_{p}^{d} is the MWNT concentration dispersed by the polymer and $c_{s@cdc}^{d}$ is the MWNT concentration dispersed by the surfactant at the *cdc* (the surfactant concentration used in the mixtures). $S > 1$ implies that the P/S mixture shows synergism in nanotube dispersibility, while $S = 1$ denotes a null effect, and $S < 1$ indicates antagonism, i.e. a detrimental effect in the ability of the mixture to disperse compared to its components.

The results are organized as follows. First, we show the dispersibility curves obtained for the selected systems, divided into i) non-ionic polymer + ionic surfactant mixtures (PVP + SDBS and PVP + CTAB) and ii) ionic polymer + non-ionic surfactant mixtures (PDDA + TX-100 and PAS + TX-100). Some molecular level considerations on the main effects observed are presented for each system. In the following section, the SEM characterization of the dispersed MWNTs is presented for those systems that yield synergism at the *plateau* of the dispersibility curve, and lastly the zeta potential of the dispersed MWNTs is shown and discussed (confirming the non-covalent functionalization of the nanotubes).

3.1.1 Non-ionic polymer/ionic surfactant mixtures

Fig. 3a) shows the dispersibility curves obtained for the non-ionic polymer PVP, the anionic surfactant SDBS and the P/S mixture. It should be noted that the dispersant concentration for the mixture is the total polymer + surfactant concentration in the system.

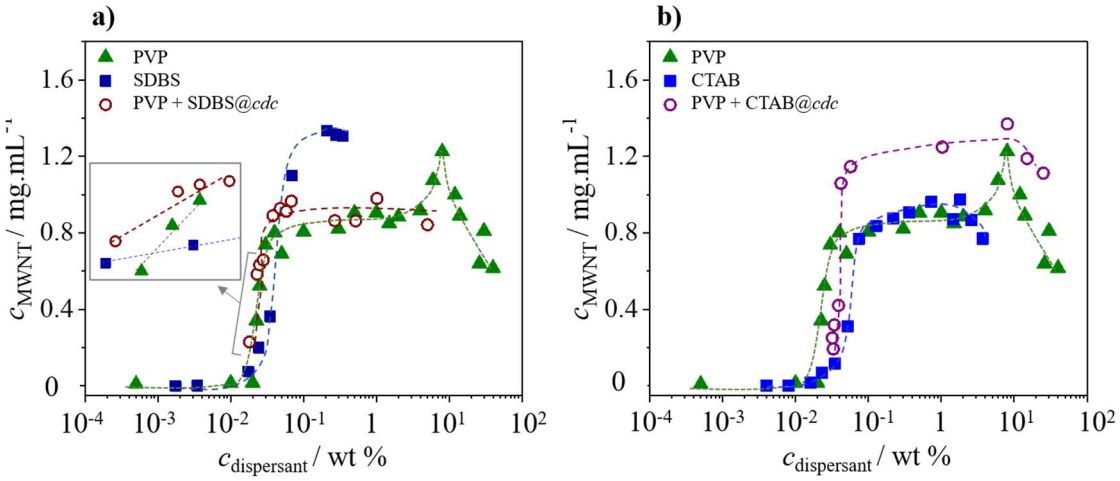

Fig. 3. Dispersibility curves obtained for a) PVP, SDBS and the mixture PVP + SDBS@*cdc* and b) PVP, CTAB and the mixture PVP + CTAB@*cdc*. Uncertainty bars are estimated as ca. ± 10 % for c_{MWNT}, based on at least 3 independent dispersions for each dispersant concentration reported. For the P/S mixtures, $c_{dispersant}$ is the total polymer + surfactant concentration; the polymer concentration is varied, while the surfactant is fixed at the *cdc*.

Table 1. Parameters obtained from the dispersibility curves of the ionic surfactants (SDBS and CTAB), non-ionic polymer (PVP) and respective mixtures (PVP + SDBS@*cdc* and PVP + CTAB@*cdc*).[a]

	PVP	**SDBS**	**CTAB**	**PVP + SDBS@*cdc***	**PVP + CTAB@*cdc***
cdc/wt%	0.019	0.018	0.032	-	0.0073
$c_{MWNT@cdc}$ /mg·mL^{-1}	0.017	0.069	0.078	-	-
$c_{disp,max}$ /wt%	0.030	0.080	0.084	0.030	0.011
$c_{MWNT,max}$ /mg·mL^{-1}	0.81	1.3	0.90	0.91	1.3
η/ %	27	44	30	30	43

[a] The precision is estimated as ca. ±10% for $c_{MWNT,max}$, while higher, ca. ±20% for the other two parameters, *cdc* and $c_{disp,max}$, since the latter depend strongly on the availability of many enough and clearly assignable points in the quickly ascending parts of the respective dispersion curves.

From Fig. 3a), it can be seen that although the polymer is *per se* a good dispersant, with an effectiveness of η = 27 % (Table 1), comparable to that of previously reported systems,[13, 14] SDBS is an even better one, showing η = 44 %. When PVP is added to SDBS (at a fixed concentration, *cdc* = 0.018 wt %) and this mixture is used as MWNT dispersant, interesting features emerge. Although at the *plateau* of the

dispersibility curve, the performance of the P/S mixture is clearly inferior to that of the surfactant alone, a beneficial effect is observed at low P + S concentrations (before the *plateau* is reached), as shown in more detail in the inset of Fig. 3a), with the mixture inducing higher MWNT dispersibility than the individual P and S dispersants. To demonstrate this point, at $c_{dispersant}$ = 0.023 wt % (where c_{PVP}= 0.005 wt % and c_{SDBS}= 0.018 wt %), c_{MWNT} of the mixture is 0.58 mg·mL^{-1}. However, at the referred concentrations, individual dispersants only reach c_{MWNT} = 0.069 mg·mL^{-1} for SDBS and c_{MWNT} = 0.012 mg·mL^{-1} for PVP. To quantify this effect, equation 1 can be applied (see S.I., Section S2 for details), yielding S = 7.2, i.e., showing that the mixture is 7 times more effective than the sum effect of the parts. Indeed, for a dispersant concentration up to 0.04 wt%, the mixture shows an average S = 5.9, that is, a strong synergistic effect of the PVP + SDBS mixture when low polymer concentrations are added to the surfactant.

These observations suggests that, at low concentrations, polymer/surfactant association may lead to enhanced ability of the dispersants to adsorb at the surface of the nanotubes. This could be a phenomenon similar to that occurring in the bulk, in which the polymer chains act as regions where the surfactant molecules tend to aggregate, giving rise to a *cac* lower than *cmc*. In the case of CNTs, the polymer (if in sufficient concentration) could readily adsorb at the clefts between entangled tubes that form due to the shear forces induced by sonication. If so, the adsorbed polymer chains could act themselves as sites for surfactant rapid binding. Alternatively, one could think that the adsorption takes place by the P/S complexes already formed, through the hydrophobic moieties. Some indirect support for this hypothesis comes from previous studies where it was experimentally observed that the anionic surfactant SDS strongly interacts with PVP.[55]

Upon increasing polymer concentration in Fig. 3a), the surfactant effect is overtaken by the high polymer concentrations. At the *plateau* of the curve, the dispersibility metrics shown in Table 1 can be applied to equation 1, and S determined. Although above 1, S decreases significantly to 1.03 and, given the uncertainty associated to the metrics, a null value can be considered. These observations suggest that at high excess of polymer compared to surfactant, the strong association between surfactant and polymer in the bulk may supersede with the adsorption at the carbon surface, resulting in a CNT dispersibility that is just dominated by the available polymer concentration and its rapid adsorption when the inter-tube clefts are produced by sonication.

The same methodology was applied using a cationic surfactant, CTAB (Fig. 3b). For these systems, although the polymer starts dispersing at lower concentrations than

the surfactant (thus being more efficient, i.e. having higher η^*), the yield performance of the individual dispersants (CTAB and PVP) is similar. When PVP is added to CTAB (again, fixed at the *cdc* of the surfactant), first, in the low dispersant concentration region, the performance of the mixture appears between that of the individual dispersants. However, and interestingly, a *plateau* appears at higher concentrations of dispersed MWNTs, indicating a higher effectiveness of the mixture. The corresponding MWNT concentration dispersed by CTAB at its *cdc* is 0.078 mg·mL^{-1}; for PVP, $c_{MWNT,max}$ = 0.81 mg·mL^{-1}. The $c_{MWNT,max}$ for this mixture is 1.3 mg·mL^{-1}, corresponding to an increase of 46 % in effectiveness (i.e., S = 1.46) and hence indicating the presence of synergism at high polymer concentrations, in contrast to the previous system. A possible explanation for the latter effect could be the onset of repulsions between polymer chains caused by the surfactant binding to the polymer.[56-58] This in turn would case the polymer chains to uncoil (i.e. become more expanded), thus providing more active sites for adsorption of surfactant unimers at the nanotube surface. This view assumes, however, that for this particular system, the polymer/surfactant bulk interaction is comparatively weaker than that occurring when a surface is available (in contrast, with the PVP/SDBS). We performed similar experiments with CTAB concentration fixed at $c_{s,max}$ (at the *plateau* of its dispersibility curve). Since one is working at the $c_{disp,max}$ of the surfactant, only the dispersion *plateau* appears, not allowing to withdraw the dispersion metrics (cf. S.I., Fig. S3.1). Also, no synergism occurs at the conditions used.

3.1.2. Ionic polymer/nonionic surfactant mixtures

The same procedure described previously was applied for ionic polymer + non-ionic surfactant systems. The surfactant concentration was fixed at its *cdc*, and polymer was added to the system at different concentrations. Figure 4a) shows the dispersibility curves for a cationic polymer, PDDA, a non-ionic surfactant, TX-100, and the mixture PDDA + TX-100. As individual dispersant, the polymer has a significantly superior performance than the surfactant. In fact, the polymer is more effective, dispersing 40% of the initial MWNTs compared to 26% for the surfactant (Table 2), and more efficient, starting the dispersion of MWNTs at a concentration 2 orders of magnitude lower than TX-100. However, using PDDA + TX-100 mixture as dispersant, the results were rather surprising. It was virtually impossible to obtain any meaningful dispersion of MWNTs with this system. A possible explanation for this effect could be the strong P/S association in the bulk driven by the hydrophobic segment of TX-100 and hydrophobic backbone of PDDA, competing with the fast adsorption of these parts at the MWNT surface, thus inhibiting any effective ability to disperse the nanotubes.

Fig. 4b) shows the MWNT dispersibility curves using an anionic surfactant, PAS. In stark contrast to PDDA, PAS shows a poor performance as MWNT dispersant, with the lowest effectiveness determined in this work, η = 4%.

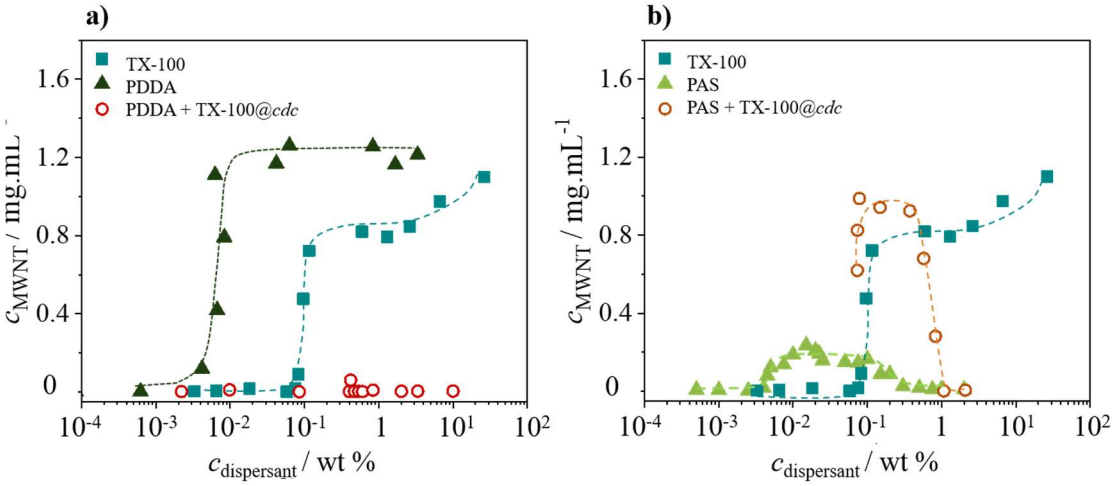

Fig. 4. Dispersibility curves obtained for a) TX-100, PDDA and the mixture PDDA + TX-100@*cdc* and b) TX-100, PAS and the mixture PAS + TX-100@*cdc*. Uncertainty bars are estimated as ca. ± 10 % for c_{MWNT}, based on at least 3 independent dispersions for each dispersant concentration reported.

Table 2. Parameters obtained from the dispersibility curves of the non-ionic surfactant (TX-100), ionic polymers (PDDA and PAS) and the mixture PAS+TX-100@*cdc*.[a]

	TX-100	**PDDA**	**PAS**	**PAS + TX-100@*cdc***
cdc /wt%	0.073	0.0018	0.0037	-
$c_{MWNT@cdc}$ / mg·mL^{-1}	0.011	0.00055	0.013	-
$c_{disp,max}$ / wt%	0.11	0.011	0.0051	-
$c_{MWNT,max}$ / mg·mL^{-1}	0.78	1.2	0.13	0.85
η / %	26	40	4	28

[a] The precision is estimated as ca. ±10% for $c_{MWNT,max}$, while higher, ca. ±20% for the other two parameters, *cdc* and $c_{disp,max}$, since the latter depend strongly on the availability of many enough and clearly assignable points in the quickly ascending parts of the respective dispersion curves.

The addition of PAS to a fixed concentration of TX-100 (0.073 wt %, corresponding to the *cdc*), and the use of the mixed system as dispersant shows, however, notable results. For the PAS+TX-100@*cdc* mixture, the existence of synergism is clear. The $c_{MWNT,max}$ of the mixture is 0.85 mg·mL^{-1}, while the values for TX-100 at the *cdc* and PAS at $c_{disp,max}$ are 0.011 and 0.13 mg·mL^{-1}, respectively, which yields S = 6, i.e. a 6-fold increase in effectiveness. PAS is a highly hydrophilic polymer, and so one can presume that the binding of surfactant molecules onto the polymer chains will introduce therein hydrophobic segments, improving the adsorption rate on the MWNT surface and

hence providing higher dispersing power to the polymer/surfactant system compared to the individual components.

3.2. Morphological characterization of MWNTs in the dispersions

The aggregation state of the dispersed carbon nanotubes is an important parameter to determine the applicability of the mixtures as dispersants. An ideal dispersant attains a high concentration of well-separated CNTs (ideally, in individual state). The systems that presented stronger synergism at the *plateau* (thus dispersing high concentration of MWNTs), PVP+CTAB@*cdc* and PAS+TX-100@*cdc*, were imaged by SEM, and the size of the tubes (individualized or in thin bundles) was measured and critically compared among individual dispersants and mixtures. For this, dispersions at the respective *plateau* regions of the dispersibility curves (Figures 3b and 4b) were analyzed. SEM representative micrographs and respective distribution of the bundle diameters are shown in Fig. 5 and 6.

The average tube diameter, *d,* was obtained through a log-normal fitting of the size distributions. Fig. 5 shows that, for PVP + CTAB system, no significative differences exist between the dispersions obtained by the individual dispersants or the mixture, with the average *d* lying in the range of 14 and 18 nm, indicative of a very high degree of individualization (since the tube diameter as indicated by the supplier is within 8-15 nm). In Fig. 6, however, one can observe a high degree of entanglement of the MWNTs dispersed by PAS (which does not allow us to get a measure of diameter for a statistically representative number of distinctly dispersed MWNTs), contrasting with the images obtained for the MWNT/TX-100 and MWNT/(PAS + TX-100) systems. In fact, the MWNT dispersions obtained by the PAS + TX-100 mixtures show a smaller average tube diameter (and a size distribution shifted to lower values) than those dispersed just by TX-100, evidencing that, for this specific system, the beneficial effect of the polymer/surfactant combination is not only quantitative, but also concerns the quality of the obtained dispersions.

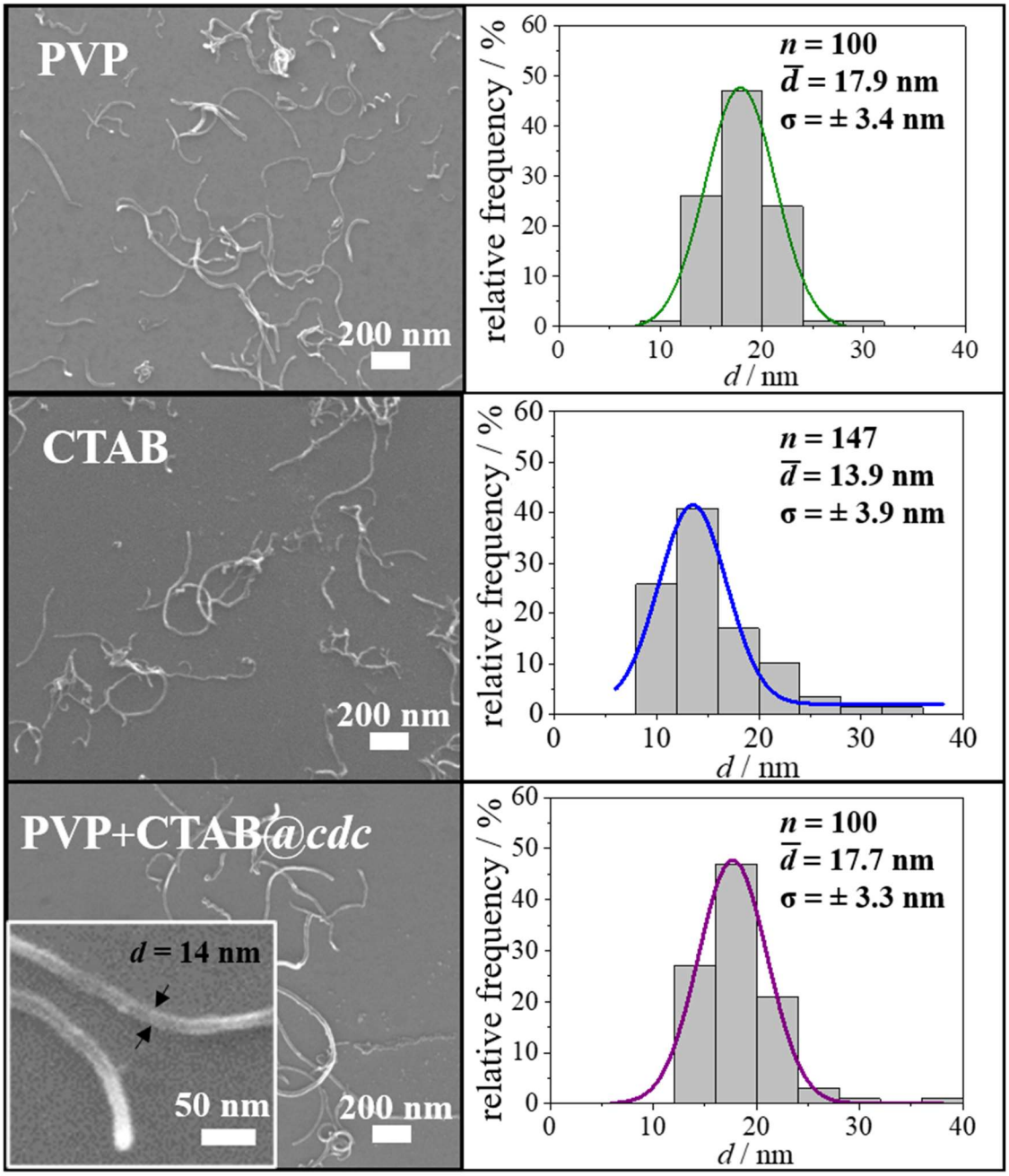

Fig. 5. Representative SEM micrographs and respective histograms of MWNT dispersed by PVP, CTAB and PVP + CTAB@*cdc*. The histograms obtained based on SEM imaging of PVP and PVP/CTAB systems were fitted to a lognormal distribution.

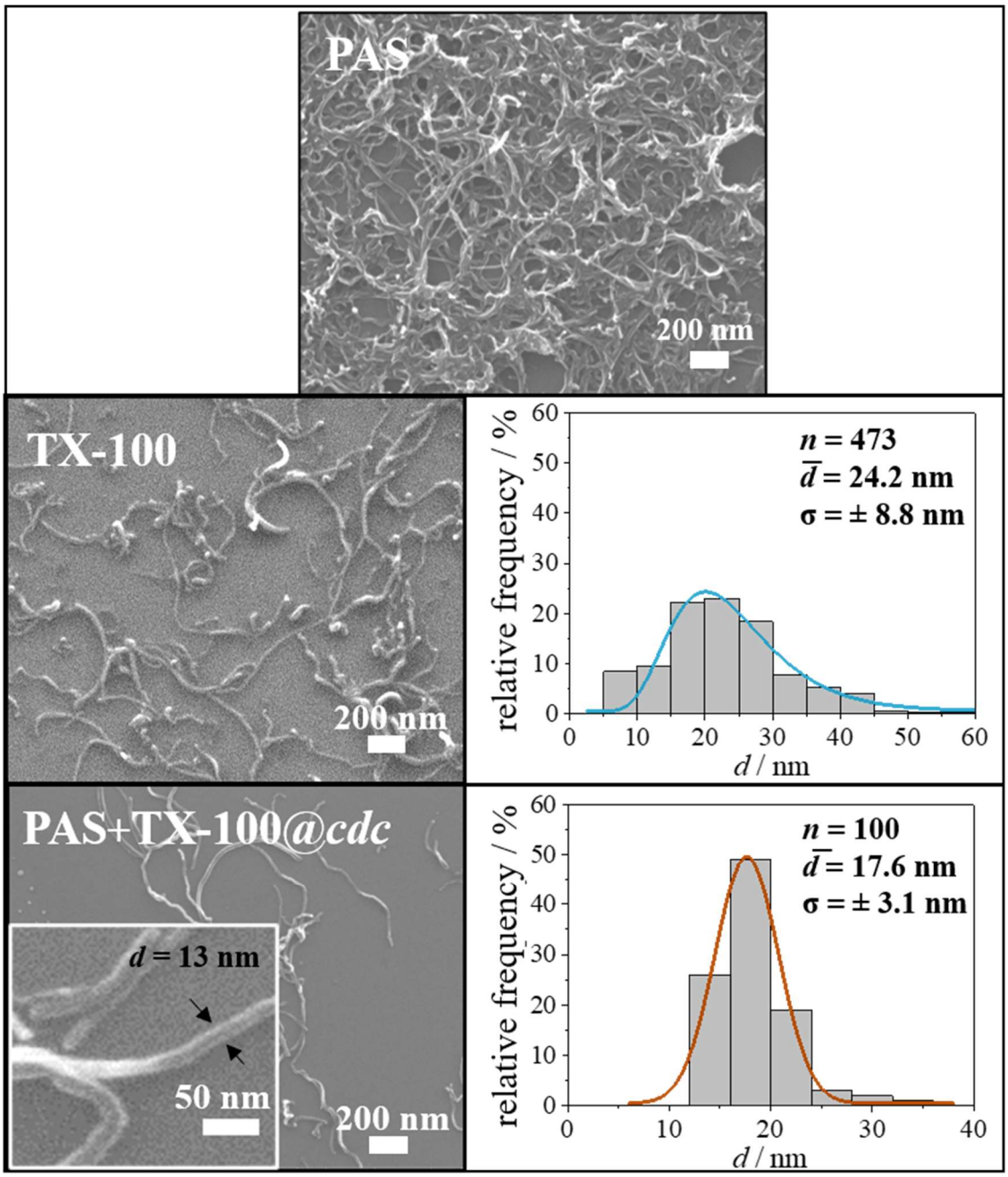

Fig. 6. Representative SEM micrographs and respective histograms of MWNT dispersed by PAS, TX-100 and PAS + TX-100@*cdc*. The histograms obtained based on SEM imaging of TX-100 and PAS + TX-100@*cdc* systems were fitted to a lognormal distribution.

3.3 Zeta potential studies of the MWNT dispersions

For most of the studied systems, electrostatic repulsions are responsible for the stabilization of the MWNTs, since the adsorbed dispersant molecules impart effective charge to the coated tubes. The extent of electrostatic repulsions can be quantified by the electric potential in the surroundings of the dispersed MWNTs.[53] Zeta potential, ζ, was measured for solutions of each dispersant (individual components and mixtures) and for their respective MWNT dispersions at the *plateau* of the dispersibility curves (Fig. 7). For the MWNT dispersions with PDDA + TX-100, ζ values could not be obtained due to the poor performance of this system as dispersant.

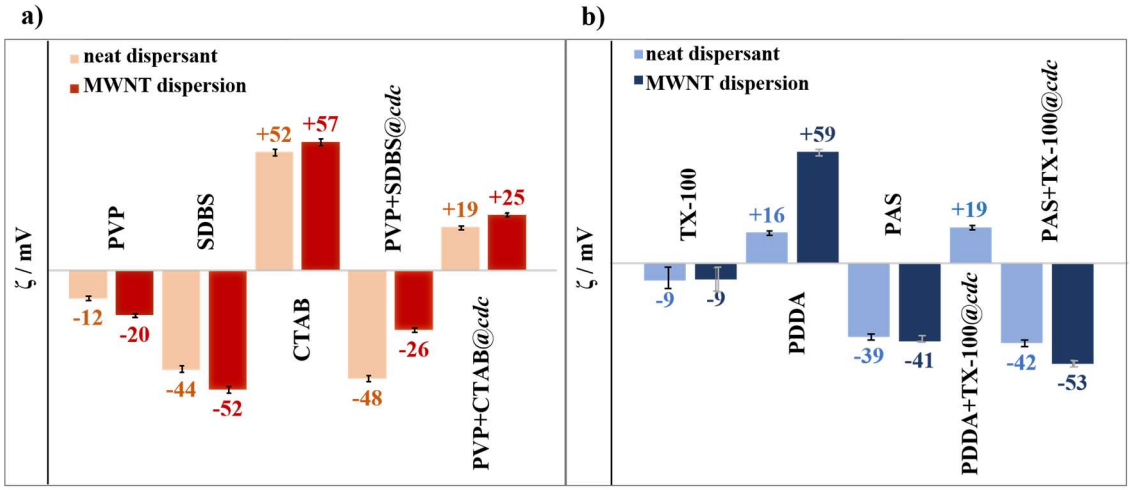

Fig. 7. Zeta potential values obtained for the solution of the neat polymers (P), neat surfactants (S) and polymer/surfactant (P/S) mixtures, and for the MWNT dispersions obtained with each type of dispersant, (P, S and P/S). a) non-ionic polymer/ ionic surfactant systems; b) ionic polymer/ non-ionic surfactant systems.

A general view of Fig. 7 shows that | ζ | for the MWNT dispersions (i.e. for the amphiphile-coated MWNTs) is similar or higher than that for the respective neat dispersant, in line with previous works.[53, 54] The exception for this trend is the PVP + SDBS@*cdc* system, which shows a ζ value less negative than the neat dispersant solution and close to the ζ of the MWNT/PVP dispersion. Zeta potentials of polymer or surfactant-coated CNTs tend to reflect the charge of the adsorbed particles.[53] Therefore, a ζ similar to that of PVP-coated MWNTs is in line with the analysis of the curve in Fig 3a, where it was observed that at high polymer concentrations (i.e. at the *plateau*) the effect of SDBS in MWNT dispersion is overshadowed by the polymer. Regarding the MWNT dispersions with PVP + CTAB@*cdc*, a zeta potential slightly inferior to + 30 mV was obtained, thus considerably less positive than that for the surfactant alone (ζ = + 57 mV). The former value can be reasonably understood, since partial charge neutralization

induced by CTAB is expected due to the negative ζ observed for the MWNT/PVP particles. Surfactant or polymer-stabilized particles are expected to show colloidal stability when | ζ | > 30 mV. If the adsorbent has a non-ionic nature, particles with | ζ | < 15 mV can also be kinetically stable due to steric repulsions.[53] Therefore, the PVP + CTAB@*cdc* dispersions, with ζ = + 25 mV, are possibly stabilized by both electrostatic and steric repulsions, imparted by the surfactant and the polymer, respectively.

Regarding the ionic-polymer/ non-ionic surfactant systems (Fig.7b), MWNT/PDDA stands out, since ζ is much more positive than the value measured for the neat polymer solution. This can be attributed to the adsorption of the polymer hydrophobic moieties on the MWNT surface, resulting in the stretching of the polymer chains on the carbon surface and consequent exposure of the charges. The PDDA + TX-100@*cdc* solution (no MWNTs present) shows a ζ value similar to that of the PDDA neat solution, suggesting the entanglement of polymeric chains and reduced charge exposure.

The enhanced dispersibility of the PAS + TX-100@*cdc* mixture observed in the dispersibility curves (Fig. 4b) indicates that this system clearly stands out regarding synergism in MWNT dispersion, as previously discussed. In fact, this polymer/surfactant mixture has more negative ζ than the polymer itself (which is a polyelectrolyte and thus the intrinsically charged component in the mixture), implying that the polymer charges are more exposed, due to the uncoiling of the polymeric chains with the surfactant binding and consequent adsorption on the nanotube surface through the hydrophobic moieties.

4. Conclusions

The effect of polymers, surfactants, and their mixtures as dispersants of multiwalled carbon nanotubes was assessed by applying a robust methodology that allowed to obtain comparable dispersibility curves and rationalize the influence of the mixture of dispersants. Six individual dispersants (SDBS, CTAB, TX-100, PVP, PDDA and PAS) and four polymer/surfactant combinations (PVP+SDBS@*cdc*, PVP+CTAB@*cdc*, PDDA+TX-100@*cdc* and PAS+TX-100@*cdc*) were studied regarding their ability to disperse in quantitative terms, their separation degree and their zeta potential. Dispersibility curves for PVP + SDBS system show synergism when low concentrations of polymer are added to the surfactant; however, the surfactant effect is overshadowed at the *plateau* of the dispersibility curve, with the mixture showing a performance close to PVP individually. Changing the surfactant to CTAB, the opposite effect is observed: at

low PVP concentrations, the mixture shows a performance between that of the individual dispersants; however, on increasing polymer concentration, a beneficial effect of the mixture is observed at the *plateau* of the dispersibility curve.

The PAS + TX-100@*cdc* mixtures show strong synergism, that is, a significant increase in the maximum concentration of MWNT dispersed, compared with that of the individual dispersants. This is attributed to the surfactant binding to the polymer, resulting in interchain repulsions and stretching of the polymer chains, hence increasing the effectiveness of dispersal. However, results for the PDDA + TX-100@*cdc* system suggest that hydrophobic effects might result in the blocking of the polymer adsorption sites, decreasing the effectiveness for these MWNT dispersions.

SEM analysis confirmed that well-dispersed MWNTs (individual or in thin bundles) are obtained in the systems that present quantitative synergism. Zeta potential results also permit us to infer that the nanotubes in the as-obtained dispersions are non-covalently functionalized and stabilized mostly by electrostatic repulsions.

Overall, the results presented in this paper unveil the potential of polymer/surfactant mixtures for producing high quality dispersions of carbon nanotubes, showing that specific mixtures yield strong synergistic effects. Moreover, one could think that the presence of polymer/surfactant moieties in the nanotube surfaces could be an interesting asset to explore, namely for the development of nanocomposites or coating films containing MWNTs.

CRediT authorship contribution statement

Bárbara Abreu: Conceptualization, Methodology, Investigation, Validation, Formal analysis, Writing – original draft. **Ana Sofia Pires:** Investigation, Formal analysis. **Andreia Guimarães:** Investigation, Formal analysis. **Ricardo Fernandes:** Conceptualization, Methodology. **Eduardo F. Marques:** Conceptualization, Methodology, Validation, Formal analysis, Writing – review & editing, Supervision, Project administration, Funding acquisition.

Declaration of Competing Interest

There are no conflicts of interest to declare.

Acknowledgments

The authors acknowledge Fundação para a Ciência e para a Tecnologia (FCT) for financial support through project UIDB/00081/2020. Bárbara Abreu also acknowledges financial support from FCT through the PhD grant PD/BD/128129/2016 from FCT.

References

1. Baughman, R. H.; Zakhidov, A. A.; De Heer, W. A., Carbon nanotubes--the route toward applications. *Science* **2002,** *297* (5582), 787-792.
2. Iijima, S., Helical microtubules of graphitic carbon. *Nature* **1991,** *354* (6348), 56-58.
3. Premkumar, T.; Mezzenga, R.; Geckeler, K. E., Carbon nanotubes in the liquid phase: Addressing the issue of dispersion. *Small* **2012,** *8* (9), 1299-1313.
4. Angelikopoulos, P.; Bock, H., The science of dispersing carbon nanotubes with surfactants. *Phys. Chem. Chem. Phys* **2012,** *14* (27), 9546-57.
5. Huang, Y. Y.; Terentjev, E. M., Dispersion of carbon nanotubes: Mixing, sonication, stabilization, and composite properties. *Polymers* **2012,** *4* (1), 275-295.
6. Dresselhaus, M. S.; Endo, M., Relation of carbon nanotubes to other carbon materials. In *Carbon Nanotubes: Synthesis, Structure, Properties, and Applications*, Dresselhaus, M. S.; Dresselhaus, G.; Avouris, P., Eds. Springer Berlin Heidelberg: Berlin, Heidelberg, 2001; pp 11-28.
7. Ma, P.-C.; Siddiqui, N. A.; Marom, G.; Kim, J.-K., Dispersion and functionalization of carbon nanotubes for polymer-based nanocomposites: A review. *Compos. Part A Appl. Sci. Manuf.* **2010,** *41* (10), 1345-1367.
8. Loh, K. J.; Lynch, J. P.; Kotov, N. A. In *Passive wireless strain and pH sensing using carbon nanotube-gold nanocomposite thin films*, 2007.
9. Pahmy, R. H.; Mohamed, A. R., Utilization of carbon nanotubes as a support material in metal-based catalyst systems: Applications in catalysis. *Recent Pat. Eng.* **2012,** *6* (1), 31-47.
10. Faba, L.; Criado, Y. A.; Gallegos-Suarez, E.; Perez-Cadenas, M.; Diaz, E.; Rodriguez-Ramos, I.; Guerrero-Ruiz, A.; Ordonez, S., Preparation of nitrogen-containing carbon nanotubes and study of their performance as basic catalysts. *Appl Catal a-Gen* **2013,** *458*, 155-161.
11. Wang, H., Dispersing carbon nanotubes using surfactants. *Curr. Opin. Colloid Interface Sci* **2009,** *14* (5), 364-371.
12. Clark, M. D.; Subramanian, S.; Krishnamoorti, R., Understanding surfactant aided aqueous dispersion of multi-walled carbon nanotubes. *J. Colloid Interface Sci.* **2011,** *354* (1), 144-51.
13. Fernandes, R. M.; Abreu, B.; Claro, B.; Buzaglo, M.; Regev, O.; Furó, I.; Marques, E. F., Dispersing carbon nanotubes with ionic surfactants under controlled conditions: Comparisons and insight. *Langmuir* **2015,** *31* (40), 10955-65.
14. Abreu, B.; Rocha, J.; Fernandes, R. M. F.; Regev, O.; Furó, I.; Marques, E. F., Gemini surfactants as efficient dispersants of multiwalled carbon nanotubes: Interplay of molecular parameters on nanotube dispersibility and debundling. *J. Colloid Interface Sci.* **2019,** *547*, 69-77.
15. Strano, M. S.; Moore, V. C.; Miller, M. K.; Allen, M. J.; Haroz, E. H.; Kittrell, C.; Hauge, R. H.; Smalley, R. E., The role of surfactant adsorption during ultrasonication in the dispersion of single-walled carbon nanotubes. *J. Nanosci. Nanotechnol.* **2003,** *3* (1-2), 81-6.
16. Jiang, L.; Gao, L.; Sun, J., Production of aqueous colloidal dispersions of carbon nanotubes. *J. Colloid Interface Sci* **2003,** *260* (1), 89-94.
17. Coleman, J. N., Liquid-phase exfoliation of nanotubes and graphene. *Adv. Funct. Mater.* **2009,** *19* (23), 3680-3695.
18. Poorgholami-Bejarpasi, N.; Sohrabi, B., Role of surfactant structure in aqueous dispersions of carbon nanotubes. *Fluid Phase Equilibr* **2015,** *394*, 19-28.
19. Saint-Aubin, K.; Poulin, P.; Saadaoui, H.; Maugey, M.; Zakri, C., Dispersion and film-forming properties of poly(acrylic acid)-stabilized carbon nanotubes. *Langmuir* **2009,** *25* (22), 13206-11.
20. Dai, J.; Fernandes, R. M.; Regev, O.; Marques, E. F.; Furó, I. n., Dispersing carbon nanotubes in water with amphiphiles: Dispersant adsorption, kinetics, and bundle size distribution as defining factors. *J. Phys. Chem. C* **2018,** *122* (42), 24386-24393.

21. Fernandes, R. M. F.; Dai, J.; Regev, O.; Marques, E. F.; Furó, I., Block copolymers as dispersants for single-walled carbon nanotubes: Modes of surface attachment and role of block polydispersity. *Langmuir* **2018,** *34* (45), 13672-13679.
22. Kwon, T.; Lee, G.; Choi, H.; Strano, M. S.; Kim, W. J., Highly efficient exfoliation of individual single-walled carbon nanotubes by biocompatible phenoxylated dextran. *Nanoscale* **2013,** *5* (15), 6773-6778.
23. Horn, D. W.; Tracy, K.; Easley, C. J.; Davis, V. A., Lysozyme dispersed single-walled carbon nanotubes: Interaction and activity. *J. Phys. Chem. C* **2012,** *116* (18), 10341-10348.
24. Huang, X.; Li, R.; Zeng, L.; Li, X.; Xi, Z.; Wang, K.; Li, Y., A multifunctional carbon nanotube reinforced nanocomposite modified via soy protein isolate: A study on dispersion, electrical and mechanical properties. *Carbon* **2020,** *161*, 350-358.
25. O'Connell, M. J.; Boul, P.; Ericson, L. M.; Huffman, C.; Wang, Y.; Haroz, E.; Kuper, C.; Tour, J.; Ausman, K. D.; Smalley, R. E., Reversible water-solubilization of single-walled carbon nanotubes by polymer wrapping. *Chem. Phys. Lett.* **2001,** *342* (3-4), 265-271.
26. Dror, Y.; Pyckhout-Hintzen, W.; Cohen, Y., Conformation of polymers dispersing single-walled carbon nanotubes in water: A small-angle neutron scattering study. *Macromolecules* **2005,** *38* (18), 7828-7836.
27. Fernandes, R. M. F.; Buzaglo, M.; Shtein, M.; Pri Bar, I.; Regev, O.; Marques, E. F.; Furó, I., Lateral diffusion of dispersing molecules on nanotubes as probed by NMR. *J. Phys. Chem. C* **2014,** *118* (1), 582-589.
28. Regev, O.; ElKati, P. N. B.; Loos, J.; Koning, C. E., Preparation of conductive nanotube-polymer composites using latex technology. *Adv. Mater.* **2004,** *16* (3), 248-+.
29. Moniruzzaman, M.; Winey, K. I., Polymer nanocomposites containing carbon nanotubes. *Macromolecules* **2006,** *39* (16), 5194-5205.
30. Liu, F.; Hu, N.; Ning, H. M.; Atobe, S.; Yan, C.; Liu, Y. L.; Wu, L. K.; Liu, X. Y.; Fu, S. Y.; Xu, C. H.; Li, Y. Q.; Zhang, J. Y.; Wang, Y.; Li, W. D., Investigation on the interfacial mechanical properties of hybrid graphene-carbon nanotube/polymer nanocomposites. *Carbon* **2017,** *115*, 694-700.
31. Punetha, V. D.; Rana, S.; Yoo, H. J.; Chaurasia, A.; McLeskey, J. T.; Ramasamy, M. S.; Sahoo, N. G.; Cho, J. W., Functionalization of carbon nanomaterials for advanced polymer nanocomposites: A comparison study between CNT and graphene. *Prog. Polym. Sci.* **2017,** *67*, 1-47.
32. Piculell, L.; Lindman, B., Association and segregation in aqueous polymer/polymer, polymer surfactant, and surfactant surfactant mixtures - Similarities and differences. *Adv. Colloid Interface Sci.* **1992,** *41*, 149-178.
33. Goddard, E. D., Polymer/surfactant interaction: Interfacial aspects. *J. Colloid Interface Sci.* **2002,** *256* (1), 228-235.
34. Antunes, F. E.; Marques, E. F.; Miguel, M. G.; Lindman, B., Polymer-vesicle association. *Adv. Colloid Interface Sci.* **2009,** *147-148*, 18-35.
35. Chiappisi, L.; Hoffmann, I.; Gradzielski, M., Complexes of oppositely charged polyelectrolytes and surfactants – recent developments in the field of biologically derived polyelectrolytes. *Soft Matter* **2013,** *9* (15), 3896-3909.
36. Burrows, H. D.; Valente, A. J. M.; Costa, T.; Stewart, B.; Tapia, M. J.; Scherf, U., What conjugated polyelectrolytes tell us about aggregation in polyelectrolyte/surfactant systems. *J. Mol. Liq.* **2015,** *210*, 82-99.
37. Guzmán, E.; Llamas, S.; Maestro, A.; Fernández-Peña, L.; Akanno, A.; Miller, R.; Ortega, F.; Rubio, R. G., Polymer-surfactant systems in bulk and at fluid interfaces. *Adv. Colloid Interface Sci* **2016,** *233*, 38-64.
38. Bai, D.; Khin, C. C.; Chen, S. B.; Tsai, C.-C.; Chen, B.-H., Interaction between a Nonionic Surfactant and a Hydrophobically Modified 2-Hydroxyethyl Cellulose. *J. Phys. Chem. B* **2005,** *109* (11), 4909-4916.
39. Regev, O.; Marques, E. F.; Khan, A., Polymer-induced structural effects on catanionic vesicles: Formation of faceted vesicles, disks, and cross-links. *Langmuir* **1999,** *15* (2), 642-645.
40. Alves, L.; Lindman, B.; Klotz, B.; Böttcher, A.; Haake, H. M.; Antunes, F. E., On the rheology of mixed systems of hydrophobically modified polyacrylate microgels and surfactants: Role of the surfactant architecture. *J. Colloid Interface Sci.* **2018,** *513*, 489-496.
41. Sharipova, A. A.; Aidarova, S. B.; Mutaliyeva, B. Z.; Babayev, A. A.; Issakhov, M.; Issayeva, A. B.; Madybekova, G. M.; Grigoriev, D. O.; Miller, R., The use of polymer and surfactants for the microencapsulation and emulsion stabilization. *Colloids Interfaces* **2017,** *1* (1), 3.

42. Malkin, A. Y.; Zuev, K. V.; Arinina, M. P.; Kulichikhin, V. G., Modifying the viscosity of heavy crude oil using surfactants and polymer additives. *Energy Fuels* **2018,** *32* (11), 11991-11999.
43. Wang, W.; Sande, S. A., Kinetics of re-equilibrium of oppositely charged hydrogel–surfactant system and its application in controlled release. *Langmuir* **2013,** *29* (22), 6697-6705.
44. Jabeen, S.; Chat, O. A.; Maswal, M.; Ashraf, U.; Rather, G. M.; Dar, A. A., Hydrogels of sodium alginate in cationic surfactants: Surfactant dependent modulation of encapsulation/release toward Ibuprofen. *Carbohydr. Polym.* **2015,** *133*, 144-153.
45. Langevin, D., Polyelectrolyte and surfactant mixed solutions. Behavior at surfaces and in thin films. *Adv. Colloid Interface Sci* **2001,** *89-90*, 467-484.
46. Nylander, T.; Samoshina, Y.; Lindman, B., Formation of polyelectrolyte-surfactant complexes on surfaces. *Adv. Colloid Interface Sci* **2006,** *123-126* (SPEC. ISS.), 105-123.
47. Bain, C. D.; Claesson, P. M.; Langevin, D.; Meszaros, R.; Nylander, T.; Stubenrauch, C.; Titmuss, S.; von Klitzing, R., Complexes of surfactants with oppositely charged polymers at surfaces and in bulk. *Adv. Colloid Interface Sci.* **2010,** *155* (1-2), 32-49.
48. Jamieson, E. J.; Fewkes, C. J.; Berry, J. D.; Dagastine, R. R., Forces between oil drops in polymer-surfactant systems: Linking direct force measurements to microfluidic observations. *J. Colloid Interface Sci.* **2019,** *544*, 130-143.
49. Shtein, M.; Pri-bar, I.; Regev, O., A simple solution for the determination of pristine carbon nanotube concentration. *Analyst* **2013,** *138* (5), 1490-6.
50. Zhang, K.; Zhang, X.; Li, H.; Xing, X.; Jin, L. e.; Cao, Q.; Li, P., Direct exfoliation of graphite into graphene in aqueous solution using a novel surfactant obtained from used engine oil. *J. Mater. Sci.* **2018,** *53* (4), 2484-2496.
51. Narayan, R.; Lim, J.; Jeon, T.; Li, D. J.; Kim, S. O., Perylene tetracarboxylate surfactant assisted liquid phase exfoliation of graphite into graphene nanosheets with facile re-dispersibility in aqueous/organic polar solvents. *Carbon* **2017,** *119*, 555-568.
52. Blanch, A. J.; Lenehan, C. E.; Quinton, J. S., Parametric analysis of sonication and centrifugation variables for dispersion of single walled carbon nanotubes in aqueous solutions of sodium dodecylbenzene sulfonate. *Carbon* **2011,** *49* (15), 5213-5228.
53. Sun, Z.; Nicolosi, V.; Rickard, D.; Bergin, S. D.; Aherne, D.; Coleman, J. N., Quantitative evaluation of surfactant-stabilized single-walled carbon nanotubes: dispersion quality and its correlation with zeta potential. *J. Phys. Chem. C* **2008,** *112* (29), 10692-10699.
54. White, B.; Banerjee, S.; O'Brien, S.; Turro, N. J.; Herman, I. P., Zeta-potential measurements of surfactant-wrapped individual single-walled carbon nanotubes. *J. Phys. Chem. C* **2007,** *111* (37), 13684-13690.
55. Cattoz, B.; Cosgrove, T.; Crossman, M.; Prescott, S. W., Surfactant-mediated desorption of polymer from the nanoparticle interface. *Langmuir* **2012,** *28* (5), 2485-2492.
56. Kamli, M.; Guettari, M.; Tajouri, T., Structure of polyvinylpyrrolidone aqueous solution in semi-dilute regime: Roles of polymer-surfactant complexation. *J. Mol. Struct.* **2019,** *1196*, 176-185.
57. Anthony, O.; Zana, R., Effect of temperature on the interactions between neutral polymers and a cationic and a nonionic surfactant in aqueous solutions. *Langmuir* **1994,** *10* (11), 4048-4052.
58. La Mesa, C., Polymer-surfactant and protein-surfactant interactions. *J. Colloid Interface Sci.* **2005,** *286* (1), 148-157.

Supporting Information

Dispersibility and noncovalent functionalization of multiwalled carbon nanotubes by polymer/surfactant mixtures of assorted composition: synergistic vs. antagonistic effects

Bárbara Abreu[1,2], Ana Sofia Pires[1], Andreia Guimarães[1], Ricardo M. F. Fernandes[1] and Eduardo F. Marques[1*]

[1]CIQUP, Departamento de Química e Bioquímica, Faculdade de Ciências, Universidade do Porto, Rua do Campo Alegre P-4169-007 Porto, Portugal.

[2]REQUIMTE-LAQV, Departamento de Química e Bioquímica, Faculdade de Ciências da Universidade do Porto, Rua do Campo Alegre P-4169-007 Porto, Portugal.

*email: efmarque@fc.up.pt

Table of Contents

Section S1: Additional data on the surfactants and polymers used

Table S1.1. Further information on the surfactants and polymers used in this work.

Surfactant / Polymer	M_w / g·mol^{-1}	*cmc* / mmol·kg^{-1}
SDBS	342.4	1.8[a]
CTAB	364.5	0.97[a]
TX-100	647.0	0.2-0.9
PVP	~40 000	-
PDDA	~200 000– 350 000	-
PAS	~15 000	-

[a] Obtained from conductivity measurements,[1] at 30 °C for CTAB and at 20-25 °C for the remaining dispersants.

Section S2: Determination of synergism

Synergism, *S*, can be calculated, as described in the MS, as:

$$S = \frac{c_{p+s}^{d}}{c_{p}^{d} + c_{s@cdc}^{d}}$$

where c_{p+s}^{d} is the MWNT concentration dispersed by the mixture of polymer+surfactant, c_{p}^{d} is the MWNT concentration dispersed by the polymer at the concentration used in the mixture (it should be noted that the dispersibility curves of the mixtures indicate the total amount of dispersant in the system, $c_{polymer}$+$c_{surfactant}$, so the $c_{polymer}$ corresponds to the subtraction of the *cdc* of the surfactant to the $c_{dispersant\ total}$), and can be determined through fittings in the linear regions of the curve (as illustrated in Fig. S2.1), and $c_{s@cdc}^{d}$ is the MWNT concentration dispersed by the surfactant at the *cdc* (the surfactant concentration used in the mixtures), in this case 0.069 mg·mL^{-1}.

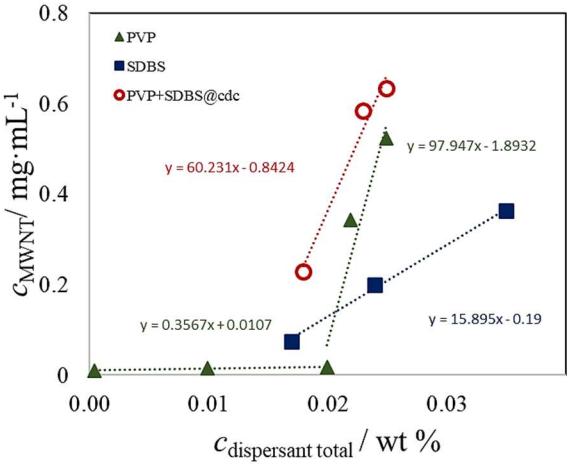

Fig. S2.1. Linear fitting of the dispersibility curves at a fixed concentration range for PVP, SDBS and PVP+SDBS@*cdc* systems.

Therefore, *S* can be determined at each point of the dispersibility curves. In the case of the PVP+SDBS@*cdc* mixture at the low dispersant concentration range (before the *plateau*), c_{p}^{d} is determined from the linear fitting of the PVP dispersibility curve in the dispersant concentration range 0.0001- 0.02 wt%. *S* at $c_{dispersant}$ = 0.023 wt % can be determined as:

$$S = \frac{0.58}{0.012 + 0.069} = 7.2$$

S > 1 indicates the presence of synergism in the mixture, therefore, at the concentration of PVP+SDBS@*cdc* considered, the system presents a strong beneficial effect when compared to the individual dispersants at the same conditions.

Section S3: Additional dispersibility curves

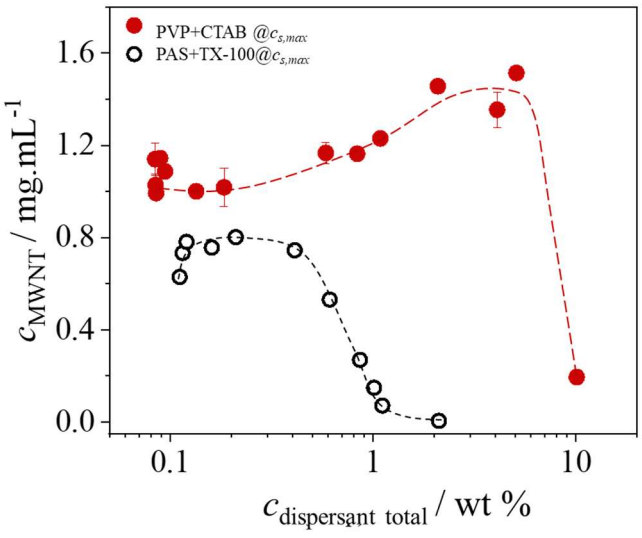

Fig. S3.1. Dispersion curves obtained for the mixtures at the surfactant $c_{s,max}$.

Table S3.1. Dispersibility parameters obtained from the dispersibility curves in Fig. S3.1. The precision is estimated as ca. ±10%.

	PVP+CTAB@$c_{disp,max}$	**PAS+TX-100@$c_{disp,max}$**
$c_{CNT,max}$ / mg·mL^{-1}	1.1	0.78
η / %	37	26

References

1. Fernandes, R. M.; Abreu, B.; Claro, B.; Buzaglo, M.; Regev, O.; Furo, I.; Marques, E. F., Dispersing Carbon Nanotubes with Ionic Surfactants under Controlled Conditions: Comparisons and Insight. *Langmuir* **2015,** *31* (40), 10955-65.

IV

On the role of ionic surfactants in the liquid-phase exfoliation of 2D graphene analogues: the case of transition metal dichalcogenides MoS_2, WS_2 and $MoSe_2$

On the role of ionic surfactants in the liquid-phase exfoliation of 2D graphene analogues: the case of transition metal dichalcogenides MoS_2, WS_2 and $MoSe_2$

Bárbara Abreu[1,2], Pedro Ferreira[1,2], Bernardo Almeida[1],
Ricardo M. F. Fernandes[1], Diana M. Fernandes[2], Eduardo F. Marques[1*]

[1]CIQUP – Departamento de Química e Bioquímica, Faculdade de Ciências da Universidade do Porto, Rua do Campo Alegre P-4169-007 Porto, Portugal.

[2]REQUIMTE-LAQV, Departamento de Química e Bioquímica, Faculdade de Ciências da Universidade do Porto, Rua do Campo Alegre P-4169-007 Porto, Portugal.

*email: efmarque@fc.up.pt

Keywords:

Inorganic graphene analogues; Layered materials; Molybdenum (IV) disulfide; Tungsten (IV) disulfide; Molybdenum diselenide; Surfactant; Liquid-phase exfoliation; Non-covalent functionalization

Abstract

The study of two-dimensional materials beyond graphene, in particular transition metal dichalcogenides (TMDs), has been gaining interest over the last decade due to their applicability in a wide number of areas. Surfactant-assisted liquid-phase exfoliation has been commonly applied as a preparation method of layered nanomaterials, giving well-exfoliated nanosheets stabilized by the amphiphiles adsorbed at the surface. However, a fundamental understanding of the TMD features that influence the dispersal process is still lacking. In this work, we present a systematic study that addresses the dispersibility of MoS_2, WS_2 and $MoSe_2$ in aqueous medium using the surfactants cetyltrimethylammonium bromide (CTAB) and sodium cholate (SC) in a representative concentration range. High precision dispersibility curves (concentration of dispersed TMD versus surfactant concentration) were obtained, allowing insight on the influence of the TMD metal and chalcogen in the dispersion, as well as the effect of surfactant charge. The metal (Mo, W) is found to influence the dispersibility at low surfactant concentrations, while the chalcogen (S, Se) plays a more significative role as the surfactant concentration is increased, determining the dispersibility yield in combination with the surfactant. Surfactant charge has a marked influence in the dispersibility profile, as evidenced by zeta potential measurements. Structural characterization provides further information on the size and number of layers of the TMDs in the as-obtained dispersions, showing that the sonication/centrifugation methodology applied gives well-exfoliated nanosheets with controlled mean lateral dimension and thickness.

1. Introduction

The interest in layered nanomaterials found a massive growth after the discovery of graphene,[1] due to the electronic, mechanical and optical properties of these nanomaterials and their potential for practical applications.[2, 3] Among the families of 2D inorganic graphene analogues that emerged, transition metal dichalcogenides (TMDs) are one of the most remarkable.[4] TMDs electronic properties range from insulators (e.g. HfS_2), semiconductors (e.g. MoS_2 and WS_2), semimetals (e.g. WTe_2 and $TiSe_2$) to true metals (e.g. NbS_2 and VSe_2),[5] finding applications in flexible transistors,[4] transparent optoelectronics[6] and nanoelectronics.[7] TMDs possess a MX_2 structure, with M being a transition metal atom (e.g. Mo, W) and X a chalcogen atom (e.g. S, Se), and can be illustrated as one layer of M atoms "sandwiched" between two layers of X atoms.[1, 7]

Due to the combination of strong in-plane chemical bonds with weak out-of-plane interactions (namely van der Waals forces), 2D sheets can be obtained from the bulk crystals of TMDs, not only preserving the bulk properties, but also leading to additional features due to confinement effects.[8] The exfoliation of nanomaterials of the MX_2 family into thin layers exposes the prismatic edges and basal planes, and hence the resulting material exhibits distinct surface chemistry, which can be additionally tuned by controlling the shape or size of the exfoliated MX_2 layers.[5, 9, 10] MoX_2 and WX_2 are among the most studied families due to their applicability in electronic devices, since they are semiconductors and the band gaps can be tuned by controlling the number of stacked layers.[3, 11]

Liquid-phase exfoliation (LPE) is a widely used and versatile method to prepare few-layer particles of 2D materials.[1, 12-16] In particular, nanosheets can be exfoliated in aqueous media and stabilized in the presence of surfactants or polymers.[17-19] This methodology involves the use of sonication or shear forces to exfoliate the 2D layers from the bulk crystal. When amphiphiles are used, the hydrophobic moieties adsorb on the freshly exposed nanosheet, while the polar segments point towards the solvent (in this case, water), stabilizing the exfoliated particles by electrostatic or steric interactions, depending on the nature of the dispersant.[19-21] This process allows to overcome the cohesive sheet-sheet energy, preventing the restacking of the suspended particles.[22]

Despite the clear interest in TMD research and their applicability over the last years, studies regarding the preparation of reproducible few-layer TMDs with controlled size, and the understanding of the dispersion process at a molecular level, did not follow the growth, remaining scarce or lacking in detail. Extensive research has been carried in this domain for carbon nanotubes[23-27] and graphene,[28-31] highlighting the importance of the experimental conditions (i.e. sonication, centrifugation) and the surfactant choice on

the dispersal yield, and final concentration and morphological characteristics of the dispersed particles. Regarding graphene inorganic analogues, and more specifically TMDs, relevant work has been carried out in the past 5 years, enhancing the importance of understanding the surfactant-assisted dispersion at molecular level and establishing methods that allow to obtain exfoliated TMDs with controlled size and thickness.[9, 10, 19, 32] Nevertheless, the influence of nanosheet features on the dispersal process still lacks understanding, due to the reduced dispersant concentration ranges usually studied and absence of systematization in the variables investigated.

In an attempt to overcome this gap in knowledge, herein we employed a systematic approach to study three different MX_2 materials, MoS_2, WS_2 and $MoSe_2$, over a wide range of surfactant concentrations. A rigorous methodology was applied, previously reported by us,[25, 26, 33] that combines sonication and centrifugation in strictly controlled conditions to disperse nanomaterials in aqueous surfactant solutions. To gain insight on the surfactant role, the three TMDs were dispersed using the surfactants cetyltrimethylammonium bromide, CTAB, cationic, and sodium cholate, SC, anionic, previously deemed as highly effective.[19, 25] The surfactant concentration range used, from 10^{-5} to 10^{2} mmol·kg^{-1}, allows a comprehensive view of the dispersing process and proper comparisons to be withdrawn. Determination of zeta potential of specific dispersions highlights the effect of surfactant charge in the dispersibility profile. Further, by comparing MoS_2 vs. WS_2 and MoS_2 vs. $MoSe_2$ the role of TMD features can be addressed, providing further insight. Finally, structural characterization of the obtained dispersions by SEM and Raman spectroscopy shows that the applied methodology leads to a controlled size and number of layers of the TMD nanosheets.

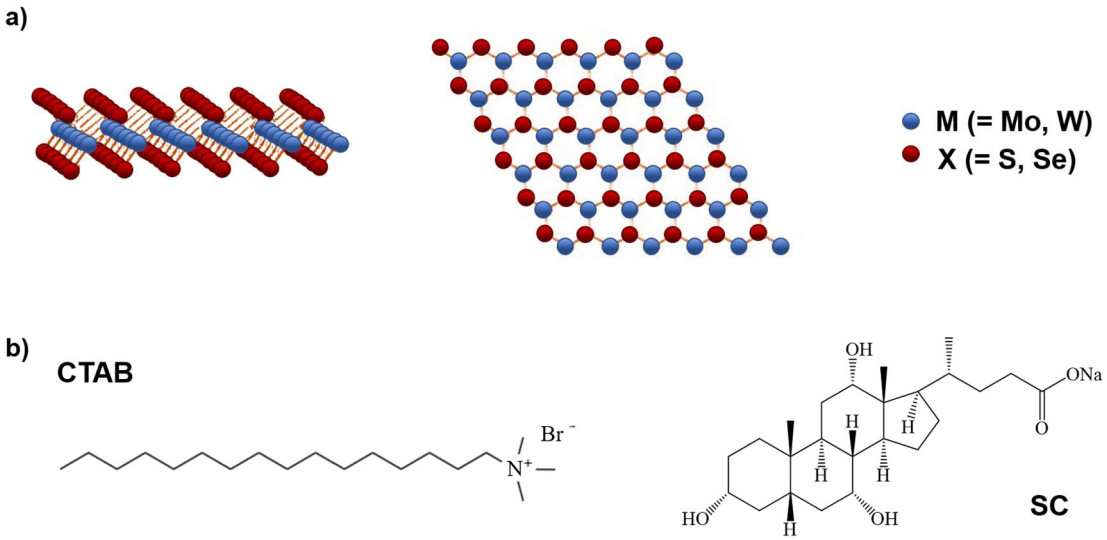

Fig. 1. Nanomaterials and surfactants used in this work: a) generic structure of MX_2 transition metal dichalcogenides; b) molecular structure of the cationic surfactant CTAB and the anionic surfactant SC.

2. Experimental Section

2.1 Materials and reagents

The transition metal dichalcogenides molybdenum (IV) sulfide, MoS_2; tungsten (IV) sulfide, WS_2; and molybdenum diselenide, $MoSe_2$, with purity ≥ 99 %, were acquired from Sigma-Aldrich®. The powders were imaged by SEM, as shown in Fig. 2, and as it can be seen they consist of aggregated or stacked particles of large sizes (hundreds of nm to µm-sized). The surfactants cetyltrimethylammonium bromide, CTAB (purity ≥ 98 % MW = 364.5 $g \cdot mol^{-1}$, *cmc* = 0.9 mM at 20-25 °C) and sodium cholate hydrate, SC (purity ≥ 99 % MW = 430.6 $g \cdot mol^{-1}$, *cmc* = 9-15 mM at 20-25 °C) were also purchased from Sigma-Aldrich®. All the materials were used as received.

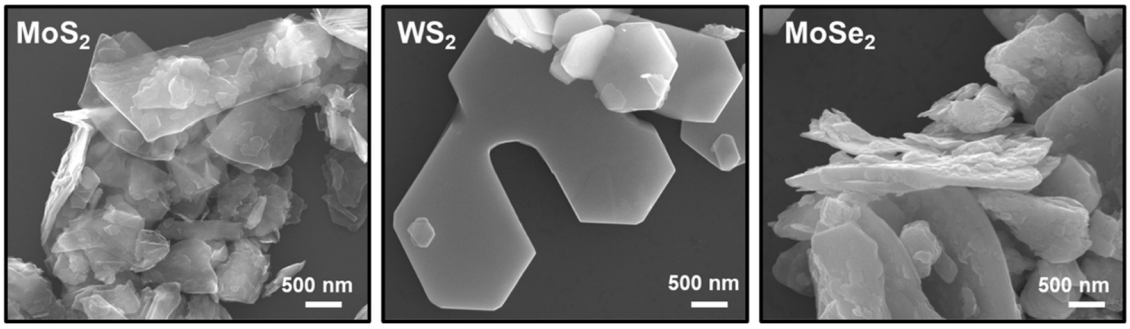

Fig. 2. Representative SEM micrographs of the TMD starting powders: MoS2, WS_2 and $MoSe_2$.

2.2 Preparation of dispersions

All the dispersions were prepared using the same stringently controlled procedure, based on previous reports.[33] The nanomaterial powder was added to the desired dispersant aqueous solution yielding an initial loading concentration of 3 $mg \cdot mL^{-1}$ in nanomaterial. These mixtures were tip-sonicated, using a freshly polished VCX500 13 mm tip (500 W, 20 kHz), with a vibration amplitude set to 50% and sonication time to 23 min, assuring the energy density transferred to the sample was kept constant at 0.8 $kJ \cdot mg^{-1}$. An external bath was used to dissipate the heat generated by the sonication procedure, stabilizing the temperature of the sample. Following sonication, the samples were centrifuged (Centurion Scientific Centrifuge Model K241R) for 10 min at 1500 g, and the top of the supernatant was carefully removed, extracting the most exfoliated materials for quantification. The nanomaterial concentration was finally determined by UV-Vis spectrophotometry, according to the procedure described in Section S1 of the Supporting Information (SI) file.

2.3 Zeta potential measurements and scanning electron microscopy (SEM)

Zeta potential measurements were performed in an Anton Paar Litesizer™ 500 equipment. In zeta potential determinations samples were placed in a disposable capillary polycarbonate U-shaped cuvette, with gold coated electrodes. Samples were left inside the instrument to reach thermal equilibrium 120 seconds at temperatures above the surfactant Krafft temperature. The electrophoretic mobility, μ, was measured using a combination of electrophoresis and laser Doppler velocimetry techniques and ζ was calculated from μ using the known Henry equation, a dielectric constant of 78.5, a medium viscosity of 0.89 cP and a f(ka) function of 1.5.[34]

To analyze the morphology of the dispersed nanomaterials, SEM imaging was performed at Centro de Materiais da Universidade do Porto (CEMUP), on a FEI Quanta 400FE microscope with an electron beam of 25 kV at different magnifications, in secondary electrons (SE) mode. The samples were prepared on pre-heated silicon wafers (>100 ºC) by drop casting 10 µL of the supernatant. The wafers were then rinsed in ethanol to remove surfactant excess. Raman spectra of the aqueous dispersions were recorded on a RAMOS RA532 Raman Analyzer using a laser emitting at 532 nm on glass cuvette, at room temperature.

3. Results and Discussion

3.1 Surfactant-assisted dispersions of TMDs

3.1.1 General features of dispersibility curves

The reproducibility of the applied methodology allows the determination of the TMD concentration in the obtained dispersions as function of surfactant concentration, c_s. These results are expressed in high precision dispersibility curves, shown in Fig. 3. A few aspects should be considered regarding the curves: i) the surfactant concentration corresponds to the initial value used to prepare the samples (the final concentration in the obtained dispersions is estimated to be approximately 60-70% of the initial value, since an amount is lost to the precipitate due to centrifugation[25, 26, 33]); ii) each point corresponds to at least 3 independent dispersions, prepared in the same exact conditions. For each dispersion, the absorbance was measured in triplicate, assuring meaningful results; iii) the zeta potential was measured for specific dispersions, in distinct regions of the curves, indicated by the black arrows in Fig. 3.

For quantitative comparisons between surfactants and TMDs, some metrics can be extracted from the plots: $c_{s,max}$, the surfactant concentration at which the maximum value of TMD dispersed is attained; $c_{TMD,max}$, the latter value; the dispersibility effectiveness (or yield), η, defined as the ratio $c_{TMD,max}/ c_{TMD,initial} \times 100$ (in this work, $c_{TMD,initial}$ = 3 mg·mL^{-1}); and efficiency, η^*, related with the surfactant concentration at which $c_{TMD,max}$ is attained and defined as η / $c_{s,max}$ and expressed in %·kg·mmol^{-1}.

The resulting curves, and their high-precision nature, allow us to get insight on the study of several effects, namely the influence of surfactant charge, the roles of the TMDs metal and dichalcogenide. Prior to a detailed analysis, a generic profile can be described from the dispersibility curves. At low surfactant concentrations, a flat trend is initially observed; upon increasing surfactant concentration, a new *plateau* level is reached, followed by a sharp decrease in the dispersibility with further surfactant addition, as also observed in previous works by us.[25, 33]

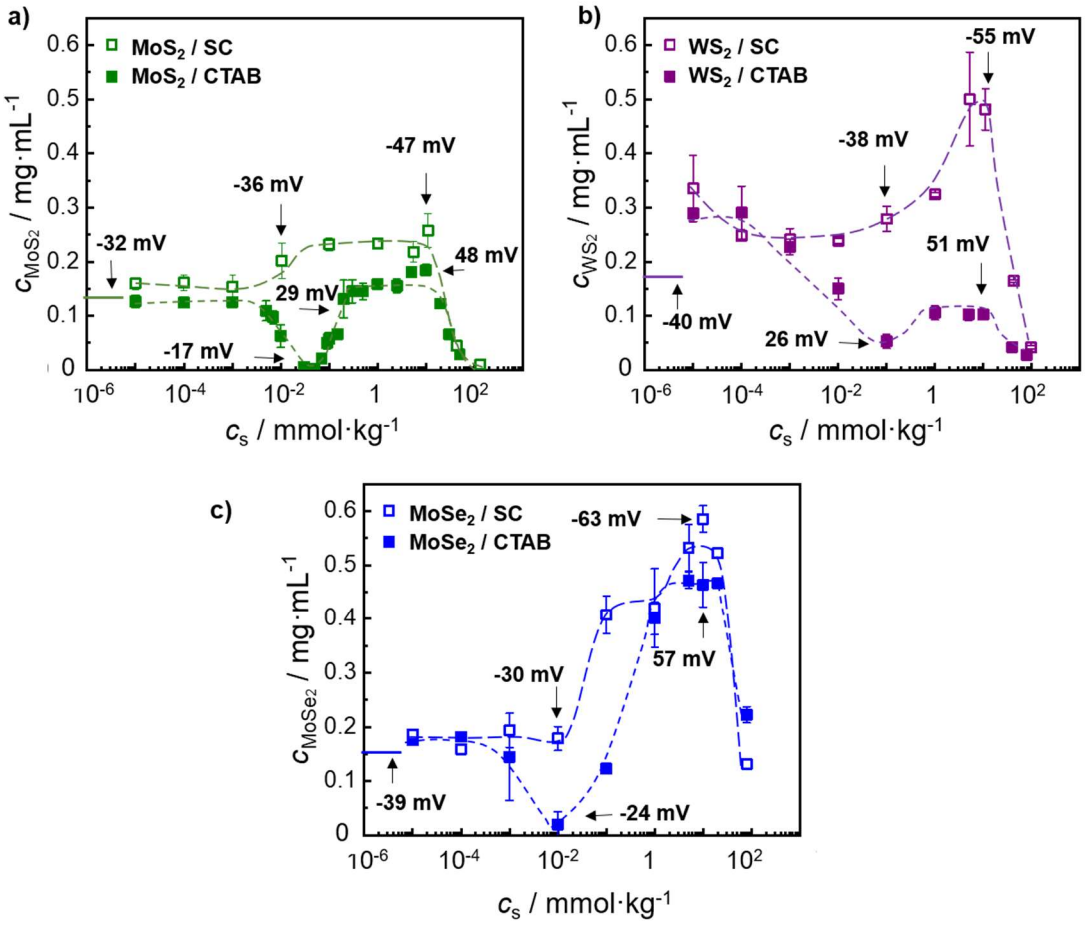

Fig. 3. Dispersibility curves of the TMDs a) MoS_2; b) WS_2; and c) $MoSe_2$ with SC and CTAB. The lines at the yy axis represent the concentration of nanomaterial dispersed in water. Dashed lines are for visual guidance. Black arrows indicate zeta potential values measured at the specific point in the curve.

A closer observation indicates, however, a fundamentally distinct profile for each surfactant: for the nanomaterials dispersed with the anionic surfactant, SC, the dispersibility increases with increasing surfactant concentration, until the *plateau* is achieved. However, when CTAB is used, a nonmonotonic variation is seen, with the dispersibility first decreasing to a minimum (virtually to null values), and then increasing again to reach the new *plateau*. The different behavior can be interpreted in terms of surfactant and nanomaterial charges and will be discussed further.

3.1.2 Molecular considerations

As described previously, the curves show common features that allow proper comparisons between the TMDs dispersibility and the surfactant performance. Some effects may overlap. Therefore, this analysis will first address the similarities and differences between the dispersibility of the TMDs as the surfactant concentration is increased (and hence the effect of metal and chalcogen in the dispersibility), and then the role of the surfactant.

Effect of metal and chalcogen on TMD dispersibility

Considering the low concentration segment of the dispersibility curves (from 10^{-6} to 10^{-3} mmol·kg^{-1}), interesting features emerge. At low surfactant concentration, for MoS_2 and $MoSe_2$ (TMDs with generic structure MoX_2) the maximum amount of nanomaterial dispersed is close to the value dispersed without surfactant; for WS_2, however, the dispersibility is two times the value dispersed without surfactant. This implies that, for low surfactant concentrations, the metal in the TMD has a stronger effect than the chalcogen. A possible explanation is the anisotropic arrangement of TMDs, that produces two types of surface sites: sulfur (or selenide)-terminated basal planes and the layer edges where metal atoms are partly exposed, exhibiting rather different chemical properties.[35] Exfoliated platelets typically have a relatively small lateral size, thus enhancing the edge effects.[18] Therefore, at first the surfactant molecules in highly diluted solution will tend to adsorb preferentially at the exposed metal atoms, irrespectively of the surfactant charge, likely due to the less polar nature of W compared to Mo. At the *plateau* of the dispersibility curves, however, the chalcogen seems to play a role in the dispersion effectiveness, η. Interestingly, in Fig.4a one observes that $MoSe_2$ attains η = 16-18 % for both surfactants, a 2-fold higher than MoS_2. The yield of WS_2 dispersibility appears to have a higher dependency on the surfactant charge, with η = 18 % for SC and only 3 % for CTAB. Since the chalcogen is the external layer of the 2D TMDs, it is reasonable that dispersibility is strongly influenced by this chemical feature of the TMD.

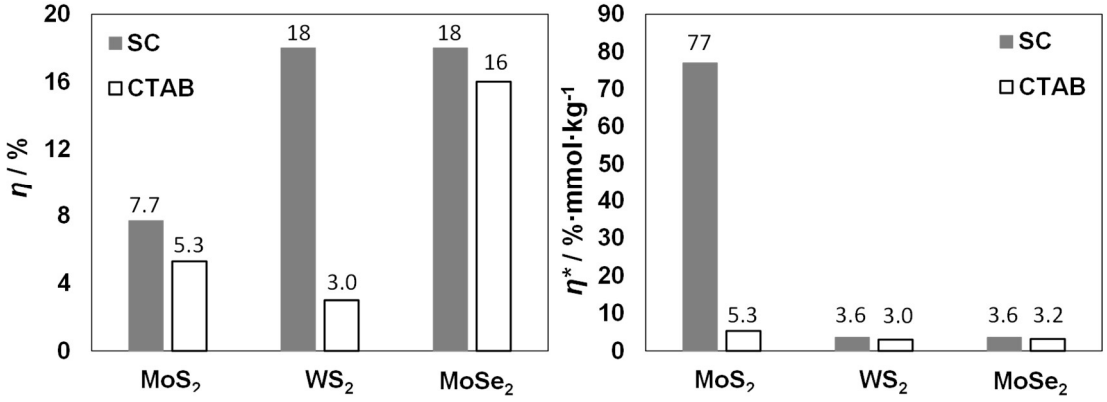

Fig. 4. Dispersibility metrics obtained from the plateau of the TMD/surfactant dispersibility curves a) effectiveness, η; and b) efficiency, η^*.

Although the effectiveness attained for these systems is lower than that obtained for carbon nanotubes, it is 2 orders of magnitude superior to the effectiveness of the 2D analogue, graphene, as reported in our previous works.[25, 33] Regarding the dispersion efficiency (Fig. 4b), the MoS_2/SC system stands out, with an efficiency of 77 %·kg·mmol^{-1} compared to the average 3.7 %·kg·mmol^{-1} obtained for the other 5 systems. This parameter falls in the values obtained for graphene nanoplatelets (1-4 %·kg·mmol^{-1}), indicating common features in the interaction of surfactant with 2D layered materials. After the *plateau*, a significant decrease in TMD dispersibility is observed for all the dispersions – this effect will be discussed below.

Effect of surfactant charge on TMD dispersibility

The effect of the surfactant charge on TMD dispersibility has been reported in the literature[20, 22] and will be now analyzed in light of the systematic work carried here. In the surfactant concentration range from 10^{-3} to 10^{2} mmol·kg^{-1}, the profile of the curves is clearly contrasting for the cationic and the anionic surfactant. Observing the curves of TMDs dispersed with CTAB, the concentration of TMD decreases to a minimum (reaching zero for MoS_2 and $MoSe_2$), which is explained by surface charge effects. The cationic charge of the surfactant neutralizes the negative charge of the nanomaterial surface upon increasing concentration of the former. At some point, typically c_s between 10^{-2} and 10^{-1} mmol·kg^{-1}, the charge of the surfactant-coated particles is null and the dispersion has no colloidal stability. This phenomenon is thus similar to a precipitation effect due to charge neutralization, induced by the surfactant. As the surfactant concentration increases and more molecules adsorb at the TMD surface, there is a

charge reversal to positive values and a new stage of colloidal stability is reached. At this point and as described previously, a *plateau* for c_{TMD} is attained.

Regarding the dispersions with the anionic surfactant, SC, higher concentrations of dispersed TMDs are obtained comparing to CTAB, evidencing higher effectiveness for this surfactant (see also Fig. 4a). This effect that can be rationalized by the high affinity of SC to the planar 2D surface. Sodium cholate, a bile salt, has an almost flat structure with a hydrophobic and a hydrophilic facet. The hydrophobic side is constituted by a rigid cholic acid ring system, which can attach to the hard 2D material basal plane. The OH groups facing the same and opposite side of the ring system, together with the anionic carboxylate headgroup, provide favorable interactions with the aqueous solvent through H-bonding and dipolar forces.[17]

As pointed before, after the *plateau* and upon increasing surfactant concentration up to 10^2 mmol·kg^{-1}, the dispersed TMD concentration falls abruptly. This effect can be attributed to colloidal depletion forces and was observed in previous studies by us, for 1D[33] and 2D carbon nanomaterials. This phenomenon is surmised to arise from a difference in the osmotic pressure, due to high concentration of bulk micelles in the vicinity of the dispersed nanomaterial particles. The solvent between these particles tends to flow to the surroundings according to its chemical potential gradient, causing the particles to flocculate. Interestingly, for the current TMD systems, the depletion flocculation seems to occur at roughly similar surfactant concentrations than observed for carbon nanotubes and graphene nanoplatelets, underpinning a fundamental aspect of the dispersibility of 1D and 2D nanomaterials by surfactants.

3.2 Structural characterization of the dispersions

3.2.1 Particle size distributions from SEM

To address the effect of the surfactant in the morphology of the final dispersed particles, scanning electron microscopy and Raman spectroscopy were performed. Representative SEM micrographs of the studied systems suggest the surfactant plays an important role in the individualization of TMD layers. The images of the nanomaterials exfoliated without surfactant show heterogeneous domains of aggregates, while the surfactant-dispersed materials appear more homogeneous and/or in particles apparently separated from the stacked flakes (Fig. 5). Moreover, the $MoSe_2$ systems show the smallest and most individualized particles. To have a clearer monitoring of the particle size, the particles in the TMD/surfactant systems were measured and the mean lateral dimension, *MLD*, was determined through the geometric mean of length and width of the

particle. For each particle, three different measurements were performed, and the average value was used to obtain the frequency histograms. The results were fit using a lognormal distribution (Fig. 6). Since the morphology of the exfoliated layers varies between systems, a representative image is shown in the inset of the histograms, with the respective measurements. Due to rapid aggregation after preparation of the dispersions, it was not possible to perform the measurements for the TMD/H_2O systems. i.e. in the absence of the surfactants.

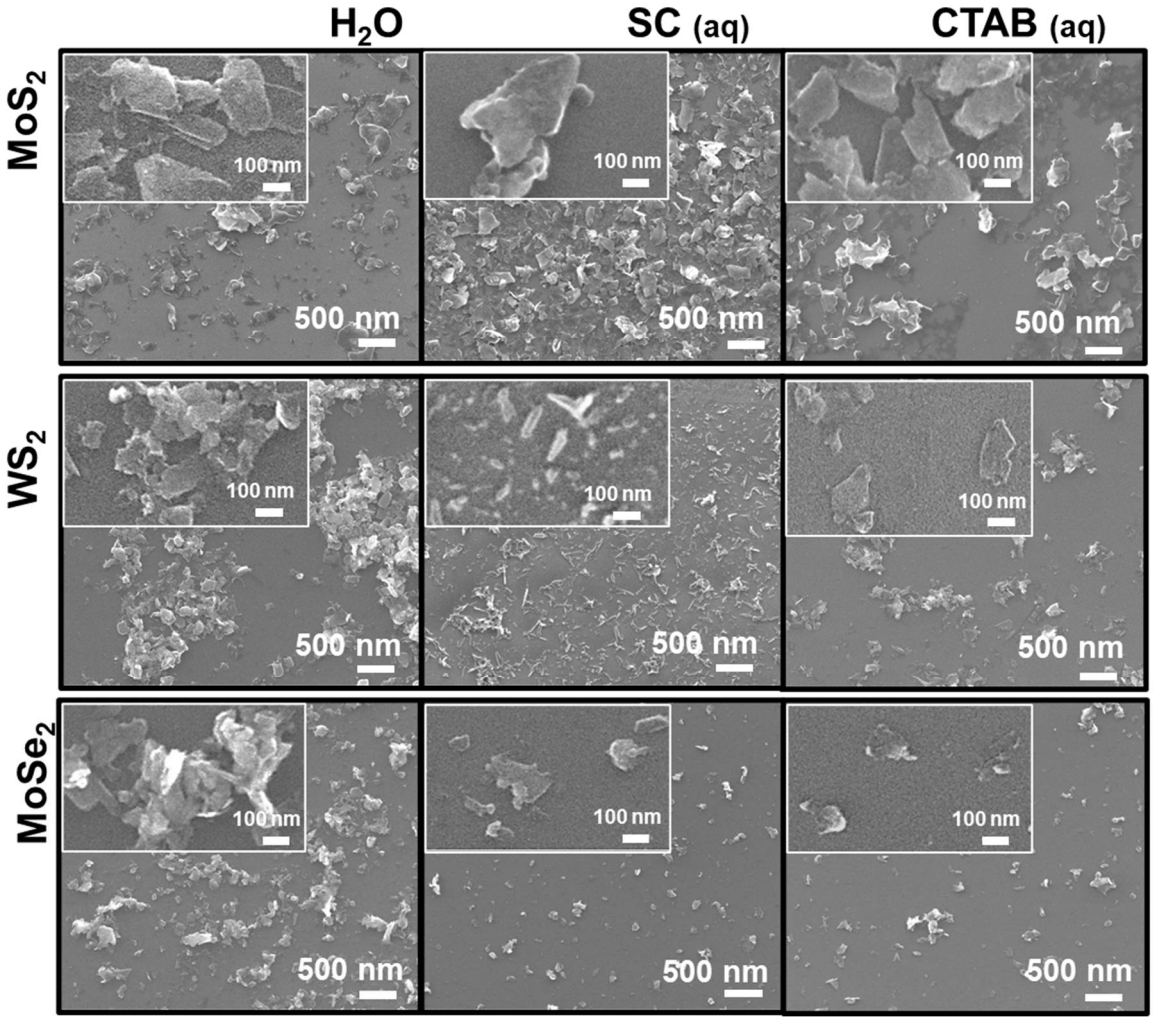

Fig. 5. Representative SEM micrographs of the obtained MoS_2, WS_2 and $MoSe_2$ dispersions without surfactant (in water), and in aqueous surfactant solutions. Insets show the particles at higher magnifications.

The histograms show clear differences between the systems. The nanomaterials dispersed with SC (Fig.6a-c) show a broad distribution of *MLD*, specially MoS_2/SC, with the larger particles showing *MLD* = 450 nm. For the TMD/CTAB systems (Fig. 6d-f), the measured particles showed an average *MLD* ≤ 100 nm. These results suggest that the applied dispersion methodology allows to control the size of the dispersed layers to a considerable extent, a commonly reported obstacle in the obtention of exfoliated TMDs.[9]

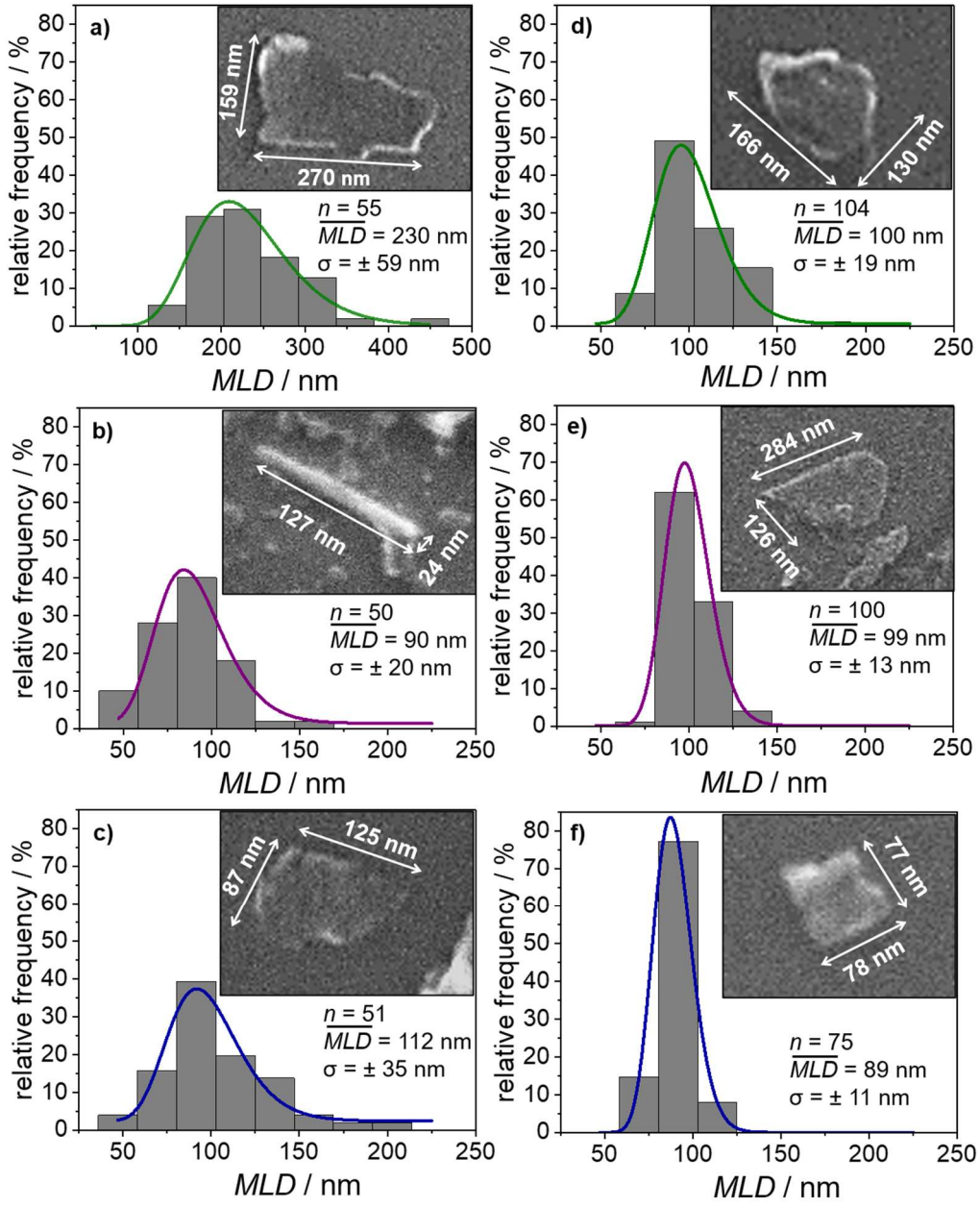

Fig. 6. Frequency histograms obtained through measurements from TMD/surfactant micrographs: a) MoS_2/SC; b) WS_2/SC; c) $MoSe_2$/SC; d) MoS_2/CTAB; e) WS_2/CTAB and f) $MoSe_2$/CTAB. Inset shows a representative particle of the dispersion. Lines represent lognormal fitting.

From a general standpoint, it can be inferred that CTAB yields the most homogeneous TMD dispersions. A possible explanation is, again, the charge effect. TMDs show a residual negative charge, so, presumably, as the ultrasonication shear forces peel off the 2D sheets from the bulk particles, rapid adsorption of the CTAB cationic molecules in the freshly exposed surface results in a high degree of individualization and stabilization of the nanosheets.[26] Despite that the hydrophobic effect is the driving force for surfactant adsorption, if the surfactant and the hard surface bear the same charge, electrostatic repulsions can act as a kinetic barrier, reducing considerably the adsorption rate. For the TMD/CTAB systems, this kinetic barrier not only does not exist, but faster adsorption and hence more extensive exfoliation can be induced due to the favorable electrostatic interactions.

3.2.2 Raman studies

To complement the structural characterization of the dispersions, Raman spectra of the dispersions were obtained (Fig. 7). Raman spectroscopy has become a pivotal characterization technique for TMDs, graphene and other layered materials.[36] For the current materials, two Raman absorption peaks can be observed, one concerning the E_{2g} (in-plane) vibration mode, and another corresponding to the A_{1g} (out-of-plane) vibration mode. The extent of exfoliation of the TMDs affects Raman shifts, as the frequencies of the Raman active modes of TMDs can be shifted from the values for the monolayer or bulk material due to the weak interlayer interactions. Generally, E_{2g} and A_{1g} modes undergo blue and red shifts, respectively, with a decreasing number of stacked layers for MoS_2, WS_2, and $MoSe_2$, that is, as the nanosheet thickness decreases.[36, 37]

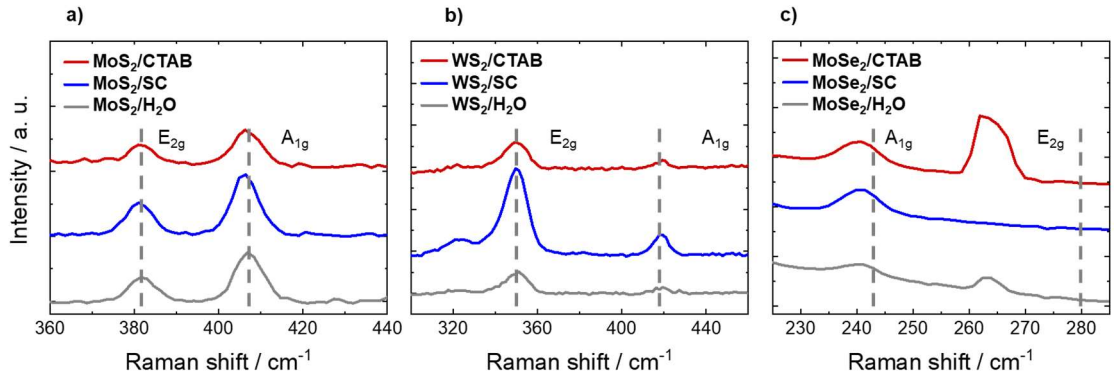

Fig. 7. Raman spectra of the TMD systems a) MoS_2; b) WS_2; and c) $MoSe_2$ in CTAB, SC and without surfactant. Dashed line represents the band assignment for few-layer materials according to ref. [37, 38]

The layer number of MX_2 particles can be assessed by the relative frequency difference, Δω, of the high-frequency modes, compared to the corresponding modes in the bulk.[39] According to Fig. 7 a), for MoS_2, Δω was determined as 25.3 for the dispersions with SC and 25.4 with CTAB and without surfactant. For WS_2 (Fig. 7b), the Δω parameter was determined as 68.3 for the dispersion with SC, 69.8 with CTAB and 68.2 without surfactant. In all cases, these values correspond to less than 5 stacked layers.[36, 39] Fig. 7c) shows, however, that for the $MoSe_2$ systems, the E_{2g} mode undergoes an evident red shift relatively to the band frequency typically assigned for the few layer material. The expected upshift of E_{2g} with decreasing thickness is assigned to a decrease in magnitude of the long-range electrostatic forces between particles. In fact, as the number of layers is reduced, electrostatic forces between the charged particles become weaker.[39-41] The observed downshift of the E_{2g} mode in $MoSe_2$ may be due to interactions between the Se outer-layer of the nanosheets and the surfactant. This is further evidenced by the $MoSe_2$/CTAB Raman spectra: since there are now attractive electrostatic forces between the positively charged CTAB and negatively charged $MoSe_2$, the magnitude of electrostatic forces increases, which could result in the observed downshift of the E_{2g} mode.

In summary, Raman spectra do not suggest significative differences in the number of layers of the dispersed systems. Therefore, when selecting the best system for further applications, other factors should be considered. Regarding the particle size, SEM analysis indicates the larger sheets are obtained for MoS_2/SC. Hence, this system shows a reduced number of layers (< 5) and higher lateral dimensions, being the most promising for further applications. Another advantage is the low surfactant concentration required to attain maximum dispersed concentration, 0.1 $mmol \cdot kg^{-1}$, according to the dispersibility curves (Fig. 3). Although higher concentrations of $MoSe_2$ can be obtained, the required surfactant concentration is superior by a 2-fold factor.

4. Conclusions

Different TMD systems were successfully dispersed and functionalized with ionic surfactants and their dispersibility behavior in aqueous solution was studied. Results indicate that at low surfactant concentrations the metal in the TMD plays a stronger role than the chalcogen or the surfactant charge. With increasing surfactant concentration, the surfactant charge shows a higher influence in the dispersibility behavior. In terms of dispersibility yield, results indicate that the chalcogen has the dominant effect on the final concentration of dispersed TMD obtained. Comparing the surfactants directly, sodium

cholate (SC) has a higher capacity to exfoliate and disperse than cetyltrimethylammonium bromide (CTAB). Structural characterization allowed to clarify the role of the surfactant in the morphology of the final dispersions. Raman spectra suggests that all the TMDs dispersions can be classified as few-layer materials, whereas SEM micrographs indicate that the systems containing surfactant are more homogeneous and show more individualized particles.

Overall, the results allow insight on the role of surfactant charge, TMD metal and chalcogen in the dispersibility behavior of this family of nanomaterials, facilitating a proper selection of systems and the processing conditions to use them for further applications.

CRediT authorship contribution statement

B. Abreu: Conceptualization, Investigation, Formal analysis, Validation, Writing - original draft. **P. Ferreira**: Investigation, Formal analysis, Writing – original draft. **B. Almeida:** Methodology. **R.M.F. Fernandes:** Conceptualization, Methodology. **D.M. Fernandes:** Validation, Writing - review & editing. **E. F. Marques:** Conceptualization, Methodology, Resources, Supervision, Funding acquisition, Writing - review & editing.

Declaration of competing interest

The authors declare that they have no known competing financial interests or personal relationships that could have appeared to influence the work reported in this paper.

Acknowledgments

The authors acknowledge Fundação para a Ciência e para a Tecnologia (FCT) for financial support through project UIDB/00081/2020. B. Abreu also acknowledges financial support from FCT through the PhD grant PD/BD/128129/2016 from FCT and DMF thanks DL57/2016–Norma transitória.

References

1. Novoselov, K. S.; Jiang, D.; Schedin, F.; Booth, T. J.; Khotkevich, V. V.; Morozov, S. V.; Geim, A. K., Two-dimensional atomic crystals. *Proc. Natl. Acad. Sci. U.S.A* **2005,** *102* (30), 10451.
2. Huang, X.; Tan, C.; Yin, Z.; Zhang, H., 25th anniversary article: Hybrid nanostructures based on two-dimensional nanomaterials. *Adv. Mater.* **2014,** *26* (14), 2185-2204.
3. Tan, C.; Cao, X.; Wu, X. J.; He, Q.; Yang, J.; Zhang, X.; Chen, J.; Zhao, W.; Han, S.; Nam, G. H.; Sindoro, M.; Zhang, H., Recent advances in ultrathin two-dimensional nanomaterials. *Chem. Rev.* **2017,** *117* (9), 6225-6331.

4. Wang, Q. H.; Kalantar-Zadeh, K.; Kis, A.; Coleman, J. N.; Strano, M. S., Electronics and optoelectronics of two-dimensional transition metal dichalcogenides. *Nat. Nanotechnol.* **2012,** *7* (11), 699-712.
5. Chhowalla, M.; Shin, H. S.; Eda, G.; Li, L. J.; Loh, K. P.; Zhang, H., The chemistry of two-dimensional layered transition metal dichalcogenide nanosheets. *Nat. Chem.* **2013,** *5* (4), 263-275.
6. Gupta, A.; Sakthivel, T.; Seal, S., Recent development in 2D materials beyond graphene. *Prog. Mater. Sci.* **2015,** *73*, 44-126.
7. Miró, P.; Audiffred, M.; Heine, T., An atlas of two-dimensional materials. *Chem. Soc. Rev.* **2014,** *43* (18), 6537-6554.
8. Niu, L.; Coleman, J. N.; Zhang, H.; Shin, H.; Chhowalla, M.; Zheng, Z., Production of two-dimensional nanomaterials via liquid-based direct exfoliation. *Small* **2016,** *12* (3), 272-293.
9. Backes, C.; Hanlon, D.; Szydlowska, B. M.; Harvey, A.; Smith, R. J.; Higgins, T. M.; Coleman, J. N., Preparation of liquid-exfoliated transition metal dichalcogenide nanosheets with controlled size and thickness: a state of the art protocol. *JoVE* **2016,** (118), e54806.
10. Synnatschke, K.; Cieslik, P. A.; Harvey, A.; Castellanos-Gomez, A.; Tian, T.; Shih, C. J.; Chernikov, A.; Santos, E. J. G.; Coleman, J. N.; Backes, C., Length- and thickness-dependent optical response of liquid-exfoliated Transition Metal Dichalcogenides. *Chem. Mater.* **2019,** *31* (24), 10049-10062.
11. Lv, R.; Robinson, J. A.; Schaak, R. E.; Sun, D.; Sun, Y.; Mallouk, T. E.; Terrones, M., Transition metal dichalcogenides and beyond: Synthesis, properties, and applications of single- and few-layer nanosheets. *Acc. Chem. Res.* **2015,** *48* (1), 56-64.
12. Bonaccorso, F.; Bartolotta, A.; Coleman, J. N.; Backes, C., 2D-crystal-based functional inks. *Adv. Mater.* **2016,** *28* (29), 6136-6166.
13. Backes, C.; Abdelkader, A. M.; Alonso, C.; Andrieux-Ledier, A.; Arenal, R.; Azpeitia, J.; Balakrishnan, N.; Banszerus, L.; Barjon, J.; Bartali, R.; Bellani, S.; Berger, C.; Berger, R.; Ortega, M. M. B.; Bernard, C.; Beton, P. H.; Beyer, A.; Bianco, A.; Bøggild, P.; Bonaccorso, F.; Barin, G. B.; Botas, C.; Bueno, R. A.; Carriazo, D.; Castellanos-Gomez, A.; Christian, M.; Ciesielski, A.; Ciuk, T.; Cole, M. T.; Coleman, J.; Coletti, C.; Crema, L.; Cun, H.; Dasler, D.; De Fazio, D.; Díez, N.; Drieschner, S.; Duesberg, G. S.; Fasel, R.; Feng, X.; Fina, A.; Forti, S.; Galiotis, C.; Garberoglio, G.; García, J. M.; Garrido, J. A.; Gibertini, M.; Gölzhäuser, A.; Gómez, J.; Greber, T.; Hauke, F.; Hemmi, A.; Hernandez-Rodriguez, I.; Hirsch, A.; Hodge, S. A.; Huttel, Y.; Jepsen, P. U.; Jimenez, I.; Kaiser, U.; Kaplas, T.; Kim, H.; Kis, A.; Papagelis, K.; Kostarelos, K.; Krajewska, A.; Lee, K.; Li, C.; Lipsanen, H.; Liscio, A.; Lohe, M. R.; Loiseau, A.; Lombardi, L.; López, M. F.; Martin, O.; Martín, C.; Martínez, L.; Martin-Gago, J. A.; Martínez, J. I.; Marzari, N.; Mayoral, A.; McManus, J.; Melucci, M.; Méndez, J.; Merino, C.; Merino, P.; Meyer, A. P.; Miniussi, E.; Miseikis, V.; Mishra, N.; Morandi, V.; Munuera, C.; Muñoz, R.; Nolan, H.; Ortolani, L.; Ott, A. K.; Palacio, I.; Palermo, V.; Parthenios, J.; Pasternak, I.; Patane, A.; Prato, M.; Prevost, H.; Prudkovskiy, V.; Pugno, N.; Rojo, T.; Rossi, A.; Ruffieux, P.; Samorì, P.; Schué, L.; Setijadi, E.; Seyller, T.; Speranza, G.; Stampfer, C.; Stenger, I.; Strupinski, W.; Svirko, Y.; Taioli, S.; Teo, K. B. K.; Testi, M.; Tomarchio, F.; Tortello, M.; Treossi, E.; Turchanin, A.; Vazquez, E.; Villaro, E.; Whelan, P. R.; Xia, Z.; Yakimova, R.; Yang, S.; Yazdi, G. R.; Yim, C.; Yoon, D.; Zhang, X.; Zhuang, X.; Colombo, L.; Ferrari, A. C.; Garcia-Hernandez, M., Production and processing of graphene and related materials. *2D Mater.* **2020,** *7* (2).
14. Coleman, J. N.; Lotya, M.; O'Neill, A.; Bergin, S. D.; King, P. J.; Khan, U.; Young, K.; Gaucher, A.; De, S.; Smith, R. J.; Shvets, I. V.; Arora, S. K.; Stanton, G.; Kim, H.-Y.; Lee, K.; Kim, G. T.; Duesberg, G. S.; Hallam, T.; Boland, J. J.; Wang, J. J.; Donegan, J. F.; Grunlan, J. C.; Moriarty, G.; Shmeliov, A.; Nicholls, R. J.; Perkins, J. M.; Grieveson, E. M.; Theuwissen, K.; McComb, D. W.; Nellist, P. D.; Nicolosi, V., Two-dimensional nanosheets produced by liquid exfoliation of layered materials. *Science* **2011,** *331* (6017), 568-571.
15. Nicolosi, V.; Chhowalla, M.; Kanatzidis, M. G.; Strano, M. S.; Coleman, J. N., Liquid exfoliation of layered materials. *Science* **2013,** *340* (6139), 1226419.
16. Smith, R. J.; King, P. J.; Lotya, M.; Wirtz, C.; Khan, U.; De, S.; O'Neill, A.; Duesberg, G. S.; Grunlan, J. C.; Moriarty, G.; Chen, J.; Wang, J.; Minett, A. I.; Nicolosi, V.; Coleman, J. N., Large-scale exfoliation of inorganic layered compounds in aqueous surfactant solutions. *Adv. Mater.* **2011,** *23* (34), 3944-8.

17. Grayfer, E. D.; Kozlova, M. N.; Fedorov, V. E., Colloidal 2D nanosheets of MoS2 and other transition metal dichalcogenides through liquid-phase exfoliation. *Adv. Colloid Interface Sci.* **2017,** *245*, 40-61.
18. Guardia, L.; Paredes, J. I.; Rozada, R.; Villar-Rodil, S.; Martinez-Alonso, A.; Tascon, J. M. D., Production of aqueous dispersions of inorganic graphene analogues by exfoliation and stabilization with non-ionic surfactants. *RSC Adv.* **2014,** *4* (27), 14115-14127.
19. Griffin, A.; Nisi, K.; Pepper, J.; Harvey, A.; Szydłowska, B. M.; Coleman, J. N.; Backes, C., Effect of surfactant choice and concentration on the dimensions and yield of liquid-phase-exfoliated nanosheets. *Chem. Mater.* **2020,** *32* (7), 2852-2862.
20. Gupta, A.; Vasudevan, S., Understanding surfactant stabilization of MoS2 nanosheets in aqueous dispersions from zeta potential measurements and molecular dynamics simulations. *J. Phys. Chem. C* **2018,** *122* (33), 19243-19250.
21. Yu, H.; Zhu, H.; Dargusch, M.; Huang, Y., A reliable and highly efficient exfoliation method for water-dispersible MoS2 nanosheet. *J. Colloid Interface Sci.* **2018,** *514*, 642-647.
22. Gupta, A.; Arunachalam, V.; Vasudevan, S., Water dispersible, positively and negatively charged MoS2 nanosheets: surface chemistry and the role of surfactant binding. *J. Phys. Chem. Lett.* **2015,** *6* (4), 739-744.
23. Blanch, A. J.; Lenehan, C. E.; Quinton, J. S., Parametric analysis of sonication and centrifugation variables for dispersion of single walled carbon nanotubes in aqueous solutions of sodium dodecylbenzene sulfonate. *Carbon* **2011,** *49* (15), 5213-5228.
24. Angelikopoulos, P.; Bock, H., The science of dispersing carbon nanotubes with surfactants. *Phys. Chem. Chem. Phys* **2012,** *14* (27), 9546-57.
25. Abreu, B.; Rocha, J.; Fernandes, R. M. F.; Regev, O.; Furó, I.; Marques, E. F., Gemini surfactants as efficient dispersants of multiwalled carbon nanotubes: Interplay of molecular parameters on nanotube dispersibility and debundling. *J. Colloid Interface Sci.* **2019,** *547*, 69-77.
26. Dai, J.; Fernandes, R. M. F.; Regev, O.; Marques, E. F.; Furó, I., Dispersing carbon nanotubes in water with amphiphiles: Dispersant adsorption, kinetics, and bundle size distribution as defining factors. *J. Phys. Chem. C* **2018,** *122* (42), 24386-24393.
27. Fernandes, R. M. F.; Buzaglo, M.; Shtein, M.; Pri Bar, I.; Regev, O.; Marques, E. F.; Furó, I., Lateral diffusion of dispersing molecules on nanotubes as probed by NMR. *J. Phys. Chem. C* **2014,** *118* (1), 582-589.
28. Coleman, J. N., Liquid-phase exfoliation of nanotubes and graphene. *Adv. Funct. Mater.* **2009,** *19* (23), 3680-3695.
29. Buzaglo, M.; Shtein, M.; Kober, S.; Lovrincic, R.; Vilan, A.; Regev, O., Critical parameters in exfoliating graphite into graphene. *Phys. Chem. Chem. Phys* **2013,** *15* (12), 4428-4435.
30. Lotya, M.; Hernandez, Y.; King, P. J.; Smith, R. J.; Nicolosi, V.; Karlsson, L. S.; Blighe, F. M.; De, S.; Wang, Z.; McGovern, I. T.; Duesberg, G. S.; Coleman, J. N., Liquid phase production of graphene by exfoliation of graphite in surfactant/water solutions. *J. Am. Chem. Soc.* **2009,** *131* (10), 3611-20.
31. Khan, U.; O'Neill, A.; Porwal, H.; May, P.; Nawaz, K.; Coleman, J. N., Size selection of dispersed, exfoliated graphene flakes by controlled centrifugation. *Carbon* **2012,** *50* (2), 470-475.
32. Backes, C.; Higgins, T. M.; Kelly, A.; Boland, C.; Harvey, A.; Hanlon, D.; Coleman, J. N., Guidelines for exfoliation, characterization and processing of layered materials produced by liquid exfoliation. *Chem. Mater.* **2017,** *29* (1), 243-255.
33. Fernandes, R. M.; Abreu, B.; Claro, B.; Buzaglo, M.; Regev, O.; Furo, I.; Marques, E. F., Dispersing carbon nanotubes with ionic surfactants under controlled conditions: Comparisons and insight. *Langmuir* **2015,** *31* (40), 10955-65.
34. White, B.; Banerjee, S.; O'Brien, S.; Turro, N. J.; Herman, I. P., Zeta-potential measurements of surfactant-wrapped individual single-walled carbon nanotubes. *J. Phys. Chem. C* **2007,** *111* (37), 13684-13690.
35. James, D.; Zubkov, T., Photocatalytic properties of free and oxide-supported MoS2 and WS2 nanoparticles synthesized without surfactants. *J. Photochem. Photobiol. A* **2013,** *262*, 45-51.
36. Saito, R.; Tatsumi, Y.; Huang, S.; Ling, X.; Dresselhaus, M., Raman spectroscopy of transition metal dichalcogenides. *J. Phys. Condens. Matter* **2016,** *28* (35), 353002.
37. Zhang, X.; Tan, Q.-H.; Wu, J.-B.; Shi, W.; Tan, P.-H., Review on the Raman spectroscopy of different types of layered materials. *Nanoscale* **2016,** *8* (12), 6435-6450.

38. Tongay, S.; Zhou, J.; Ataca, C.; Lo, K.; Matthews, T. S.; Li, J.; Grossman, J. C.; Wu, J., Thermally driven crossover from indirect toward direct bandgap in 2D semiconductors: MoSe2 versus MoS2. *Nano Lett.* **2012,** *12* (11), 5576-5580.
39. Zhang, X.; Qiao, X.-F.; Shi, W.; Wu, J.-B.; Jiang, D.-S.; Tan, P.-H., Phonon and Raman scattering of two-dimensional transition metal dichalcogenides from monolayer, multilayer to bulk material. *Chem. Soc. Rev.* **2015,** *44* (9), 2757-2785.
40. Liang, L.; Meunier, V., First-principles Raman spectra of MoS2, WS2 and their heterostructures. *Nanoscale* **2014,** *6* (10), 5394-5401.
41. Wang, F.; Kinloch, I. A.; Wolverson, D.; Tenne, R.; Zak, A.; O'Connell, E.; Bangert, U.; Young, R. J., Strain-induced phonon shifts in tungsten disulfide nanoplatelets and nanotubes. *2D Mater.* **2016,** *4* (1), 015007.

Supporting Information

On the role of surfactants in the liquid phase exfoliation of 2D graphene analogues: the case of transition metal dichalcogenides MoS_2, WS_2 and $MoSe_2$

Bárbara Abreu[1,2], Pedro Ferreira[1,2], Bernardo Almeida[1],
Ricardo M. F. Fernandes[1], Diana M. Fernandes[2], E. F. Marques[1*]

[1]CIQUP – Departamento de Química e Bioquímica, Faculdade de Ciências da Universidade do Porto, Rua do Campo Alegre P-4169-007 Porto, Portugal.

[2]REQUIMTE-LAQV, Departamento de Química e Bioquímica, Faculdade de Ciências da Universidade do Porto, Rua do Campo Alegre P-4169-007 Porto, Portugal.

Table of contents

Section S1. Quantification of TMD concentration

The apparent extinction coefficient for each nanomaterial used in this work was determined by UV-Vis spectroscopy. The extinction coefficient is an intrinsic property of the sample and its value can be determined from an absorbance calibration curve. The amount of nanomaterial dispersed in a sample can consequently be determined by measuring the absorbance relatively to an aqueous dispersion of known nanomaterial concentration.

To quantify the nanomaterial concentration, an accurate volume of the supernatant of nanomaterial/water dispersion was dried for 24 hours. The resulting dry powder was weighted, and the concentration of nanomaterial in the dispersion was determined. The apparent extinction coefficient, ε, can be estimated for a wavelength, λ, by measuring the optical density for the same stock dispersion. The spectra were obtained using a single beam Agilent 8453 spectrometer (Fig. S1.), and ε was thereafter determined. The nanomaterial concentration in each dispersion can be easily determined from the absorbance through the Beer-Lambert equation. The apparent extinction coefficient for each nanomaterial used - MWNT, GnPs, MoS_2, WS_2 and $MoSe_2$ – was determined at specific wavelengths. Absorbance was recorded at λ = 660 nm for carbon nanomaterials and $MoSe_2$ (to eliminate the surfactant absorbance contribution),[1, 2] and at the absorption peak for MoS_2 and WS_2: λ = 678 nm for MoS_2 and λ = 630 nm for WS_2, in line with previous reports.[3, 4]

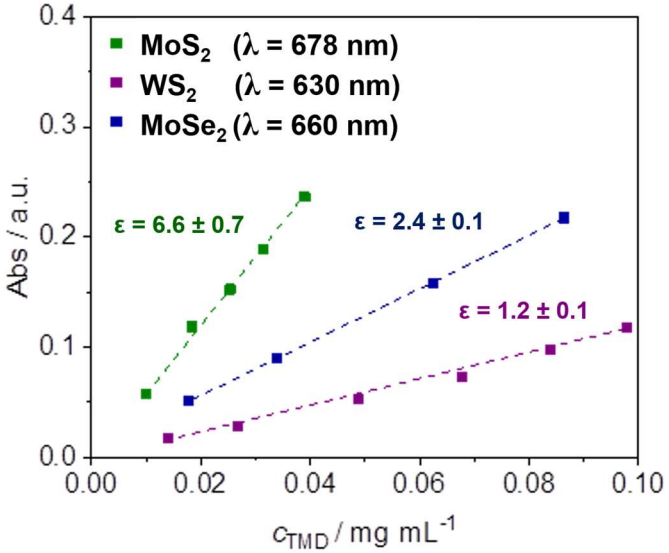

Fig. S1. Apparent absorbance versus TMD concentration for the systems studied. Each calibration curve represents the average of at least 3 different measurements.

Section S2. Colloidal stability of the obtained TMD dispersions

Smith et al. studied the preparation of SC-coated MoS_2 nanosheets and the zeta potential was measured to be -40 mV, suggesting high colloidal stability for the particles in aqueous solution.[3] However, herein we show that the profile of the dispersibility curves differs among surfactants and among MX_2 materials. The stability of the obtained dispersions is an important aspect since some applications may require higher preparation times. Therefore, this parameter was evaluated by zeta potential measurements for 3 weeks, since the charge of the hard surfaces relates with its colloidal stability. Analyzing zeta potential results, this parameter does not vary significantly with time for all the systems investigated, suggesting the degree of surface coverage by the ionic surfactants does not change appreciably. This constancy of zeta potential with time is especially seen in the case of the CTAB dispersions. This may have to do with the different charges of the materials, anionic TMDs and cationic CTAB. Colloidal dispersions can be considered kinetically stable when | ζ |> 30 mV; the higher | ζ |, the higher stability. Thus, from the observation of Fig. S2 one can infer that surfactant-exfoliated nanomaterials are expected to be more than the materials exfoliated without dispersant.

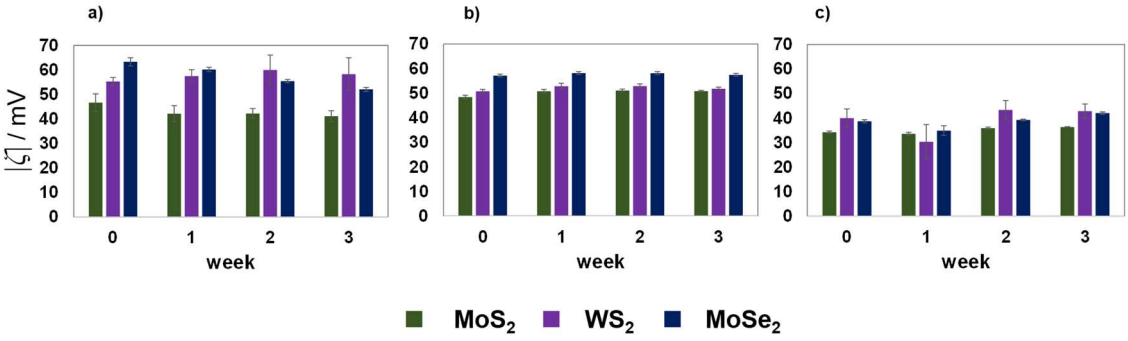

Fig. S2. Variations in zeta potential of the dispersed nanomaterials through time: a) TMDs dispersed with SC; b) TMDs dispersed with CTAB; and c) TMDs dispersed without surfactant.

References

1. Zhang, H.; Cong, L.; Wang, J.; Wang, X.; Liu, G.; Yu, W.; Zhang, H.; Dong, X.; Fan, W., Impact of CTAB on morphology and electrochemical performance of MoS2 nanoflowers with improved lithium storage properties. *J. Mater. Sci.: Mater. Electron.* **2018,** *29* (5), 3631-3639.
2. Narayan, R.; Lim, J.; Jeon, T.; Li, D. J.; Kim, S. O., Perylene tetracarboxylate surfactant assisted liquid phase exfoliation of graphite into graphene nanosheets with facile re-dispersibility in aqueous/organic polar solvents. *Carbon* **2017,** *119*, 555-568.
3. Smith, R. J.; King, P. J.; Lotya, M.; Wirtz, C.; Khan, U.; De, S.; O'Neill, A.; Duesberg, G. S.; Grunlan, J. C.; Moriarty, G.; Chen, J.; Wang, J.; Minett, A. I.; Nicolosi, V.; Coleman, J. N., Large-scale exfoliation of inorganic layered compounds in aqueous surfactant solutions. *Adv. Mater.* **2011,** *23* (34), 3944-8.
4. Liu, H.-L.; Shen, C.-C.; Su, S.-H.; Hsu, C.-L.; Li, M.-Y.; Li, L.-J., Optical properties of monolayer transition metal dichalcogenides probed by spectroscopic ellipsometry. *Appl. Phys. Lett.* **2014,** *105* (20), 201905.

V

Carbon nanotube/graphene nanocomposites built via surfactant-mediated colloid assembly as metal-free catalysts for the oxygen reduction reaction

Carbon nanotube/graphene nanocomposites built via surfactant-mediated colloid assembly as metal-free catalysts for the oxygen reduction reaction

Bárbara Abreu,[1,2] Marcos Rocha,[1] Marta Nunes,*[2] Cristina Freire,[2] and Eduardo F. Marques*[1]

[1]*CIQUP, Departamento de Química e Bioquímica, Faculdade de Ciências, Universidade do Porto 4169-007 Porto, Portugal*

[2]*REQUIMTE-LAQV, Departamento de Química e Bioquímica, Faculdade de Ciências, Universidade do Porto 4169-007 Porto, Portugal*

*email: marta.nunes@fc.up.pt; efmarque@fc.up.pt

Keywords:

Composite nanomaterials ; Nanocarbon ; Surfactants and Polymers ; Electrocatalysis ; Oxygen reduction reaction

Abstract

The development of composites from 1D and 2D nanocarbon building blocks, namely carbon nanotubes and graphene layers, with enhanced properties or novel functionalities is an emerging challenge in material science. Herein, we developed a colloid-based approach using surfactants and polymers to non-covalently functionalize multiwalled carbon nanotubes (MWNTs) and graphene nanoplatelets (GnPs), and to fabricate GnP@MWNT nanocomposites via an electrostatic-driven assembly process in aqueous solution. In the assembly process, two building methods were used and compared (bulk mixing and adapted layer-by-layer assembly), using surfactant and polymer/surfactant combinations as the dispersants for the initial nanomaterials. After their characterization by scanning electron microscopy, Raman spectroscopy and BET analysis, the nanocomposites were evaluated as electrocatalysts for the oxygen reduction reaction (ORR). Results show that the type of the dispersant (namely the presence of polymer) plays a more relevant role than the specific building method in almost all the ORR parameters. Further, the nanocomposites show selectivity towards the 2-electron pathway oxygen reduction for the electrochemical production of hydrogen peroxide. The development and optimization of further nanocomposite electrocatalysts can be pursued using this type of versatile and robust assembly method.

1. Introduction

During the past decades, research in carbon has focused on the study of its low-dimensional forms – 0D fullerenes, 1D carbon nanotubes (CNTs) and 2D graphene (G) – unraveling and rationalizing their properties.[1-3] After the discovery of these archetypical forms, however, there has also been great interest in combining them into more complex architectures, namely different types of hierarchical nanocomposites, in order to create synergisms and obtain novel or more advanced functionalities.[1] For instance, 0D/1D nanocomposites (involving fullerenes and CNTs) have been fabricated[4-6] and characterized in terms of their optical,[7] thermal,[8] and electrocatalytic[9] properties. The building of 0D/2D structures has revealed promising features for applications as support materials for electrochemical reactions[10] and photovoltaic devices.[11] Strategies to combine 0D with 1D and 2D nanomaterials have also been developed resorting to molecular dynamics simulations[12] and experimental studies.[13]

Other emerging architectures using lower dimension nanocarbons involve the combination of nanotubes and graphene sheets.[14-18] The building of the mentioned hybrid CNT/G structures is a considerable challenge, and essentially two major routes can be followed. It can be achieved by covalent (i.e. chemical) functionalization of one or both of the carbon nanomaterials involved[14, 16, 17, 19-22] or through non-covalent methods.[23, 24] While chemical functionalization may change the carbon surface and its properties, non-covalent functionalization (e.g. by physical adsorption of amphiphilic dispersants such as surfactants and polymers) is suitable if one wants to preserve the original properties of CNTs and G.[3, 25, 26] In the hybrid, the interposed CNTs and G layers could either lie mutually parallel or mutually perpendicular (see Fig. 1), as the limiting cases, or in a combination of both in the same material. In the former case, i.e. if the nanotubes lie horizontally within large-area graphene sheets, the mechanical strength of the latter could be significantly reinforced due to the excellent flexibility and strength of CNTs.[1] Conversely, in the perpendicular arrangement, aggregation of the G layers would be avoided and thus electronic transport,[27] thermal transport,[28] and hydrogen storage[29] could be enhanced. Studies regarding the design and building of CNT/G hybrid materials via non-covalent functionalization (using surfactants or polymers) are still very scarce, indicating that this area of research remains largely unexplored and unexploited. The exfoliation and dispersion of carbon nanotubes or graphene nanoplatelets with ionic surfactants would impart the carbon surface with charge due to the charged surfactant headgroups that remain exposed to water, while the hydrophobic chains adsorb onto the

surface. Furthermore, the use of polymer/surfactant mixtures as dispersants could enhance the organization of the obtained materials.[30, 31]

Among the possible applications for the CNT/G hybrids, sustainable electrochemical-related technologies, in particular, have gained increasing attention over the last years.[32] The hybrids could be applied as metal-free electrocatalysts for the oxygen reduction reaction (ORR), a sustainable and cost-effective alternative to the state-of-the-art platinum-based catalysts.[33-35] In this realm, the reduction of oxygen can follow two pathways: the direct 4-electron process, generating water; or the indirect 2-electron process, generating hydrogen peroxide as an intermediate product.[36] ORR via direct pathway is a pivotal reaction in fuel cells, the most promising of the clean energy generation devices.[37, 38] Fuel cells can convert chemical energy directly into electricity with high efficiencies.[39] The oxygen reduction occurs at the cathode of the cell and controls the global device performance due to its slow kinetics,[40] making the use of an effective electrocatalyst a crucial feature.[41] In parallel, the indirect pathway presents applicability in the electrochemical production of H_2O_2, and could be employed to replace the anthraquinone oxidation process (i.e. the main industrial process for H_2O_2

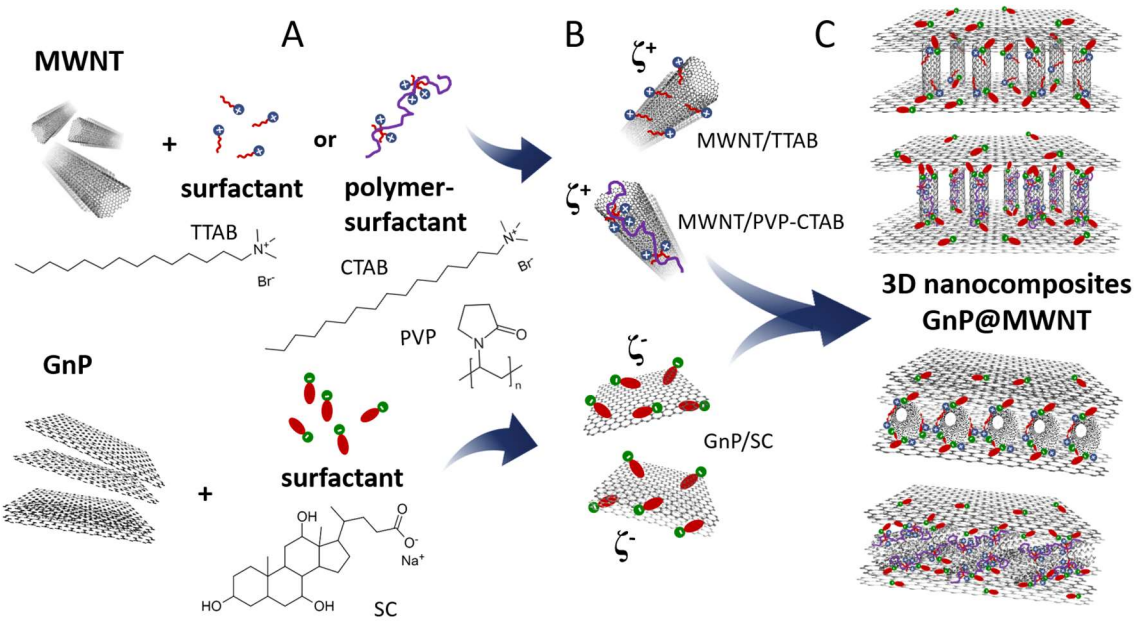

Fig. 1. Schematic representation of the building process of the 3D GnP@MWNT nanocomposites. A: exfoliation and dispersal of the 1D blocks, MNWTs, by surfactant TTAB or polymer/surfactant PVP-CTAB complexes (top) and similar process for the 2D blocks, GnPs, by surfactant SC (bottom). B: formation of aqueous dispersions of positively charged MWNTs and negatively charged GnPs. C: assembly of the nanocomposites via electrostatic attractions, with two possible limiting configurations shown: top two structures, layers of orthogonally placed MWNTs alternating with GnP layers; bottom two structures, MWNT layers lying horizontally over the GnP layers, with the lowest sketch showing the MWNTs coated by the polymer-surfactant (PVP-CTAB) complexes.

generation), which currently requires massive infrastructures, significant energy input and involves hazards and high costs.[42]

In this work, we have developed 3D composites from multiwalled carbon nanotubes (MWNTs) and graphene nanoplatelets (GnPs) using an original non-covalent colloid assembly approach, and then explored the obtained materials as electrocatalysts for oxygen reduction reactions as a proof of concept. The individual carbon building blocks were prepared using amphiphiles as dispersants (namely, two cationic alkyltrimethylammonium bromide surfactants, TTAB and CTAB, the anionic surfactant sodium cholate, SC, and the neutral polymer polyvinylpyrrolidone, PVP) and a strictly controlled dispersal procedure in aqueous media.[26, 43] The rationale relies on taking advantage of electrostatic interactions between the surfaces of the two types of blocks by previously functionalizing them separately with oppositely charged amphiphiles. A schematic depiction of the assembly process is conveyed in Fig. 1. In step A, the entangled MWNT powders are exfoliated and dispersed by sonication using either TTAB or a PVP-CTAB mixture, while the GnP powder undergoes a similar process using SC. The surfactants or polymer/surfactant aggregates adsorb onto the surface of the nanocarbons by mainly hydrophobic interactions owing to their hydrocarbon chains, while the charged surfactant headgroups are exposed to the aqueous medium. Two types of dispersions, step B, are thus obtained: those containing positively charged well-dispersed MWNTs (or thin bundles thereof) and those having negatively charged dispersed GnPs, with both types of particles having their respetive electrical double layers and zeta potential (z) values. In step C, mixing the two types of functionalized blocks leads to the assembly of the composites via electrostatic attractions. As mentioned before, two idealized configurations of the resulting materials are shown. The two uppermost sketches in Fig. 1C depict snapshots of the composite structure where the nanotubes are positioned perpendicularly to the graphene layers, with the surfactant or polymer/surfactant molecules acting as gluing moieties. Conversely, the two bottom sketches depict structures where the nanotubes lie horizontally over the graphene layers, with the lowest sketch depicting the tubes covered by the cationic polymer-surfactant (PVP-CTAB) complexes interacting with the anionic SC-coated graphene layers, where the polymer may act as further reinforcement agent. Other assorted intermediate configurations are likely formed, with randomly tilted MWNTs between GnP layers or mixed orthogonal/parallel/tilted nanotubes.

Two procedures were tested and compared, designated here as i) bulk method (BM) and ii) adapted layer-by-layer deposition method (LM). These methodologies were aimed at the fabrication of reproducible nanocomposites under optimized conditions. A

key aspect of this work in relation to the literature is the building of the 3D carbon structures using a mild experimental method, namely an assembly process in aqueous solution via non-covalent functionalization. This procedure bears strong advantages compared to the more conventional fabrication methods, which typically rely on covalent functionalization[44] and/or use of organic solvents.[25, 45] We deem it facile, cost-effective, sustainable and timesaving. The designed materials were characterized using a combination of techniques, and their performance as electrocatalysts for the oxygen reduction reaction was assessed. We highlight that the use of controlled experimental conditions (i.e. delivered energy per carbon mass, and type and concentration of surfactant used), inexpensive materials and equipment can be extended to other nanocomposites and applications, and may also open the door to scale-up processes.

2. Experimental Section

2.1. Materials

Multiwalled carbon nanotubes from Cheaptubes® (outer diameter *d* = 8-15 nm and length *L* = 10-50 μm) and graphene nanoplatelets (xGnP® Graphene Nanoplatelets Grade M-5) from XG Sciences were used as received. The commercial surfactants, tetradecyltrimethylammonium bromide (TTAB), cetyltrimethylammonium bromide (CTAB), sodium cholate hydrate (SC), all with purity ≥ 99 %, and the polymer polyvinylpyrrolidone (PVP), were acquired from Sigma-Aldrich and used as received. The reagents used in the electrocatalytic studies, namely potassium hydroxide (KOH, Riedel-de-Häen), Nafion (Aldrich, 5 wt% solution in lower aliphatic alcohols and water), 2-propanol (Aldrich, 99.5 %), and 20 wt% Pt/C (HiSPEC® 3000, Alfa Aesar) were also used as obtained. All aqueous solutions and dispersions were prepared using ultra-pure water from a Millipore system (resistivity 18.2 MΩ cm at 25 °C).

2.2. Surfactant-mediated preparation of building blocks

All the aqueous dispersions of MWNTs and GnPs were prepared according to a published method that combines tip-sonication and centrifugation.[26] To build the 3D materials, the surfactants were chosen according to our previous studies[26, 43] considering the following aspects: i) the building blocks were functionalized with ionic surfactants of opposite charge, since electrostatic interactions are the driving force for the composite assembly; ii) TTAB was selected as the cationic surfactant to functionalize MWNTs, due to its high effectiveness in dispersing the nanotubes and its low Krafft temperature[43]; iii) given the importance of using polymers to obtain robust and well-structured composites,[30, 31] the polymer/surfactant mixture PVP-CTAB was also used to

functionalize the MWNTs owing to the highly effective dispersing ability of this mixture and the net positive charge obtained (cf. Supporting Information, section S1); iv) SC was used as the anionic surfactant to functionalize GnPs, as it shows also good effectiveness in dispersing graphene (cf. S.I., section S2) and is oppositely charged to TTAB; v) the surfactant concentration for each system was selected from the respective dispersion curves, at the maximum dispersibility, according to previous studies.[26, 43]

All preparation steps were carefully monitored. To prepare the dispersions of building blocks, the nanocarbon powders (MWNTs and GnPs) were weighted, followed by addition of the desired aqueous surfactant solution, resulting in an initial *m*/*v* loading of 3 mg·mL^{-1} of nanocarbon in water. The samples were then tip-sonicated, with a total of energy delivered of 0.6 kJ·mL^{-1}. Sonication was carried out using a Sonics VCX500 probe (500 W output power; 20 kHz processing frequency) with a freshly polished 13 mm tip, at 60 % amplitude. Temperature was controlled with a thermostated bath, to avoid overheating. After sonication, the MWNT dispersions were centrifuged for 20 min at 4000 g, and the supernatant collected. Centrifugation causes the larger aggregates, *viz.* impurities and big bundled MWNT particles, to precipitate, hence providing isolated tubes and thin bundles. For the GnP dispersions, the centrifugation step was seen to cause sedimentation of the larger 2D particles and drastically reduce the sheet mean lateral dimension (cf. S.I., section S2), as also reported before.[46] Therefore, for GnPs, this processing step was eliminated and the final concentration of GnPs remained equal to the initial loading (3 mg·mL^{-1}).

2.3. Nanocomposite assembly

Two approaches were followed to build the GnP@MWNT nanocomposites: i) bulk mixing method and ii) adapted layer-by-layer method. [18, 47] i) In the bulk mixing method (B-method), identical volumes of MWNT/TTAB (or MWNT/PVP-CTAB) supernatants and GnP/SC as-obtained dispersions (without centrifugation) were added to a vial and tip-sonicated using the same energy density applied to the starting dispersions. The obtained dispersion was vacuum-filtered using a cellulose acetate membrane, rinsed with ethanol to remove the excess of surfactant, and dried overnight. ii) In the adapted layer-by-layer (LbL) method (L-method), identical aliquots of MWNT/TTAB (or MWNT/PVP-CTAB) supernatants and GnP/SC dispersions were added alternately to a cellulose acetate membrane, inserted in a vacuum filtration system. Each layer was deposited after the previous one was apparently dried and at the end, the film was rinsed with ethanol and dried overnight.

For easier understanding henceforth, the composites built using MWNT/TTAB and GnP/SC dispersions (i.e. with only surfactants as building agents), are denoted as

S/S. When a polymer/surfactant (PS) mixture is used to functionalize the MWNT, the resulting composites are denoted as PS/S. The prefixes B or L refer to the building method, bulk or adapted LbL, respectively.

2.4. Materials characterization

The zeta potential, ζ, of the water-dispersed particles (MWNT and GnP) was measured at 25 ºC using an Anton Paar LitesizerTM 500 with a 40 mW semiconductor laser (658 nm) and DTS 1060C disposable zeta cells. The electrophoretic mobility, μ, was measured using a combination of electrophoresis and laser Doppler velocimetry techniques and ζ was calculated from μ using the known Henry equation, a dielectric constant of 78.5, a medium viscosity of 0.89 cP and a f(κa) function of 1.5.[48, 49] SEM images of the MWNT, GnP and nanocomposite powder materials were obtained at Centro de Materiais da Universidade do Porto (CEMUP), on a FEI Quanta 400FE microscope with an electron beam of 25 kV at different magnifications. The nanocomposite films were fractured in liquid nitrogen to obtain cross-section images. Raman spectra of the solid-state nanocomposites were recorded on a RAMOS RA532 Raman Analyzer using a laser emitting at 532 nm on a glass cuvette, at room temperature. The surface area and pore size of the nanocomposites were determined by a nitrogen adsorption analyzer (TriStar Plus, Micromeritics, Norcross, USA). The samples were dried at 100 ºC and treated under nitrogen flow overnight. The specific surface area (SSA) was evaluated using the BET method, and the average pore diameter (Dp) using the BJH theory applied to the desorption branch of the isotherm.[50]

2.5. Electrocatalytic activity towards the oxygen reduction reaction (ORR)

The catalytic performances towards ORR of MWNT, GnP and as-produced GnP@MWNT nanocomposites were assessed at room temperature in a three electrode compartment cell. A rotating disk electrode (RDE) of glassy carbon (3 mm of diameter, Metrohm) was used as working electrode, an Ag/AgCl (3 mol dm^{-3} KCl, Metrohm) as reference electrode and a glassy carbon rod (2 mm of diameter, Metrohm) as auxiliary electrode. The modified electrodes were prepared by the following procedure: 1 mg of the prepared material was dispersed by ultrasonication (for 15 min) in 250 µL of a mixture of isopropanol/water (1:1 v/v) and Nafion (20 µL) to form a homogeneous ink. Then, three drops of 2.5 µL of the selected ink were deposited onto the RDE surface and dried under an air flux, yielding an electrocatalyst loading of 99.05 $\mu g \cdot cm^{-2}$. Prior to modification, the

electrode was conditioned by a polishing/cleaning procedure (cf. S.I., section S3, for further details).

The electrocatalytic tests were performed in N_2- or O_2-saturated (purged for 30 min before the measurements) 0.1 mol dm^{-3} KOH solutions. Cyclic voltammetry (CV) experiments were conducted at the scan rate of 0.005 V s^{-1} and the linear sweep voltammetry (LSV) measurements at 0.005 V s^{-1} for rotation speeds ranging from 400 to 3000 rpm. The ORR current was obtained by subtracting the current measured in N_2-saturated electrolyte from the current measured in O_2-saturated electrolyte. The onset potential (E_{onset}), defined as the potential at which the O_2 reduction reaction starts, was calculated as the potential at which the slope of the voltammogram exceeds 0.1 mA cm^{-2} V^{-1}, as described elsewhere.[39] The
LSV data was analyzed by the Koutecky-Levich (K-L) equation (cf. S.I., section S3, for further details).[40, 51]

For the bipotentiostat measurements, a rotating ring-disk electrode (RRDE) of glassy carbon disk (d = 5 mm) with a platinum ring (d = 375 µm, Metrohm) was used as working electrode. The modified disk-electrode was swept cathodically at a scan rate of 0.005 V s^{-1} and 1600 rpm in O_2-saturated 0.1 mol dm^{-3} KOH solution, while the potential of the Pt ring was kept constant at E = 0.2 V vs. Ag/AgCl to assure the oxidation of the hydrogen peroxide species formed during the ORR. Calculation of the peroxide percentage was performed according to established methods (cf. also S.I., section S3).[52] The evaluation of the electrochemical stability was performed by chronoamperometry in O_2-saturated 0.1 mol dm^{-3} KOH solution, with the RDE electrode at E = −0.45 V vs. Ag/AgCl and 1600 rpm during 20000 s. To facilitate comparisons with the literature, the E values determined vs. Ag/AgCl were converted to the reversible hydrogen electrode (RHE) scale according to the Nernst equation (cf. S.I., section S3).[53]

3. Results and Discussion

3.1. Structural characterization of the nanocomposites

The assembly of MWNTs and GnPs into the 3D composite structures is expected to occur via electrostatic attractive interactions between the carbon surfaces functionalized with surfactants of opposite charge. This type of non-covalent functionalization occurs through the adsorption of the hydrophobic moieties of the surfactant or polymer/surfactant system at the carbon surface. The hydrophilic groups point towards the solvent, conferring charge to the nanomaterials. To confirm this charge functionalization, the zeta potential was measured for the building block dispersions, and the results are shown in Fig. 2. The graphic also shows the zeta potential for the GnP@MWNT nanocomposite dispersions, measured after the B-method was applied and before vacuum filtration, i.e. immediately after sonication of the mixture of MWNT and GnP dispersions (note that the L-method does not produce composite dispersions). The zeta potential of the MWNT dispersions show positive values, as expected, since the nanotubes are coated with cationic surfactant, either TTAB (yielding $\zeta \approx +37$ mV) or the CTAB-PVP mixture ($\zeta \approx +17$ mV); conversely, the GnP dispersions are negatively charged due to the adsorption of anionic surfactant ($\zeta \approx -54$ mV).

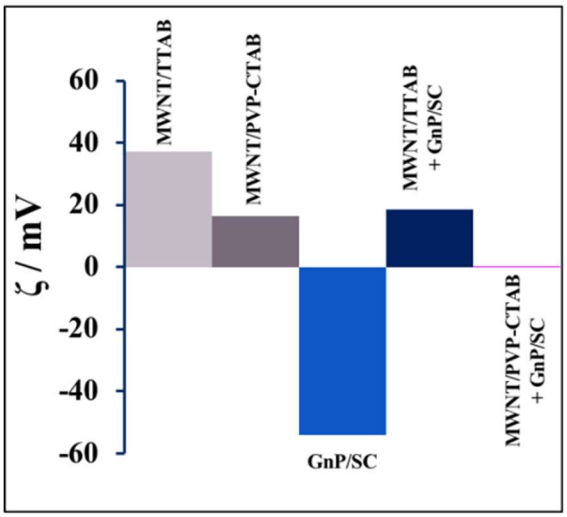

Fig. 2. Zeta potential values of the aqueous dispersions of the 1D (MWNT), 2D (GnP) and final 3D (GnP@MWNT) nanomaterials; uncertainty bars within ± 5%.

The GnP@MWNT nanocomposite obtained using TTAB shows $\zeta \approx +18$ mV, a value intermediate in module compared to the initial building blocks (hence indicating partial charge cancelling), but positive, suggesting that the exposed surfaces of the composite particles may be slightly enriched with TTAB or TTAB/MWNT. Significantly, the other GnP@MWNT based on CTAB-PVP shows virtually null surface charge, hence suggesting in this case full charge neutralization and the formation of precipitate-like particles of the composite. These results overall confirm the non-covalent functionalization via surfactant (or polymer/surfactant) adsorption and indicate that electrostatic attractions are indeed the driving force for composite assembly.

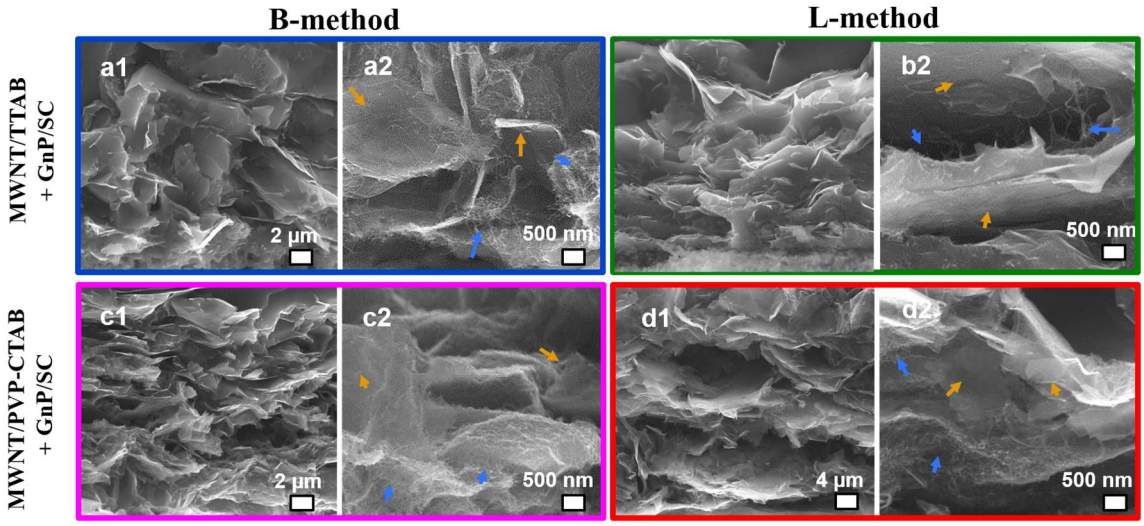

Fig. 3. Representative SEM micrographs of cross-section cuts of the built MWNT/GnP nanocomposites: top, MWNT/TTAB + GnP/SC solid prepared by the bulk (B) method, a1-a2, or adapted layer-by-layer (L) method, b1-b2; bottom, the MWNT/PVP-CTAB + GnP/SC solid prepared by the B-, c1-c2, or L-, d1-d2, methods, respectively. The blue and orange arrows point to specific morphological features described in the main text.

To evaluate the structure of the obtained GnP@MWNT composites and gauge their level of organization, these materials were characterized by SEM. Representative micrographs are depicted in Fig. 3, through a cross-section view. At least 3 different samples of each composite were analyzed, and several sections were scanned to establish and consolidate the observations. The results show a clear influence of both the assembly method and the use of polymer in the structure of the resulting composite materials. Fig. 3a1 and a2 show a random distribution of the MWNTs and GnPs when surfactants are used as dispersants and the bulk method is employed (B_S/S material). In contrast, and as might be expected, one observes an organized structure of the layer-

by-layer composites, L_S/S and L_PS/S (Fig. 3b1 and 3d1, respectively), with visible layers of nanotubes (blue arrows in Fig. 3b2 and d2) and parallelly stacked graphene nanoplatelet layers (yellow arrows in Fig. 3b2 and 3d2). Regardless of being built via the bulk methods, the B_PS/S composite (Fig. 3c1 and c2) also exhibits a parallelly-stacked structure, clearly contrasting with the aforementioned B_S/S. Therefore, the results show an evident influence of both the assembly method and the use of polymer in the structure of the resulting composite materials. From this analysis we can infer that polymer/surfactant mixtures as functionalizing agents of MWNTs, even at low concentration, play a relevant role in the fabrication of organized 3D architectures. Further, the combination of this dispersant composition with a LbL building procedure gives the most organized composites, with defined and continuous layers of MWNTs and parallel GnPs. Regarding the orientation of MWNTs, SEM results suggest that they do not acquire a preferred orientation between the GnPs. Nevertheless, vertical tubes between the GnP layers are observed (blue arrows in Fig. 3b2), which is a further indication of the strong interaction between the two building blocks.

The materials were milled to smaller fragments for Raman and BET analysis, and redispersed to form an ink for the modification of the electrode in electrocatalytic studies. The obtained milled powders and ink were characterized by SEM (cf. S.I., section S4) confirming that these preparations retain a similar structure with respect to the original composites, with MWNTs placed between the GnP layers.

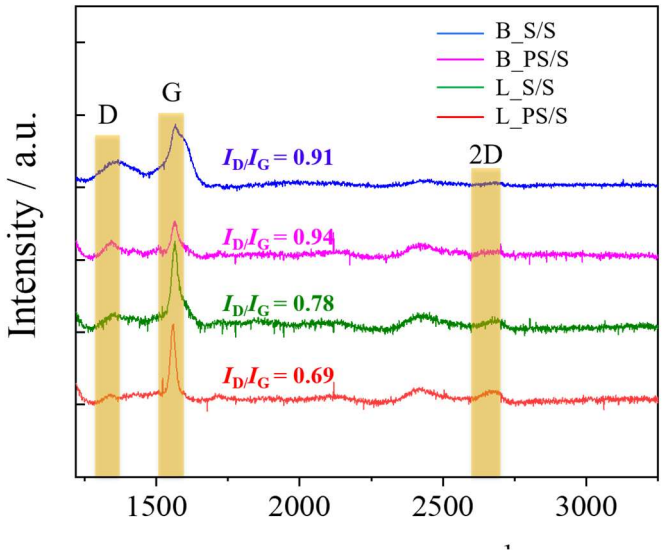

Fig. 4. Raman spectra and respective I_D/I_G ratios obtained for the four composites.

To provide further insight on the structure and defects of the four composites, Raman spectroscopy was also carried out (Fig. 4). The Raman spectra of carbon nanomaterials shows three characteristic peaks: i) the D band (~1360 cm^{-1}), assigned to the breathing modes of the sp^2 atoms in rings, and related with structural defects and disorder on the sp^2 domain; ii) the G band (~1560 cm^{-1}), due to the bond stretching of all pairs of sp^2 atoms, thus related to the C atoms in the bulk of the graphitic layers and iii) the 2D band (~ 2700 cm^{-1}), due to second order phonons and related to the number of layers of the carbon nanomaterial.[54, 55] In the case of graphene, the 2D band tends to disappear when the material has more than five layers.[39] From the I_D/I_G ratio in Raman spectra, one can obtain information on the defective features of the carbon composites. The higher the ratio, the more disordered the carbon material.[15, 54] B-method materials show the higher I_D/I_G ratios, which reflects the observations of SEM imaging: for the composite B_S/S, MWNTs and GnPs are randomly distributed, making their defective edges more exposed. The lower I_D/I_G values obtained for the L-method composites suggest a decrease of the defect density, particularly for the material prepared with carbon nanotubes non-covalently functionalized with a polymer/surfactant mixture (L_PS/S). A possible justification for this effect is the increased organization of the material, as observed by SEM imaging, which masks the defects of the building blocks, since the edges of GnPs are parallelly stacked and MWNTs stand between the horizontal sheets.

BET analysis was performed for a better understanding of the porosity and surface area of the composites (Fig. 5). The N_2 adsorption-desorption isotherms of the four GnP@MWNT composites belong to type II,[50] characteristic of non-porous or

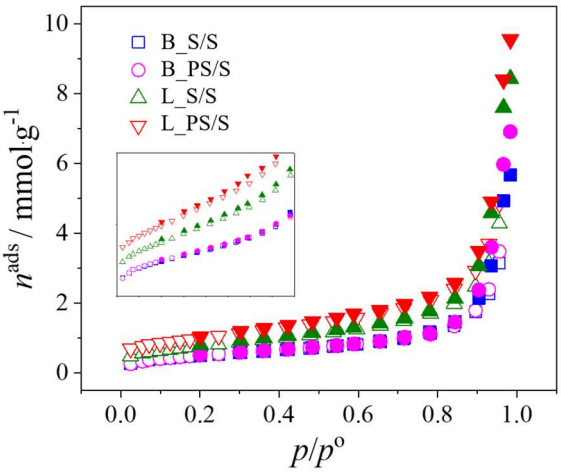

Fig. 5. N_2 adsorption-desorption isotherms at -196 ºC, closed symbols represent the desorption points; inset shows the isotherms between 0 < p/p° < 0.6.

macroporous materials. The gradual curvature at lower p/p^o suggests an overlap of monolayer coverage and the onset of multilayer adsorption.[56]

Table 1. Textural properties of the MWNT/GnP composites, obtained from N2 adsorption-desorption isotherms at -196 ºC.

Composite	BET surface area / $m^2\ g^{-1}$
B_S/S	41.1 ± 0.2
B_PS/S	42.2 ± 0.2
L_S/S	61.2 ± 0.1
L_PS/S	78.3 ± 0.3

The determined BET surface area (Table 1) is significantly lower for the composites built by bulk method, indicating a stronger packing of MWNTs and GnPs in the 3D assembly. The higher BET surface area obtained for L_PS/S composite is consistent with the imaging results, which shows more organized, detached layers for this material, and with the Raman results, that indicate lower defect density.

Thus, the combination of SEM, Raman and BET results suggests that the composites can be qualitatively sorted by structuration degree, as follows: B_S/S < B_PS/S < L_S/S < L_PS/S.

3.2. ORR electrocatalytic activity of the nanocomposites

Following the building of the 3D nanocomposites, alongside the assessment of the effect of dispersant and assembly method on their final organization, we proceeded to evaluate their effectiveness as electrocatalysts for the electrochemical oxygen reduction reaction. Our goal here was two-fold: (i) to probe the materials performance towards ORR catalysts as a proof-of-concept; (ii) to gauge the effect of the preparation methods on this performance. For this, the ORR electrocatalytic activity of the built composites was evaluated in alkaline medium (0.1 mol dm^{-3} KOH). The obtained results are shown in Figs. 6 and 7, and complementary electrochemical data is also provided in Supporting Information, section S3.

Cyclic voltammograms (CVs) obtained for the four composite-modified electrodes in N_2- and O_2- saturated solutions are shown in Fig. 6a (cf. also S.I., section S3, Fig. S3.1, for the separate voltammograms of starting MWNTs, GnPs and the four GnP@MWNT composites). The voltammograms show that no electrochemical processes occur in N_2-saturated solution, while all the materials display an irreversible electrochemical process in O_2-saturated solution, indicative of their electrocatalytic activity for ORR. As can be seen in Fig. 6a, the composites have cathodic peaks at E =

0.65 V vs. RHE for L_S/S and at *E* = 0.71 V vs. RHE for B_S/S and the materials containing polymer/surfactant mixtures, B_PS/S and L_PS/S.

The electrocatalytic activity of the four composites in ORR can be compared regarding onset potential, diffusion-limited current density, and number of exchanged electrons. These parameters can be determined from the linear sweep voltammetry (LSV) plots.[39] The linear sweep voltammograms (LSVs) obtained on RDE, at 1600 rpm in O_2-saturated solution are shown in Fig. 6b. For comparison, the LSVs of 20 wt % Pt/C, of the non-modified glassy carbon electrode (GCE), and of the starting nanomaterials (non-covalently functionalized MWNTs and GnPs) are presented. The ORR polarization curves at several rotation rates for the four composites can be found in S.I., section S3, Fig. S3.2. Since the surfactant was rinsed in the preparation of the MWNTs for electrocatalysis, the aggregation state of this material after sonication and centrifugation is expected to influence its electrocatalytic performance. We also note that preliminary characterization studies suggest that there is similar debundling degree of nanotubes for

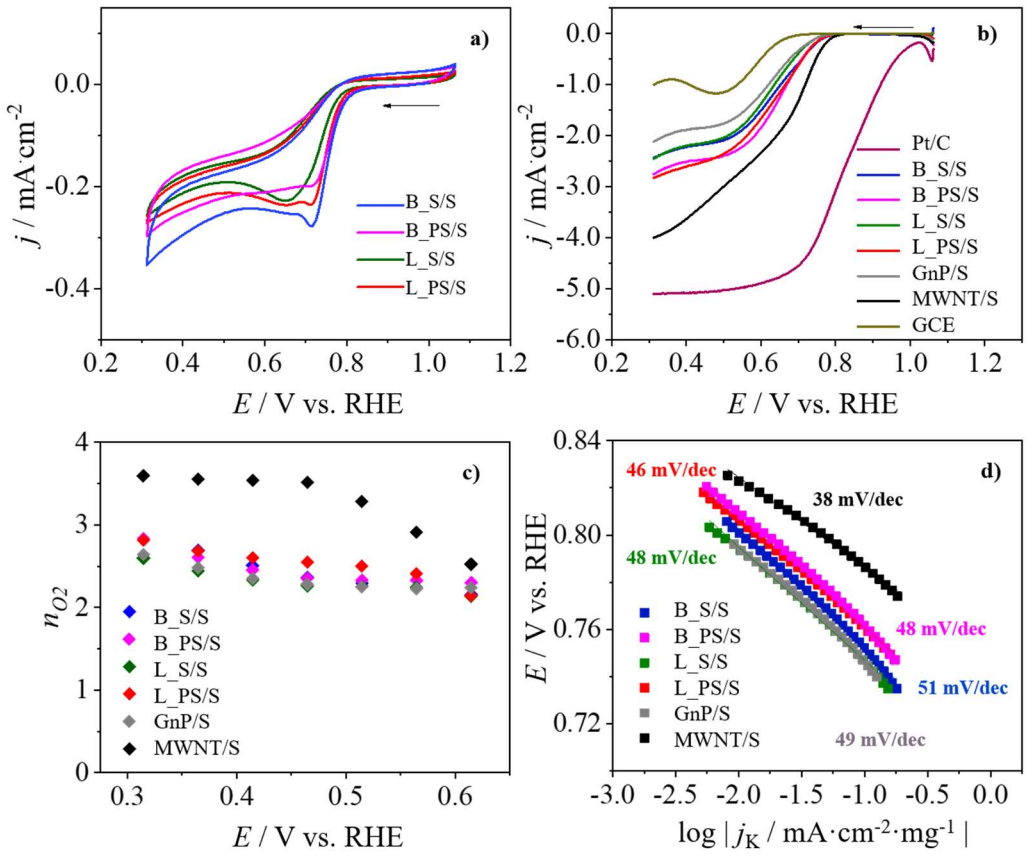

Fig. 6. a) CVs using RDE in N_2-saturated (dashed line) and O_2-saturated (full line) 0.1 mol·dm^{-3} KOH solution at 1600 rpm and 0.005 V s^{-1}. b) LSV using RDE in O_2 saturated 0.1 mol·dm^{-3} KOH solution at 1600 rpm and 0.005 V·s^{-1}; c) number of electrons transferred at different potential values, determined through the Koutecky-Levich equation; d) respective ORR Tafel plots.

the MWNT/TTAB and MWNT/PVP-CTAB dispersions, and hence only one system, MWNT/S (or MWNT/TTAB), was used for comparison with the composites.

The performance of the four composites lies between that of the starting materials, GnPs and MWNTs, with the first showing the lowest diffusion current value ($j_{\mathrm{L(0.32\ V,1600\ rpm)}} = -2.1\ \mathrm{mA \cdot\ cm^{-2}}$) and the latter presenting the higher diffusion current value ($j_{\mathrm{L(0.32\ V,1600\ rpm)}} = -4.0\ \mathrm{mA \cdot\ cm^{-2}}$), only inferior to the value obtained for the commercial Pt/C (20 wt%) reference ($j_{\mathrm{L(0.32\ V,1600\ rpm)}} = -5.1\ \mathrm{mA \cdot\ cm^{-2}}$). Despite the lower electrocatalytic performance of the composites compared to one of their building blocks, MWNTs, and with commercial Pt/C (20 wt%), the composites show higher diffusion current values than the bare GCE ($j_{\mathrm{L(0.32\ V,1600\ rpm)}} = -1.0\ \mathrm{mA \cdot\ cm^{-2}}$), which shows the advantage of the GCE modification with these materials. Furthermore, the electrochemical performance of the nanocomposites is enhanced compared to the performance of the starting GnPs, revealing the combination with MWNTs as a route towards optimization of the GnP properties. All composites show similar onset potentials ($E_{\mathrm{onset}} \approx 0.76\ \mathrm{V\ vs.\ RHE}$), in line with the values previously reported for doped graphene/carbon nanotube nanostructures($E_{\mathrm{onset}} = 0.8\ \mathrm{V\ vs.\ RHE}$)[15] and more positive than the bare GCE ($E_{\mathrm{onset}} = 0.6\ \mathrm{V\ vs.\ RHE}$).The results provide insight on the effect of the dispersant and building method on the final electrocatalytic activity of the materials, offering the route to optimization in future work. Diffusion currents are slightly higher for composites containing polymer ($j_{\mathrm{L(0.32\ V,1600\ rpm)}} = -2.5\ \mathrm{mA \cdot\ cm^{-2}}$ for materials containing only surfactant, B_S/S and L_S/S, and $j_{\mathrm{L(0.32\ V,1600\ rpm)}} = -2.8\ \mathrm{mA \cdot\ cm^{-2}}$ for the composites containing polymer, B_PS/S and L_PS/S). We note here that Chen *et al.* reported similar diffusion currents for nitrogen-doped graphene/carbon nanotube composites.[15] The structures reported are, nevertheless, doped, requiring additional preparation steps compared to the methodology used in our work.

The slight difference in the diffusion currents for polymer-containing composites can be explained by the polymer-surfactant interactions, since neutral polymers interacting with charged surfactants can effectively act as polyelectrolytes.[57] Wang *et al.* found that for the polycation PDDA, the quaternary ammonium functional groups along the backbone have a strong electron-acceptor ability, withdrawing electrons from carbon atoms in the nanotube surface to induce a net positive charge, hence facilitating the ORR catalytic activity of the CNTs.[58]

Similarly, the complex formed by neutral PVP chains with CTAB molecules, which have quaternary ammonium polar headgroups, can be conceived to behave as a polyelectrolyte on the MWNTs surface, increasing the ORR activity of the composites.

The ORR kinetics of the materials were evaluated by the Koutecky-Levich (K-L) plots at various potential values, using the LSVs obtained at different rotation rates (cf S.I., section S3, Figs. S3.2 and S3.3).

The increase of limiting current density with rotation rate for all materials reveals that the electron transfer reaction is limited by diffusion. The K–L plots of the four nanocomposites exhibit a linear relationship between j^{-1} and $\omega^{-1/2}$, suggesting a first-order electrocatalytic O_2 reduction reaction with respect to the concentration of dissolved O_2. Furthermore, almost parallel straight lines and, consequently, similar slopes over the

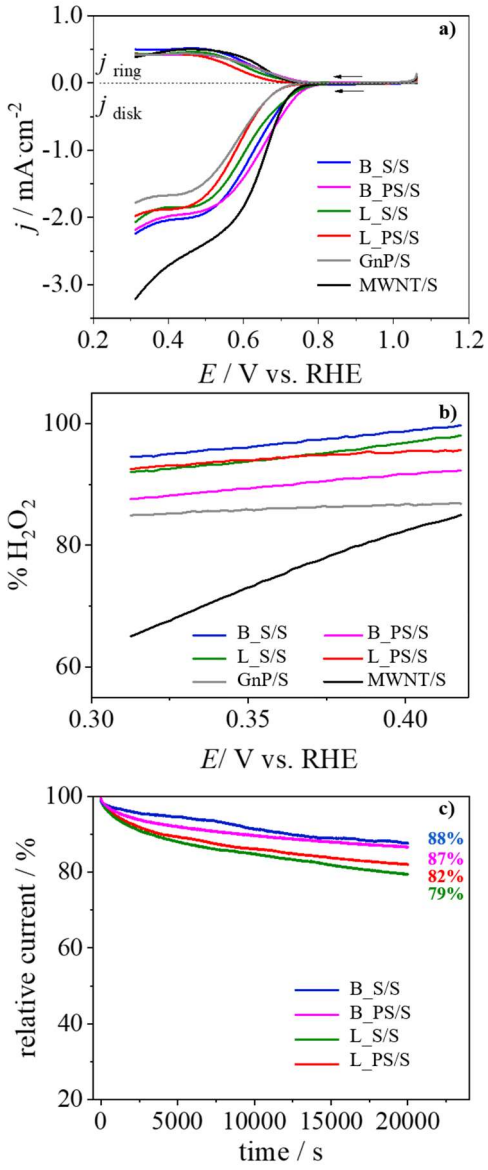

Fig. 7. a) LSV using RRDE in O_2 saturated 0.1 mol·dm^{-3} KOH solution at 1600 rpm and 0.005 V·s-1; b) Estimated percentage of H_2O_2 formed; c) chronoamperometric responses of the materials at E = 0.51 V vs RHE, in O_2 saturated 0.1 mol·dm^{-3} KOH solution at 1600 rpm for 20000 s.

potential range analyzed were obtained, which suggests an independence of the transferred electron number, *n*, over 0.32 and 1.05 V vs. RHE.

To gain insight on the ORR mechanism of the built electrocatalysts, the number of electrons was determined for several potentials (Fig. 6c), through the K-L plots. MWNTs show a strong dependence of n_{O2} with potential, increasing from n_{O2} = 2.5 at more positive potentials to n_{O2} = 3.6 electrons as the potential becomes less positive, suggesting no selectivity for either the 2- or 4-electron process. This dependence, although existent and typical of carbon nanomaterials, is less prominent in the composites, which show an almost constant n_{O2} through the potential range analyzed. An average n_{O2} of 2.3 for B_S/S and L_S/S, $\tilde{n}_{O2}$ = 2.5 for B_PS/S and $\tilde{n}_{O2}$ = 2.6 for L_PS/S, were obtained indicating a higher selectivity of the composites for the 2-electron process (indirect reduction through peroxide pathway).

The diffusion-corrected Tafel plots for the nanocomposites and the building blocks (Fig. 6d) were obtained from the LSV curves (Fig. 6b). In the low current density region, ranging from *E* = 0.84 to 0.70 V vs. RHE, the lowest Tafel slope of 38 mV dec^{-1} was obtained for MWNTs. The four composites show similar slopes, ranging from 46 mV dec^{-1} (for L_PS/S) to 51 mV dec^{-1} (for B_S/S), which indicates a similar ORR mechanism for the built nanocomposites.[59, 60]

To validate an apparent selectivity of the nanocomposites for the 2-electron process, and to evaluate their possible application in the electrocatalytic production of hydrogen peroxide, LSV studies in the bipotentiostatic mode using a RRDE electrode were performed. Fig. 7a shows the LSVs obtained at the electrode disk and ring. Considering the potential of 0.40 V vs. RHE, at which the reaction occurs at full extension, Fig. 7b shows that all composites produce higher percentages of H_2O_2 than the starting materials, exhibiting higher selectivity and higher applicability for this process. At the defined potential, the determined $\%H_2O_2$ produced reaches 99% for B_S/S, 97% for L_S/S, 95% for L_PS/S and 92 % for B_PS/S. For the building blocks, however, the values are significantly lower: 82% for MWNT/S and 86% for GnP/S. The results suggest that similar $\%H_2O_2$ is attained for the same material composition, independently of the building method. As expected, this feature relates with the $\tilde{n}_{O2}$ determined through the K-L plots, slightly higher for the materials built using the polymer/surfactant mixture as the MWNT dispersant. At less positive potential values, among the composites, B_S/S still shows the highest $\%H_2O_2$ (95 %) while B_PS/S shows the lowest (87 %), However, the LbL materials exhibit similar performances for H_2O_2 production at 0.32 V vs. RHE (92%). The values obtained for MWNT show a dependency of process selectivity with the potential, with a $\%H_2O_2$ decreasing from 90 % to approximately 65 %.

We further evaluated the electrochemical stability of the GnP@MWNT composites using chronoamperometry, in O_2-saturated 0.1 mol dm^{-3} KOH solution during 20 000 s (Fig. 7c). The chronoamperogram shows a higher current decay for the L-method nanocomposites, suggesting that the materials produced via the B-method have higher stability. This is consistent with the BET results presented above: the B-method composites possess lower specific surface area, which can be due to a higher packing density, a consequence of the more abundant contact sites between MWNTs and GnPs due to a lower degree of organization. Finally, we note that the composite B_S/S, which exhibits higher selectivity for the production of H_2O_2 and higher stability, has the potential to be further studied for electro-Fenton process,[61] to expand its range of applicability.

The reported electrocatalysts were built using a facile and time-saving methodology, that uses electrostatic attraction between non-covalently funcionalized surfaces. Additionally, the use of mild temperatures and water as dispersion medium facilitates further scale-up processes. This methodology differs from reported procedures that typically use high temperatures, organic solvents, covalently functionalized nanomaterials (CNTs, graphene, or both) or add a graphene reduction step to the procedure, when graphene oxide is used as a building block.[14, 16-19, 32, 45] Previous studies published by our group also show that the choice of surfactant plays a determinant role in the dispersibility of carbon nanotubes.[26, 43] Thus, through proper selection of dispersant (surfactant or polymer/surfactant mixture), the versatility of the procedure allows to extend its applicability to other families of nanomaterials.

4. Conclusions

Multiwalled carbon nanotubes and graphene nanoplatelets were employed to form nanocomposites resorting to two simple, cost-effective and mild procedures, taking advantage of electrostatic interactions between previous non-covalent functionalization of the carbon surfaces. The influence of the fabrication method and choice of dispersant (surfactant vs. polymer/surfactant mixture) on the final structuration and electrocatalytic performance of the material was evaluated. Characterization by SEM imaging, Raman spectroscopy and BET analysis overall indicate a higher MWNT/GnP organization in the composites built via adapted layer-by-layer (L) methods (namely MWNT layers placed between parallelly packed GnP layers) than in the structures built via the bulk (B) method. This organization increases when MWNTs are functionalized by a polymer/surfactant mixture, PVP-CTAB.

The electrocatalytic activity towards ORR was evaluated for the four composites. The choice of the dispersant has a stronger influence than the building procedure in

almost all the ORR parameters, with composites containing polymer presenting higher diffusion current values, and the materials containing only surfactant possessing a marked selectivity for the oxygen reduction via a 2-electron pathway. This selectivity was evaluated through RRDE, confirming that high amounts of H_2O_2 are produced. Chronoamperometry studies indicate higher stability for the materials built via B-method, which may be attributed to the stronger MWNT/GnP packing of these materials, as determined by the lower BET surface area.

This work contributes to the understanding of the parameters that influence the hierarchical organization of 3D structures using simple 1D and 2D blocks, while establishing a facile and versatile procedure for their fabrication. When tested for proof-of-concept functionality with respect to ORR, the produced materials exhibit selectivity towards the 2-electron pathway, with the electrochemical production of hydrogen peroxide. We envisage future development and optimization towards both direct and indirect pathways of oxygen reduction, and related applications, using the general assembly strategies presented in this work.

CRediT authorship contribution statement

B. Abreu: Investigation, Formal analysis, Validation, Writing - original draft. **M. Rocha:** Investigation. **M. Nunes:** Methodology, Validation, Writing - review & editing. **C. Freire:** Validation. **E. F. Marques:** Conceptualization, Methodology, Resources, Supervision, Funding acquisition, Writing - review & editing.

Conflicts of Interest

The authors declare no conflict of interest.

Acknowledgements

The authors acknowledge Fundação para a Ciência e a Tecnologia (FCT) for financial support through project UIDB/00081/2020. Prof. M. Azenha and coworkers are acknowledged for the support with Raman and BET experiments. B. Abreu also acknowledges financial support from FCT through the PhD grant PD/BD/128129/2016. M. Nunes acknowledges project PTDC/QUI-ELT/28299/2017 by its work contract, funded by FCT/MCTES through national funds and co-funded by FEDER (POCI-01-0145-FEDER-28299).

References

1. Zhang, J.; Terrones, M.; Park, C. R.; Mukherjee, R.; Monthioux, M.; Koratkar, N.; Kim, Y. S.; Hurt, R.; Frackowiak, E.; Enoki, T.; Chen, Y.; Chen, Y. S.; Bianco, A., Carbon science in 2016: Status, challenges and perspectives. *Carbon* **2016,** *98* (70), 708-732.
2. Georgakilas, V.; Perman, J. A.; Tucek, J.; Zboril, R., Broad family of carbon nanoallotropes: Classification, chemistry, and applications of fullerenes, carbon dots, Nnanotubes, graphene, nanodiamonds, and combined superstructures. *Chem. Rev.* **2015,** *115* (11), 4744-4822.
3. Tasis, D.; Tagmatarchis, N.; Georgakilas, V.; Prato, M., Soluble carbon nanotubes. *Chem. Eur. J* **2003,** *9* (17), 4000-4008.
4. Guldi, D. M.; Menna, E.; Maggini, M.; Marcaccio, M.; Paolucci, D.; Paolucci, F.; Campidelli, S.; Prato, M.; Rahman, G. M. A.; Schergna, S., Supramolecular hybrids of [60]fullerene and single-wall carbon nanotubes. *Chem. Eur. J* **2006,** *12* (15), 3975-3983.
5. Nasibulin, A. G.; Pikhitsa, P. V.; Jiang, H.; Brown, D. P.; Krasheninnikov, A. V.; Anisimov, A. S.; Queipo, P.; Moisala, A.; Gonzalez, D.; Lientschnig, G., A novel hybrid carbon material. *Nat. Nanotechnol* **2007,** *2* (3), 156.
6. Wei, T.; Martin, O.; Chen, M.; Yang, S.; Hauke, F.; Hirsch, A., Covalent Inter-Carbon-Allotrope Architectures Consisting of the Endohedral Fullerene Sc3N@C80 and Single-Walled Carbon Nanotubes. *Angew. Chem. Int. Ed.* **2019,** *58* (24), 8058-8062.
7. MacKiewicz, N.; Bark, T.; Cao, B.; Delaire, J. A.; Riehl, D.; Ling, W. L.; Foillard, S.; Doris, E., Fullerene-functionalized carbon nanotubes as improved optical limiting devices. *Carbon* **2011,** *49* (12), 3998-4003.
8. Dong, H.; Fan, Z.; Qian, P.; Ala-Nissila, T.; Su, Y., Thermal conductivity reduction in carbon nanotube by fullerene encapsulation: A molecular dynamics study. *Carbon* **2020,** *161*, 800-808.
9. Hasanzadeh, A.; Khataee, A.; Zarei, M.; Zhang, Y., Two-electron oxygen reduction on fullerene C60-carbon nanotubes covalent hybrid as a metal-free electrocatalyst. *Sci. Rep* **2019,** *9* (1), 13780.
10. Zhang, X.; Zhang, J. W.; Xiang, P. H.; Qiao, J., Fabrication of graphene-fullerene hybrid by self-assembly and its application as support material for methanol electrocatalytic oxidation reaction. *Appl. Surf. Sci.* **2018,** *440*, 477-483.
11. Yang, J.; Heo, M.; Lee, H. J.; Park, S.-M.; Kim, J. Y.; Shin, H. S., Reduced Graphene Oxide (rGO)-wrapped fullerene (C60) wires. *Acs Nano* **2011,** *5* (10), 8365-8371.
12. Zhang, G.; Glukhova, O. E., New automatic method for generating atomistic models of multi-branched and arbitrary-shaped seamless junctions of carbon nanostructures. *Comput. Mater. Sci* **2020,** *184*, 109943.
13. Wei, T.; Hauke, F.; Andreas, H., Covalent Inter-Synthetic-Carbon-Allotrope Hybrids. *Acc. Chem. Res* **2019,** *52* (8), 2037-2045.
14. Hong, T. K.; Lee, D. W.; Choi, H. J.; Shin, H. S.; Kim, B. S., Transparent, flexible conducting hybrid multilayer thin films of multiwalled carbon nanotubes with graphene nanosheets. *ACS Nano* **2010,** *4* (7), 3861-3868.
15. Chen, P.; Xiao, T.-Y.; Qian, Y.-H.; Li, S.-S.; Yu, S.-H., A nitrogen-doped graphene/carbon nanotube nanocomposite with synergistically enhanced electrochemical activity. *Adv. Mater.* **2013,** *25* (23), 3192-3196.
16. Pham, D. T.; Lee, T. H.; Luong, D. H.; Yao, F.; Ghosh, A.; Le, V. T.; Kim, T. H.; Li, B.; Chang, J.; Lee, Y. H., Carbon nanotube-bridged graphene 3D building blocks for ultrafast compact supercapacitors. *ACS Nano* **2015,** *9* (2), 2018-2027.
17. Oh, J. Y.; Kim, Y. S.; Jung, Y.; Yang, S. J.; Park, C. R., Preparation and exceptional mechanical properties of bone-mimicking size-tuned graphene oxide@carbon nanotube hybrid paper. *ACS Nano* **2016,** *10* (2), 2184-92.
18. Pansri, S.; Noothongkaew, S., MWCNTs/r-GO hybrid films fabricated by layer by layer assembly for supercapacitor electrodes. *J. Energy Storage* **2019,** *22*, 153-156.
19. Wei, C.; Wang, H.; Eid, K.; Kim, J.; Kim, J. H.; Alothman, Z. A.; Yamauchi, Y.; Wang, L., A three-dimensionally structured electrocatalyst: Cobalt-embedded nitrogen-doped carbon nanotubes/nitrogen-doped reduced graphene oxide hybrid for efficient oxygen reduction. *Chem. Eur. J* **2017,** *23* (3), 637-643.
20. Lei, Z. B.; Shi, F. H.; Lu, L., Incorporation of MnO2-coated carbon canotubes between graphene sheets as supercapacitor electrode. *Acs Appl Mater Inter* **2012,** *4* (2), 1058-1064.

21. Park, J. S.; Cho, S. M.; Kim, W. J.; Park, J.; Yoo, P. J., Fabrication of graphene thin films based on layer-by-layer self-assembly of functionalized graphene nanosheets. *Acs Appl Mater Inter* **2011,** *3* (2), 360-8.
22. Tung, V. C.; Chen, L.-M.; Allen, M. J.; Wassei, J. K.; Nelson, K.; Kaner, R. B.; Yang, Y., Low-Temperature Solution Processing of Graphene−Carbon Nanotube Hybrid Materials for High-Performance Transparent Conductors. *Nano Lett.* **2009,** *9* (5), 1949-1955.
23. Abedi, M.; Fangueiro, R.; Correia, A. G., An Effective Method for Hybrid CNT/GNP Dispersion and Its Effects on the Mechanical, Microstructural, Thermal, and Electrical Properties of Multifunctional Cementitious Composites. *J. Nanomater.* **2020,** *2020*.
24. Huang, J.; Her, S.-C.; Yang, X.; Zhi, M., Synthesis and characterization of multi-walled carbon nanotube/graphene nanoplatelet hybrid film for flexible strain sensors. *Nanomaterials* **2018,** *8* (10), 786.
25. Coleman, J. N., Liquid-phase exfoliation of nanotubes and graphene. *Adv. Funct. Mater* **2009,** *19* (23), 3680-3695.
26. Fernandes, R. M.; Abreu, B.; Claro, B.; Buzaglo, M.; Regev, O.; Furo, I.; Marques, E. F., Dispersing carbon nanotubes with ionic surfactants under controlled conditions: Comparisons and insight. *Langmuir* **2015,** *31* (40), 10955-65.
27. Novaes, F. D.; Rurali, R.; Ordejon, P., Electronic transport between graphene layers covalently connected by carbon nanotubes. *ACS Nano* **2010,** *4* (12), 7596-7602.
28. Varshney, V.; Patnaik, S. S.; Roy, A. K.; Froudakis, G.; Farmer, B. L., Modeling of thermal transport in pillared-graphene architectures. *ACS Nano* **2010,** *4* (2), 1153-61.
29. Dimitrakakis, G. K.; Tylianakis, E.; Froudakis, G. E., Pillared graphene: a new 3-D network nanostructure for enhanced hydrogen storage. *Nano Lett.* **2008,** *8* (10), 3166-70.
30. Shen, J.; Hu, Y.; Qin, C.; Ye, M., Layer-by-layer self-assembly of multiwalled carbon nanotube polyelectrolytes prepared by in situ radical polymerization. *Langmuir* **2008,** *24* (8), 3993-3997.
31. Marmisollé, W. A.; Azzaroni, O., Recent developments in the layer-by-layer assembly of polyaniline and carbon nanomaterials for energy storage and sensing applications. from synthetic aspects to structural and functional characterization. *Nanoscale* **2016,** *8* (19), 9890-9918.
32. Faisal, S. N.; Subramaniyam, C. M.; Haque, E.; Islam, M. M.; Noorbehesht, N.; Roy, A. K.; Islam, M. S.; Liu, H. K.; Dou, S. X.; Harris, A. T.; Minett, A. I., Nanoarchitectured nitrogen-doped graphene/carbon nanotube as high performance electrodes for solid state supercapacitors, capacitive deionization, Li-ion battery, and metal-free bifunctional electrocatalysis. *ACS Appl. Energy Mater.* **2018,** *1* (10), 5211-5223.
33. Sideri, I. K.; Tagmatarchis, N., Noble-metal-free doped carbon nanomaterial electrocatalysts. *Chem. Eur. J* **2020,** *26* (67), 15397-15415.
34. Fernandes, D. M.; Mathumba, P.; Fernandes, A. J.; Iwuoha, E. I.; Freire, C., Towards efficient oxygen reduction reaction electrocatalysts through graphene doping. *Electrochim. Acta* **2019,** *319*, 72-81.
35. Qiao, M.; Titirici, M.-M., Engineering the interface of carbon electrocatalysts at the triple point for enhanced oxygen reduction reaction. *Chem. Eur. J* **2018,** *24* (69), 18374-18384.
36. Tao, H.; Gao, Y.; Talreja, N.; Guo, F.; Texter, J.; Yan, C.; Sun, Z., Two-dimensional nanosheets for electrocatalysis in energy generation and conversion. *J. Mater. Chem. A* **2017,** *5* (16), 7257-7284.
37. Zhang, H.; Wang, Y.; Wang, D.; Li, Y.; Liu, X.; Liu, P.; Yang, H.; An, T.; Tang, Z.; Zhao, H., Hydrothermal transformation of dried grass into graphitic carbon‐based high performance electrocatalyst for oxygen reduction reaction. *Small* **2014,** *10* (16), 3371-3378.
38. Nunes, M.; Fernandes, D. M.; Rocha, I. M.; Pereira, M. F. R.; Mbomekalle, I.-M.; de Oliveira, P.; Freire, C., Phosphomolybdate@Carbon-based nanocomposites as electrocatalysts for oxygen reduction reaction. *ChemistrySelect* **2016,** *1* (19), 6257-6266.
39. Daems, N.; Sheng, X.; Vankelecom, I. F. J.; Pescarmona, P. P., Metal-free doped carbon materials as electrocatalysts for the oxygen reduction reaction. *J. Mater. Chem. A* **2014,** *2* (12), 4085-4110.
40. Nunes, M.; Rocha, I. M.; Fernandes, D. M.; Mestre, A. S.; Moura, C. N.; Carvalho, A. P.; Pereira, M. F. R.; Freire, C., Sucrose-derived activated carbons: Electron transfer properties and application as oxygen reduction electrocatalysts. *RSC Adv.* **2015,** *5* (124), 102919-102931.
41. Zhao, Y.-M.; Yu, G.-Q.; Wang, F.-F.; Wei, P.-J.; Liu, J.-G., Bioinspired transition-metal complexes as electrocatalysts for the oxygen reduction reaction. *Chem. Eur. J* **2019,** *25* (15), 3726-3739.

42. Campos-Martin, J. M.; Blanco-Brieva, G.; Fierro, J. L. G., Hydrogen peroxide synthesis: An outlook beyond the anthraquinone process. *Angew. Chem. Int. Ed.* **2006,** *45* (42), 6962-6984.
43. Abreu, B.; Rocha, J.; Fernandes, R. M. F.; Regev, O.; Furó, I.; Marques, E. F., Gemini surfactants as efficient dispersants of multiwalled carbon nanotubes: Interplay of molecular parameters on nanotube dispersibility and debundling. *J. Colloid Interface Sci.* **2019,** *547*, 69-77.
44. Georgakilas, V.; Otyepka, M.; Bourlinos, A. B.; Chandra, V.; Kim, N.; Kemp, K. C.; Hobza, P.; Zboril, R.; Kim, K. S., Functionalization of graphene: covalent and non-covalent approaches, derivatives and applications. *Chem. Rev* **2012,** *112* (11), 6156-214.
45. Song, H.; Yang, L.; Tang, Y.; Dafeng, Y.; Liu, C.; Luo, S., Three-dimensional nitrogen-doped reduced graphene oxide-carbon nanotubes architecture supporting ultrafine palladium nanoparticles for highly efficient methanol electrooxidation. *Chem. Eur. J.* **2015,** *21*.
46. Khan, U.; O'Neill, A.; Porwal, H.; May, P.; Nawaz, K.; Coleman, J. N., Size selection of dispersed, exfoliated graphene flakes by controlled centrifugation. *Carbon* **2012,** *50* (2), 470-475.
47. Elosua, C.; Lopez-Torres, D.; Hernaez, M.; Matias, I. R.; Arregui, F. J., Comparative study of layer-by-layer deposition techniques for poly(sodium phosphate) and poly(allylamine hydrochloride). *Nanoscale Res. Lett* **2013,** *8* (1), 539-539.
48. White, B.; Banerjee, S.; O'Brien, S.; Turro, N. J.; Herman, I. P., Zeta-potential measurements of surfactant-wrapped individual single-walled carbon nanotubes. *J. Phys. Chem. C* **2007,** *111* (37), 13684-13690.
49. Sun, Z.; Nicolosi, V.; Rickard, D.; Bergin, S. D.; Aherne, D.; Coleman, J. N., Quantitative evaluation of surfactant-stabilized single-walled carbon nanotubes: dispersion quality and its correlation with zeta potential. *J. Phys. Chem. C* **2008,** *112* (29), 10692-10699.
50. Thommes, M.; Kaneko, K.; Neimark, A. V.; Olivier, J. P.; Rodriguez-Reinoso, F.; Rouquerol, J.; Sing, K. S. W., Physisorption of gases, with special reference to the evaluation of surface area and pore size distribution (IUPAC Technical Report). *Pure Appl. Chem* **2015,** *87* (9-10), 1051.
51. Liu, F.; Peng, H. J.; You, C.; Fu, Z.; Huang, P.; Song, H.; Liao, S., High-performance doped carbon catalyst derived from nori biomass with melamine promoter. *Electrochim. Acta* **2014,** *138*, 353-359.
52. Delmondo, L.; Salvador, G. P.; Muñoz-Tabares, J. A.; Sacco, A.; Garino, N.; Castellino, M.; Gerosa, M.; Massaglia, G.; Chiodoni, A.; Quaglio, M., Nanostructured MnxOy for oxygen reduction reaction (ORR) catalysts. *Appl. Surf. Sci.* **2016,** *388*, 631-639.
53. Hoang, S.; Guo, S.; Hahn, N. T.; Bard, A. J.; Mullins, C. B., Visible light driven photoelectrochemical water oxidation on nitrogen-modified TiO2 nanowires. *Nano Lett.* **2012,** *12* (1), 26-32.
54. Ferrari, A. C., Raman spectroscopy of graphene and graphite: Disorder, electron-phonon coupling, doping and nonadiabatic effects. *Solid State Commun.* **2007,** *143* (1-2), 47-57.
55. Malard, L. M.; Pimenta, M. A.; Dresselhaus, G.; Dresselhaus, M. S., Raman spectroscopy in graphene. *Phys. Rep* **2009,** *473* (5), 51-87.
56. Ornelas, M.; Azenha, M.; Araujo, M. J.; Marques, E. F.; Dias-Cabral, A. C.; Pereira, C.; Silva, A. F., Acylated-naproxen as the surface-active template in the preparation of micro- and nanospherical imprinted xerogels by emulsion techniques. *J. Chromatogr. A* **2016,** *1437*, 107-115.
57. Goddard, E. D., Polymer/surfactant interaction: Interfacial aspects. *J. Colloid Interface Sci.* **2002,** *256* (1), 228-235.
58. Wang, S.; Yu, D.; Dai, L., Polyelectrolyte Functionalized Carbon Nanotubes as Efficient Metal-free Electrocatalysts for Oxygen Reduction. *J. Am. Chem. Soc* **2011,** *133* (14), 5182-5185.
59. Zhang, Y.; Fugane, K.; Mori, T.; Niu, L.; Ye, J., Wet chemical synthesis of nitrogen-doped graphene towards oxygen reduction electrocatalysts without high-temperature pyrolysis. *J. Mater. Chem. A* **2012,** *22* (14), 6575-6580.
60. Shinagawa, T.; Garcia-Esparza, A. T.; Takanabe, K., Insight on Tafel slopes from a microkinetic analysis of aqueous electrocatalysis for energy conversion. *Sci. Rep* **2015,** *5* (1), 13801.
61. Oturan, N.; Oturan, M. A., Chapter 8 - Electro-Fenton Process: Background, New Developments, and Applications. In *Electrochemical Water and Wastewater Treatment*, Martínez-Huitle, C. A.; Rodrigo, M. A.; Scialdone, O., Eds. Butterworth-Heinemann: 2018; pp 193-221.

Supporting Information

Carbon nanotube/graphene nanocomposites built via surfactant-mediated colloid assembly as metal-free catalysts for the oxygen reduction reaction

Bárbara Abreu,[1,2] Marcos Rocha[1] Marta Nunes*[2], Cristina Freire[2], and Eduardo F. Marques**[1]

[1]*CIQUP, Departamento de Química e Bioquímica, Faculdade de Ciências, Universidade do Porto 4169-007 Porto, Portugal*

[2]*REQUIMTE-LAQV, Departamento de Química e Bioquímica, Faculdade de Ciências, Universidade do Porto 4169-007 Porto, Portugal*

*marta.nunes@fc.up.pt
**efmarque@fc.up.pt

Table of Contents

S1. Dispersion of MWNT with polymer/surfactant mixture PVP/CTAB

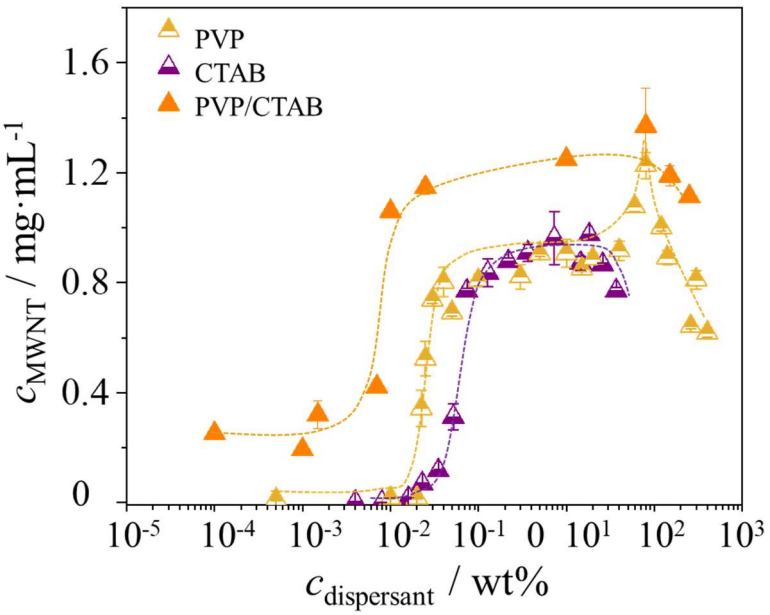

Fig. S1. Dispersibility curves for MWNT using polymer PVP, surfactant CTAB and a mixture of PVP/CTAB. The polymer/surfactant mixture is more effective in dispersing MWNT than the polymer and surfactant per se.

S2. Dispersion of GnP with surfactant SC and SEM characterization

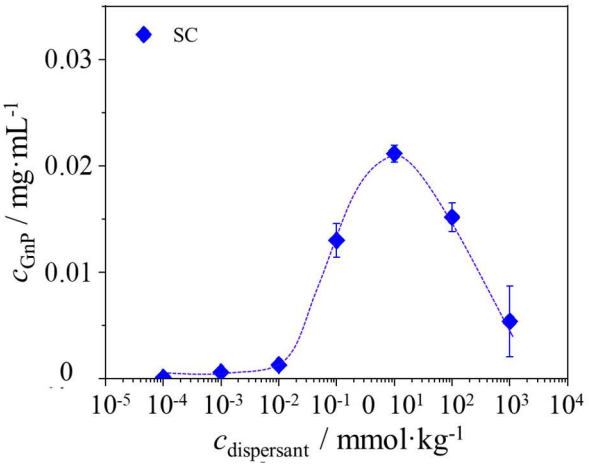

Fig. S2.1. Dispersibility curves for GNP using surfactant sodium cholate.

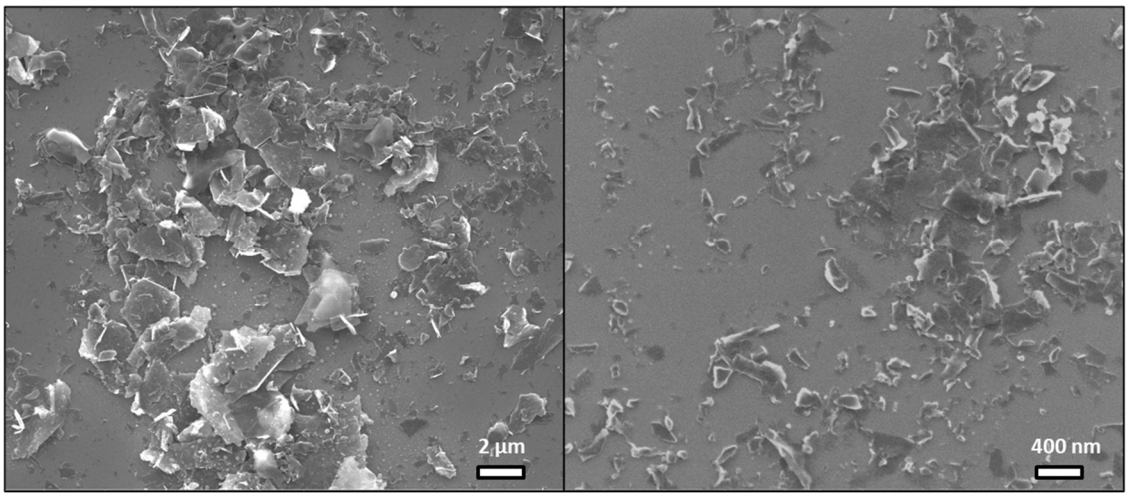

Fig. S2.2. Representative micrographs of GnP dispersions without centrifugation (left) and after centrifugation (right).

S3. Supplementary electrochemical information and data

The electrochemical measurements were carried out using an Autolab PGSTAT 302N potentiostat/galvanostat (EcoChimie B.V.), controlled by NOVA 2.0 software.

The electrode polishing/cleaning procedure (cf. S.I., S3, for further details) was performed using diamond pastes of 6, 3 and 1 μm (MetaDi II, Buehler) and aluminum oxide of particle size 0.3 μm (Buehler), on a microcloth polishing pad (BAS Bioanalytical Systems Inc.).

S3.1 LSV data analysis

LSV data was analyzed through Koutecky-Levich (K-L) equation (S1). The number of electrons transferred per O_2 molecule (n_{O_2}) in the ORR process was calculated from the slopes of the K-L plot [1, 2]:

$$\frac{1}{j} = \frac{1}{j_L} + \frac{1}{j_k} = \frac{1}{B\omega^{1/2}} + \frac{1}{j_k} \quad \text{(S1)}$$

where j is the experimentally measured current density, j_L is the diffusion-limiting current density, j_k is the kinetic current density and ω is the angular velocity; B is related to the diffusion limiting current density expressed by the Equation (S2):

$$B = 0.2 n_{O_2} F (D_{O_2})^{2/3} v^{-1/6} C_{O_2} \quad \text{(S2)}$$

where F is the Faraday constant (96 485 C mol^{-1}), C_{O_2} is the bulk concentration of O_2 (1.15×10^{-3} mol dm^{-3} in 0.1 mol dm^{-3} KOH), v is the kinematic viscosity of the electrolyte (0.008977 cm^2 s^{-1} for 0.1 mol dm^{-3} KOH) and D_{O_2} is the diffusion coefficient of O_2 (1.95×10^{-5} cm^2 s^{-1} in 0.1 mol dm^{-3} KOH). The constant 0.2 was adopted, once the rotating speed is in rpm.[3] The Tafel plots (E_{RHE} $vs.$ $\log i_k$) for oxygen reduction kinetics were obtained after the measured currents in LSV were corrected for diffusion to give the kinetic currents. The mass transport correction was made using the diffusion-limiting current density j_L, calculated by combination of equations (S1) and (S2).[4]

S3.2 Calculation of hydrogen peroxide percentage

The hydrogen peroxide percentage (%H_2O_2) was calculated based on Eq. (S3) [5]:

$$\%\mathrm{H_2O_2} = 200 \times \frac{i_\mathrm{g}/N}{i_D + i_\mathrm{R}/N} \quad \text{(S3)}$$

where i_D and i_R are the disk and ring currents, respectively, and *N* is the current collection efficiency of the Pt ring (calculated as *N* = 0.25). [6]

S3.3 Conversion of E values vs. RHE

The *E* values determined vs. Ag/AgCl were converted to the reversible hydrogen electrode (RHE) scale according to the Nernst equation:

$$E_\mathrm{RHE} = E_\mathrm{Ag/AgCl} + 0.059\mathrm{pH} + E^\circ_\mathrm{Ag/AgCl} \quad \text{(S4)}$$

where E_RHE is the converted potential vs. RHE, $E^\circ_\mathrm{Ag/AgCl}$ = 0.1976 at 25 ºC and $E_\mathrm{Ag/AgCl}$ is the experimentally measured potential against Ag/AgCl reference.[7]

S3.4 Complementary electrochemical data

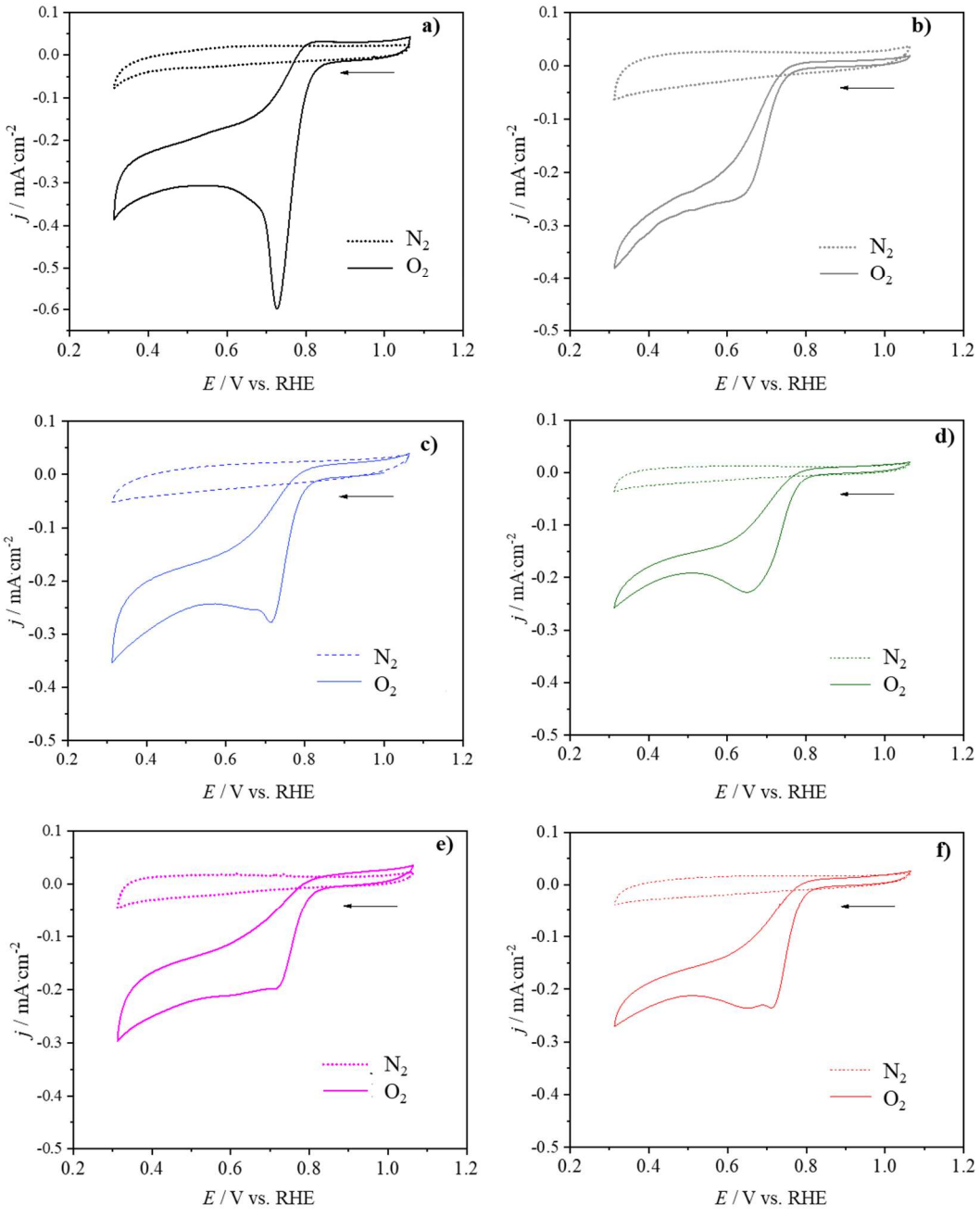

Fig. S3.1. CVs of the (a) MWNT/S, (b) GnPs/S, (c) B_S/S (d) L_S/S, (e) B_PS/S and (f) L_PS/S electrocatalysts in 0.1 mol dm^{-3} KOH N_2- and O_2-saturated solutions at 0.005 V s^{-1}.

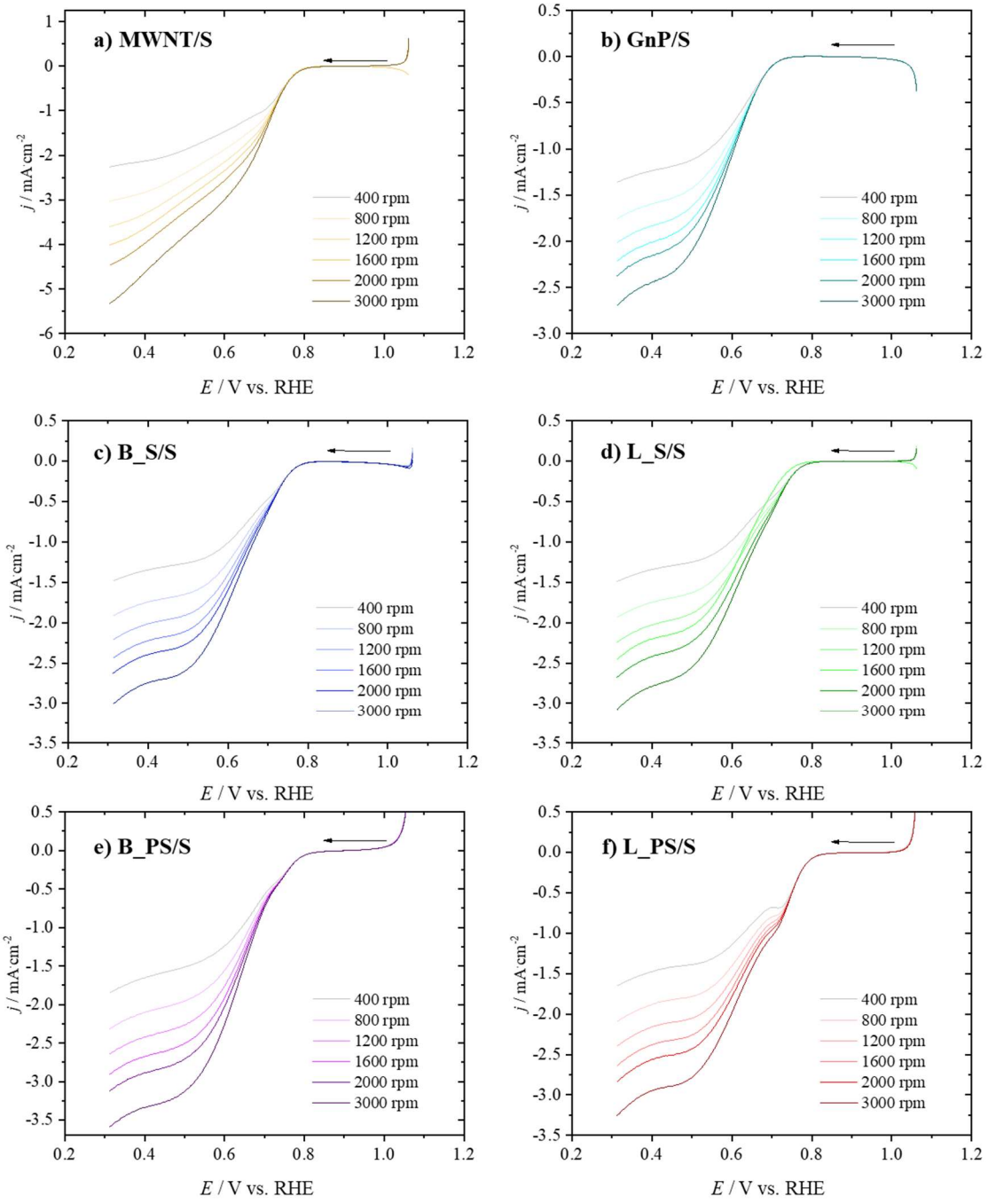

Fig. S3.2. ORR polarization plots of (a) MWNT/S, (b) GnP/S, (c) B_S/S (d) L_S/S, (e) B_PS/S and (f) L_PS/S at several rotation rates and 0.005 V s^{-1}, in 0.1 mol dm^{-3} KOH electrolyte.

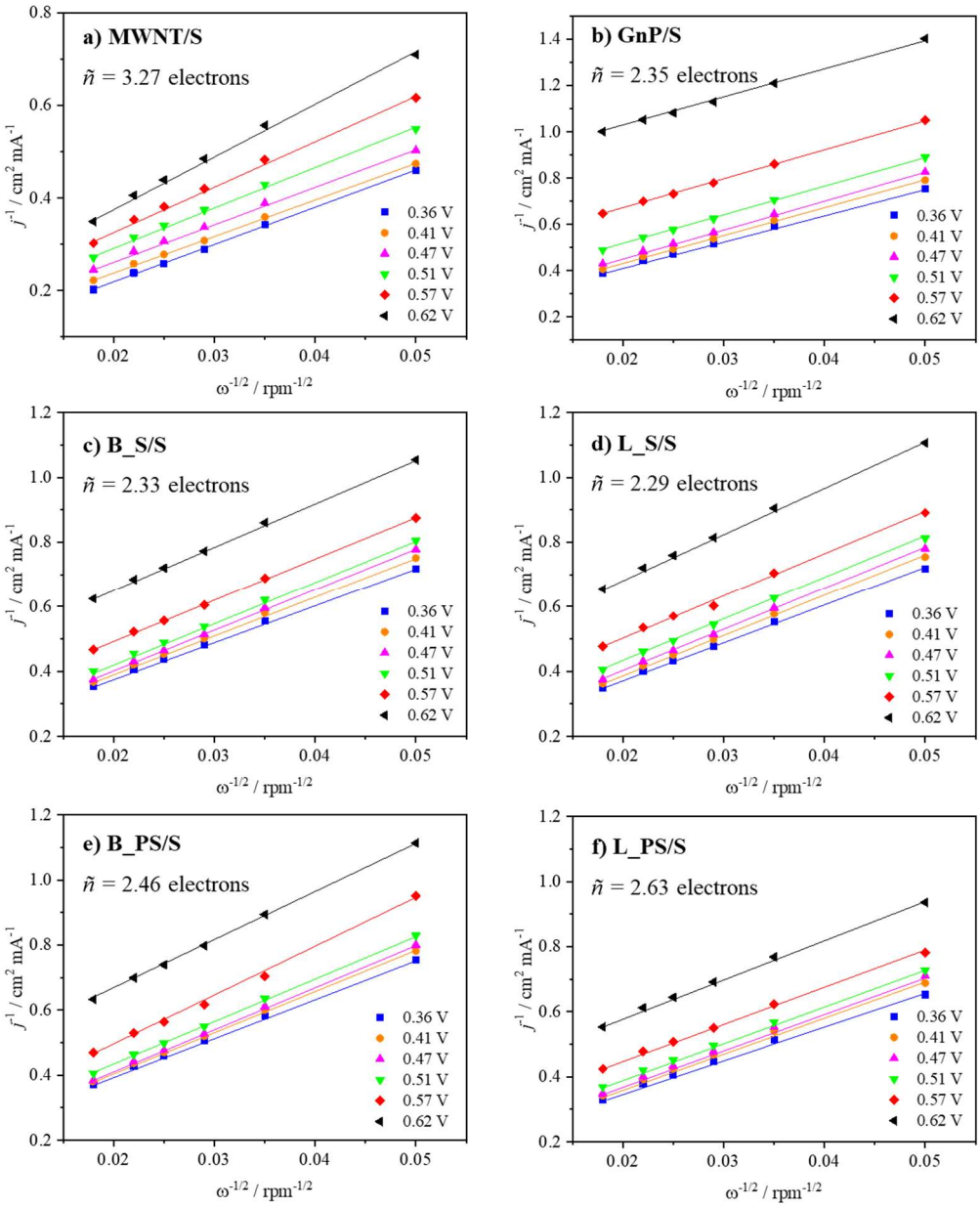

Fig. S3.3. ORR polarization Koutecky-Levich (K-L) plots of (a) MWNT/S, (b) GnP/S, (c) B_S/S (d) L_S/S, (e) B_PS/S and (f) L_PS/S obtained from data in Figure S3.

S4. SEM imaging of milled powders and inks for electrode modification

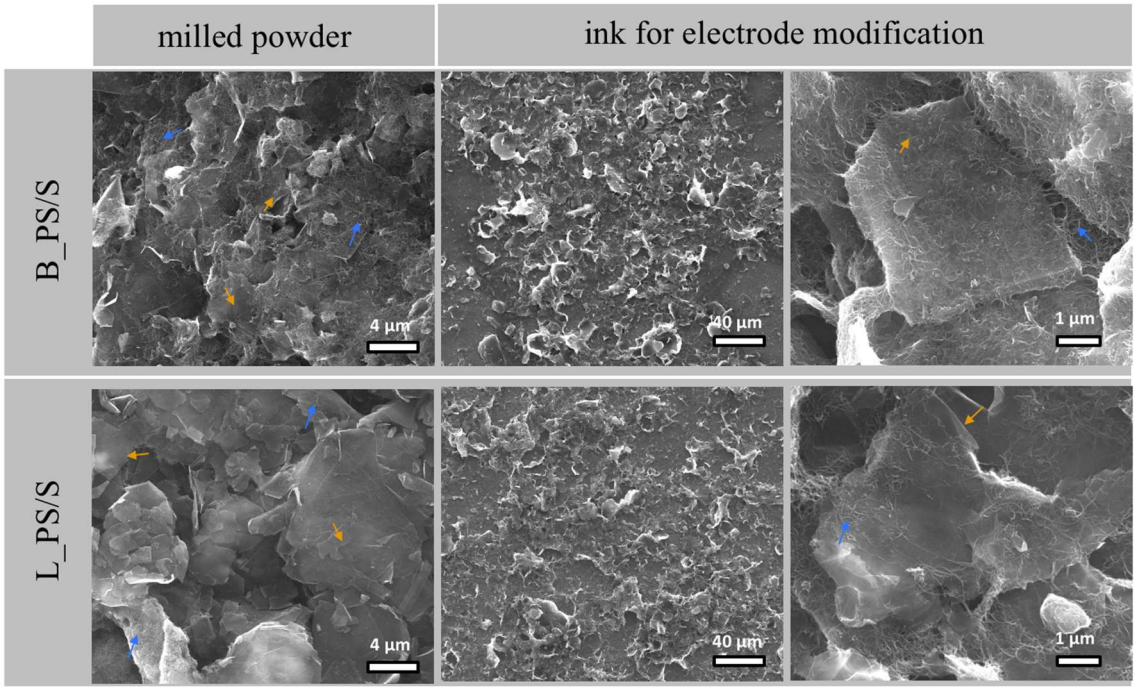

Fig. S4 Representative micrographs of two composites, B_PS/S (up) and L_PS/S (down) built using the two different procedures, after milling (left) and ink preparation for the electrode modification (centre and right), as described in the experimental section. Blue arrows point the MWNT domains, yellow arrows indicate the GnP.

References

1. Nunes, M.; Rocha, I. M.; Fernandes, D. M.; Mestre, A. S.; Moura, C. N.; Carvalho, A. P.; Pereira, M. F. R.; Freire, C., Sucrose-derived activated carbons: Electron transfer properties and application as oxygen reduction electrocatalysts. *RSC Adv.* **2015,** *5* (124), 102919-102931.
2. Liu, F.; Peng, H. J.; You, C.; Fu, Z.; Huang, P.; Song, H.; Liao, S., High-performance doped carbon catalyst derived from nori biomass with melamine promoter. *Electrochim. Acta* **2014,** *138*, 353-359.
3. Mani, A.; Birss, V. I., Dependence of the oxygen reduction reaction at sol–gel derived Co-based catalysts on acidic solution pH and temperature. *J. Electroanal. Chem* **2012,** *687*, 102-110.
4. Gao, S.; Fan, H.; Zhang, S., Nitrogen-enriched carbon from bamboo fungus with superior oxygen reduction reaction activity. *J. Mater. Chem. A* **2014,** *2* (43), 18263-18270.
5. Delmondo, L.; Salvador, G. P.; Muñoz-Tabares, J. A.; Sacco, A.; Garino, N.; Castellino, M.; Gerosa, M.; Massaglia, G.; Chiodoni, A.; Quaglio, M., Nanostructured MnxOy for oxygen reduction reaction (ORR) catalysts. *Appl. Surf. Sci.* **2016,** *388*, 631-639.
6. Swesi, A. T.; Masud, J.; Nath, M., Nickel selenide as a high-efficiency catalyst for oxygen evolution reaction. *Energy Environ. Sci* **2016,** *9* (5), 1771-1782.
7. Hoang, S.; Guo, S.; Hahn, N. T.; Bard, A. J.; Mullins, C. B., Visible light driven photoelectrochemical water oxidation on nitrogen-modified TiO2 nanowires. *Nano Lett.* **2012,** *12* (1), 26-32.

VI

Nanocomposites prepared from carbon nanotubes and the transition metal dichalcogenides WS_2 and MoS_2 via surfactant-assisted dispersions as electrocatalysts for oxygen reactions

materials

MDPI

Article

Nanocomposites Prepared from Carbon Nanotubes and the Transition Metal Dichalcogenides WS_2 and MoS_2 via Surfactant-Assisted Dispersions as Electrocatalysts for Oxygen Reactions

Pedro Ferreira [1,2], Bárbara Abreu [1,2], Cristina Freire [2], Diana M. Fernandes [2,*] and Eduardo F. Marques [1,*]

[1] Centro de Investigação em Química, Departamento de Química e Bioquímica, Faculdade de Ciências, Universidade do Porto, 4169-007 Porto, Portugal; up201407953@fc.up.pt (P.F.); barbara.teixeira@fc.up.pt (B.A.)
[2] REQUIMTE-LAQV, Departamento de Química e Bioquímica, Faculdade de Ciências, Universidade do Porto, 4169-007 Porto, Portugal; acfreire@fc.up.pt
* Correspondence: diana.fernandes@fc.up.pt (D.M.F.); efmarque@fc.up.pt (E.F.M.)

Abstract: Fuel cells are emerging devices as clean and renewable energy sources, provided their efficiency is increased. In this work, we prepared nanocomposites based on multiwalled carbon nanotubes (MWNTs) and transition metal dichalcogenides (TMDs), namely WS_2 and MoS_2, and evaluated their performance as electrocatalysts for the oxygen evolution reaction (OER) and the oxygen reduction reaction (ORR), relevant to fuel cells. The one- and two-dimensional (1D and 2D) building blocks were initially exfoliated and non-covalently functionalized by surfactants of opposite charge in aqueous media (tetradecyltrimethylammonium bromide, TTAB, for the nanotubes and sodium cholate, SC, for the dichalcogenides), and thereafter, the three-dimensional (3D) MoS_2@MWNT and WS_2@MWNT composites were assembled via surfactant-mediated electrostatic interactions. The nanocomposites were characterized by scanning electron microscopy (SEM) and structural differences were found. WS_2@MWNT and MoS_2@MWNT show moderate ORR performance with potential onsets of 0.71 and 0.73 V vs. RHE respectively, and diffusion-limiting current densities of -1.87 and -2.74 mA·cm^{-2}, respectively. Both materials present, however, better tolerance to methanol crossover when compared to Pt/C and good stability. Regarding OER performance, MoS_2@MWNT exhibits promising results, with η_{10} and j_{max} of 0.55 V and 17.96 mA·cm^{-2}, respectively. The fabrication method presented here is cost-effective, robust and versatile, opening the doors for the optimization of electrocatalysts' performance.

Keywords: nanocomposites; transition metal dichalcogenides; carbon nanotubes; surfactants; non-covalent functionalization; electrocatalysis; oxygen reactions

Citation: Ferreira, P.; Abreu, B.; Freire, C.; Fernandes, D.M.; Marques, E.F. Nanocomposites Prepared from Carbon Nanotubes and the Transition Metal Dichalcogenides WS_2 and MoS_2 via Surfactant-Assisted Dispersions as Electrocatalysts for Oxygen Reactions. *Materials* **2021**, *14*, 896. https://doi.org/10.3390/ma14040896

Academic Editor: Alessandro Dell'Era
Received: 21 January 2021
Accepted: 5 February 2021
Published: 13 February 2021

1. Introduction

Long-lasting and clean energies are vital to the development of future energetic sustainability. The search for electrocatalyst-mediated energy conversion processes has delivered some technologies that, when coupled with renewable energies, are able to convert molecules present in the atmosphere (water, nitrogen or carbon dioxide) in added-value products (hydrogen, hydrocarbons and ammonia). Such processes can be found in many energy storage and conversion devices like metal-air batteries and fuel cells [1–3].

The charge and discharge processes of fuel cells and metal-air batteries are dominated by the oxygen-based reactions, oxygen evolution reaction (OER) and oxygen reduction reaction (ORR), respectively. However, the kinetics of these reactions are slow, making them difficult to trigger. Therefore, electrocatalysts are pivotal to increase the rate, efficiency and selectivity of these chemical reactions [1,3,4]. High-performance electrocatalysts should also feature high stability/durability and ORR electrocatalysts resistance to methanol (in direct methanol fuel cells) crossover, something that the current noble metal electrocatalysts

do not provide. In addition, due to their scarcity and high price, noble metal catalysts are economically unviable, which promotes the search for more stable and cost-effective alternatives [3–5]. Ideally, in reversible fuel cells, electrocatalysts should be bifunctional for ORR and OER and equally high performing. In practice, platinum-based electrocatalysts are deemed the best for ORR, but not sufficiently effective for OER (Pt oxidizes easily at large overpotentials). Likewise, the state-of-the-art OER electrocatalysts (RuO_2 and IrO_2) are less effective for ORR [2,3].

In this context, carbon-based nanomaterials emerged as potential alternatives to Pt-based electrocatalysts, and, therefore, have been increasingly investigated. Carbon quantum-dots (CQDs) [6,7], N-doped carbon nanotubes [8,9] and N-doped graphene [10,11] have been reported to have good electrocatalytic behavior towards ORR. Graphene quantum dots, either heteroatom-doped [12] or decorated with non-Pt metals [13,14], have also been described as good ORR electrocatalysts. Many other materials have also exhibited good electrocatalytic behavior toward oxygen reactions, among them polyoxometalates (POMs) [4], perovskites [15], organometallics [16] and spinel family [17] compounds. With respect to transition metal dichalcogenides (TMDs), they have been extensively reported as promising hydrogen evolution reaction (HER) electrocatalysts [18–20], and their potential as single materials for oxygen reactions has also been investigated [21–23]. Recently, Pumera et al. have studied the ORR electrocatalytic properties of undoped MoS_2 and WS_2 and Ti-, V-, Mn- and Fe-doped layered WS_2 and MoS_2 [24], demonstrating that not all doping is beneficial. As concerning the use of WS_2 or MoS_2 sheets as building blocks of nanocomposite catalysts for ORR, there are only a few reports in the literature [25–27].

A promising route for the development and optimization of electrocatalysts is the combination of basic building blocks into new structures, such as one/two-dimensional (1D/2D) composites. In particular, the combination of carbon nanotubes and graphene has been largely studied and was found to result in enhanced properties [28–31]. Nonetheless, the replacement of graphene with 2D analogues, e.g., TMDs, in such hierarchical structures could unveil improved features [32]. In fact, graphene analogues possess remarkable electronic properties that are tunable according to the number of stacked layers (e.g., bulk 2H-MoS_2 shows an indirect band gap, but a direct band gap when exfoliated into monolayers) [33–35]. Such properties vary relatively weakly with the number of layers as compared to graphene, a material that in contrast requires full exfoliation to monolayers in order to unfold its maximum potential [36].

Some studies regarding the building of CNT/TMD hybrids and their application as electrocatalysts for energy conversion reactions have been reported, mostly dealing with HER [37–41]. Huang et al. fabricated a composite of multiwalled carbon nanotubes (MWNTs) and MoS_2 using solvothermal synthesis, with the coupling between covalently functionalized nanotubes and MoS_2 leading to remarkable performance towards HER [37]. A similar type of electrocatalyst was developed by Ahn et al., who applied layer-by-layer assembly to fabricate a MWNT/MoS_2 thin film, finding the catalytic performance to be dependent on the 1D/2D bilayer number and hence demonstrating the importance of composite architecture for electrocatalytic activity [38]. Notwithstanding their proven applicability for HER, CNT/TMD structures have remained scantly investigated for oxygen reactions, despite revealing potential benefits [42,43]. Recently, Lee et al. found a significant synergistic effect for ORR electrocatalysis from the combination, via hydrothermal method, of functionalized MWNTs and MoS_2 into a three-dimensional (3D) architecture [42]. In the work of Tiwari et al., WS_2 and CNTs were interconnected via chemical bonding by the formation of tungsten carbide bonding [43]. These authors showed that WS_2 sheets on CNT surfaces provide active sites for electrocatalytic activity, while CNTs offer conducting channels and a large surface area, resulting in a bifunctional electrocatalyst for both ORR and OER, with performance comparable to state-of-the-art catalysts (e.g., Pt, RuO_2).

In this work, we report the assembly of nanocomposites combining MWNTs and two TMDs, WS_2 and MoS_2, and the performance of the obtained WS_2@MWNT and MoS_2@MWNT materials as ORR and OER electrocatalysts. The individual building blocks

were prepared using surfactants as dispersants and a strictly controlled dispersal procedure in aqueous media [44–47]. A schematic representation of the process, and its underlying rationale, is shown in Figure 1A–C. As depicted in Figure 1A, the entangled MWNT powder are first exfoliated (by tip sonication) and dispersed using a cationic surfactant (tetradecyltrimethylammonium bromide, TTAB), while the aggregated TMD powder is similarly separated and dispersed using an anionic surfactant (sodium cholate, SC). The surfactants adhere onto the surface of materials essentially by hydrophobic interactions through their hydrocarbon tails, leaving the charged headgroups exposed to the aqueous environment. The obtained dispersions, as shown in Figure 1B, thus consist of positively charged individual MWNTs (or thin bundles thereof), on one side, and negatively charged particles of metal dichalcogenides, on the other side. Both types of surfactant-coated particles possess their electrical double layers and some values of positive and negative zeta potential, respectively. In Figure 1C, mixing of the functionalized blocks in specific proportions leads to the assembly of the composites via electrostatic attractions mediated by the surfactants. In a simplified view, Figure 1C shows two limiting (or idealized) configurations of the resulting materials: in the topmost sketch, the MWNTs are orthogonally placed with respect to the TMD layers (basal planes), and alternate 1D/2D layers are formed; in the bottom one, the MWNTs lie horizontally over the TMD basal planes, forming more tightly bound alternate layers. In reality, it is likely that assorted intermediate configurations will form, such as those having randomly tilted MWNTs or mixed orthogonal/parallel/tilted MWNT layers.

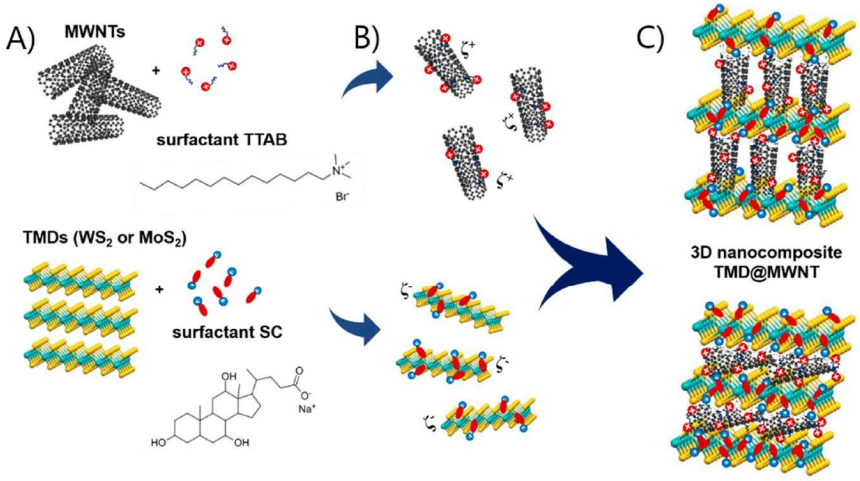

Figure 1. Schematic representation of the assembly process of nanocomposites of multiwalled carbon nanotubes (MWNTs) and transition metal dichalcogenides (TMDs), TMD@MWNT: (**A**) exfoliation and dispersal of the 1D and 2D blocks by cationic surfactant tetradecyltrimethylammonium bromide (TTAB) and anionic surfactant sodium cholate (SC), respectively, (**B**) formation of aqueous dispersions of the charged surfactant-coated particles, and (**C**) assembly of the TMD@MWNT composites via electrostatic attractions, with two possible extremes configurations shown (top, orthogonal layers, and bottom, parallel layers).

A relevant aspect of this work in relation to the above-mentioned literature is the building of 3D structures resorting to a facile, cost-effective and mild experimental method in aqueous solution via non-covalent functionalization. This methodology aims at fabricating reproducible nanocomposites under controlled and optimizable conditions. After their formation, the designed materials were structurally characterized using SEM and their individual performance as ORR and OER electrocatalysts was assessed. For this, we used both cyclic (CV) and linear sweep voltammetry (LSV) as well as chronoamperometry for the stability and methanol crossover studies. We also present some possible explanations for the relation between the morphological structure and the electrocatalytic behavior of the developed nanocomposites.

2. Materials and Methods

2.1. Materials and Characterization Methods

Multiwalled carbon nanotubes, produced by catalytic chemical vapor deposition and with purity > 95%, were purchased from Cheap Tubes Inc. (Grafton, MA, USA), having outer diameter d = 8–15 nm and length L = 10–50 μm. Transmission electron microscopy (TEM) imaging of the as-purchased MWNTs confirmed the absence of metal catalyst impurities; see Supplementary Material, Figure S1.1. Furthermore, SEM imaging of the dispersed MWNTs (described in detail below) further confirmed the supplied dimensions and absence of impurities (Figure 2A, and Figure S1.2). WS_2, MoS_2, tetradecyltrimethylammonium bromide (TTAB) and sodium cholate hydrate (SC), all with purity ≥ 99%, were acquired from Sigma-Aldrich (St. Louis, MO, USA) and used without further purification. Reagents used for the preparation and performance testing of the electrocatalysts, namely potassium hydroxide (KOH, Riedel-de-Häen, Seelze, Germany), 2-propanol (99.5%, Sigma-Aldrich), Nafion (5 wt% solution in lower aliphatic alcohols and water, Sigma-Aldrich) methanol and 20 wt% Pt/C (HiSPEC® 3000, Alfa Aesar, Haverhill, MA, USA) were used as received. Ultra-pure Milli-Q® (Merck KGaA, Darmstad, Germany) water, with resistivity 18.2 MΩ cm at 25 °C, was used in the preparation of all solutions.

Characterization of the individual surfactant-assisted dispersions of the building blocks, MWNTs and TMDs, was performed by SEM to show the good degree of exfoliation of the materials (Figure 2A,B, and Supplementary Figures S1.2 and S1.3). A FEI Quanta 400FE SEM microscope (Hillsboro, OR, USA) at Centro de Materiais da Universidade do Porto (CEMUP), was used, operating with an electron beam of 25 kV, at different magnifications and secondary electron (SE) mode. Detailed SEM studies were also carried out for the fabricated nanocomposites (Figure 2C1–D2). For imaging of the MWNT and TMD dispersions, the samples were prepared by drop casting 10 μL of each dispersion on a pre-heated silicon wafer (>100 °C, assuring fast solvent evaporation). The fabricated nanocomposite films were fractured in liquid nitrogen, allowing a clean fracture, and the samples were analyzed in a cross-section view for a better visualization of the nanocomposite structure.

2.2. Assembly of the Nanocomposite Materials

The assembly process started with the preparation of two dispersions, by surfactant-assisted liquid phase exfoliation, using a previously reported procedure [46]. Briefly, 60 mg of the nanomaterial powder (MWNTs or TMDs) were added to 20 mL of a surfactant aqueous solution (resulting in a 3 mg·mL^{-1} initial loading of the dispersion). The surfactant concentrations used were 5 mmol·kg^{-1} TTAB for MWNTs and 10 mmol·kg^{-1} SC for TMDs. These values of surfactants concentrations were chosen to ensure that maximum dispersibility of each nanomaterial was attained, according to our previous studies with MWNTs [44–46] and to recent data on dispersibility of the two TMDs using SC (see Supplementary Figure S1.4a).

Both mixtures were then tip-sonicated, using a Sonics VC 505 with a freshly polished 13 mm tip (500 W, 20 kHz). The vibration amplitude and sonication time were set to 60% and 5 min for MWNTs, and 50% and 23 min for TMDs, as previously optimized [44–46]. The total energy transferred per unit mass was 0.20 kJ·mg^{-1} for MWNTs and 0.84 kJ·mg^{-1} for TMDs. An external bath was used to stabilize the temperature of the dispersions. Following sonication, the MWNT dispersions were centrifuged (Centurion Scientific K241R, equipped with a BRK5324 rotor) for 20 min at 4000× g, in order to remove impurities (including any residual metal catalyst particles) and large undispersed MWNT agglomerates [46,48–50], and the supernatant was collected to build the composites. In the case of the TMD dispersions, it was observed by SEM that the centrifugation step led to a significant reduction of the size of the 2D particles in suspension (mean lateral dimension, MLD < 0.3 μm), and since large sheets (typically, MLD > 1 μm) were needed to build a well-structured composite, this experimental step was eliminated to build the films (see Supplementary Figure S1.3). Therefore, the final concentration of dispersed TMD nanomaterial corresponds to its initial loading on the samples (since no material is lost to

centrifugation). A nominal TMD/MWNT mass ratio of ≈3:1 was used to build the composites; as concerning the negative-to-positive charge ratio (due to the adsorbed surfactants), it is also roughly 3:1 (taking into account that a fraction of the cationic surfactant TTAB in the MWNTs is lost to the sediment due to centrifugation [44]). Overall, this implies net excess of negative charge (owing to the SC-coated TMDs) in the preparation of the nanocomposites, and so the underlying assumption is that basically all the TTAB-coated MWNTs assemble into the composite material.

The individual as-obtained dispersions of the MWNTs and TMDs were then mixed and sonicated together to form the nanocomposites, using the same value of energy per mass used for the MWNTs (0.20 kJ·mg^{-1}), to avoid fracture of the nanotubes at higher energy density. After this procedure, the composite samples were vacuum-filtered, rinsed with ethanol and dried overnight.

2.3. Evaluation of the Electrocatalytic Activities

A potentiostat/galvanostat PGSTAT 302N (Metrohm Autolab B.V., Utrecht, The Netherlands), controlled by Nova v2.1 software, was used to carry out all electrochemical studies. A conventional three-electrode cell setup was used: a glassy carbon rotating disk electrode (RDE, diameter of 3 mm, Metrohm) as working electrode, a Ag/AgCl (Metrohm, 3 mol·dm^{-3} KCl(aq)) as reference electrode and a carbon rod (Metrohm, diameter of 2 mm) for ORR or a platinum wire (Goodfellow, diameter of 0.6 mm, *l* = 0.5 m, >99.99%) for OER as the counter electrode. All studies were performed at room temperature.

The RDE was conditioned with a polishing process using diamond pastes (Buehler, MetaDI II, Lake Bluff, IL, USA) with particle sizes of 6, 3 and 1 μm, before being modified with the samples. Electrode modification consists of dropping two 2.5 μL droplets of a dispersion containing the materials onto the glassy carbon surface of the RDE, and letting it dry under a constant flux of hot air. The dispersions used to modify the RDE were prepared by mixing the selected nanomaterial (1 mg) with 125 μL of 2-propanol, 125 μL of ultrapure water and 20 μL of Nafion® 117, followed by a 15 min bath ultrasonication (Fisherbrand FB11201, Hampton, VA, USA).

2.4. ORR Performance

All ORR studies used KOH aqueous solution (0.1 mol·dm^{-3}, 100 mL) saturated with oxygen or nitrogen gas as the electrolyte. To ensure proper gas saturation of the solution, an initial degassing process was done for at least 30 min prior to the study. N_2-saturated studies served as a blank for the O_2-saturated ones, and, thus, the current obtained in the former was subtracted from that in the latter. Electrocatalytic performance of the materials toward ORR was studied by cyclic voltammetry (CV) and linear sweep voltammetry (LSV). The scan rate for both was 5 mV·s^{-1}, and the rotation speed for LSV was 400, 800, 1200, 1600, 2000 and 3000 rpm.

The E_{onset} vs. Ag/AgCl values were converted to E_{onset} vs. RHE (reversible hydrogen electrode), using Equation (1):

$$E_{RHE} = E_{Ag/AgCl} + 0.059\ pH + E^{o}_{Ag/AgCl} \quad (1)$$

where E_{RHE} is potential vs. RHE, $E_{Ag/AgCl}$ is potential vs. Ag/AgCl and $E^{o}{}_{Ag/AgCl}$ = 0.1976 V (at 25.0 °C).

The onset potential, defined as the potential at which the reduction of oxygen starts, can be determined by different methods [3,51] and is generally assumed as the potential at which the ORR current is 5% of the diffusion-limiting current density. Alternatively, it can be calculated as the potential at which the slope of the voltammogram exceeds a threshold value (j = 0.1 mA cm^{-2}) [3,51,52]. Here, we considered both methods.

To determine the number of electrons being transferred per O_2 molecule (n_{O2}) with LSV data, the Koutecky-Levich (K-L) Equation (2) was used:

$$\frac{1}{j} = \frac{1}{j_L} + \frac{1}{j_k} = \frac{1}{B\omega^{1/2}} + \frac{1}{j_k} \quad (2)$$

where j is the measured current density, and j_L and j_k are the diffusion-limiting current density and the kinetic current density, respectively. The angular velocity is represented by ω and B is related to the diffusion-limiting current density, as shown in Equation (3):

$$B = 0.2\, n_{O_2}\, F\, (D_{O_2})^{2/3}\, v^{-1/6}\, C_{O_2} \quad (3)$$

where F = 96,485 C·mol^{-1}, D_{O_2} is the O_2 diffusion coefficient (1.95 × 10^{-5} cm^2·s^{-1} for this electrolyte), v is the electrolyte kinematic viscosity (8.977 × 10^{-3} cm^2·s^{-1}) and C_{O_2} is the bulk concentration of O_2 (1.15 × 10^{-3} mol·dm^{-3} in this electrolyte). A constant of 0.2 was used, since the rotation speeds are given in rpm.

Methanol resistance was carried out by chronoamperometry in O_2-saturated KOH for 2500 s, at a fixed potential of E = −0.55 V vs. Ag/AgCl and speed rotation or 1600 rpm, where, at 500 s, 2 mL of methanol was added to the electrolyte. Stability tests were conducted by chronoamperometry in O_2-saturated KOH for 20,000 s, at E = −0.55 V vs. Ag/AgCl and 1600 rpm.

2.5. OER Performance

OER studies were carried out with an aqueous solution of KOH (0.1 mol·dm^{-3}, 100 mL) degassed with oxygen gas. These studies involved acquiring LSV polarization curves from 1.0 to 1.8 V vs. RHE, at a scan rate of 5 mV·s^{-1} and a speed rotation of 1600 rpm. The i_R-compensation (90% of uncompensated resistances, R_u) was applied to all LSV tests where the R_u values were estimated from *i*-interrupt tests.

3. Results and Discussion

3.1. Structural Characterization of the Materials by SEM

The morphological features of the 1D and 2D building blocks were characterized by microscopy methods in the bulk pristine state, and after the surfactant-assisted exfoliation and dispersal process (see Supplementary Figures S1.1–1.3), in the light of previous works [44,53]. Representative SEM micrographs of the dispersed MWNTs and TMDs are shown in Figure 2A,B, respectively. Figure 2A shows that after the sonication-centrifugation preparation method, the MWNTs are well-dispersed and individualized in aqueous dispersion by the cationic surfactant TTAB, from the initial bundled agglomerates. Most of the tubes appear isolated (widths of less than 20 nm, consistent with the nominal width provided by the supplier, 8–15 nm) and curvilinear in shape, with lengths of few tenths of nm up to about 2 μm. In Figure 2B, it can be observed that the negatively charged SC-dispersed MoS_2 particles (sonicated but not centrifuged, as mentioned in Section 2.2), have mean lateral dimensions mostly in the range of 0.5–2 μm (similar results were obtained for WS_2, processed under exactly the same conditions). Following characterization of the individual building blocks, the prepared WS_2@MWNT and MoS_2@MWNT composites were also characterized by SEM, as illustrated in Figure 2C1–D2. For both materials, the images suggest that the 1D and 2D blocks interact, forming tightly bound and mixed composites, as could be expected from the fact that the blocks are coated by surfactants of opposite charge, and hence strong electrostatic interactions in solution are at play (see also Supplementary Figure S1.4b). It is worth mentioning that nanocomposites based on a similar approach, using ionic surfactants and electrostatic interactions as an assembly driving force, have been previously reported [38,54]. Some differences can be seen, however, between the WS_2@MWNT and the MoS_2@MWNT materials. Figure 2C1 shows that the WS_2@MWNT composite is mostly characterized by regions of entangled MWNTs (blue arrows), and embedded and coated WS_2 2D particles (orange arrows). Figure 2C2, at

higher magnification, reveals further details: some of the TMD particles seem to be deeply embedded in dense networks of MWNTs, with both the basal planes and edges of particles covered by the tubes (as indicated by the dashed ovals).

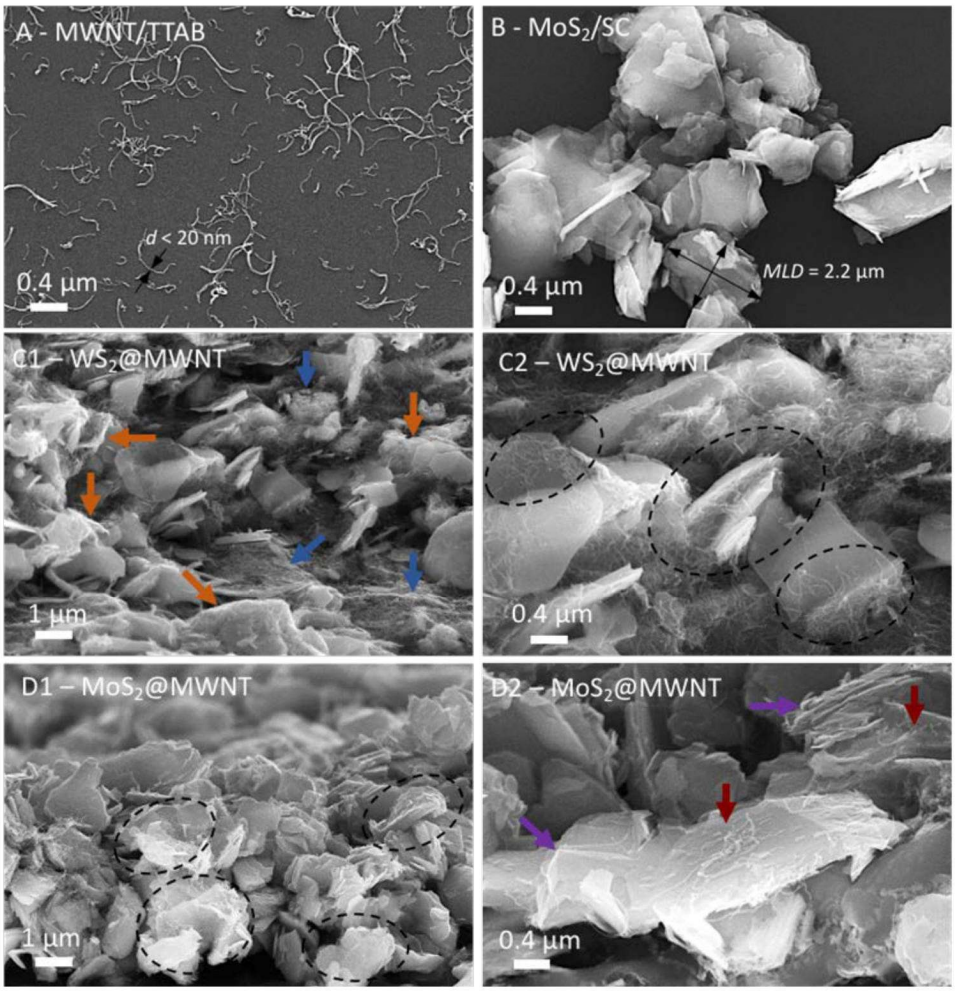

Figure 2. Scanning electron microscopy (SEM) micrographs of the nanocomposite films: (**A**) well-dispersed MWNTs using surfactant TTAB, with arrows showing typical tube widths (<20 nm). (**B**) MoS_2 particles dispersed by surfactant SC, with the calculation of a typical mean lateral dimension (*MLD*) illustrated. (**C1**,**C2**), WS_2@MWNT composites, (**D1**,**D2**), MoS_2@MWNT composites. The arrows and dashed ovals in C1–D2 highlight particular features described in detail in the text.

In contrast, Figure 2D1 and 2D2 show that the MoS_2@MWNT composite seems to be mostly composed of the 2D particles alternating with horizontally placed MWNTs (dashed ovals), presumably resulting in more compact, stacked layers of the 1D and 2D blocks than the previous material. Figure 2D2, in particular, shows that the nanotubes are lying essentially on the basal planes of the particles (red arrows), with a relatively even separation between them, presumably leaving the TMD edges more exposed to the medium (violet arrows). Whether or not these differences in morphological features between the obtained composites will reflect on their electrocatalytic behavior remained to be seen and was subject to investigation in the next section.

3.2. ORR Activity of the Composite Materials

The ORR electrocatalytic performances of pristine WS_2, WS_2/SC, MWNT/TTAB, WS2@MWNT, pristine MoS_2, MoS_2/SC, centrifuged MoS_2/SC (MoS_2/SC w/CF) and MoS_2@MWNT were initially evaluated by cyclic voltammetry, in N_2- and O_2-saturated

0.1 mol·dm^{-3} KOH solution. The results are provided in Supplementary Figure S2.1. In the N_2-saturated electrolyte solution, none of the studied materials show electrochemical processes in the potential window studied. In contrast, in the O_2-saturated electrolyte, an ORR peak can be distinguished for all the materials. This peak occurs at E_{pc} = 0.58, 0.50, 0.52, 0.58, 0.54, 0.55, 0.55 and 0.72 V vs. RHE for MWNT/TTAB, WS_2 pristine, WS_2/SC, WS_2@MWNT, MoS_2 pristine, MoS_2/SC w/CF, MoS_2/SC and MoS_2@MWNT, respectively. This confirms the electrocatalytic activity of the materials toward ORR.

Figure 3A shows the CVs in O_2-saturated KOH for WS_2@MWNT, MoS_2@MWNT and the benchmark electrocatalyst Pt/C. It can be seen that the obtained results for the nanocomposites are still somewhat inferior compared to that obtained for Pt/C (E_{pc} = 0.86 V). Still, there are differences between the composites, with MoS_2@MWNT showing better performance than WS_2@MWNT.

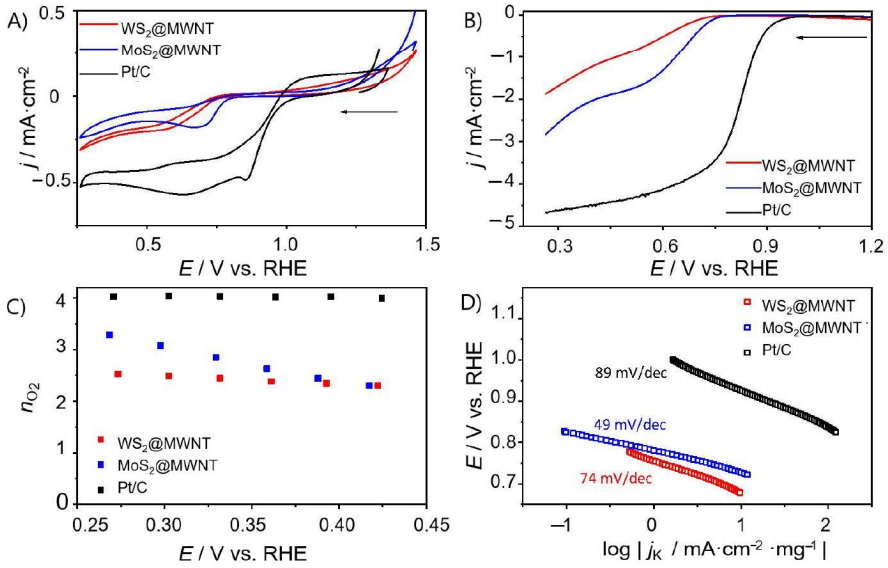

Figure 3. Electrochemical studies on WS2@MWNT, MoS2@MWNT and Pt/C. (**A**) Cyclic voltammograms (CVs) (O_2-saturated 0.1 mol·dm^{-3} KOH, v = 0.005 V·s^{-1}), (**B**) Linear sweep voltammograms (LSVs) at 1600 rpm (O_2-saturated 0.1 mol·dm^{-3} KOH, v = 0.005 V·s^{-1}), (**C**) n_{O2} at different potentials, (**D**) Tafel plots.

To unfold the kinetics of the ORR process at the prepared materials, LSV studies were carried out in a N_2- and O_2-saturated electrolyte solution (0.1 mol·dm^{-3} KOH), at different rotation speeds. The LSVs at 1600 rpm for WS_2@MWNT and MoS_2@MWNT are presented in Figure 3B. From the LSV curves, onset potential (E_{onset}), current densities (j_L) and the number of electrons transferred per O_2 molecule (n_{O2}) were obtained and are represented in Table 1. The values obtained for MoS_2@MWNT (E_{onset} = 0.73 V vs. RHE and j_L = −2.74 mA·cm^{-2}) are comparable to those obtained for WS_2@MWNT (E_{onset} = 0.71 V vs. RHE and j_L = −1.87 mA·cm^{-2}), however, both are still far from those obtained for the Pt/C electrocatalyst (E_{onset} = 0.91 V vs. RHE and j_L = −4.67 mA·cm^{-2}). The differences observed in the E_{onset} values are not significant and fall within the experimental uncertainty (<3%).The slightly better performance of MoS_2@MWNT in terms of j_L values (uncertainty in j_L < 7%) may be related to the fact that, in this nanocomposite, the TMD edges are more exposed to the medium, as observed by SEM.

The number of electrons transferred per O_2 molecule was estimated through Equations (2) and (3). Figure 3C shows the n_{O2} values at different potentials for WS_2@MWNT, MoS_2@MWNT and Pt/C, while the results for the other materials can be found in the Supplementary Material, Figures S2.2 and S2.3c. WS_2@MWNT shows a n_{O2} value close to 2 electrons, suggesting that the oxygen reduction reaction occurs via the 2-electron indirect mechanism. Nevertheless, the n_{O2} values estimated do not vary with the applied potential.

For MoS_2@MWNT, the mean n_{O2} value is close to 3 but the potential applied has an impact on the n_{O2} values, which decrease as the potential increases. A n_{O2} = 3 suggests that the reaction occurs via a mixed 2- and 4-electron mechanism. Although not optimal, since a 4-electron regime was not achieved, these results leave room for improvement.

Table 1. ORR (oxygen reduction reaction) activity parameters (E_{onset}, j_L and n_{O2}) for WS_2@MWNT, MoS_2@MWNT and Pt/C.

Sample	E_{onset}/V vs. RHE (5% of j)	E_{onset}/V vs. RHE [1] (j = 0.1 mA·cm^{-2})	j_L/mA·cm^{-2}	n_{O2}
WS_2@MWNT	0.71	0.70	−1.87	2.41
MoS_2@MWNT	0.73	0.74	−2.74	2.87
Pt/C	0.91	0.93	−4.67	4.00

[1] RHE—reversible hydrogen electrode.

A possible reason for these results may be related to the particle size of MoS_2 and WS_2. According to Li et al. [55], the catalytic activity toward both HER and ORR increased with the decrease in particle size and more importantly, their results showed that selectivity for the 4-electron process may also be related to the Mo edges on the extremely small MoS_2 nanoparticles (≈2 nm). As referred to in Section 2.2, larger sheets of the TMDs were needed for the construction of the structured composites, justifying the elimination of the centrifugation step. Although, apparently, no significant differences were observed in the electrocatalytic activity of MoS_2/SC by removing the centrifugation step (Supplementary Figure S2.3), we cannot entirely exclude that in our final materials, the presence of larger particles may affect the ORR activity. Recent work has also shown that different multi-crystalline structures of TMDs, with distinct surface property and electronic performance, greatly impact the materials' performance in energy storage and conversion, with the metallic phases presenting better results [56]. In our studies, we used the trigonal prismatic structure which, on one hand, is better for exfoliation treatments but, on the other hand, as we find out, leads to worse ORR performance.

Tafel plots, shown in Figure 3D, were obtained from LSV data in Figure 3B at 1600 rpm, in O_2-saturated KOH. The ORR process exhibits Tafel slopes of 74, 49 and 110 mV·dec^{-1} for WS_2@MWNT, MoS_2@MWNT and Pt/C, respectively. These results suggest that for the built nanocomposites, the conversion of MOO^- (the intermediate surface-adsorbed species) to MOOH (where M is an empty site on the electrocatalyst surface) rules the global reaction rate, while for Pt/C, it is likely the first discharge step or the consumption of the MOOH species that determines the reaction rate [57].

The ORR performance of the building blocks of the nanocomposites, in various steps of the process, were also studied, and the results are shown in Supplementary Figures S2.2 and S2.3 (data in Supplementary Table S2.1). All TMDs, in the different stages of the process (pristine WS_2 and MoS_2, WS_2/SC, MoS_2/SC and MoS_2/SC w/CF), show similar results. This suggests that the presence of the selected surfactants used in this work has little effect on the performance of the materials as electrocatalysts. Nonetheless, in the final step of the assembly process, the nanocomposites were rinsed with ethanol to remove the excess surfactant. Special attention was given to this as, according to recent published works [18,20], the surfactant may play an important role in the electrochemical performance. For example, de-Mello et al. [20] showed that the activity of MoS_2 towards the HER was enhanced when the surfactant was absent. However, our studies show that presence or absence of surfactant has no impact on the ORR activity.

Another relevant parameter that was subject to investigation was the tolerance of the electrocatalysts to methanol crossover. In methanol-based fuel cells, fuel crossover from the anode to the cathode may occur and hence reduce cathodic performance, if electrocatalysts are sensitive to it [58]. As such, tolerance to methanol was evaluated using chronoamperometric tests lasting 2500 s, at 1600 rpm and at E = 0.41 V vs. RHE. At the 500 s mark, 2 mL of methanol were injected in the electrolyte (0.1 mol·dm^{-3} KOH). These

results are collected in Figure 4A. As it can be observed, Pt/C underwent a decrease in ORR activity of 48%. In contrast, both nanocomposite materials showed better methanol tolerance, with MoS_2@MWNT retaining 82% of its activity and WS_2@MWNT 80%. Even though Pt-based materials have better ORR performance than most electrocatalysts, they have the disadvantage of being highly reactive to the methanol oxidation reaction. This affects its ORR activity performance, lowering the obtained current density [3,4]. CV tests were also performed before and after the addition of methanol to further study its effect, and results are depicted in Supplementary Figure S2.4. Once again, it is clear the effect of methanol on the electrocatalytic activity of Pt/C towards ORR in contrast to the little effect on the prepared electrocatalysts.

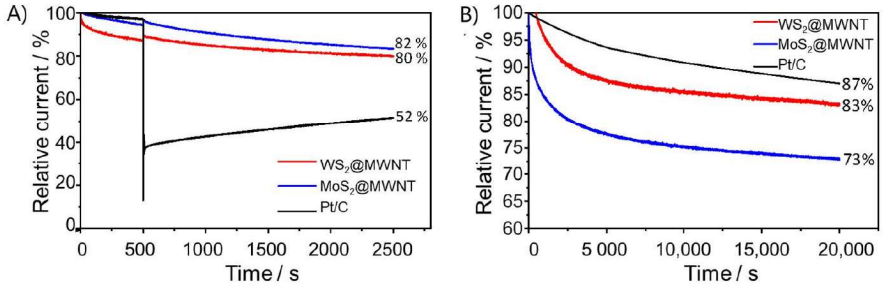

Figure 4. Methanol resistance and stability studies of the WS_2@MWNT, MoS_2@MWNT and Pt/C: (**A**) chronoamperometric responses with the addition of 0.5 mol·dm^{-3} methanol (at 500 s) and (**B**) chronoamperometric response at E = 0.41 V vs. RHE (O_2-saturated 0.1 mol·dm^{-3} KOH, and at 1600 rpm) for 20,000 s.

Long-term stability of the electrocatalysts, another very critical point in the selection of a good electrocatalyst, was also assessed. It was performed by CA during 20,000 s, in O_2-saturated 0.1 mol·dm^{-3} KOH, at 1600 rpm, and at E = 0.41 V vs. RHE, and the obtained results are shown in Figure 4B. After 20,000 s, WS_2@MWNT retains 83% of its initial current, while MoS_2@MWNT retains 73%. Even though these values are somewhat lower than that obtained for Pt/C (87%), they suggest good stability of the prepared electrocatalysts.

3.3. OER Activity of the Composite Materials

The electrocatalytic performance of the nanocomposite materials towards OER was also evaluated. For that, LSV studies were carried out, in a O_2-saturated 0.1 mol·dm^{-3} KOH electrolyte, at a scan rate of v = 0.005 V·s^{-1} and 1600 rpm. The polarization curves obtained are presented in Figure 5. As for ORR, the results were benchmarked using, in this case, one of the state-of-the-art OER electrocatalysts (RuO_2).

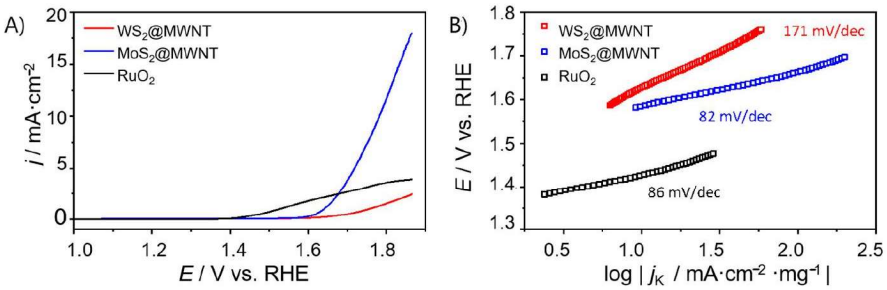

Figure 5. (**A**) OER polarization curves obtained by LSV (O_2-saturated 0.1 mol·dm^{-3} KOH, v = 0.005 V·s^{-1}, 1600 rpm) for WS_2@MWNT, MoS_2@MWNT and RuO_2, and (**B**) respective Tafel plots.

As it can be observed in Figure 5A, WS_2@MWNT did not present OER activity reaching a value of j_{max} of only 2.45 mA·cm^{-2}. On the other hand, MoS_2@MWNT showed good OER activity with a j_{max} of 17.96 mA·cm^{-2} and an overpotential of 0.55 V vs. RHE at j = 10 mA·cm^{-2}. Regarding the benchmark material, RuO_2, its polarization curves show

much lower current density than expected. However, this benchmarking is not completely reliable since the materials compared have different structures and consequently, very different surface areas.

Table 2 gathers the main OER activity parameters, derived from the LSV plots. The values of j at E = 1.8 V vs. RHE ($j_{1.8}$) were also included since neither WS_2@MWNT nor RuO_2 reached j = 10 mA·cm^{-2}.

Table 2. OER (oxygen evolution reaction) activity parameters (η_{10}, j_{max}, and $j_{1.8}$) for WS_2@MWNT, MoS_2@MWNT and RuO_2.

Sample	H_{10}/V (j = 10 mA·cm^{-2})	j_{max}/mA·cm^{-2}	$j_{1.8}$/mA·cm^{-2}
WS_2@MWNT	-	2.45	1.57
MoS_2@MWNT	0.55	17.96	11.88
RuO_2	-	3.94	3.64

Like for the ORR studies, the Tafel slopes were determined (Figure 5B) to get an insight into the OER kinetics. Both MoS_2@MWNT and RuO_2 presented relatively low values (82 and 86 mV·dec^{-1}) when compared with WS_2@MWNT (171 mV·dec^{-1}). The elevated Tafel slope values for OER are characteristic of slow (rate-determining) initial steps, comprising the adsorption of OH- groups on active sites. Therefore, the reduction of the Tafel slope value for the MoS_2@MWNT in comparison with WS_2@MWNT indicates that the access of the OH- groups to the active sites is favored in the former nanocomposite.

The building blocks of the nanocomposites (MWNT/TTAB, and pristine and SC-coated WS_2 and MoS_2) were also studied for OER (Supplementary Figures S2.5 and S2.6, data in Supplementary Table S2.2). MWNT/TTAB has OER activity, while the pristine TMDs and TMDs with surfactant show poor results. Regarding MoS_2@MWNT, the nanocomposite has better OER electrocatalytic performance than the sum of its constituents, and hence synergism of properties is suggested.

In short, concerning the electrocatalytic performance of the nanocomposite materials towards the OER, results showed a large difference between them. While MoS_2@MWNT presented j_{max} values of 17.96 mA·cm^{-2} and η_{10} = 0.55 V, WS_2@MWNT only reached current densities of j_{max} = 2.45 mA·cm^{-2}.

Overall, MoS_2@MWNT has better electrocatalytic performance than WS_2@MWNT towards the oxygen reactions. While ORR activity is modest, OER activity is good, suggesting that the nanocomposites may be developed towards bifunctional electrocatalysts, using this fabrication method.

4. Conclusions

In this work, nanocomposites of multiwalled carbon nanotubes and TMDs were successfully assembled via a colloidal method based on surfactant-assisted dispersions and electrostatic interactions between oppositely charged surfaces. The final nanocomposite materials were attained in aqueous media, by a simple and cost-effective process that can be easily tuned to adjust the MWNT/TMD ratio. SEM studies showed that, morphologically, the WS_2@MWNT composite is essentially composed of dense regions of entangled MWNTs with embedded and coated WS_2 particles, while MoS_2@MWNT seems to be a tighter composite with MWNTs layers adsorbed horizontally onto to the TMD layers, leaving the edges of the dichalcogenide exposed to the medium.

These materials were then tested as electrocatalysts for both oxygen reactions, showing electrochemical activity towards ORR, with modest performance and good methanol tolerance. The MoS_2@MWNT nanocomposite had a value of n_{O2} close to 3 (indicating a mixed 2- and 4-electron mechanism) and a better overall ORR activity, E_{onset} and j_L values of 0.73 V vs. RHE and −2.74 mA·cm^{-2} respectively, when compared to WS_2@MWNT (E_{onset} = 0.71 V vs. RHE; j_L = −1.87 mA·cm^{-2}). Additionally, MoS_2@MWNT showed good OER activity, with η_{10} and j_{max} values of 0.55 V and 17.96 mA·cm^{-2}, respectively.

These findings point towards potential improvement of the nanocomposites, in order, for instance, to select the best TMD/MWNT combination and develop a good ORR and/or OER electrocatalyst, while having a facile and cost-effective assembly method. Future work will include studies on the role of the TMD/MWNT combination and also the use of hetero-atom-doped MWNTs and other carbon materials, like graphene.

Supplementary Materials: The following are available online at https://www.mdpi.com/1996-1944/14/4/896/s1, Section S1 includes additional characterization data. Figure S1.1: representative TEM images of the pristine MWNT powder; Figure S1.2: SEM micrographs of the MWNT/TTAB dispersions at high magnifications. Figure S1.3: SEM imaging of the bulk MoS_2, after sonication in SC aqueous solution, and after the complete sonication/centrifugation procedure. A Raman spectrum of the latter is also shown. Figure S1.4: dispersibility curves for the TMD/surfactant systems and zeta potential values for the building block particles. In Section S2, further electrochemical data is included. Figure S2.1: CVs of (a) MWNT/TTAB, (b) WS_2 pristine, (c) WS_2/SC, (d) WS_2@MWNT, (e) MoS_2 pristine, (f) MoS_2/SC w/CF, (g) MoS_2/SC, and (h) MoS_2@MWNT obtained in N_2 and O_2-saturated 0.1 mol·dm^{-3} KOH solution, at v = 0.005 V·s^{-1}. Figure S2.2: electrochemical studies of Pt/C, WS_2@MWNT nanocomposite, and its building blocks, WS_2 pristine, WS_2/SC and MWNT/TTAB. (a) CVs (O_2-saturated 0.1 mol·dm^{-3} KOH, v = 0.005 V·s^{-1}), (b) LSVs at 1600 rpm (O_2-saturated 0.1 mol·dm^{-3} KOH, v = 0.005 V·s^{-1}), (c) n_{O2} at different potentials, (d) Tafel plots. Figure S2.3: electrochemical studies on Pt/C, MoS_2@MWNT nanocomposite, and its building blocks, MoS_2 pristine, MoS_2/SC w/CF, MoS_2/SC, and MWNT/TTAB. (a) CVs (O_2-saturated 0.1 mol·dm^{-3} KOH, v = 0.005 V·s^{-1}), (b) LSVs at 1600 rpm (O_2-saturated 0.1 mol·dm^{-3} KOH, v = 0.005 V·s^{-1}), (c) n_{O2} at different potentials, (d) Tafel plots. Figure S2.4: methanol resistance studies: (a) chronoamperometric responses of the WS_2@MWNT, MoS_2@MWNT and Pt/C materials with the addition of 0.5 mol·dm^{-3} methanol (at 500 s), (b) CV of WS_2@MWNT before and after methanol addition, (c) CV of MoS_2@MWNT before and after methanol addition, (d) CV of Pt/C before and after methanol addition. Figure S2.5 presents the OER polarization curves obtained by LSV (O_2-saturated 0.1 mol·dm^{-3} KOH, v = 0.005 V·s^{-1}, 1600 rpm) for MWNT/TTAB, WS_2 pristine, WS_2/SC, WS_2@MWNT and RuO_2; Figure S2.6 shows the OER polarization curves obtained by LSV (O_2-saturated 0.1 mol·dm^{-3} KOH, v = 0.005 V·s^{-1}, 1600 rpm) for MWNT/TTAB, MoS_2 pristine, MoS_2/SC, MoS_2@MWNT and RuO_2. Table S2.1: ORR activity parameters (E_{onset}, j_L, and n_{O2}) for MWNT/TTAB, WS_2 pristine, WS_2/SC, WS_2@MWNT, MoS_2 pristine, MoS_2/SC w/CF, MoS_2/SC, and MoS_2@MWNT. Table S2.2: OER activity parameters (η_{10}, j_{max}, and $j_{1.8}$) for MWNT/TTAB, WS_2 pristine, WS_2/SC, WS_2@MWNT, MoS_2 pristine, MoS_2/SC w/CF, MoS_2/SC, MoS_2@MWNT, and RuO_2.

Author Contributions: Conceptualization, C.F., D.M.F. and E.F.M.; funding acquisition, C.F. and E.F.M.; investigation, P.F. and B.A.; resources, C.F. and E.F.M.; supervision, D.M.F. and E.F.M.; validation, B.A., C.F., D.M.F. and E.F.M.; writing—original draft, P.F. and B.A.; writing—review and editing, D.M.F. and E.F.M. All authors have read and agreed to the published version of the manuscript.

Funding: This work was supported by project UIDB/00081/2020 and UIDB/50006/2020, funded by Fundação para a Ciência e a Tecnologia (FCT), and by project UNIRCELL—POCI-01-0145-FEDER-16422, funded by European Structural and Investment Funds (FEEI) through Programa operacional Competitividade e Internacionalização—COMPETE2020, and by FCT, I.P. Bárbara Abreu also acknowledges financial support from FCT through the PhD grant PD/BD/128129/2016.

Institutional Review Board Statement: Not applicable.

Informed Consent Statement: Not applicable.

Data Availability Statement: Data is contained within the article or supplementary material.

Conflicts of Interest: The authors declare no conflict of interest.

References

1. Seh, Z.W.; Kibsgaard, J.; Dickens, C.F.; Chorkendorff, I.; Nørskov, J.K.; Jaramillo, T.F. Combining theory and experiment in electrocatalysis: Insights into materials design. *Science* **2017**, *355*, B517. [CrossRef]
2. Kuang, M.; Zheng, G. Nanostructured bifunctional redox electrocatalysts. *Small* **2016**, *12*, 5656–5675. [CrossRef]
3. Freire, C.; Fernandes, D.M.; Nunes, M.; Abdelkader, V.K. POM & MOF-based electrocatalysts for energy-related reactions. *ChemCatChem* **2018**, *10*, 1703–1730.

4. Fernandes, D.M.; Novais, H.C.; Bacsa, R.; Serp, P.; Bachiller-Baeza, B.; Rodriguez-Ramos, I.; Guerrero-Ruiz, A.; Freire, C. Polyoxotungstate@ Carbon nanocomposites as oxygen reduction reaction (ORR) electrocatalysts. *Langmuir* **2018**, *34*, 6376–6387. [CrossRef]
5. Jiao, Y.; Zheng, Y.; Jaroniec, M.; Qiao, S.-Z. Design of electrocatalysts for oxygen- and hydrogen-involving energy conversion reactions. *Chem. Soc. Rev.* **2015**, *44*, 2060–2086. [CrossRef] [PubMed]
6. Niu, W.-J.; Zhu, R.-H.; Yan-Hua, Y.; Zeng, H.-B.; Cosnier, S.; Zhang, X.-J.; Shan, D. One-pot synthesis of nitrogen-rich carbon dots decorated graphene oxide as metal-free electrocatalyst for oxygen reduction reaction. *Carbon* **2016**, *109*, 402–410. [CrossRef]
7. Zhou, L.; Fu, P.; Wang, Y.; Sun, L.; Yuan, Y. Microbe-engaged synthesis of carbon dot-decorated reduced graphene oxide as high-performance oxygen reduction catalysts. *J. Mater. Chem. A* **2016**, *4*, 7222–7229. [CrossRef]
8. Tuci, G.; Zafferoni, C.; Rossin, A.; Milella, A.; Luconi, L.; Innocenti, M.; Phuoc, L.T.; Duong-Viet, C.; Pham-Huu, C.; Giambastiani, G. Chemically functionalized carbon nanotubes with pyridine groups as easily tunable N-decorated nanomaterials for the oxygen reduction reaction in alkaline medium. *Chem. Mater.* **2014**, *26*, 3460–3470. [CrossRef]
9. Vikkisk, M.; Kruusenberg, I.; Ratso, S.; Joost, U.; Shulga, E.; Kink, I.; Rauwel, P.; Tammeveski, K. Enhanced electrocatalytic activity of nitrogen-doped multi-walled carbon nanotubes towards the oxygen reduction reaction in alkaline media. *RSC Adv.* **2015**, *5*, 59495–59505. [CrossRef]
10. Mathumba, P.; Fernandes, D.M.; Matos, R.; Iwuoha, E.I.; Freire, C. Metal oxide (Co_3O_4 and Mn_3O_4) impregnation into S, N-doped graphene for oxygen reduction reaction (ORR). *Materials* **2020**, *13*, 1562. [CrossRef]
11. Wu, J.; Ma, L.; Yadav, R.M.; Yang, Y.; Zhang, X.; Vajtai, R.; Lou, J.; Ajayan, P.M. Nitrogen-doped graphene with pyridinic dominance as a highly active and stable electrocatalyst for oxygen reduction. *ACS Appl. Mater. Interfaces* **2015**, *7*, 14763–14769. [CrossRef] [PubMed]
12. Fan, T.; Zhang, G.; Jian, L.; Murtaza, I.; Meng, H.; Liu, Y.; Min, Y. Facile synthesis of defect-rich nitrogen and sulfur Co-doped graphene quantum dots as metal-free electrocatalyst for the oxygen reduction reaction. *J. Alloys Compd.* **2019**, *792*, 844–850. [CrossRef]
13. Faraji, M.; Derakhshi, P.; Tahvildari, K.; Yousefian, Z. High performance Fe and N-codoped graphene quantum dot supported Pd_3Co catalyst with synergistically improved oxygen reduction activity and great methanol tolerance. *Solid State Sci.* **2018**, *83*, 152–160. [CrossRef]
14. Liu, K.; Song, Y.; Chen, S. Oxygen reduction catalyzed by nanocomposites based on graphene quantum dots-supported copper nanoparticles. *Int. J. Hydrogen Energy* **2016**, *41*, 1559–1567. [CrossRef]
15. Suntivich, J.; May, K.J.; Gasteiger, H.A.; Goodenough, J.B.; Shao-Horn, Y. A Perovskite oxide optimized for oxygen evolution catalysis from molecular orbital principles. *Science* **2011**, *334*, 1383–1385. [CrossRef] [PubMed]
16. Wurster, B.; Grumelli, D.; Hotger, D.; Gutzler, R.; Kern, K. Driving the oxygen evolution reaction by nonlinear cooperativity in bimetallic coordination catalysts. *J. Am. Chem. Soc.* **2016**, *138*, 3623–3626. [CrossRef] [PubMed]
17. Liping, G.; Xiong, Y.; Liu, X.; Bo, X.; Zhang, Y.; Han, C.; Guo, L. Facile synthesis of electrospun MFe_2O_4(M = Co, Ni, Cu, Mn) spinel nanofibers with excellent electrocatalytic properties for oxygen evolution and hydrogen peroxide reduction. *Nanoscale* **2015**, *7*, 8920–8930. [CrossRef]
18. Voiry, D.; Salehi, M.; Silva, R.; Fujita, T.; Chen, M.; Asefa, T.; Shenoy, V.B.; Eda, G.; Chhowalla, M. Con-ducting MoS_2 nanosheets as catalysts for hydrogen evolution reaction. *Nano Lett.* **2013**, *13*, 6222–6227. [CrossRef] [PubMed]
19. Cheng, Y.J.; Song, H.; Wu, H.; Zhang, P.; Tang, Z.Y.; Lu, S.Y. Defects enhance the electrocatalytic hydro-gen evolution properties of MoS_2-based materials. *Chem. Asian J.* **2020**, *15*, 3123–3134. [CrossRef] [PubMed]
20. De-Mello, G.B.; Smith, L.; Rowley-Neale, S.J.; Gruber, J.; Hutton, S.J.; Banks, C.E. Surfactant-exfoliated 2D molybdenum disulphide (2D-MoS_2): The role of surfactant upon the hydrogen evolution reaction. *RSC Adv.* **2017**, *7*, 36208–36213. [CrossRef]
21. Rowley-Neale, S.J.; Smith, G.C.; Banks, C.E. Mass-producible 2D-MoS_2-impregnated screen-printed electrodes that demonstrate efficient electrocatalysis toward the oxygen reduction reaction. *ACS Appl. Mater. Interfaces* **2017**, *9*, 22539–22548. [CrossRef]
22. Rowley-Neale, S.J.; Fearn, J.M.; Brownson, D.A.; Smith, G.C.; Ji, X.; Banks, C.E. 2D molybdenum disulphide (2D-MoS_2) modified electrodes explored towards the oxygen reduction reaction. *Nanoscale* **2016**, *8*, 14767–14777. [CrossRef]
23. Wu, J.; Liu, M.; Chatterjee, K.; Hackenberg, K.P.; Shen, J.; Zou, X.; Yan, Y.; Gu, J.; Yang, Y.; Lou, J.; et al. Exfoliated 2D Transition metal disulfides for enhanced electrocatalysis of oxygen evolution reaction in acidic medium. *Adv. Mater. Interfaces* **2016**, *3*, 31500669. [CrossRef]
24. Urbanová, V.; Lazar, P.; Antonatos, N.; Sofer, Z.; Otyepka, M.; Pumera, M. Positive and negative effects of dopants toward electrocatalytic activity of MoS_2 and WS_2: Experiments and theory. *ACS Appl. Mater. Interfaces* **2020**, *12*, 20383–20392. [CrossRef]
25. Huang, H.; Zhang, X.; Zhang, Y.; Huang, B.; Cai, J.; Lin, S. Facile synthesis of laminated porous WS_2/C composite and its electrocatalysis for oxygen reduction reaction. *Int. J. Hydrogen Energy* **2018**, *43*, 8290–8297. [CrossRef]
26. Vattikuti, S.V.P.; Nagajyothi, P.C.; Devarayapalli, K.C.; Shim, J. Depositing reduced graphene oxide onto tungsten disulfide nanosheetsviamicrowave irradiation: Confirmation of four-electron transfer-assisted oxygen reduction and methanol oxidation reaction. *N. J. Chem.* **2020**, *44*, 10638–10647. [CrossRef]
27. Du, C.; Huang, H.; Feng, X.; Wu, S.; Song, W. Confining MoS_2 nanodots in 3D porous nitrogen-doped graphene with amendable ORR performance. *J. Mater. Chem. A* **2015**, *3*, 7616–7622. [CrossRef]

28. Fu, K.; Wang, Y.; Qian, Y.; Mao, L.; Jin, J.; Yang, S.; Li, G. Synergistic effect of nitrogen doping and MWCNT intercalation for the graphene hybrid support for pt nanoparticles with exemplary oxygen reduction reaction performance. *Materials* **2018**, *11*, 642. [CrossRef]
29. Faisal, S.N.; Subramaniyam, C.M.; Haque, E.; Islam, M.; Noorbehesht, N.; Roy, A.K.; Islam, M.S.; Liu, H.K.; Dou, S.; Harris, A.T.; et al. Nanoarchitectured nitrogen-doped graphene/Carbon nanotube as high performance electrodes for solid state supercapacitors, capacitive deionization, li-ion battery, and metal-free bifunctional electrocatalysis. *ACS Appl. Energy Mater.* **2018**, *1*, 5211–5223. [CrossRef]
30. Tian, G.-L.; Zhao, M.-Q.; Yu, D.; Kong, X.-Y.; Huang, J.-Q.; Zhang, Q.; Wei, F. Nitrogen-Doped graphene/carbon nanotube hybrids: In situ formation on bifunctional catalysts and their superior electrocatalytic activity for oxygen evolution/reduction reaction. *Small* **2014**, *10*, 2251–2259. [CrossRef] [PubMed]
31. Daems, N.; Sheng, X.; Vankelecom, I.F.; Pescarmona, P.P. Metal-free doped carbon materials as electrocatalysts for the oxygen reduction reaction. *J. Mater. Chem. A* **2014**, *2*, 4085–4110. [CrossRef]
32. Alzahly, S.; Yu, L.; Shearer, C.J.; Gibson, C.T.; Shapter, J.G. Efficiency improvement using molybdenum disulphide interlayers in single-wall carbon nanotube/silicon solar cells. *Materials* **2018**, *11*, 639. [CrossRef] [PubMed]
33. Saito, R.; Tatsumi, Y.; Huang, S.; Ling, X.; Dresselhaus, M.S. Raman spectroscopy of transition metal dichalcogenides. *J. Phys. Condens. Matter* **2016**, *28*, 353002. [CrossRef]
34. Lv, R.; Robinson, J.A.; Schaak, R.E.; Sun, D.; Sun, Y.; Mallouk, T.E.; Terrones, M. Transitionmetal dichalcogenides and beyond: Synthesis, properties, and applications of single- and few-layer nanosheets. *Acc. Chem. Res.* **2015**, *48*, 56–64. [CrossRef]
35. Zhang, X.; Qiao, X.-F.; Shi, W.; Wu, J.-B.; Jiang, D.-S.; Tan, P. Phonon and Raman scattering of two-dimensional transition metal dichalcogenides from monolayer, multilayer to bulk material. *Chem. Soc. Rev.* **2015**, *44*, 2757–2785. [CrossRef] [PubMed]
36. Smith, R.J.; King, P.J.; Lotya, M.; Wirtz, C.; Khan, U.; De, S.; O'Neill, A.; Duesberg, G.S.; Grunlan, J.C.; Moriarty, G.; et al. Large-scale exfoliation of inorganic layered compounds in aqueous surfactant solutions. *Adv. Mater.* **2011**, *23*, 3944–3948. [CrossRef]
37. Huang, H.; Huang, W.; Yang, Z.; Huang, J.; Lin, J.; Liu, W.; Liu, Y. Strongly coupled MoS_2 nanoflake-carbon nanotube nanocomposite as an excellent electrocatalyst for hydrogen evolution reaction. *J. Mater. Chem. A* **2017**, *5*, 1558–1566. [CrossRef]
38. Ahn, E.; Kim, B.-S. Multidimensional thin film hybrid electrodes with MoS_2 Multilayer for electrocatalytic hydrogen evolution reaction. *ACS Appl. Mater. Interfaces* **2017**, *9*, 8688–8695. [CrossRef] [PubMed]
39. Chen, M.; Jian, X.; Wu, H.; Huang, J.; Liu, W.; Liu, Y. Facile synthesis of Mn-doped MoS_2 nanosheets on car-bon nanotubes as efficient electrocatalyst for hydrogen evolution reaction. *Nanotechnology* **2020**, *31*, 205403. [CrossRef]
40. Jayabal, S.; Saranya, G.; Liu, Y.; Geng, D.; Meng, X. Unravelling the synergy effects of defect-rich 1T-MoS_2/carbon nanotubes for the hydrogen evolution reaction by experimental and calculational studies. *Sustain. Energy Fuels* **2019**, *3*, 2100–2110. [CrossRef]
41. Cao, J.; Zhou, J.; Zhang, Y.; Liu, X. A clean and facile synthesis strategy of MoS_2 nanosheets grown on multi-wall CNTs for enhanced hydrogen evolution reaction performance. *Sci. Rep.* **2017**, *7*, 1–8. [CrossRef]
42. Lee, C.; Ozden, S.; Tewari, C.S.; Park, O.-K.; Vajtai, R.; Chatterjee, K.; Ajayan, P.M. MoS2-carbon nanotube porous 3 D network for enhanced oxygen reduction reaction. *ChemSusChem* **2018**, *11*, 2960–2966. [CrossRef] [PubMed]
43. Tiwari, A.P.; Kim, D.; Kim, Y.; Lee, H. Bifunctional oxygen electrocatalysis through chemical bonding of transition metal chalcogenides on conductive carbons. *Adv. Energy Mater.* **2017**, *7*, 1602217. [CrossRef]
44. Abreu, B.; Rocha, J.; Fernandes, R.M.; Regev, O.; Furó, I.; Marques, E.F. Gemini surfactants as efficient dispersants of multiwalled carbon nanotubes: Interplay of molecular parameters on nanotube dispersibility and debundling. *J. Colloid Interface Sci.* **2019**, *547*, 69–77. [CrossRef]
45. Dai, J.; Fernandes, R.M.; Regev, O.; Marques, E.F.; Furó, I. Dispersing carbon nanotubes in water with amphiphiles: Dispersant adsorption, kinetics, and bundle size distribution as defining factors. *J. Phys. Chem. C* **2018**, *122*, 24386–24393. [CrossRef]
46. Fernandes, R.M.; Abreu, B.; Claro, B.; Buzaglo, M.; Regev, O.; Furó, I.; Marques, E.F. Dispersing carbon nanotubes with ionic surfactants under controlled conditions: Comparisons and insight. *Langmuir* **2015**, *31*, 10955–10965. [CrossRef]
47. Fernandes, R.M.; Buzaglo, M.; Regev, O.; Marques, E.F.; Furó, I. Surface coverage and competitive adsorption on carbon nanotubes. *J. Phys. Chem. C* **2015**, *119*, 22190–22197. [CrossRef]
48. Yu, A.; Bekyarova, E.; Itkis, M.E.; Fakhrutdinov, D.; Webster, R.; Haddon, R.C. Application of centrifugation to the large-scale purification of electric arc-produced single-walled carbon nanotubes. *J. Am. Chem. Soc.* **2006**, *128*, 9902–9908. [CrossRef]
49. Vichchulada, P.; Cauble, M.A.; Abdi, E.A.; Obi, E.I.; Zhang, Q.; Lay, M.D. Sonication power for length control of single-walled carbon nanotubes in aqueous suspensions used for 2-dimensional network formation. *J. Phys. Chem. C* **2010**, *114*, 12490–12495. [CrossRef]
50. Nepal, D.; Kim, D.S.; Geckeler, K.E. A facile and rapid purification method for single-walled carbon nanotubes. *Carbon* **2005**, *43*, 660–662. [CrossRef]
51. Zhou, X.; Qiao, J.; Yang, L.; Zhang, J. A review of graphene-based nanostructural materials for both catalyst supports and metal-free catalysts in PEM fuel cell oxygen reduction reactions. *Adv. Energy Mater.* **2014**, *4*, 1301523. [CrossRef]
52. Jarrais, B.; Guedes, A.; Freire, C. Heteroatom-doped carbon nanomaterials as metal-free catalysts for the reduction of 4-Nitrophenol. *ChemistrySelect* **2018**, *3*, 1737–1748. [CrossRef]
53. Loos, J.; Grossiord, N.; Koning, C.E.; Regev, O. On the fate of carbon nanotubes: Morphological characterisations. *Compos. Sci. Technol.* **2007**, *67*, 783–788. [CrossRef]

54. Pham, D.T.; Lee, T.H.; Luong, D.H.; Yao, F.; Ghosh, A.; Le, V.T.; Kim, T.H.; Li, B.; Chang, J.; Lee, Y.H. Carbon nanotube-bridged graphene 3D building blocks for ultrafast compact supercapacitors. *ACS Nano* **2015**, *9*, 2018–2027. [CrossRef]
55. Wang, T.; Gao, D.; Zhuo, J.; Zhu, Z.; Papakonstantinou, P.; Li, Y.; Li, M. Size-dependent enhancement of electrocatalytic oxygen-reduction and hydrogen-evolution performance of MoS_2 particles. *Chem. Eur. J.* **2013**, *19*, 11939–11948. [CrossRef] [PubMed]
56. Yang, C.; Wang, H.-F.; Xu, Q. Recent advances in two-dimensional materials for electrochemical energy storage and conversion. *Chem. Res. Chin. Univ.* **2020**, *36*, 10–23. [CrossRef]
57. Fernandes, D.M.; Mathumba, P.; Fernandes, A.J.; Iwuoha, E.I.; Freire, C. Towards efficient oxygen reduction reaction electrocatalysts through graphene doping. *Electrochim. Acta* **2019**, *319*, 72–81. [CrossRef]
58. Zhang, B.T.; Zheng, X.; Li, H.F.; Lin, J.M. Application of carbon-based nanomaterials in sample preparation: A review. *Anal. Chim. Acta* **2013**, *784*, 1–17. [CrossRef]

materials

MDPI

Supplementary Material

Nanocomposites Prepared from Carbon Nanotubes and the Transition Metal Dichalcogenides WS_2 and MoS_2 via Surfactant-assisted Dispersions as Electrocatalysts for Oxygen Reactions

Pedro Ferreira[1,2], Bárbara Abreu[1,2], Cristina Freire[2], Diana M. Fernandes[2*] and Eduardo F. Marques[1]**

[1] Centro de Investigação em Química, Departamento de Química e Bioquímica, Faculdade de Ciências, Universidade do Porto 4169-007 Porto, Portugal; up201407953@fc.up.pt (P.F.); barbara.teixeira@fc.up.pt (B.A.)

[2] REQUIMTE-LAQV, Departamento de Química e Bioquímica, Faculdade de Ciências, Universidade do Porto 4169-007 Porto, Portugal; acfreire@fc.up.pt

* Correspondence: diana.fernandes@fc.up.pt (D.M.F.); efmarque@fc.up.pt (E.F.M.)

Section S1: Additional data on nanomaterial characterization

S1.1. Purity and exfoliation state of the dispersed materials

The morphology of the purchased MWNTs was evaluated by TEM using a Jeol JEM 1400 with STEM detector. The nanotube powder was mixed in ethanol and deposited on a Cu grid for analysis. TEM imaging allows the identification of catalyst impurities as dark spots in the micrographs, due to the higher atomic weight of these particles, as reported by Loos *et al* [1]. Figure S1.1 (representative TEM micrographs) shows that there is no significant presence of catalyst impurities in the as-received MWNTs used here. Due to the 2D projection of TEM, the few darker regions seen are due to mass-thickness contrast resulting from bending of the MWNTs or superimposed nanotube regions.

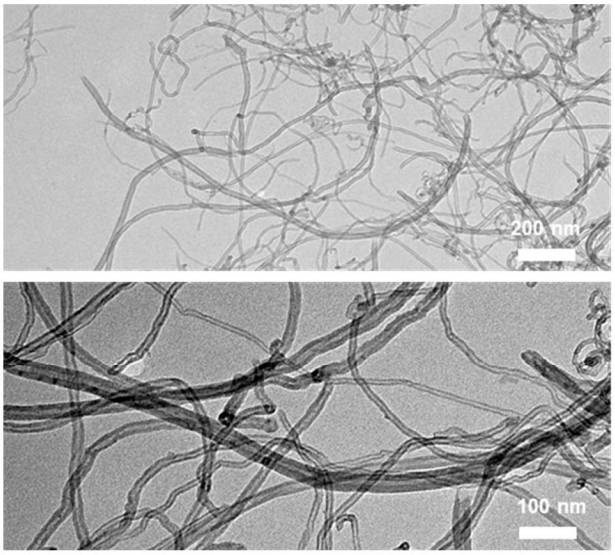

Figure S1.1. Representative TEM micrographs of the commercial MWNTs used in this work.

After dispersion with surfactant TTAB, MWNTs were imaged by SEM (Figure S1.2). The measured MWNT width is typically < 20 nm (consistent with the supplier's range, 8-15 nm) and no trace of metal catalyst particles (bright particles [1]) is seen.

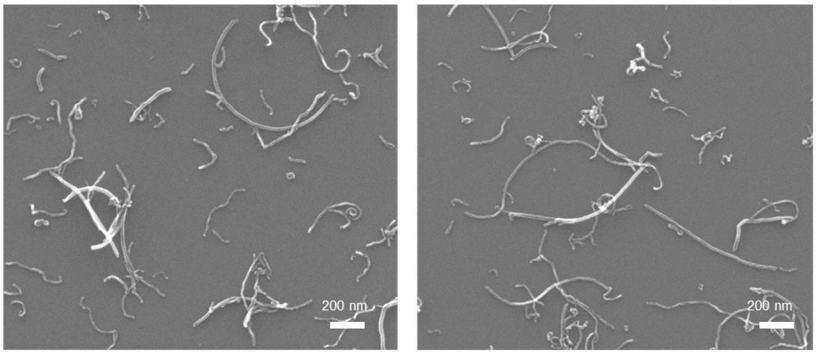

Figure S1.2. Representative SEM micrographs of the MWNT/TTAB dispersions.

Figure S1.3 depicts images of MoS_2 in three different conditions: as-received, after sonication in SC aqueous solution and after the complete sonication/centrifugation procedure described in the experimental section. To evaluate the exfoliation of the TMDs after centrifugation, Raman spectroscopy of the final MoS_2/SC aqueous dispersion was performed on a RAMOS RA532 Raman Analyzer using a laser emitting at 532 nm on glass cuvette, at room temperature. The obtained spectrum is depicted in Figure S1.3 and indicates the presence exfoliated MoS_2, as described in the work of Saito *et al.* and Zhang *et al.* [2,3].

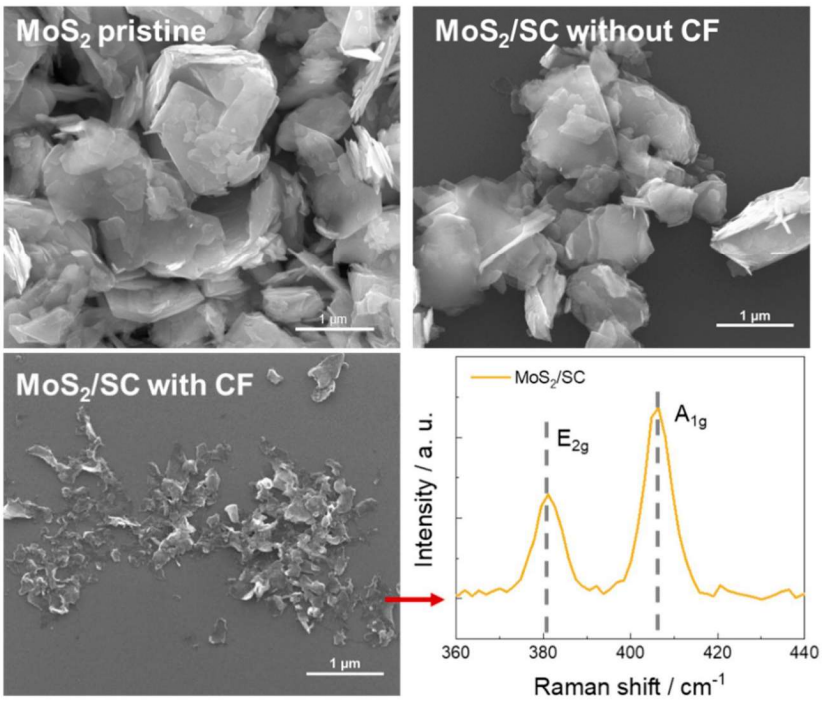

Figure S1.3. Representative SEM micrographs of the pristine MoS_2 and MoS_2/SC dispersions, without centrifugation (CF) and with centrifugation and Raman spectrum of the MoS_2/SC centrifuged sample.

S1.2 Non-covalent functionalization of MWNTs and TMDs

Before the assembly of the nanocomposites, MWNTs and TMDs were physically functionalized using oppositely charged surfactants. To select the optimal surfactant concentration to attain maximum nanomaterial dispersibility, dispersion curves were obtained for all the systems. The MWNT/TTAB curve is reported in [4]. The curves obtained for WS_2 and MoS_2 dispersed with the anionic surfactant SC are shown in Figure S1.4-a). To confirm the non-covalent functionalization of the nanomaterials (i.e. surface charge conferred by the adsorbed surfactant), zeta potential was measured for the dispersions at the selected surfactant concentrations (c_{SC} = 10 mmol·kg^{-1} for WS_2 and MoS_2; c_{TTAB} = 5 mmol·kg^{-1} for MWNTs). The zeta potential was measured at 25 °C using using a LitesizerTM 500 (Anton Paar, Graz, Austria) and DTS 1060C disposable zeta cells.

a)

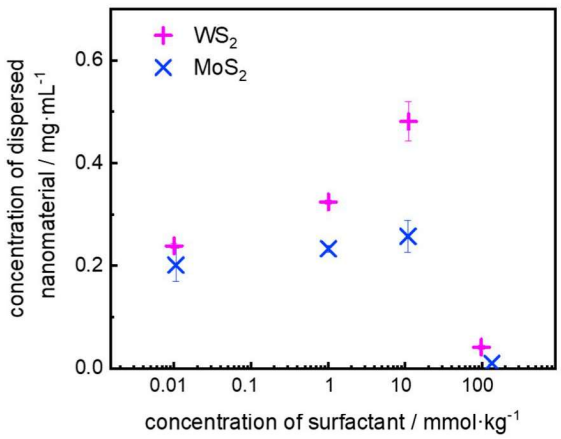

b)

Sample	Zeta potential / mV (*)
WS_2/SC	- 55
MoS_2/SC	- 47
MWNT/TTAB	+ 37

(*) Uncertainty within ± 5%.

Figure S1.4. Dispersion curves obtained for TMDs/SC systems (**a**) and zeta potential determined at the maximum dispersibility point (**b**).

Section S2: Further electrochemical data

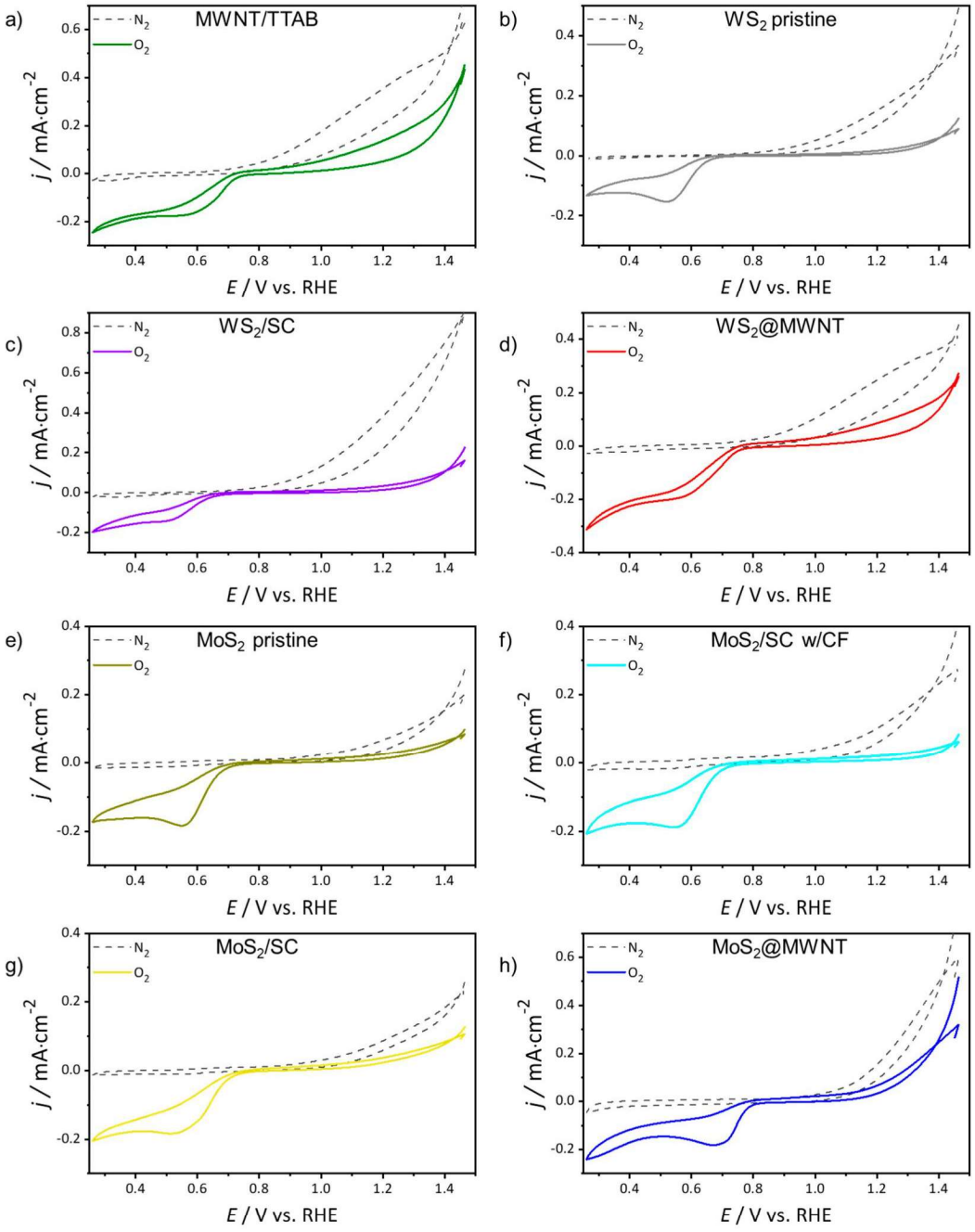

Figure S2.1. CVs of **a**) MWNT/TTAB, **b**) WS_2 pristine, c) WS_2/SC, **d**) WS_2@MWNT, **e**) MoS_2 (pristine), **f**) MoS_2/SC w/CF, **g**) MoS_2/SC (without CF), and **h**) MoS_2@MWNT obtained in N_2- (dashed line) and O_2-saturated (full line) 0.1 mol·dm^{-3} KOH solution, at $v = 0.005$ V·s^{-1}.

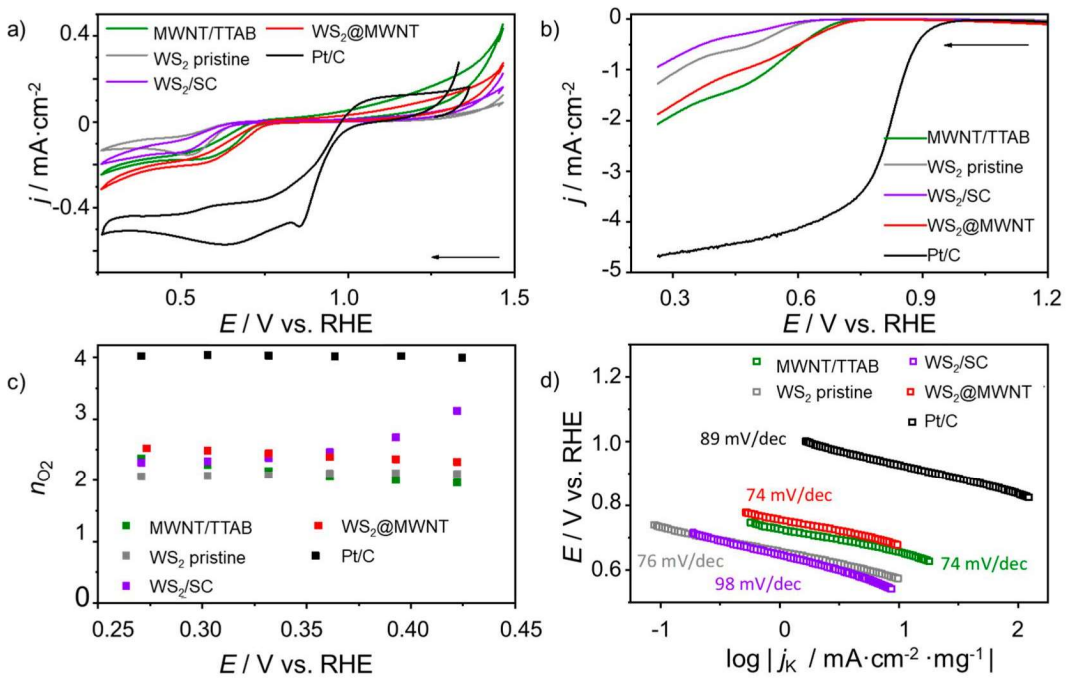

Figure S2.2. Electrochemical studies of Pt/C, WS_2@MWNT nanocomposite, and its building blocks, WS_2 (pristine), WS_2/SC and MWNT/TTAB: **a**) CVs (O_2-saturated 0.1 mol·dm^{-3} KOH, v = 0.005 V·s^{-1}); **b**) LSVs at 1600 rpm (O_2-saturated 0.1 mol·dm^{-3} KOH, v = 0.005 V·s^{-1}); **c**) n_{O2} at different potentials; **d**) Tafel plots.

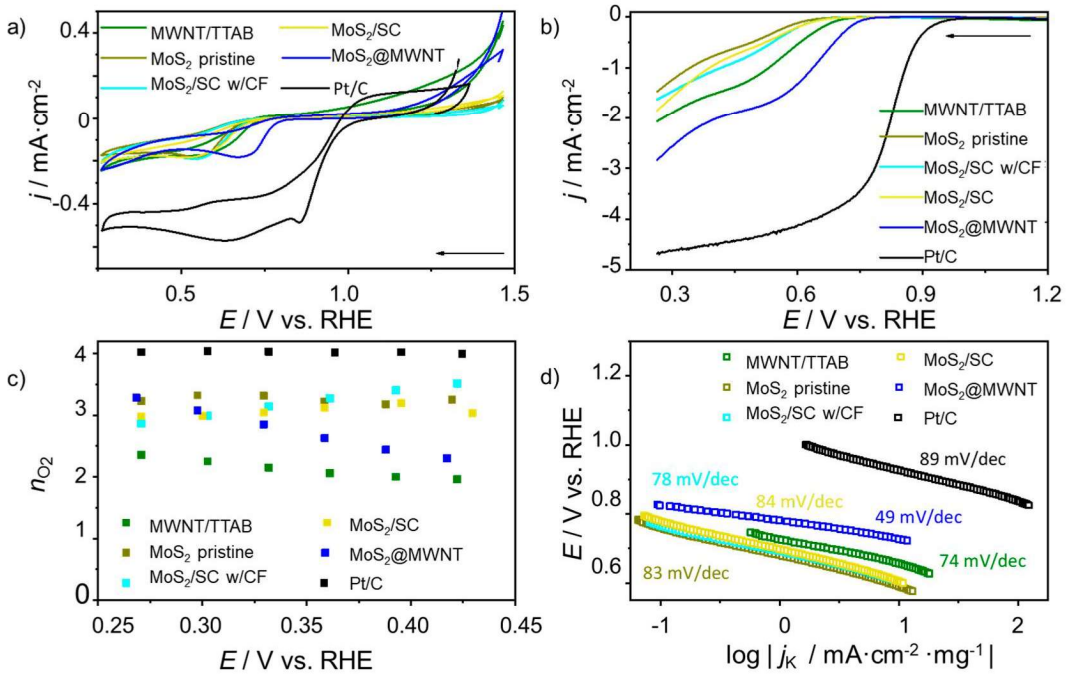

Figure S2.3. Electrochemical studies of Pt/C, MoS_2@MWNT nanocomposite, and its building blocks, MoS_2 (pristine), MoS_2/SC w/CF, MoS_2/SC (without CF), and MWNT/TTAB: **a**) CVs (O_2-saturated 0.1 mol·dm^{-3} KOH, v = 0.005 V·s^{-1}); **b**) LSVs at 1600 rpm (O_2-saturated 0.1 mol·dm^{-3} KOH, v = 0.005 V·s^{-1}); c) n_{O2} at different potentials; d) Tafel plots.

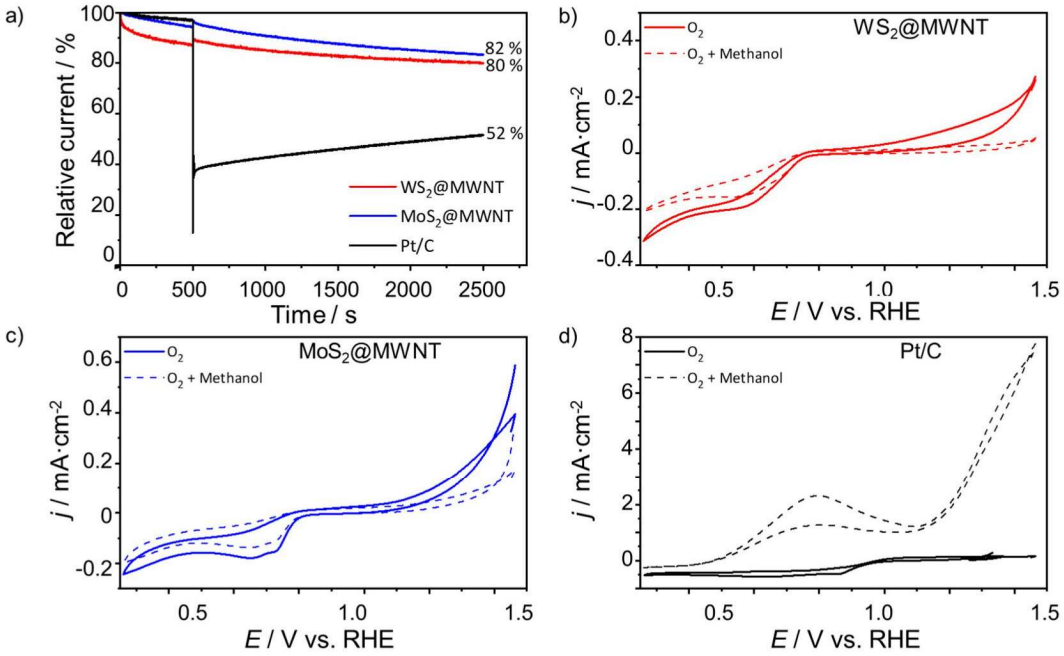

Figure S2.4. Methanol resistance studies: **a**) chronoamperometric responses of the WS_2@MWNT, MoS_2@MWNT and Pt/C materials with the addition of 0.5 mol·dm^{-3} methanol (at 500 s); **b**) CV of WS_2@MWNT before and after methanol addition; **c**) CV of MoS_2@MWNT before and after methanol addition; **d**) CV of Pt/C before and after methanol addition.

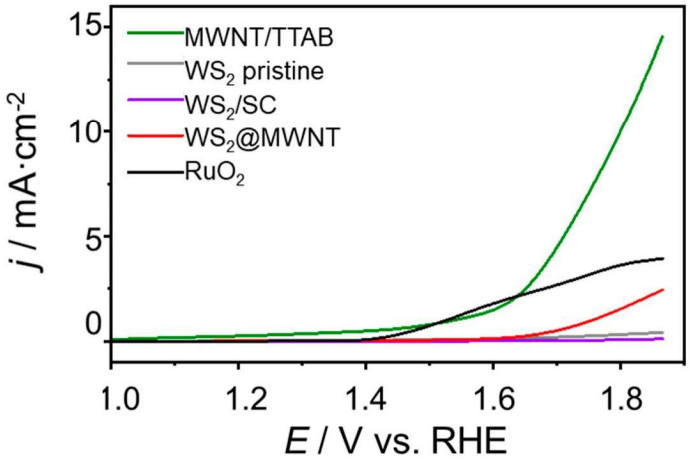

Figure S2.5. OER polarization curves obtained by LSV (O_2-saturated 0.1 mol·dm^{-3} KOH, v = 0.005 V·s^{-1}, 1600 rpm) for MWNT/TTAB, WS_2 (pristine), WS_2/SC, WS_2@MWNT and RuO_2.

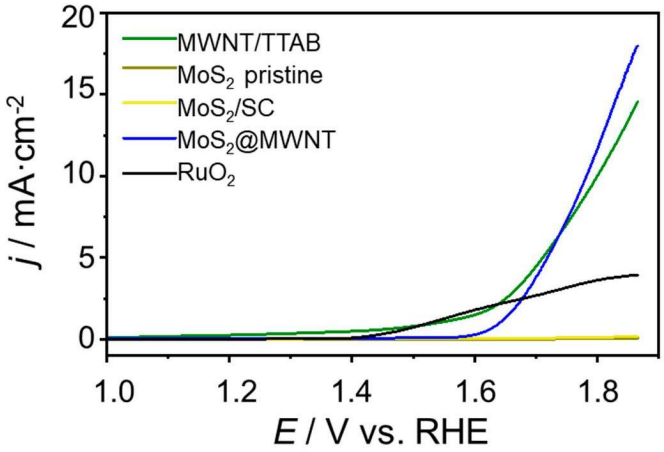

Figure S2.6. OER polarization curves obtained by LSV (O_2-saturated 0.1 mol·dm^{-3} KOH, v = 0.005 V·s^{-1}, 1600 rpm) for MWNT/TTAB, MoS_2 (pristine), MoS_2/SC, MoS_2@MWNT and RuO_2.

Table S2.1. ORR activity parameters (E_{onset}, j_L, and n_{O2}) for MWNT/TTAB, WS_2 pristine, WS_2/SC, WS_2@MWNT, MoS_2 (pristine), MoS_2/SC w/CF, MoS_2/SC, and MoS_2@MWNT.

Sample	E_{onset} / V vs. RHE (5% of j_{max})	E_{onset} / V vs. RHE (j = 0.1 mA·cm^{-2})	j_L / mA·cm^{-2}	n_{O_2}
MWNT/TTAB	0.68	0.68	−2.07	2.13
WS_2 pristine	0.62	0.60	−1.27	2.09
WS_2/SC	0.61	0.57	−0.94	2.36
WS_2@MWNT	0.71	0.70	−1.87	2.41
MoS_2 pristine	0.63	0.62	−1.63	3.25
MoS_2/SC w/CF	0.64	0.63	−1.51	3.20
MoS_2/SC	0.64	0.63	−1.90	2.81
MoS_2@MWNT	0.73	0.74	−2.74	2.87

Table S2.2. OER activity parameters (η_{10}, j_{max}, and $j_{1.8}$) for MWNT/TTAB, WS_2 pristine, WS_2/SC, WS_2@MWNT, MoS_2 pristine, MoS_2/SC w/CF, MoS_2/SC, MoS_2@MWNT, and RuO_2.

Sample	η_{10} / V (j = 10 mA·cm^{-2})	j_{max} / mA·cm^{-2}	$j_{1.8}$ / mA·cm^{-2}
MWNT/TTAB	0.59	14.55	10.15
WS_2 pristine	-	0.42	0.32
WS_2/SC	-	0.12	0.076
WS_2@MWNT	-	2.45	1.57
MoS_2 pristine	-	0.071	0.039
MoS_2/SC	-	0.17	0.12
MoS_2@MWNT	0.55	17.96	11.88
RuO_2	-	3.94	3.64

References

1. Loos, J.; Grossiord, N.; Koning, C.E.; Regev, O. On the fate of carbon nanotubes: Morphological characterisations. *Compos. Sci. Technol.* **2007**, *67*, 783–788.
2. Saito, R.; Tatsumi, Y.; Huang, S.; Ling, X.; Dresselhaus, M.S. Raman spectroscopy of transition metal dichalcogenides. *J. Phys. Condens. Matter* **2016**, *28*, 353002.
3. Zhang, X.; Qiao, X.-F.; Shi, W.; Wu, J.-B.; Jiang, D.-S.; Tan, P. Phonon and Raman scattering of two-dimensional transition metal dichalcogenides from monolayer, multilayer to bulk material. *Chem. Soc. Rev.* **2015**, *44*, 2757–2785, doi:10.1039/c4cs00282b.

4. Abreu, B.; Rocha, J.; Fernandes, R.M.; Regev, O.; Furó, I.; Marques, E.F. Gemini surfactants as efficient dispersants of multiwalled carbon nanotubes: Interplay of molecular parameters on nanotube dispersibility and debundling. *J. Colloid Interface Sci.* **2019**, *547*, 69–77.

Chapter 4 Conclusions and Future Perspectives

4.1 Main conclusions

The combination of nanomaterials to build 3D composites is an emerging research topic in a wide range of scientific and technical areas, from colloid and interface science to material science, and nanotechnology. The building of these structures usually involves three main tasks, that constituted the backbone of this work: i) preparation of the building blocks; ii) fabrication of the composite and iii) application-related studies. For the first task, a strictly controlled procedure, previously developed by our group, was applied to disperse multiwalled carbon nanotubes and optimized to exfoliate and disperse graphite, graphene nanoplatelets and three transition metal dichalcogenides, namely molybdenum (IV) disulfide, tungsten (IV) disulfide and molybdenum selenide. These systems were systematically studied, allowing insight on the molecular aspects that govern surfactant/nanomaterial interactions and opening the path for the optimization of these systems in the future.

First, multiwalled carbon nanotubes were exfoliated and non-covalently functionalized using gemini surfactants (12-*s*-12, 14-*s*-14 and 16-*s*-16, *s* = 2, 6, 12 for the C12 and C14 tails, and *s* = 2, 12 for the C16 tail) and their monomeric analogues (DTAB, TTAB and CTAB). It was observed that lower concentration of gemini surfactant is required to disperse the same amount of MWNT compared to the monomeric analogue. However, the maximum MWNT concentration dispersed is similar. Comparing the gemini surfactants, although the dispersion effectiveness appears to be independent of the spacer and tail length, the concentration of surfactant at which the $c_{MWNT,max}$ is attained reduces with increasing spacer length. Thus, the spacer length is deemed to be the key structural parameter that dictates the dispersion efficiency; for higher spacer lengths, the tail effect is masked. Furthermore, and importantly, this study suggested that the dispersibility process is independent of the assembly state of the surfactant (i.e. unimer or micellar form).

The dispersibility process of 1D carbon nanotubes was compared with that of 2D nanocarbon materials in another study, by using two different surfactants, sodium cholate and TX-100 in strictly controlled processing conditions. Regarding the preparation of the layered materials, the first step was the exfoliation of graphite – the cost-effective bulk reservoir of graphene. Additionally, commercial graphene nanoplatelets were dispersed, for further comparisons. One of the most important outcomes was that a master dispersion curve was found for 5 of the 6 systems studied (with the exception of the MWNT/TX-100 system), indicating that dispersibility process follows common fundamental aspects for 1D and 2D nanocarbons. Structural characterization confirmed the obtention of few-layer graphene from graphite.

Nonionic polymers and polyelectrolytes are widely applied to build composite materials. The interaction of polymers and surfactants brings about interesting features that led us to conduct the next part of this work. Several polymer/surfactant systems were studied, comparing the influence of ionic surfactants interacting with non-ionic polymers (PVP+SDBS and PVP+CTAB), and the effect of polyelectrolytes interacting with a neutral surfactant (PDDA+TX-100 and PAS+TX-100). Interestingly, synergistic effects are found for PVP/CTAB and PAS/TX-100 systems when the surfactant concentration is fixed at the *cdc*. For the first system, the surfactant interaction at the hydrophobic moieties of the polymer causes the chains to uncoil, stretching the polymer and enhancing the adsorption at the nanotube surface. For the PAS/TX-100 system, the surfactant likely adds hydrophobic segments to the hydrophilic polymer, increasing the affinity with the carbon nanotube and improving the effectiveness of the system by a factor of 6. The non-covalent functionalization of the MWNTs was confirmed by zeta potential.

As an alternative to graphene, a similar comparative study was performed for other class of layered materials – transition metal dichalcogenides. Three materials with general structure X-M-X were selected, to compare not only the surfactant effect, but also the influence of the metal (M) and chalcogenide (X) on the dispersion of these materials. The charge of surfactant plays an important role in TMD dispersibility, due to the negative charge shown by the suspended nanomaterials. Interestingly, the results suggest that the TMD feature that rules dispersibility varies with surfactant concentration: at low c_s, the metal seems to have a stronger effect; however, the chalcogen governs the maximum concentration of TMD dispersed. Structural characterization indicated that the applied methodology yields well-dispersed, few-layered nanosheets of TMDs.

The preparation of well-dispersed, non-covalently functionalized 1D and 2D nanomaterials based on a robust methodology allowed their applicability in composite fabrication. Using electrostatic attractive interactions as the as driving force for composite assembly, two procedures were applied to build the 3D structures: i) oppositely charged MWNT and GnP aqueous dispersions were mixed and sonicated together, followed by deposition in a membrane under vacuum filtration (bulk method); ii) identical aliquots of the dispersions were added alternately in a membrane, under vacuum filtration, in an adapted layer-by-layer approach. For each procedure, two combinations of 1D and 2D systems were selected (based on the results of the first part of this project), namely MWNT/TTAB@GnPs/SC and MWNT/PVP-CTAB@GnPs/SC. Both the dispersant and building method play a relevant role on the organization of the final nanocomposite, with the combination MWNT/PVP-CTAB@GnPs/SC built by the adapted layer-by-layer

approach showing the most organized structure. The applicability of the four composites as electrocatalysts for the oxygen reduction reaction was evaluated. Although their performance was modest and inferior to the state-of-the-art catalyst, important comparisons and effects were addressed: i) the material composition has a stronger influence in ORR performance than the building method, with the materials containing polymer showing a slightly better ORR activity; ii) regarding the material stability, bulk composites present better results, which can be attributed to the lower specific surface area (suggestive of a higher packing of the MWNTs and GnPs in the final structure). The four materials showed selectivity towards the indirect pathway (or 2-electron) oxygen reduction. This selectivity was evaluated through RRDE, confirming that high amounts of H_2O_2 are produced.

Considering the higher stability of the composites built through the bulk procedure and the simplicity of the process, this methodology was applied to build TMD@MWNT structures. Although the materials built with WS_2@MWNT presented poor results for oxygen reactions, when the metal of the TMD was changed interesting effects appeared. The MoS_2@MWNT composite yields better results for both ORR and OER than the building blocks, which can be interpreted as synergism from the combination of the 1D and 2D nanomaterials. This nanocomposite displays no selectivity towards the 2- or 4-electron mechanism of ORR (with a value of n_{O2} close to 3). Combined with the good OER activity obtained, these results open a route to further performance improvement.

In conclusion, in this work, experimental developments and conceptual insights were directed to the exfoliation and non-covalent functionalization of nanomaterials, ultimately aiming at their application as building blocks for functional 3D structures. With the selected systems, two simple, reproducible, time-saving, and environmental-friendly methodologies to build 3D composites were established, using electrostatic attraction as the driving force of assembly. One of the methodologies was applied with different 2D materials, proving the applicability beyond the first tests. Application-related studies were carried out, providing understanding on the influence of building method and dispersant on the electrochemical performance of the composites.

4.2 Future perspectives

The research work developed in this thesis left some open questions and further research opportunities. Two major research lines could be explored. Firstly, regarding the fundamental understanding of the nanomaterial dispersion using surfactants (or polymers), it would be interesting to expand the methodology to other layered materials (e.g. clays), to investigate the existence of common features in the dispersion process beyond the nanomaterials covered in this work. Secondly, the methodologies developed to build the composite materials pave the way for innumerous combinations of nanomaterials, due to the relative simplicity of the procedure and the versatility of the surfactant-assisted non-covalent functionalization of the hard surfaces. These composites could be further tested for a wide range of applications.

Regarding the composites built in this work, the MWNT/GnPs composites exhibit low BET surface areas, suggesting a strong packing of the materials. This feature may be explored in the context of components for electronic devices, or mechanical reinforcement of materials. Tribological studies could also be carried using the materials built via layer-by-layer, taking advantage of their parallel-type organization.

The electrocatalytic studies conducted throughout this work indicated the selectivity of the composites for the oxygen reduction through the indirect pathway, generating hydrogen peroxide. Electro-Fenton studies could give further information on the applicability of the materials.